UNIVERSIDAD POLITÉCNICA DE CARTAGENA

DEPARTMENT OF COMMUNICATIONS AND INFORMATION TECHNOLOGIES

UNIVERSITDAD POLITÉCNICA DE CARTAGENA

E.T.S.I.T

Analysis and Design of Hybrid Leaky-Wave Antennas Loaded with Frequency Selective Surfaces

(Doctoral Thesis)

Dissertation written by

María García Vigueras

under the supervision of

Dr. José Luis Gómez Tornero

Cartagena, July 2012

Universidad Politécnica de Cartagena

DT-12

CONFORMIDAD DE SOLICITUD DEAUTORIZACIÓN DE DEPÓSITO DE TESIS DOCTORAL POR EL/LA DIRECTOR/A DE LA TESIS

D. José Luis Gómez Tornero Director/a de la Tesis doctoral "Analysis and Design of Hybrid Leaky-Wave Antennas Loaded with Frequency Selective Surfaces"

INFORMA:

Que la referida Tesis Doctoral, ha sido realizada por Dª María García Vigueras, dando mi conformidad para que sea presentada ante la Comisión de Doctorado.

La rama de conocimiento por la que esta tesis ha sido desarrollada es:

- ☐ Ciencias
- ☐ Ciencias Sociales y Jurídicas
- ✓ Ingeniería y Arquitectura

En Cartagena, a 21 de Junio de 2012

LOS/LAS DIRECTORES/AS DE LA TESIS

Fdo.: José Luis Gómez Tornero

COMISIÓN DE DOCTORADO

Universidad Politécnica de Cartagena

DT-13

CONFORMIDAD DE DEPOSITO DE TESIS DOCTORAL POR LA COMISIÓN ACADÉMICA DEL PROGRAMA

D. Fernando D. Quesada Pereira, Presidente/a de la Comisión Académica del Programa "Tecnologías de la Información y las Comunicaciones"

INFORMA:

Que la Tesis Doctoral titulada, **"Analysis and Design of Hybrid Leaky-Wave Antennas Loaded with Frequency Selective Surfaces ",** ha sido realizada por Dª. María García Vigueras, bajo la dirección y supervisión del Dr. José Luis Gómez Tornero, dando su conformidad a la misma la Comisión Académica, con la finalidad de que sea presentada ante la Comisión de Doctorado.

La Rama de conocimiento por la que esta tesis ha sido desarrollada es:

□Ciencias
□Ciencias Sociales y Jurídicas
X Ingeniería y Arquitectura

En Cartagena, a 21 de Junio de 2012

EL PRESIDENTE DE LA COMISIÓN ACADÉMICA DEL PROGRAMA

Fdo: Fernando D. Quesada Pereira

COMISIÓN DE DOCTORADO

"Cuando creíamos que teníamos
todas las respuestas, de pronto,
cambiaron todas las preguntas."

Mario Benedetti

Acknowledgements

La realización de esta tesis ha significado para mí uno de los periodos de mayor crecimiento personal y profesional. Durante este proceso de evolución y cambios, he contado con el cariño, la ayuda y el apoyo de grandes personas, lo que me hace sentir profundamente afortunada.

Sin lugar a dudas quiero comenzar por José Luis; tu intuición y criterio han sido fundamentales en este proyecto. Gracias por haber confiado en mí, compartiendo desde el primer día tanta ilusión, tiempo y esfuerzo. Espero poder seguir aprendiendo contigo, dire.

También ha sido inestimable la ayuda de los profesores George Goussetis, Alejandro Melcón, Paco Mesa, Paco Medina, Jay Guo, Andrew Weily y Vincent Fusco. Gracias por vuestro apoyo científico y humano, en especial a Paco Mesa, por tus sabios consejos y por brindarme tu amistad.

Gracias a mis compañeros de laboratorio y amigos: Alejandro, Attieh, Conchi, José Antonio, Jorge, Manuel, Mónica, Pablo de Lara, Raúl y Sebas. Con vosotros el doctorado ha sido mucho más que un trabajo, por vuestro buen humor, compañía, las sonrisas cómplices de buenos días, los ratos en Calacortina, los juegos de sillas, cafés, conciertos, congresos… A JS, por hacerme de guía y también un hueco en su corazón.

Agradezco el apoyo de todos los profesores del grupo GEAT, del departamento TIC y de la UPCT, de los que tanto he aprendido durante la carrera, y después como compañeros. Me gustaría resaltar a José Víctor, David, Fernando, Jorge, Joan, Ramón, Leandro y Juan Morales, por escucharme, motivarme y hacerme el camino un poco más fácil en momentos clave.

A los que me descubrieron la magia de Sevilla durante mi estancia y ahora cuidan de la parte de mí que permanecerá siempre allí: Armando, Paco, Ana, Raúl, Manu, María, Rafa y Josemi.

To my Greek family, for receiving me with such generosity in Belfast, for taking so good care of during my research stay, cheering me up in the distance, and celebrating with me the end of this thesis.

A mis imprescindibles, mis hermanas de vida: Eli, Luci, Mar y Sonia. A Ángel, Juan, Julia, Antonio, Ana, Elena, Espe y Pablo, porque, como dice la película "*tu país son tus amigos, y eso sí se extraña*".

Finalmente, quiero agradecer a mi familia su paciencia y cariño incondicionales; por llenar mi vida de sentido, alegría, retos e ilusiones, a vosotros os dedico esta tesis.

Contents

Chapter 1:

General introduction

1.1 Context and objectives

1.1.1 High gain antennas

Since the birth of satellite communications and the development of radar during World War II, considerable research and progress in high gain antennas have been conducted. Gain is an antenna property which measures its ability to efficiently distribute the energy input through space [Balanis 2005]. High gain antennas are those which have the ability to efficiently direct the injected power in a desired direction of free space, or equivalently, to receive energy preferentially from a desired direction. Thus, gain is a measure that takes into account the performance of an antenna in terms of directivity and efficiency [Johnson 1993], [Balanis 2005]. It is well known that, at a fixed frequency, the antenna gain is closely related to its radiating aperture size [Johnson 1993], [Balanis 2005], for this reason, the radiators that provide high gain are normally electrically long.

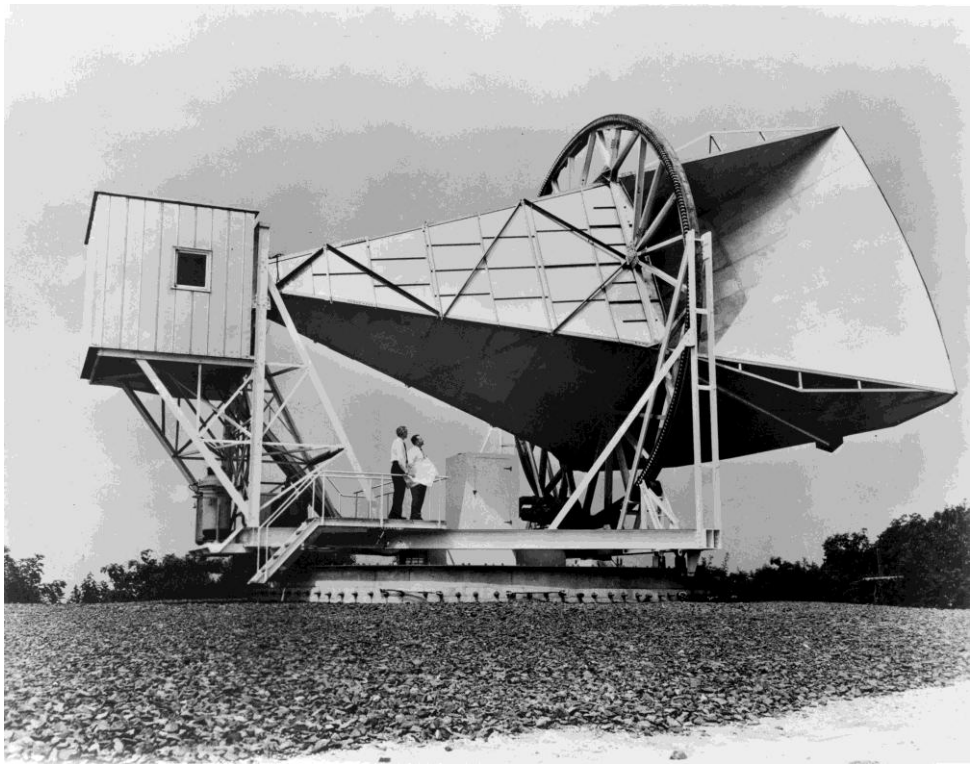

Fig. 1.1.1 Horn-reflector antenna invented by Albert Beck and Harald Friis in 1941 and developed in 1961 by D. C. Hogg at Bell Labs (courtesy: Great Images in NASA).

A variety of antenna types with enhanced gain and complexity has been proposed, the most notable examples are **reflector** antennas, **lens** antennas, **phased arrays**, **reflectarrays**, and more recently **Fabry-Perot** leaky-wave antennas ([Johnson 1993], [Oliner 2007], [Jackson 2008]). The first design used for satellite communications is the horn-reflector antenna shown in Fig. 1.1.1, which was constructed in the 1960s and consists of a reflector mounted in the mouth of a horn antenna. The high gain antennas developed to date span a wide range of applications such as mobile telephony, satellite television, radio astronomy and other deep-space purposes, military radar, cloud/precipitation radars, microwave communications, terrestrial microwave relay communication systems and other commercial applications.

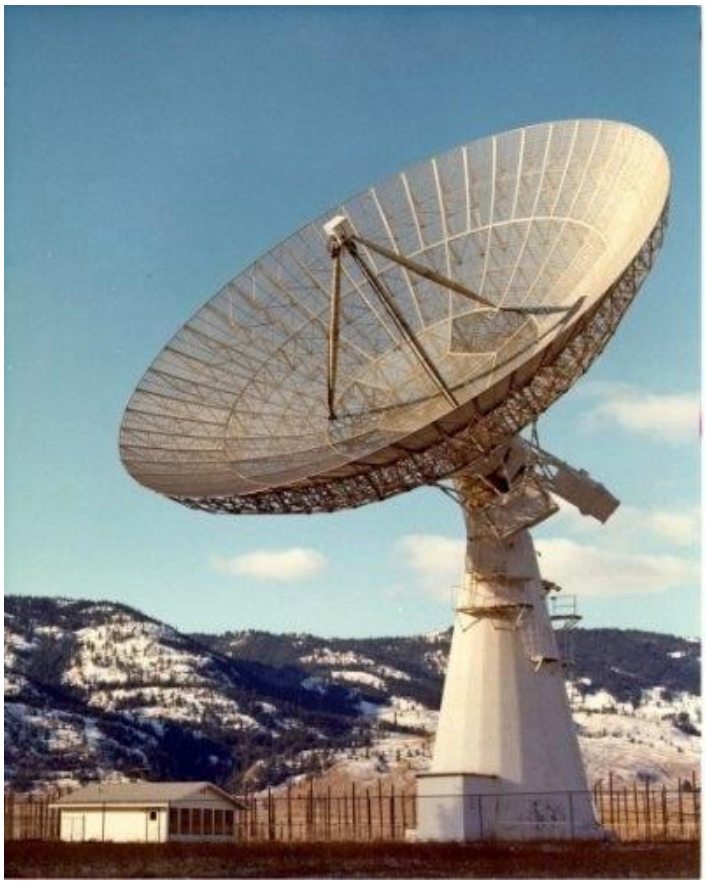

Fig. 1.1.2 Parabolic antenna in Canada, Institute of Astrophysics of Herzberg, radio astrophysical observatory (courtesy: ASTROLAB of the National park of the Mount-Mégantic).

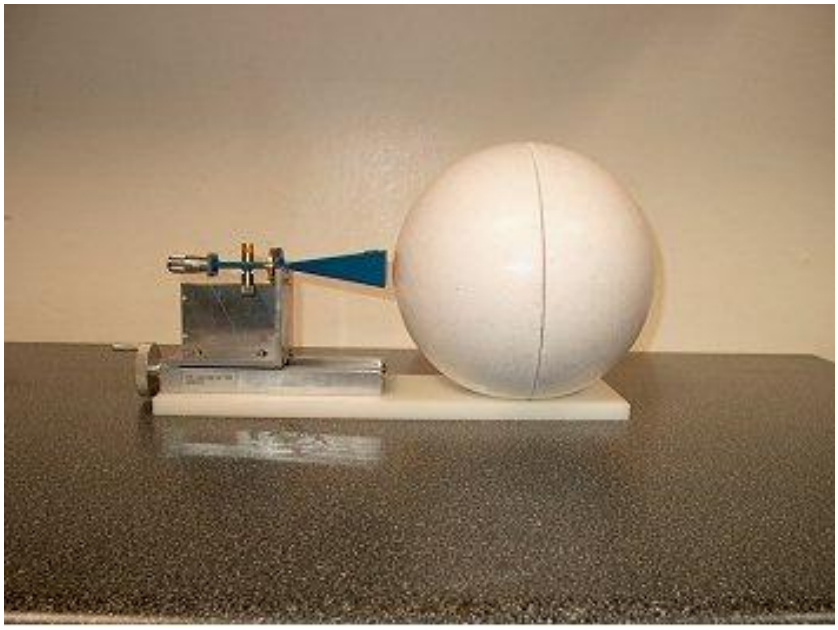

Fig. 1.1.3 Luneburg lens antenna (courtesy: Rozendal Associates, Inc.).

Conventional **reflector antennas** are the high-gain radiators most widely used. They provide high gain, narrow beamwidth and wide bandwidth (since they have no resonant elements) while having low losses and sidelobe control [Johnson 1993. Ch. 17]. The reflector shape is generally a paraboloid of revolution, as the one shown in Fig. 1.1.2. Dielectric **lenses** are also used as collimating elements in microwave antennas [Johnson 1993, Ch. 16], playing a similar role to that of reflectors. Both, lenses and reflectors are externally fed by an antenna which is usually simpler and smaller, such as a horn (see Fig. 1.1.2). Thus, these two types of antennas are generally bulky in size and beam steering is only mechanically achieved. Thus, a more flexible alternative is the **phased array** [Johnson 1993, Ch. 20] which has been traditionally used for military radar applications for many decades. Enhanced directivity is here obtained by grouping radiators into an array. In particular, phased arrays consist of a planar array of radiators that are individually fed with a phase and amplitude that can be controlled in order to produce a radiated beam with a desired shape. An interesting example of a phased array mounted on a Galileo satellite is shown in Fig. 1.1.4. The direction of the radiated beam can be swept by electronically varying the phase of the array components, producing a moving radiation pattern without the need of mechanical movements and in planar technology. This electronic beam steering is orders of magnitude faster than the traditional reflectors based on mechanical rotation. However, phased arrays need many microwave phase shifters, a control signal for each of them and both a low noise amplifier and a power amplifier at each element for receive and transmit. For these reasons, high gain phased arrays composed by a considerable amount of elements may not be feasible as they can be quite expensive.

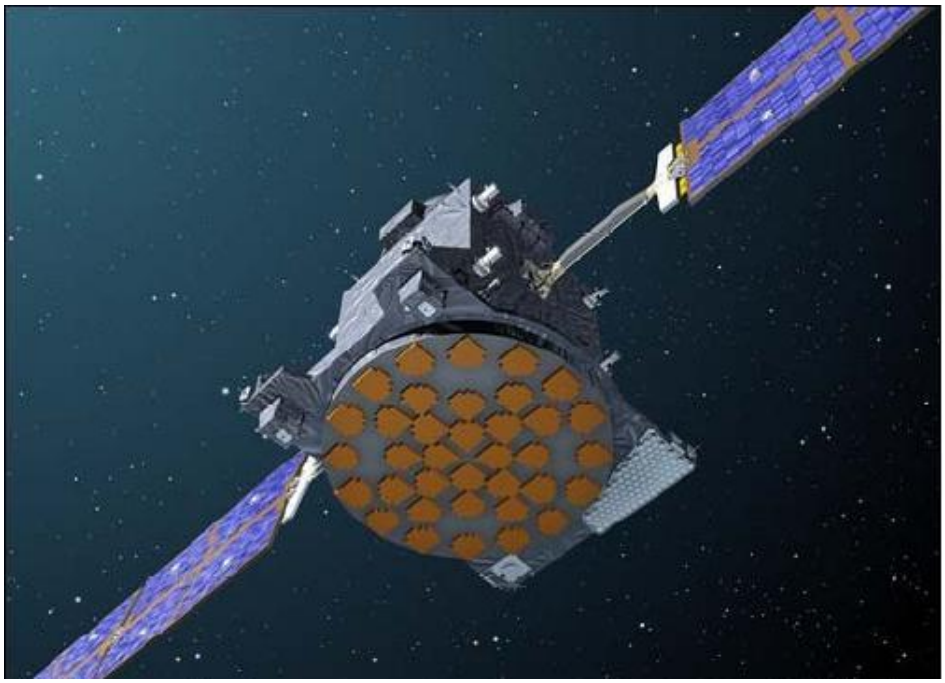

Fig. 1.1.4 Bottom view of a Galileo satellite showing the phased array antenna elements (courtesy: ESA)

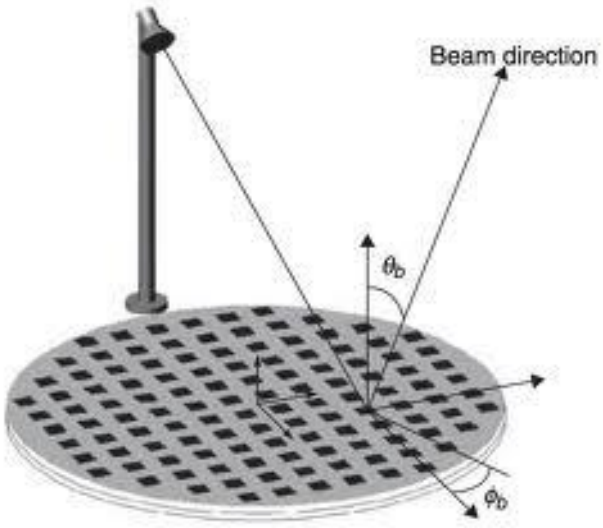

Fig. 1.1.5 General scheme of a printed reflectarray antenna (from [Huang 2008]).

Reflectarrays combine the advantages of both phased arrays and parabolic reflectors, and thus, these high gain antennas have found numerous applications such in satellite communications, contoured beam space antennas or radar. Their operation principle is explained in detail in books such as [Huang 2008]. A reflectarray basically works like a conventional reflector antenna where the reflector is replaced by a planar printed surface (its general scheme is depicted in Fig. 1.1.5.). Here, the reflected radiation pattern is directed by controlling the

reflection phase produced by each of the elements of the planar reflector. Therefore, by properly synthesizing a phase distribution in the array, it is possible to obtain a desired reflected beam. Compared to reflectors and lenses, reflectarrays provide the advantages of being low profile and having low fabrication cost. However, the main drawback of these antennas is their narrow bandwidth, which is inherent to printed resonant structures (the response of the elements in the array is very sensitive to frequency) [Collin 2000], [Huang 2008]. At present, the interest in reflectarrays is mainly focused in its reconfigurability. The scanning of the radiated beam at a fixed frequency can be achieved by employing reconfigurable cells which make use of PIN or varactor diodes [Sievenpiper 2003], [Hum 2007], ferroelectric materials [Romanofsky 2006], liquid crystal [Hu 2008] or MEMS [Perruisseau-Carrier 2008]. These elements/materials allow the electronic control of the radiation features, at the expense of a cost increase.

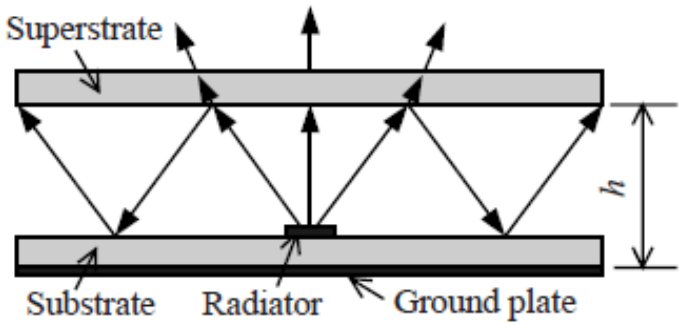

Fig. 1.1.6 Schematic diagram of a PRS LWA (from [Liu 2009]).

Highly directive radiation patterns can also be obtained using **Fabry-Perot Leaky-Wave Antennas** (FP LWAs). Their general structure is shown in Fig. 1.1.6, and it basically consists of a resonant cavity created between a Partially Reflective Surface (PRS) and a metal-backed substrate. The height of this cavity determines the operation frequency of the antenna. This configuration is fed by a simple low-directive radiator that is embedded inside the structure (see Fig. 1.1.6). The waves launched by this source become leaky modes [Oliner 1993] of the resonant cavity due to the leakage allowed by the top partially reflective superstrate. This simple mechanism of exciting a leaky wave allows to illuminate a large radiating area, and consequently, to achieve high gain. This type of structure is named as Fabry-Perot

resonator due to its analogy with optical interferometer cavities, where the waves are bounced forth and back between two partially reflective mirrors. Moreover, they are also commonly referred to as PRS antennas. The integrated feeding mechanism of this antenna involves a considerable reduction of volume, in comparison to reflectarrays, dielectric lenses and conventional reflectors, which are externally fed. In addition, FP LWAs become an attractive solution also when they are compared to arrays, which need much more complicated feeding networks.

This dissertation is focused on the efficient and systematic synthesis of this last type of high gain antenna. Although detailed background knowledge and state-of-the-art revision is provided along the following chapters, a brief overview is now given in order to clarify the context that has motivated this Ph. D. The main principles of FP LWAs were firstly explained in [Trentini 1956], where several types of PRS were considered: an array of metallic patches, a metallic plate perforated with holes, and a one-dimensional array of metallic wires. Later, the enhancement of the directivity was explored using other PRS superstrates, such as one or more high permittivity dielectric layers [Jackson 1985, 1988, 1993], [Yang 1987], [Akalin 2002]. These structures have appeared in the literature as EBG antennas, since stacked dielectric layers form an Electromagnetic Bandgap (EBG) structure. Photonic bandgap materials have also been exploited to form FP cavities [Thèvenot 1999], [Temelkuaran 2000], [Biswas 2001] [Fehrembach 2001], [Cheype 2002]. In [Feresidis 2001], the attention was again brought back to PRS structures based on doubly periodic arrangement of printed-circuit scatterers. Other similar configurations were later proposed in [Zhao 2005-II and III], [Gardelli 2006], [Guérin 2006] and [Boutayeb 2006]. By that time, a general explanation of the working mechanism of PRS printed resonators was also given in [Zhao 2005-I]. That same year, it was proposed to replace the bottom metallic screen by a High Impedance Surface (HIS) to reduce the cavity height [Feresidis 2005]. Later, FP LWAs based on a wire medium were presented in [Lovat 2006-I and II] and [Burghignoli 2008]. Recently, many other papers can be found in the literature which exploit other types of FP structures, or where certain properties

are enhanced, such as polarization purity [Burghignoli 2010], or profile reduction [Mateo-Segura 2012].

All the examples of FP LWAs previously mentioned are uniform, which means that their geometry is invariant along the antenna length. However, by modulating the shape of the LWA along its length, many interesting new features can be achieved [Oliner 1993]. The process of modulating the propagation of leaky waves is called taper and implies a change of the natural antenna aperture illumination [Oliner 1993]. The first example of a tapered one-dimensional FP LWA can be found in [Honey 1959], were sidelobe level reduction was obtained as a result of the variation of the antenna geometry. However, the only attempts of two-dimensional tapering in FP LWAs were performed much later, pursuing gain and bandwidth enhancement [Yeo 2009], [Wu 2010]. In these works, no accurate control over the propagation of the leaky waves was performed, and the designs relied on full-wave simulations of the whole antenna. It must be noticed that, the characterization of these antennas using 3D full-wave models can be extremely computationally costly, due to the complexity of these resonant structures and due to the large electrical size of high gain antennas. In contrast, employing leaky-wave theory and characterizing the dispersion of the constituent leaky modes, the analysis and design of FP LWAs is highly accurate, efficient and less time consuming. It is worth highlighting that a tool which allows the efficient and systematic design of tapered FP LWAs has not been proposed yet.

1.1.2 Motivation and objectives

Despite the high amount of research carried out in the field of Fabry-Perot (FP) Leaky-Wave Antennas (LWAs), still, **no optimal FP LWA designs have been proposed that take full advantage of their physical dimensions**. More precisely, accurate solutions to optimize the illumination efficiency of the antenna radiating aperture have not been proposed so far. In addition, detailed analysis and systematic synthesis of prescribed aperture distributions on FP LWA designs have not been performed either.

The illumination or aperture efficiency of an antenna is the relation between the effective radiating area and the total physical area [Balanis 2005]. Thus, if we design a FP LWA with low aperture efficiency (for instance 25%), the effective radiating area is only a quarter of the physical aperture. Leaky waves decay exponentially when they propagate along uniform structures [Oliner 1993]. As a result, to produce a high-directive beam, one needs to oversize the surface of the PRS, leading to low aperture efficiency. This efficiency can be improved by increasing the PRS reflectivity, at the cost of decreasing the radiation efficiency and increasing the quality factor of the resonator which implies a bandwidth reduction [Alkhatib 2007]. Multiple fed FP LWAs have also been proposed to increase the bandwidth and illumination efficiency at the expense of a much more complex array feeding network [Weily 2007], [Leger 2005], losing one of the most interesting features of FP LWAs which is their simple feeding scheme. The use of double-layer PRS with slightly different resonant frequencies can extend the bandwidth; however, the reported gain and aperture efficiency are still deficient [Vu 2007], [Moustafa 2008]. Therefore, there seems to be a trade-off between radiation and aperture efficiencies in uniform FP LWAs. **In this dissertation it is aimed for the first time the efficient synthesis of tapered FP LWAs**. More precisely, we will focus here on the double-layered FP antenna proposed in [Feresidis 2005]; both periodic layers (PRS and HIS) will be modulated in order to obtain high radiation and aperture efficiencies. **The achievement of this goal would allow to synthesize any aperture illumination, and therefore, to design for the first time high gain FP LWAs which are highly efficient** (providing both, radiation and aperture efficiency rates over 80%).

In order to achieve the previous main objective, several specific steps have been followed progressively. Firstly, the periodic layers that form the PRS and HIS of the FP LWA must be properly characterized. It is of high importance that these layers are accurately modeled by equivalent pseudo-analytical closed-form expressions that can be later employed for the characterization of the whole FP structure. Secondly, the analysis and design of uniform FP LWA will be carried out. A complete dispersion analysis of the uniform structure will be performed in order to find the way to control the propagation of the constituent leaky waves. Finally, modulated (tapered) FP LWAs will be synthesized. Both in the second and third steps, the one-dimensional scenario will be firstly considered as an approximation of the two-dimensional one, and the applications of tapering in 1D and 2D FP LWA will be exploited.

Therefore, the previous general objective can be broken down to the following seven specific objectives that would together achieve the overall goal of the thesis:

O1. Characterization of printed dipole-based FSS by closed-form equivalent impedances.

O2. Dispersion analysis of EBG structures conceived from the insertion of dipole-based FSS inside rectangular waveguides.

O3. Development of a graphical user interface (GUI) for the easy insertion of data and systematic retrieval of results.

O4. Analysis and design of double-layer uniform one-dimensional Fabry-Perot leaky-wave antennas.

O5. Analysis and design of double-layer uniform two-dimensional Fabry-Perot leaky-wave antennas.

O6. Analysis and design of double-layer tapered one-dimensional Fabry-Perot leaky-wave antennas.

O7. Analysis and design of double-layer tapered two-dimensional Fabry-Perot leaky-wave antennas.

1.1.3 Framework of the research

This Ph. D. research has been carried out within the Group of Electromagnetism Applied to Telecommunications (GEAT) in the department of Information and Communication Technologies (TIC) at the Universidad Politécnica de Cartagena (UPCT), Cartagena, Murcia, Spain. The whole work has been supervised by Dr. José Luis Gómez Tonero.

Several prestigious institutions have collaborated with the development of this dissertation, which main contribution has been:

- Radio Frequency and Microwave Group of the School of Engineering and Physical Science at **Heriot-Watt University**, Edinburgh (UK): characterization of uniform Fabry-Perot leaky-wave antennas. More precisely, this work was done in collaboration with Dr. George Goussetis and Dr. Carolina Mateo Segura.

- Microwaves Group of the Faculty of Physics at the **University of Seville**, Seville (Spain): quasi-analytical modeling of frequency selective surfaces. This work was developed under the supervision of the professors Francisco Medina and Francisco Mesa.

- The Wireless Technologies Laboratory at the Commonwealth Scientific and Industrial Research Organisation (**CSIRO**), ICT Centre, Sydney (Australia): fabrication facilities and far-field measurements of versatile one-dimensional FP leaky-wave antennas. Professor Y. Jay Guo and Dr. Andrew Weily supervised all the process.

- The Institute of Electronics, Communications and Information Technology (ECIT) in **Queen´s University of Belfast**, Northern Ireland (UK): analysis and design of tapered Fabry-Perot leaky-wave antennas. This collaboration was possible thanks to Dr. George Goussetis and Prof. Vincent Fusco.

Moreover, the work has been developed within a UPCT program that has been awarded the "*Mention of Excellence*" by the Spanish Ministry of Education.

The work here presented is within the framework of the following research projects: TEC2007-67630-C03-02/TCM, from the *Ministerio de Industria, Turismo y Comercio* of Spain, 02972/PI/05, from the Fundación Séneca of Murcia, Spain and TEC2010-21520-C04-04/TCM, from the *Ministerio de Educación y Ciencia*.

The work has been fully financially supported by a four-year scholarship awarded from UPCT (ref. R578-08). The stages at the University of Seville and Queen´s University of Belfast have been funded also by UPCT (refs. PMPDI-UPCT-2010 and PMPDI-UPCT-2011, respectively).

1.2 Outline and original contributions

In this section, the organization of this thesis is described and some comments about the original contributions are provided and linked to each chapter.

Chapter 2: Frequency selective surfaces characterization by equivalent circuits

Description: The main aim of this chapter is the modeling by pseudo-analytical equivalent networks of printed periodic surfaces based on the doubly-periodic arrangement of dipoles. A brief introduction about Frequency Selective Surfaces (FSS) is firstly given. Later, two different approaches have been followed in order to perform FSS modeling: the first one is based on a pole-zero expansion, and the second one is based on waveguide discontinuities. A software tool that implements the first approach has been programmed in order to systematize the analysis of more complex structures which make use of FSSs inside rectangular waveguides. The fulfillment of the objectives O1, O2 and O3 listed in Section 1.1.2 is here pursued.

Original contribution: The equivalent circuits here developed are useful, not only for the analysis and design of FP LWAs, but also for other microwave devices that employ printed dipole-based frequency selective surfaces. These periodic

surfaces are here modeled as a function of frequency and geometry with an original pole-zero method. The dipoles length appears as a variable in the analytical dispersion equation, thus allowing for the first time, to perform efficient dispersion analysis as a function of the dipoles length with the only restriction of single Floquet mode propagation. The second approach proposed in this chapter, which is based on the physical modal decomposition of the electromagnetic fields around the scatterers (printed dipoles), is also completely original. This circuit model reproduces, for the first time, the exact behavior of the printed FSS from a very few full-wave simulations. Particularly, this model not only account for FSS conventional resonances but also for extraordinary ones. In addition, it provides a theoretical frame for understanding the qualitative performance of the patterned surface and to design devices based on such structures.

Chapter 3: Analysis and design of uniform double-layer Fabry-Perot LWA

Description: Firstly, it is given a summary of the basic concepts about leaky-wave antennas and a review of the different radiation mechanisms proposed so far. Later, it is presented an original one-dimensional (1D) double-layer Fabry-Perot LWA in hybrid technology that allows the flexible control over the propagation constant of the constituent leaky waves. Here it is explained how the pointing angle and beamwidth of the FP LWA can be independently controlled, and how the frequency scanning behavior can also be successfully controlled and enhanced. Experimental results on fabricated prototypes are reported showing very good agreement with the theoretical results. Finally, two-dimensional (2D) double-layer FP LWAs are analyzed and designed employing the tool developed in Chapter 2 by making an approximation towards one-dimensional structures. The fulfillment of objectives O4 and O5 from the list of Section 1.1.2 is here aimed.

Original contribution: A completely novel one-dimensional FP LWA is here presented, which main feature is that it provides independent control over the real and imaginary parts of the leaky wavenumber. This allows, for the first time, to control the beamwidth and pointing angle of a one-dimensional FP LWA, which is proven by experimental results. Also, efficient leaky-wave dispersion results for

the analysis and design of two-dimensional double-layer FP LWAs are obtained from a simple and novel transverse equivalent network. The accuracy and limitations of the proposed method are validated by comparing previously 2D FP antennas designed with full-wave analysis techniques.

Chapter 4: Synthesis of tapered double-layer Fabry-Perot LWA

Description: After a state-of-the-art review about the tapering of LWAs, in this chapter it is presented an efficient technique for the synthesis of tapered double-layer FP LWAs. This technique is employed to shape the near field patterns of 1D FP LWAs and reduce their sidelobes level for any desired scanning angle. Numerical and experimental results are shown in order to prove the efficiency of the synthesis approach. Later, the control of the illumination of both 1D and 2D FP LWAs which point at broadside is achieved. A quasi-uniform taper is here proposed in order to achieve high aperture efficiency, while assuring high radiation efficiency and to minimize diffraction and standing waves. Thus, objectives O6 and O7 from the list of Section 1.1.2 are here accomplished in this chapter.

Original contribution: An original synthesis technique is here presented, which is specifically suited to the design of tapered FP LWAs and that accurately takes into account the coupling between the geometrical parameters of the antenna and the complex leaky wavenumber. This approach involves the solution of two simple equations, implying a drastic computational cost reduction in comparison to the synthesis techniques that have been proposed so far. The previous approach allows the optimization of the aperture illumination and radiation efficiencies, both in 1D and 2D FP LWAs, which is here proposed and achieved for the first time.

Chapter 5: Final conclusions and perspectives

In this chapter, the main conclusions and results will be summarized, together with the discussion about the further research that this Ph. D. suggests.

Chapter 2:

Equivalent circuits for dipole-based frequency selective surfaces

Frequency selective surfaces play a key role in this dissertation due to the fact that they are employed to conceive an original and more complex type of structure (leaky-wave antenna) and therefore, their analysis and characterization is essential and will be developed in this chapter. Taking into account the general objectives listed in Chapter 1, the following ones will be aimed in this chapter:

O1. Characterization of printed dipole-based FSS by closed-form equivalent impedances.

O2. Dispersion analysis of EBG structures conceived from the insertion of dipole-based FSS inside rectangular waveguides.

O3. Development of a graphical user interface (GUI) for the easy insertion of data and systematic retrieval of results.

This chapter is organized as follows:

Firstly, a state-of-the-art review on Frequency Selective Surfaces (FSS), their applications and characterization will be given in **Section 2.1**.

Secondly, in **Section 2.2** it is explained a modified pole-zero technique which is proposed for the modeling of dipole-based FSS printed on stratified dielectric media. The main advantage of this approach is that the dipole length appears as a variable in the analytical equivalent impedance (in addition to frequency and wavenumber). This technique can be very useful for the efficient analysis and design of Electromagnetic Bandgap Structures (EBG) conceived from FSSs due to the fact that it allows to obtain geometry-dispersion curves.

The previous pole-zero method is applied in **Section 2.3** in order to characterize the dispersion of structures where FSSs are inserted inside a rectangular waveguide. In order to perform frequency and geometry dispersion analysis, a software tool has been developed using MATLAB®. Modal dispersion curves as a function of the dipoles length and frequency can be easily obtained with the only restriction of single Floquet mode propagation. In particular, two practical EBG structures have been analyzed: a waveguide loaded with a high impedance surface and a leaky-wave antenna using a partially reflective surface. The results obtained are compared with full-wave 2D and 3D simulations showing excellent agreement, thus validating the proposed technique and illustrating its utility for practical designs.

In **Section 2.4** the modeling of dipole-based FSS is performed by a more insightful equivalent circuit. In this case, the equivalent circuit comes up after taking advantage of the periodicity of the structures, which allows reformulating the original problem as a certain equivalent waveguide scattering problem. This approach helps to simplify the original complex electromagnetic problem and also allows for a good understanding of periodic surface behavior. In this case, no restriction over the operation modal regime is made, and the variables in the equivalent circuit are the frequency and wavenumber. This fact enables the analysis of electromagnetic bandgap structures composed by dipole-based FSS, not only in the conventional single mode operation regime, but also when grating

lobes appear. In addition, as no assumption on the length of the scatterers is made, both conventional and extraordinary FSS total reflection are characterized, as well as other high frequency effects such as Wood´s anomalies and grating lobes.

Finally, in **Section 2.5** the main conclusions and results will be summarized, together with the discussion about the achievement of the aimed objectives.

It is important to point out that the software tool explained in Section 2.3 will be employed in next chapters for the analysis and design of FSS-based leaky-wave antennas. Besides, as FSS are widely used, the equivalent circuits proposed in this chapter may significantly enhance the modeling and synthesis of many other practical devices, such as polarizers [Doumanis 2011 and 2012], dichroic mirrors [Besso 2003], reflectarrays [Huang 2007]… It is worth mentioning that, for the analysis of reflectarrays, an extended version of the pole-zero technique explained in Section 2.2 has already been recently published in [Florencio 2011].

2.1 Introduction

Frequency Selective Surfaces (FSSs) have recently attracted much interest in the field of engineering and physics due to the high amount of applications that they have found in fields such as the synthesis of microwave and optical filters/resonators and antenna enhancement. A FSS is generally any **surface construction which acts as a "filter" for plane waves**. Typical FSSs, such as the one shown in Fig. 2.1.1(a), usually consist of a doubly periodic arrangement of planar metallic scatterers (or its dual structure, periodic arrays of apertures made in a thin metallic surface). Many different shapes of the FSS elements have been proposed, some of them are shown in Fig. 2.1.1(b), the election depends on the FSS application. The scattered fields will exhibit resonances as the excitation frequency is varied. Particularly, these surfaces exhibit total reflection (patches) or total transmission (apertures) which generally occur when the size of the scatterer is an integer number of half wavelength. For conventional FSS operation, the size and shape of the array elements is tailored in order to control the characteristics of the first resonance. However, as it will be later explained, for subwavelength scatterers, a total reflection/transmission peak is also found. This latter resonance has been considered "extraordinary" since it is not directly related to the electrical length of the scatterers, but to the periodicity of the array.

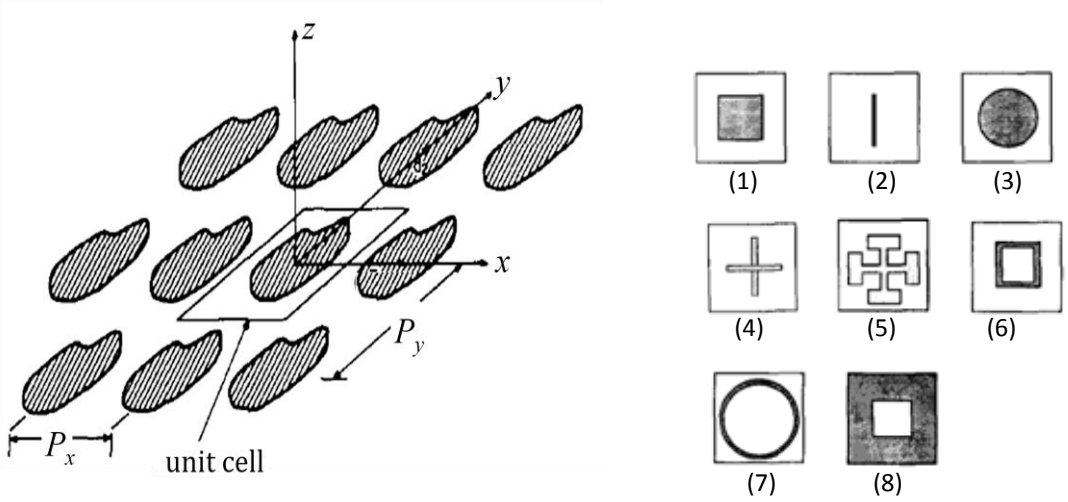

(a) (b)

Fig. 2.1.1 (a)Scheme of a patch-based free-standing FSS. (b)Some typical FSS unit cell geometries: (1) square patch, (2)dipole, (3)circular patch, (4)cross dipole, (5)Jerusalem cross, (6)square loop, (7)circular loop, (8)square aperture (Figs. 1 and 5 in [Mittra 1988]).

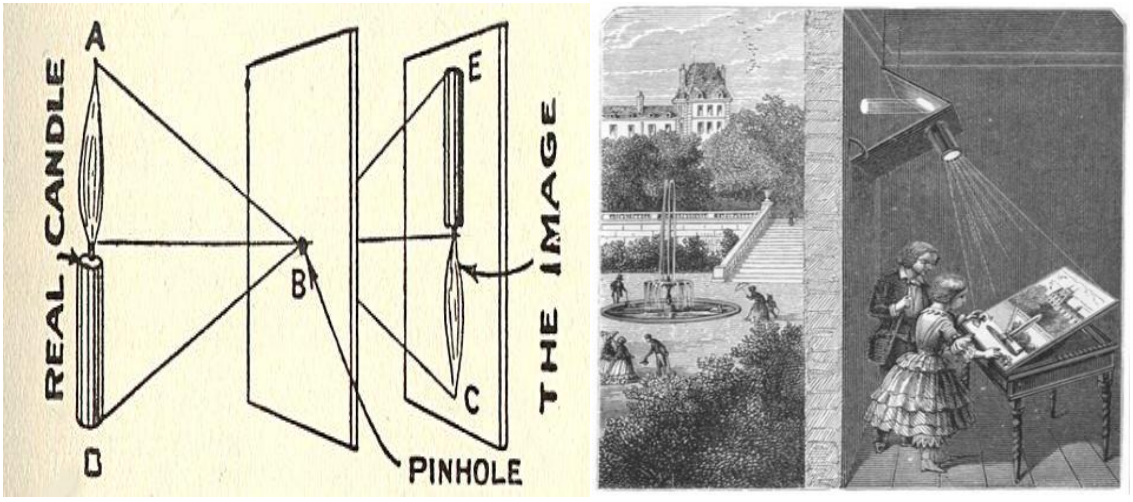

(a) (b)

Fig. 2.1.2 (a)Light transmission through a pinhole (b)Transfer of an image to a canvas in a *camera obscura*.

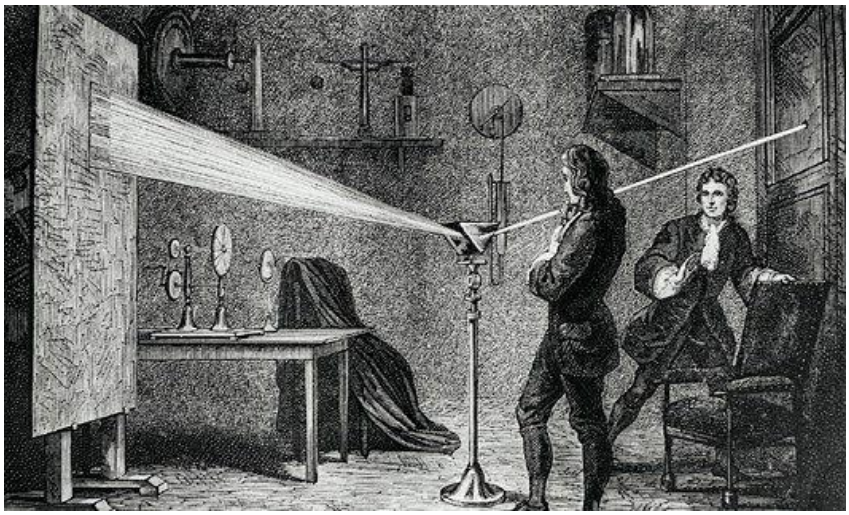

Fig. 2.1.3 Newton's prism experiments in 1660s, splitting light into its component colors.

The scattering of propagating waves at periodic gratings has been intensely researched for ages. Historically, **the principles underlying the physics of frequency selective surfaces directly evolve from the investigation of diffraction gratings in optics** ([Mittra 1988]). The simple case shown in Fig. 2.1.2(a) of light transmission through a hole in a screen, has aroused curiosity since Greek times. For example, in the form of obscure cameras, it became essential for the work of great painters such as Vermeer (see Fig. 2.1.2(b)). Since the seventeenth century, light propagation has inspired the work of brilliant mathematicians, astronomers, inventors, physicists, opticians and artists, such as Isaac Newton, James Gregory, Francesco Grimaldi, David Rittenhouse, Siméon Denis Poisson, Joseph von Fraunhofer, Gustav Kirchhoff, Christiaan Huygens, Robert Hook, Augustin Fresnel… A typical seventeenth century light experiment is shown in Fig. 2.1.3, where Newton proved that white light is a mixture of many different types of rays; each one is refracted at a slightly different angle and is responsible for producing a given spectral color. The principles of diffraction gratings were discovered by James Gregory, about a year after Newton's prism experiments, initially with artifacts such as bird feathers. Francesco Grimaldi introduced for the first time the “fourth manner” of propagation of light, which is “not only directly, and by refraction and reflection, but also by diffraction“, his book was published in 1665 ([Grimaldi 1665]). It was Rittenhouse who first reported that a noncontinuous surface can present different reflecting/transmitting properties for different operating frequencies

([Rittenhouse 1786]). He described how he discovered this phenomenon by observing the filtering of white light at a grating he had constructed from equally spaced hairs. The possibility of explaining diffraction effects on the basis of a wave theory was noticed in 1818, when Fresnel´s memoir on diffraction was published ([Meyer 1934]). He showed that diffraction can be explained by the application of Huygens´ wave theory together with the principle of interference. Later, in 1882, Kirchhoff provided an exact mathematical basis to Fresnel´s analysis. The subject has since then been extensively discussed by many writers.

periodic surfaces	operation regime	periodicity of the array	common frequency range
diffraction grating	Multimode (grating lobes)	greater than the wavelength	optics
FSS	single mode	comparable to the wavelength	microwaves

Table 2.1.1 Operation regime of periodic surfaces, depending on the application frequency range (before the 20th century).

The manipulation of light and the theoretical work done by the previous scientists evidenced the simplicity of **controlling the propagation of electromagnetic waves by employing diffraction gratings**. Therefore, these structures have been extended to many areas of Engineering and Science. It is important to highlight the fact that, depending on the modal regime in which they operate, **periodic surfaces are commonly called either FSS or diffraction gratings**, as it is schemed in Table 2.1.1. Before the twentieth century, in optical regime applications (associated to wavelengths on the order of a micrometer) the dimensions of the periodic gratings were greater than the wavelength due to technical limitations, and thus, they were referred as diffraction gratings characterized by multimode operation. This means that, when light impinges on the periodic surface, propagative spatial harmonics are excited in the structure which contribute to radiation (the hence called **grating lobes**). However, periodic surfaces are usually called FSS when applied in the microwave spectrum. Single mode operation is normally required in this case and the periodicity of the array is designed to be comparable to the wavelength (without technical limitations, since

it is now millimetric). In this scenario, as the impinging wave reaches the periodic surface, no energy is transferred to any other spatial harmonic, due to the fact that they are now evanescent.

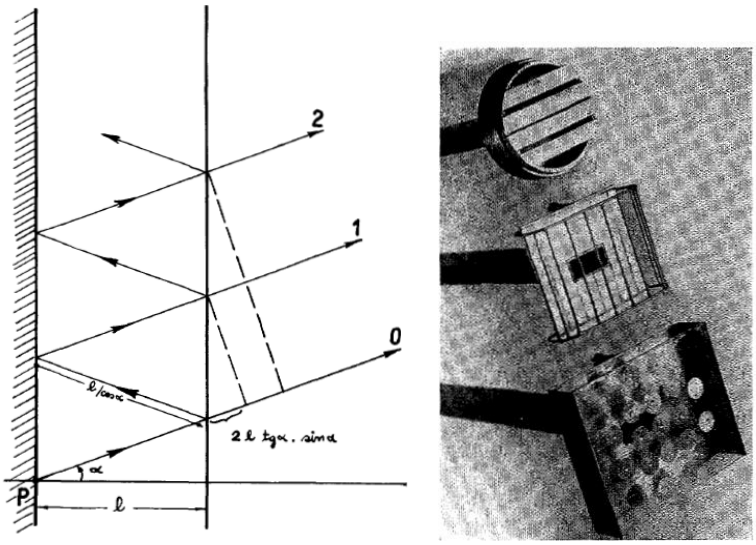

(a) (b)

Fig. 2.1.4 (a)Scheme of multiple reflections between reflector an PRS, (b)PRS-loaded designed antennas. (Figs. 1 and 7 in [Trentini 1956]).

At the beginning of the twentieth century, G. Marconi and C. S. Franklin patented the first FSS structure applied to the microwave region, where the FSS was employed as parabolic reflector of wire sections for wireless telegraphy ([Marconi 1919]). Later, Von Trentini showed the increase in directivity that resulted by placing a FSS in front of an antenna with a reflecting screen (see the antenna scheme in Fig. 2.1.4(a) and the designed prototypes in Fig. 2.1.4(b)). In this scenario, Von Trentini conceived FSSs as **Partially Reflecting Sheets** (PRS) for electromagnetic waves ([Trentini 1956]). Another early patent on FSS can be found in [O'Nians 1966]; again the FSS is employed to make more efficient reflector antennas. The great potential for military applications boosted the study of periodic surfaces in the middle 1960s, thus, many interesting work done by scientist such as B. A. Munk, was kept in secrecy for years ([Munk 1970, 1971, 1974, 1976, 1977, 1979 and 2000], [Richmond 1974], [Burrell 1976] and [Pelton 1976]). In this context, there was an increasing tendency to describe the interaction between FSSs with electromagnetic waves. Some examples of the first works on diffraction at planar gratings and its characterization by equivalent

circuits and multimode networks can be found in [Oliner 1960], [Palocz 1970], [Chen 1971 and 1973] and [Guglielmi 1989-I and II]. A similar work was also carried out in the far infrared regime, where FSSs were used as polarizers, beam splitters, submillimeter filters, mirrors for lasers… ([Ulrich 1967-I and II, Cunningham 1983, Irwin 1993]). Periodic screens were also applied to the near-infrared and visible portions of the spectrum. An interesting example can be found in [Horwitz 1974], where FSSs were proposed to improve the efficiency of solar cells. Specifically, this solar selective surface is designed to be essentially transparent in the frequency band where the solar cells are most efficient, reflecting frequencies outside this band.

FSS have also been included in guiding structures in order to modify the propagation of waves along them, achieving diffraction characteristics such as frequency stop-bands, pass-bands and band-gaps. These structures have been recently classified under the broad terminology of **"Electromagnetic Band-gap (EBG)" materials**. Good examples can be found in [Sievenpiper 1999] or [Shumpert 1999], where EBG substrates are proposed to enhance the bandwidth in low profile antennas. In particular, Sievenpiper showed for the first time that EBG substrates can behave as **High Impedance Surfaces** (HIS), which present a reflection coefficient with a reflection phase that can be flexibly varied as a function of the FSS dimensions. An interesting operation regime of a HIS is when it presents a reflection phase of zero degrees, behaving as an **Artificial Magnetic Conductor** (AMC).

From 1969 until the end of 2000, hundreds of papers were published containing the keyword "frequency selective surface". The application areas were mainly filtering (with respect to frequency, polarization, angle…), antenna enhancement, EBG structures, radomes (terrestrial and airborne), missiles and electromagnetic shielding applications. Recent examples of the application FSSs can be found in [Vardaxoglou 1997], [Feresidis 2001], [Maci 2003], [Zhao 2005], [Kosmas 2007], [Balanis 2008], [Seman 2011]. During the last decade the interest on periodic structures within the microwave/millimeter wave domains has been focused on the analysis of artificial magnetic conductors, hard and soft electromagnetic surfaces, partially reflecting surfaces, and other structures

conceived mainly for antenna applications ([Feresidis 2001], [Luukkonen 2008]). Multilayer stacked periodic structures for the implementation of wideband canonical filters have received considerable attention during the last few years ([Bayatpur 2008-I and II], [Al-Joumayly 2009], [Behdad 2009]). A large variety of geometries have been employed in the past few years to realize other EBG structures and Artificial Magnetic Conductors (AMC) [Goussetis 2006-I,II and 2007-I,II], as well as Left-Handed metamaterials [Caiazzo 2004]. In this context, there is an **increased tendency to describe the interaction between FSSs and electromagnetic waves** by equivalent homogenized parameters, such as generalized sheet transition conditions [Vardaxoglou 1997], averaged boundary conditions [Munk 2000] or equivalent impedance/ admittance [Tretyakov 2003], [Maci 2005], [Luukkonen 2008].

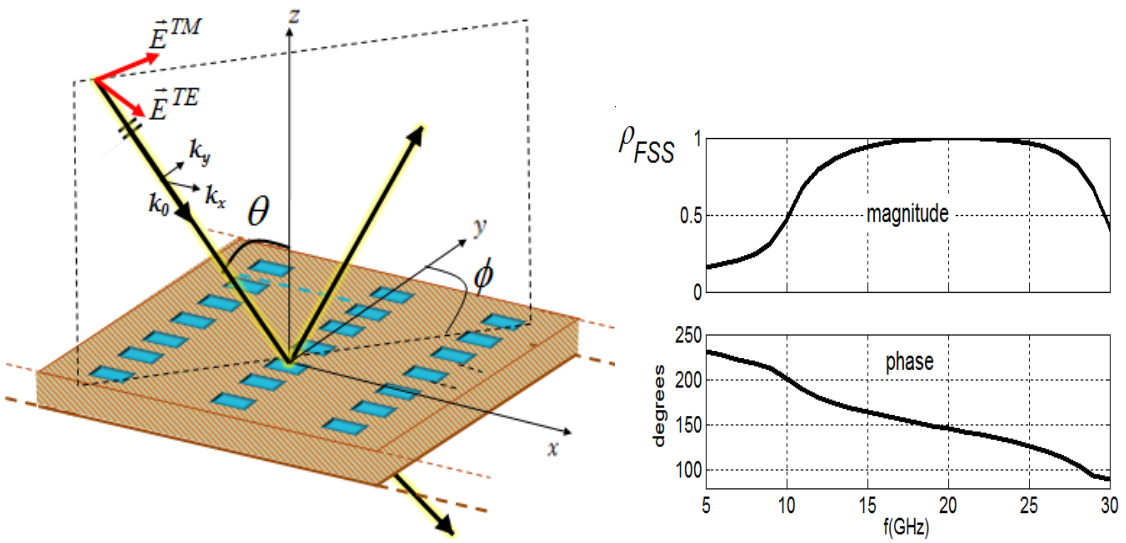

(a) (b)

Fig. 2.1.5 FSS reflection squeme (a) Plane-wave incidence on printed dipole-based FSS (b)Reflection coefficient vs. frequency.

It is worth mentioning that, depending on the application, the **analysis of a FSS can consist either on a "study of reflection" or a "study of dispersion"** (a detailed explanation on this issue can be found in [Maci 2005]). When the **emphasis is made on the reflection properties** of the FSS (outlined in Fig. 2.1.5(a)), the aim is to obtain its reflection coefficient (ρ_{FSS}) as a function of frequency, for various plane-wave incidence angles (θ, ϕ) and for both TE and TM

polarizations. This scenario is well described in books such as [Vardaxoglou 1997] or [Munk 2000]. The analysis of ρ_{FSS} is based on the expansion of the field in terms of Floquet waves with known wavenumbers (since k_x and k_y are directly related to the FSS orientation, frequency and incidence angles). Reflection vs. frequency curves such as the ones in Fig. 2.1.5(b) can be directly derived using numerical techniques. Among those, the integral equation and its subsequent solution using the method of moments (MoM) is a popular due to its fast and efficient features.

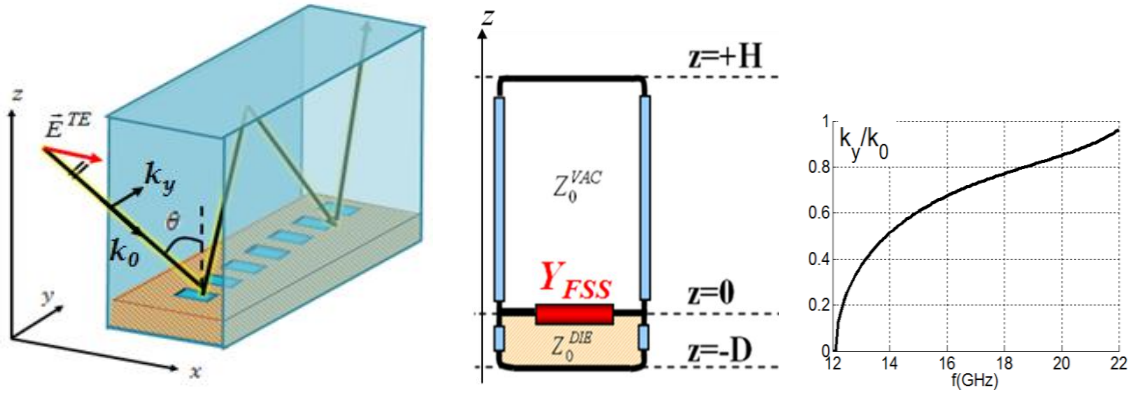

(a) (b) (c)

Fig. 2.1.6 FSS dispersion squeme (a) Wave propagation inside FSS-loaded waveguide (b) Transverse Equivalent Network (c) Dispersion with frequency.

On the other hand, when **the FSS is part of an EBG structure** (as shown in the example of Fig. 2.1.6(a)), the analysis consists in obtaining its dispersion diagram. This situation is completely different from the previous one; the wavenumber (k_y) is now the unknown of the problem and it is commonly found by solving a Transverse Resonance Equation (TRE). The FSS is modeled by an equivalent impedance (Y_{FSS}), which when employed in equivalent circuits, can be used to obtain dispersion diagrams such as the one in Fig. 2.1.6(c). It is worth appreciating that **Y_{FSS} must be function of k_y** so that the modal solutions of the structure can be found by solving the previous TRE at a specific frequency and for a given geometry. Analytical expressions have been derived to produce the equivalent far-field surface impedance for specific element geometries; an excellent summary of the state-of-the-art can be found in [Tretyakov 2003], and a more recent

contribution in [Luukkonen 2008]. However their application is limited to those geometries for which analytical solutions have been obtained. Recently a pole-zero method was proposed by Maci et al [Maci 2005], which employing full-wave results and Foster's theorem, can derive the equivalent impedance of periodic surfaces.

In the frame of this thesis, the first goal is **the synthesis of printed dipole-based FSSs which can be used to conceive more complex EBG structures**, as Leaky-Wave Antennas (LWA). In particular, the FSSs will perturb the leaky-modes propagating through the structure, providing the control over its radiation properties. In order to characterize the dispersion of such LWAs, a TEN must be constructed, in which the FSSs are modeled by equivalent admittances. Despite the extensive literature available for the analysis of periodic structure, there is relatively limited published material on the **inverse problem of synthesis**. Assuming that the value of the equivalent impedance required by a periodic surface is known, the synthesis problem aims to derive the geometrical characteristics of the array unit cell. Analytical techniques, such as those reported in [Tretyakov 2003] and [Luukkonen 2008], can be employed for this purpose. However, for the case of a dipole arrays, the dependence of the equivalent impedance on the dipole length has not been accurately derived. Brute force simulations have been recently reported [Goussetis 2007-I], but this is computationally expensive. Yet, this synthesis procedure is essential for the efficient design of components employing such periodic surfaces. **A modified pole-zero technique has been developed for the characterization of doubly periodic arrays of dipoles.** This approach (which is explained in detail in Section 2.2), provides an equivalent sheet impedance which analytically depends on the dipole length, hence allowing to perform synthesis. This approach is employed in Section 2.3, in order to obtain the modal dispersion curves of practical EBG structures. The analysis technique is divided in several steps, which have been implemented in a software tool using MATLAB®.

At the beginning of the twentieth century, parallel to the application of FSSs explained above, the **whole complexity of the electromagnetic nature of light was again studied in depth**. The interaction between light, gratings and metal attracted the attention of researchers such as R. W. Wood and Lord Rayleigh. In 1902, R. W. Wood experimentally reported the unexpected narrow bright and dark bands in the spectrum of an optical reflection grating illuminated by a light source ([Wood 1902 and 1912]). This phenomenon, known as "Wood´s anomaly", was later theoretically treated by Rayleigh in [Rayleigh 1907-I and II]. Almost 30 years later, the phenomenon was reinterpreted by Fano ([Fano 1941]), who distinguished between two types of anomalies. Afterwards, Hessel and Oliner provided a clear answer to the phenomenon, considering the two types of Wood´s anomaly resonances: one due to branch point singularities that correspond physically to the onset of a new propagating spectral order (the so called "Wood-Rayleigh anomalies", first indicated by Lord Rayleigh), and the other due to pole singularities that correspond to the condition of resonance for leaky surface waves guided by the structure (also called "resonance anomalies"). These authors proposed for the first time a simple closed form solution in [Hessel 1965], based on analysis of electromagnetic scattering. More experimentation was also done, relating the anomalies to the excitation of surface plasmons, which are essentially electromagnetic waves trapped at a metallic surface through their interaction with the free electrons of the metal [Ritchie 1957]. This effect was soon after described in terms of excitation of electromagnetic evanescent waves at the surface of the metal [Burstein 1974].

In the 1940s, microwave technology advanced rapidly, due to the huge research and development demands of World War II. Regarding periodic structures, interest shifted to subwavelength scatterers. Bethe studied the diffractive properties of an idealized subwavelength hole. In coherence with the principles of diffraction ([Born 1999]), he reported that the optical transmission would be very weak when the optical elements were miniaturized. Decades later, Ebbessen showed that orders of magnitude more light than Bethe´s prediction could be transmitted through an opaque metal screen milled with subwavelength holes [Ebbessen 1998]. This unexpected phenomenon was therefore called

"**extraordinary optical transmission**" (EOT), and generated a renewed interest on the modeling of this class of electromagnetic structures, see the comprehensive reviews in [Genet 2007], [García de Abajo 2007], [Bliokh 2008], [García-Vidal 2010], [Gordon 2010] and references therein. However, this phenomenon is not exclusively associated with optical frequencies but has also been reported at millimeter wave [Beruete 2004, 2005 and 2007-I] as well as THz frequencies [Azad 2005], [Kuznetsov 2009], [Carbonell 2010]. In spite of some relevant differences among the various frequency regimes owing to the different behavior of metals at different frequency regions, all the above problems share a similar physical background. Therefore, two different natures of the resonance of a frequency selective surface can be distinguished. On the one hand, the previously explained **conventional resonance** is presented by FSS with scatterers comparable to the wavelength [Trentini 1956]. In this case, the size and shape of the scatterer controls the first resonance of the periodic sheet [Lee 2000], [Feresidis 2001]. On the other hand, FSS with subwavelength scatterers also present an **extraordinary total reflection/transmission peak** before the onset of the first grating lobe. This resonance is not directly related to the electrical length of the scatterers, but to the periodicity of the array. In this context, a new row should be added to Table 2.1.1, as shown in Table 2.1.2.

periodic surfaces	operation regime	periodicity of the array	size of the scatterer	common frequency range
diffraction grating	Multimode (grating lobes)	greater than the wavelength	any	optics
conventional FSS	single mode	comparable to the wavelength	comparable to the wavelength	microwaves
extraordinary FSS			subwavelength	microwaves/ optics

Table 2.1.2 Operation regime of periodic surfaces, depending on the application frequency range.

The most widely accepted paradigm explains EOT in terms of the interaction of the impinging electromagnetic wave with Surface Plasmon Polaritons (SPP) supported by the periodic structure [Pendry 2004]. However, **a point of view on EOT alternative to SPP theory was reported in [Medina**

2008], where an electrically small aperture was modeled as a reactive discontinuity in the path of an electromagnetic mode propagating along a waveguide. This waveguide can be a real one (*i.e.*, the circular-section guide considered in [Medina 2009 and 2010-II]), or an equivalent one which characterizes a unit cell of a periodic sheet (this case is considered in [Medina 2008], [Schuchinsky 2005] and [Beruete 2007-II]). Therefore, Medina´s fruitful point of view consists in the reduction of the original problem to an equivalent one which consists in the scattering of a guided wave incident on a transverse discontinuity. Its main advantages are, on the one hand, that it can benefit of the great deal of work carried out previously on waveguide discontinuities [Oliner 1960], [Palocz 1970], [Miles 1946], [Marcuvitz 1986], [Wexler 1967] and, on the other hand, that it allows for a rephrasing of the original complex electromagnetic problem in terms of an equivalent circuit network. This last feature means that the potentially complicated wideband frequency response of the system can be accounted for by a small number of parameters. These parameters can eventually be known in closed form for some limited cases ([Marqués 2009]) but, in general, they should be obtained from just a few full-wave computations. **Medina´s contribution was centered in the characterization of extraordinary transmission; however, due to the physical insight of his approach, it can be used to model the general scenario of dispersion at a periodic surface.** In particular, it has been adapted to various structures, such as simple and compound slit gratings [Medina 2010-I].

Therefore, in the frame of this thesis, the same approach presented in [Medina 2008] is extended in order to model more complex and practical scenarios. In particular, an **equivalent circuit is proposed to model oblique plane-wave incidence over dipole-based periodic surfaces sandwiched between dielectric slabs** (no assumption on the electric length of the scatterers is made and the dependence with the angle of incidence is explicitly considered)**.** It should be understood that the equivalent-circuit methodology here proposed is not a complete substitute of the full-wave methods but a very convenient complement that helps to reduce drastically the computational effort. In fact, due to the currently disposal of full-wave electromagnetic simulators, the numerical

benefit given by the equivalent circuit may not be so crucial. However, another key feature of the equivalent-circuit approach is that it provides a simple and accurate comprehension of the problem, which makes possible many important predictions on the behavior and role of the different elements of the structure under study. This predictive nature can be fundamental for many analysis and/or design applications. This contribution is explained in detail in Section 2.4.

2.2 Modified pole-zero technique

The proposed approach is an extension of the pole zero technique proposed by Stefano Maci in [Maci 2005 and 2003], which consists in an efficient method to extract the equivalent sheet impedance of doubly periodic arrays and its variation with frequency from a limited number of full wave simulations. In its contribution, Maci states that it is possible to characterize the FSS' equivalent admittance through an analytical and polynomial expression ($Y_{FSS}(k_y, \omega)$, Eq. 2.2.1). Y_{FSS} is a function of frequency and also of the unknown propagating constant in the longitudinal y axis $(k_y$, Fig. 2.2.1$)$, which is the goal of a dispersion analysis. It is proven in [Maci 2005] that, for every real k_y, $Y_{FSS}(k_y, \omega)$ satisfies Foster´s theorem and therefore, has the same analytic properties as an LC network in frequency. These properties are: the poles and zeros are in the real ω axis, they are simple and alternate; and there must be a pole or zero in $\omega = 0$. After a full-wave analysis of the FSS' reflection coefficient, $Y_{FSS}(k_y, \omega)$ can be approximated by this rational function:

$$Y_{FSS} = \frac{j\omega C_0 \left(\omega^2 - \left[\omega_{z1}(k_y)\right]^2\right)\left(\omega^2 - \left[\omega_{z2}(k_y)\right]^2\right)\ldots}{\left(\omega^2 - \left[\omega_{p1}(k_y)\right]^2\right)\left(\omega^2 - \left[\omega_{p2}(k_y)\right]^2\right)\ldots} \qquad (2.2.1)$$

where $\omega_{z1}(k_y)<\omega_{p1}(k_y)<\omega_{z2}(k_y)<\omega_{p2}(k_y)\ldots$ are the frequencies where the poles and zeros of Y_{FSS} are located. In order to find these values, a full-wave analysis of

the two scenarios shown in Fig.2.2.1 is needed. In the first scenario, it is computed the reflection phase of the FSS printed on its dielectric substrate over a ground plane (Fig. 2.2.1(a)). In the second scenario, the same cavity–backed dielectric slab is analyzed in the absence of the FSS (Fig. 2.2.1(b)). The reflection coefficient ($\rho(\theta,\omega)$) is obtained in both cases using a full-wave method (for example, using the technique described in [Goussetis 2006-I). Particularly, the phase of this coefficient (θ_{FSS}) will centre our attention, because its module will always be equal to one (all the incident energy is reflected, either by the FSS or the ground plane under the dielectric).

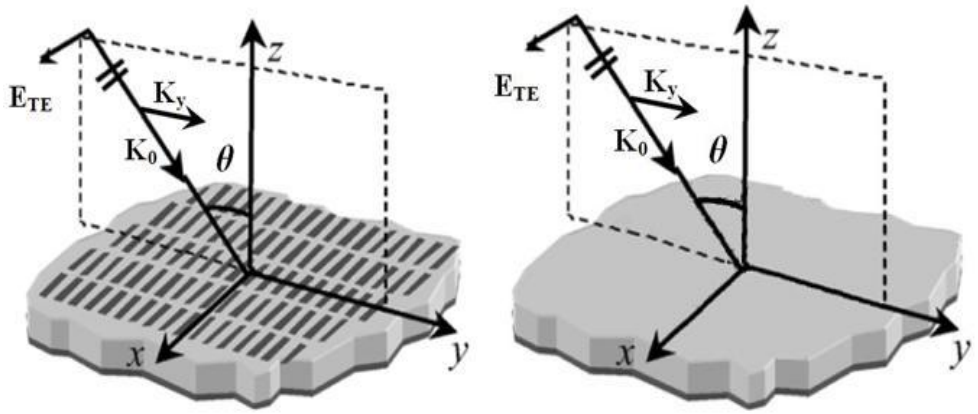

(a) (b)

Fig. 2.2.1 Analyzed scenarios to obtain the poles and zeros of the FSS (Fig.1 in [Maci2005]).

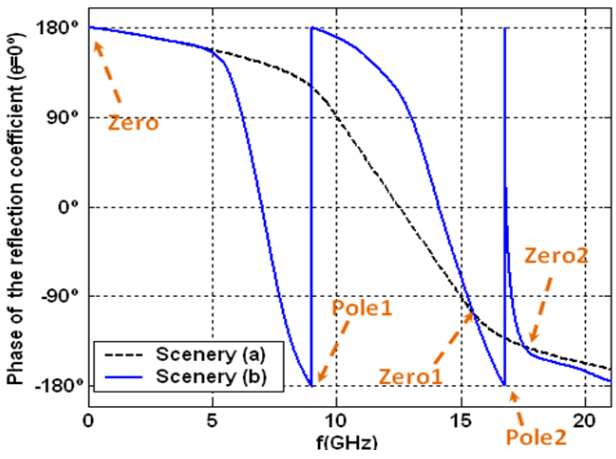

Fig. 2.2.2 Phase of the reflection coefficient under normal incidence ($\theta = 0°$).

For every k_y, and therefore, for every angle of incidence θ (due to the relation $k_y = k_0 sin\theta$, as we can seen in Fig. 2.2.1), the poles $\omega_{pi}(k_y)$ are located at

those frequencies at which θ_{FSS} is equal to 180º. In these situations, the FSS behaves as a shortcircuit, and Y_{FSS} will be infinite, leading to a pole of the polynomial expression of (2.2.1). On the other hand, to identify the zeros, we must compare θ_{FSS} of the FSS (Fig. 2.2.1(a)) with the phase of the reflection coefficient associated to the same structure but without FSS (Fig. 2.2.1(b)). When both phases coincide, the FSS will be invisible to the incident wave. At this frequency, the FSS behaves as an open circuit (Y_{FSS} will be equal to zero), leading to a zero $\omega_{zi}(k_y)$ in (2.2.1). In Fig. 2.2.2 it is illustrated an example of the identification of two poles and two zeros under normal incidence, following the described method.

This same concept is now employed to extract the impedance of doubly periodic dipole arrays and its variation with the dipole length. The schematic of the structure under consideration is shown in Fig. 2.2.3.

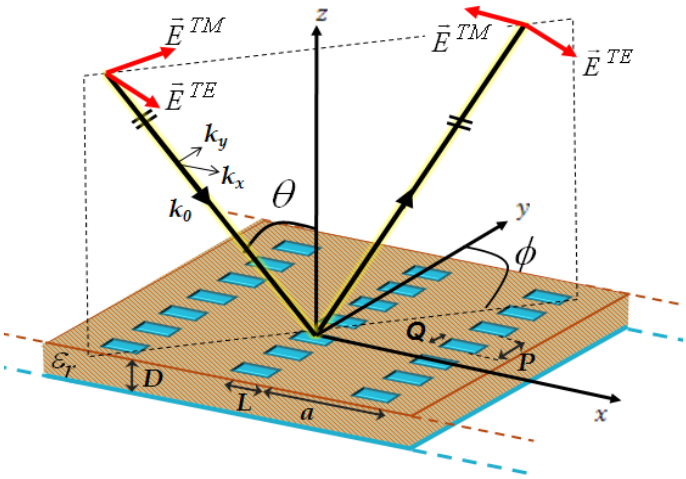

Fig. 2.2.3 Doubly periodic dipole array over a dielectric substrate under arbitrary plane wave incidence.

This structure can be analyzed under an arbitrary direction of incidence at an elevation angle θ and azimuth ϕ (see Fig. 2.2.3). Assuming thin metallic dipoles (Q << L in Fig. 2.2.1), at low frequencies they will only interact with the x-component of the incident electric field. When the plane of incidence is yz ($\phi = 0°$ in Fig. 2.2.3) TE polarized waves will be affected by the dipoles, while the TM will only experience a metal-backed dielectric substrate. In this case, the transverse propagation constant is $k_y = k_0 \sin\theta$ (Fig. 2.2.3). The analogous situation is presented when the incidence is in the xz plane, the TM polarization will interact with the

dipoles, and the waves in the structure will propagate through the *x* axis with a constant $k_x = k_0 \sin\theta$.

Many numerical fittings can be employed to model the admittance of the FSS, for example: splines, rational or polynomic fittings. Specifically, and in analogy with [Maci 2005], we propose an analytical expression of the equivalent admittance as a function of the dipoles length L, given by:

$$Y_{FSS}^{TE,TM}(k_{y,x}, L) = j \frac{L(L - L_{z1}(k_{y,x}))...(L - L_{zn}(k_{y,x}))}{(L - L_{p1}(k_{y,x}))...(L - L_{pm}(k_{y,x}))} \qquad (2.2.2)$$

Depending on the incidence, k_y/k_x are used in (2.2.1) for the TE /TM respectively. If ϕ is such that TE and TM polarization are coupled, the admittance can be described as a matrix changing the problem into calculating a TE admittance and a TM one, following [Maci 2005]. In this way, not only dipole-based FSS can be analyzed but also rectangular strips or square patches.

A simple comparison between the above expression with Eqs. (4) and (5) in [Maci 2005] reveals that the dependence of Y_{FSS} on L in (2.2.2) is assumed to be similar to that with frequency. This similarity between the dependence with frequency and L comes from the fact that the dipoles are resonant in the direction of their length, and therefore both variables are expected to have a similar influence on the behaviour of Y_{FSS}. Thus, the task of obtaining an expression for the equivalent admittance as a function of L can then be reduced to extracting a set of poles and zeros (which are assumed to vary slowly with the wavenumber [Maci 2005]). This rational fitting can be carried out by any of the standard procedures available in the literature; in our case we have used a least squares scheme. Using a full-wave analysis tool (for instance the MoM employed in [Goussetis 2006-I]), we compute the reflection phase experienced by an incident plane wave on the FSS printed on a conductor-backed dielectric substrate. In particular, we obtain the variation of the reflection phase (θ_{FSS}) with the dipole length, L, for different angles of incidence θ (the admittance can be readily obtained from these values).

Next, this proposal is illustrated by means of an example involving an FSS with dimensions P = 1.5 mm, Q = 0.5 mm, a = 11 mm, D = 1.13 mm, and ε_r = 2.2

(Fig. 2.2.3). This structure is characterized under TE incidence in the *yz* plane (the index TE will be omitted in the following expressions for convenience). In this case, the propagation of the waves in the structure will be in the *y* axis with wavenumber k_y. The same approach can be used for the TM case without losing validity. Figure 2.2.4 shows the full-wave values of the reflection phase for the FSS under consideration varying the length *L*, at different elevation angles of incidence θ=0º, 27 º, 54 º, 81º, and for the frequency of 20 GHz. For comparison purposes, the values of the proposed rational fitting approach are also shown in this figure.

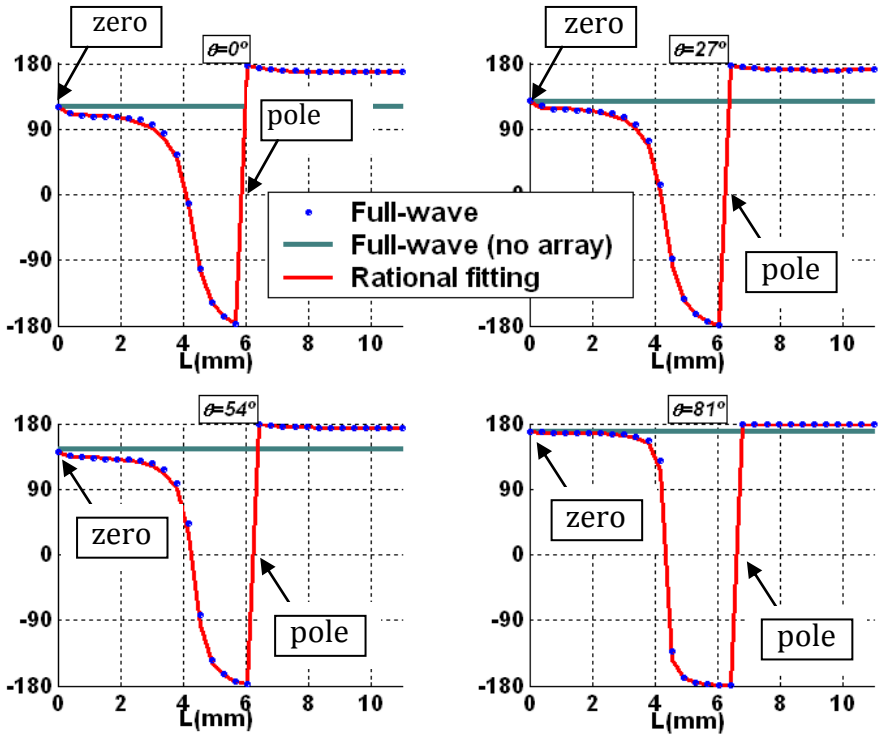

Fig. 2.2.4 Phase of the reflection coefficient of the FSS (θ_{FSS}) of Fig. 2.2.3 varying *L* at *20GHz*, and for different incidence elevation angles. Incidence is in the plane *yz* ($\phi = 0°$) under TE polarization. Dimensions: *P*=1.5mm, *Q*=0.5mm, *a*=11mm, *D*=1.13mm, ε_r=2.2.

The lengths *L* for which the FSS appears as a short circuit, and the reflection phase takes the value of 180º, should appear as real poles in the admittance. On the other hand, the values of *L* where the reflection phase is equal to that obtained by the same structure in the absence of the periodic array should correspond to real zeros in (2.2.2). In this latter case, the FSS appears transparent to incident plane waves. The full-wave results in Fig. 2.2.4 show the presence of a zero at *L* =

0, which is explicitly accounted for by the factor L in the numerator of (2.2.2). The location of these poles and zeros are marked in Fig. 2.2.4. Other zeros and poles should also appear in the rational fitting of (2.2.2) in order to have a good numerical matching. Specifically, the rational fitting shown in the figure has been computed with just two poles and two zeros, which has provided a maximum relative error of 10^{-4} with the use of 10 full-wave simulations (per angle of incidence). A similar good numerical performance has been obtained for other cases.

In analogy to what happens with the frequency dependence discussed in [Maci 2005], although Y_{FSS} can vary rapidly with L, the values of the poles and zeros, $L_{pm}(k_y)$ and $L_{zn}(k_y)$, vary slowly with respect to the incidence angle. It allows these poles/zeros can be interpolated and/or extrapolated via a low order polynomial (in our case we have performed a spline interpolation). This aspect is well illustrated in Fig. 2.2.5, where it is shown the poles and zeros obtained for the example under study. This figure shows that the two zeros, L_{z1} and L_{z2}, are complex conjugate, as expected (for other cases the poles can be both real). It can also be observed that the pole L_{p1}, placed around 6 mm, corresponds to the physically meaningful pole expected from the discussions on Fig. 2.2.4.

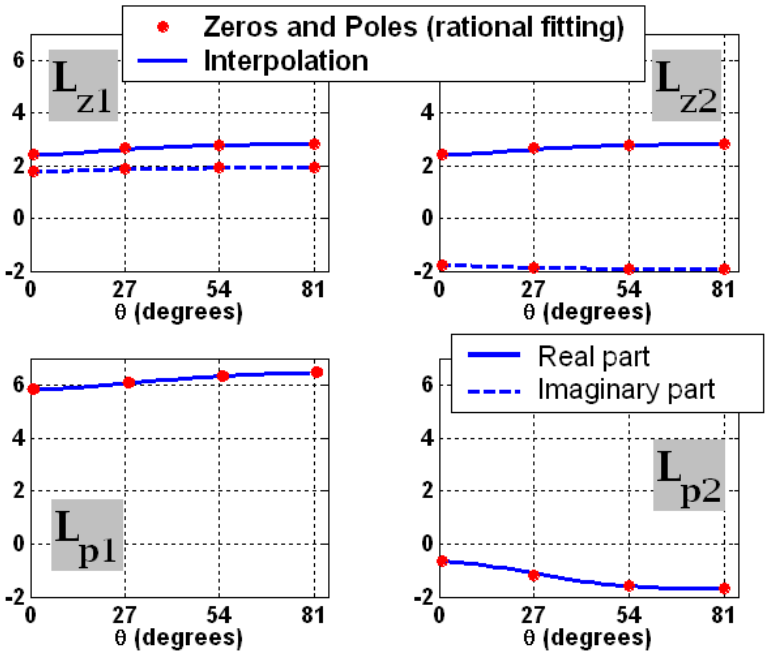

Fig. 2.2.5 Zeros and poles found in the rational fitting and its spline interpolation with the angle of incidence.

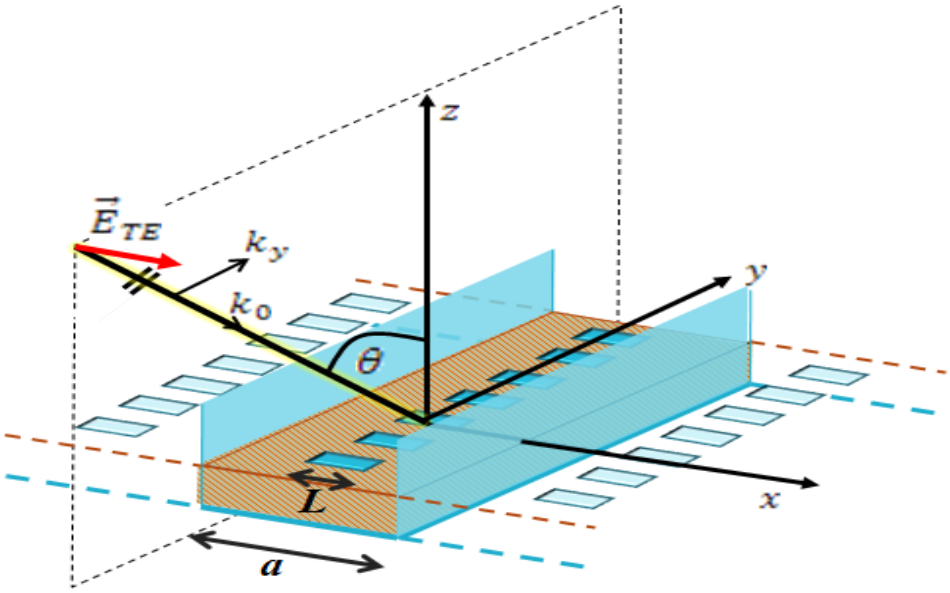

Fig. 2.2.6 Dipole FSS under consideration for TE incidence. The metallic walls are shown to demonstrate the equivalence between a 2D FSS structure and a 1D FSS inside a parallel plate waveguide.

This modified pole-zero method will be employed in next sections in order to model a periodic FSS located inside a parallel-plate waveguide. In order to study propagation of TE modes, these structures will be excited by TE-polarized plane waves assuming the setup shown in Fig. 2.2.6 (plane-wave incidence in the *yz* plane). Due to symmetry, the proposed FSS-loaded waveguide in Fig. 2.2.6 is equivalent to the two dimensional free-standing FSS in Fig. 2.2.3, with the period in the *x*-dimension being equal to the width "*a*" of the parallel-plate guide.

2.3 Software tool for the analysis of waveguides loaded with dipole-based FSS

A software tool has been developed in MATLAB® which analyzes the dispersion of EBGs consisting on a FSS introduced inside a waveguide (such as the ones shown in Fig. 2.3.1). Both the pole-zero presented by Maci, and the extended version explained in the previous section, are implemented in the tool in order to obtain frequency and geometry dispersion curves of the structures.

1.1.4 Tool description

The inclusion of FSS inside waveguides has attracted much interest in the last decade. Interesting properties can be achieved, such as quasi TEM propagation [Seager 1999], [Yang 1999], generation of bandgaps [Sievenpiper 1999], [Goussetis 2006-I and II], size reduction [Goussetis 2007-II], [Caiazzo 2004], dispersion compensation [Goussetis 2007-I] or low profile and high gain leaky-wave antennas [Feresidis 2001]. In particular, this tool will be employed in next Chapter of this thesis for the analysis of EBG structures such as the ones shown in Fig. 2.3.1.

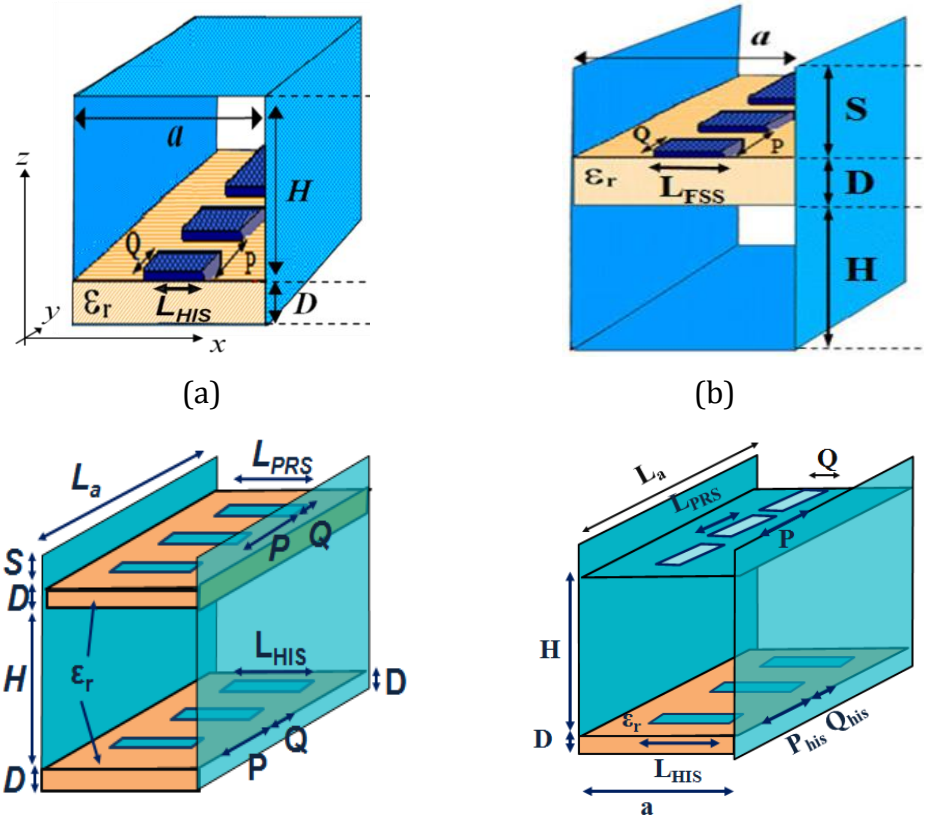

Fig. 2.3.1 Rectangular waveguides loaded with metallodielectric FSSs

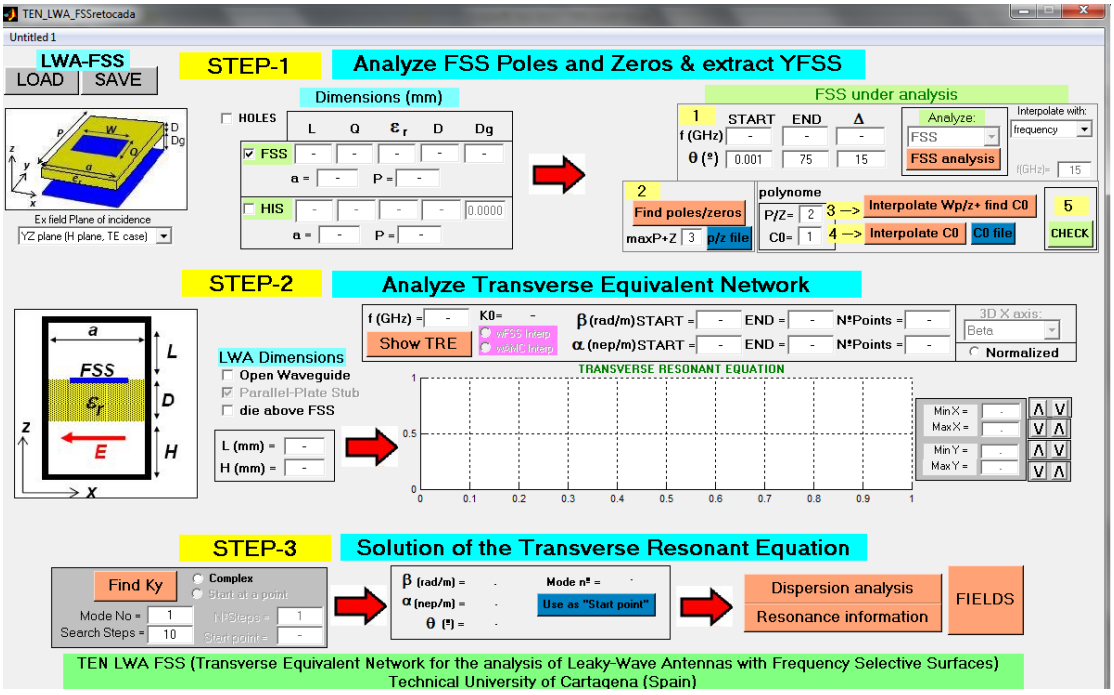

Fig. 2.3.2 Graphical user interface of the tool implemented in MATLAB®.

As it was explained in the introduction of this chapter, the analysis of FSS can be approached from different perspectives. On the one hand, they are analyzed by the illumination of a plane wave with a certain polarization and angle of incidence. This FSS analysis aims at obtaining the reflection and transmission coefficients as a function of frequency, angle of incidence and polarization [Munk 2000]. On the other hand, it is also common to load waveguides with periodic circuits in order to obtain frequency responses with bandgaps, resulting in EBG waveguides. The analysis of these EBG structures involves modal dispersion diagrams, which represent the dependence of the propagation constant of the mode under study on frequency, $k(\omega)$. It is possible to combine both analyses when dealing with EBGs consisting on a FSS introduced inside a waveguide. In this situation, the dispersion diagrams can be obtained from the analysis of the FSS' reflection coefficient, and then applying a transverse equivalent network (TEN), as described in [Maci 2005]. The analysis technique here implemented follows the previous pole-zero matching methods to find a closed-form expression of the FSS equivalent admittance Y_{FSS}. With this Y_{FSS}, a TEN can be build, which will be used to formulate the associated TRE (Transverse Resonance Equation), whose solutions will provide the dispersion diagrams that characterize the EBG. The tool´s graphical interface (implemented in MATLAB®) is shown in Fig. 2.3.2. The analysis method is based on three consecutive steps (as it can be noticed in Fig. 2.3.2). The developed tool helps the user so that he can supervise and verify the results at each step and then take the next one.

STEP 1: Closed-form expression of the FSS Equivalent Admittance.

In the first step of the analysis method, the FSSs in the structure are characterized by an equivalent circuit. The part of the GUI in which this step is developed is shown in Fig. 2.3.3.

Firstly, the user chooses if the structure has an FSS, a HIS, or both, and introduces the dimensions of their unit cells (see Fig. 2.3.3(a)). The user can also choose in this step the polarization and the plane in which the exciting plane wave

impinges on the FSS. As it has been marked in Fig. 2.3.3(a), the user can choose between two cases, TE incidence in H-plane and TM on E-plane.

Slotted FSS can be also modeled when they are free standing (not printed over a dielectric substrate or a metal), as the one considered in the structure of Fig. 2.3.1(b). In this case, the slotted FSS can be considered the complementary structure of a dipole-based one, and Babinet's principle can be applied [Balanis 2005]. Therefore, when the option "Holes" is selected, the complimentary dipole structure is analyzed and later, the equivalent admittance is calculated by:

$$Y_{slotted-FSS} = \frac{4}{Y_{dipole-FSS}} \frac{\varepsilon_0}{\mu_0} \tag{2.3.1}$$

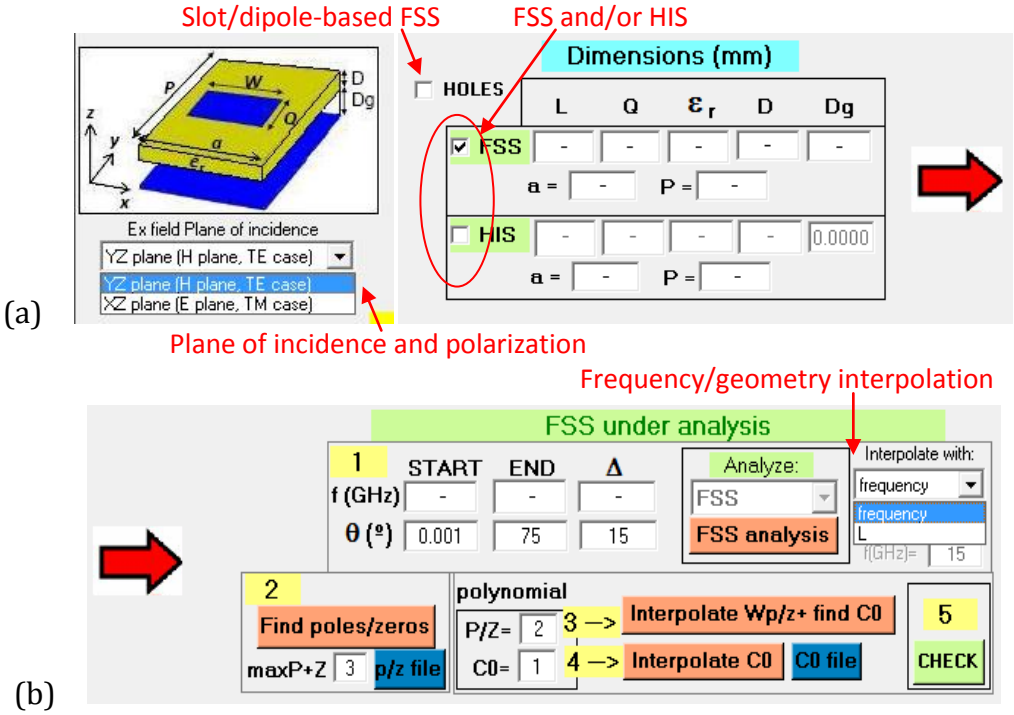

Fig. 2.3.3 Part of the graphical interface that implements the STEP 1
(a) Introducing the dimensions of the FSSs unit cell (b)Pole-zero matching method.

Figure 2.3.3 shows the part of the GUI which performs the pole-zero analysis. The user can choose either to characterize the periodic surface as a function of frequency for a fixed geometry, or as a function of the length of the dipoles for a fixed frequency. In the first case, Maci´s pole-zero technique is applied and, following equation (2.2.1), an equivalent admittance is obtained which analytically depends on the frequency and the wavenumber ($Y_{FSS}(k_y, f)$).

On the other hand, when the second option is chosen, the modified pole-zero method presented in Section 2.2 is employed. Following equation (2.2.2), an equivalent admittance is obtained which is only valid for a fixed frequency and depends on the wavenumber and the length of the dipoles ($Y_{FSS}(k_y, L)$).

As it can also be seen in Fig. 2.3.3(b), the number of poles and zeros in the previous admittances can be specified by the user, together with the grade of the polynomials that interpolate the poles and zeros with k_y.

STEP 2: TEN analysis.

In this step, it is developed the transverse equivalent network that characterizes the structure under analysis. The software tool allows the analysis of an open or closed rectangular waveguide, loaded with a FSS and/or a HIS. For the sake of simplicity, the simple cases of Fig. 2.3.4 will be firstly considered, where a rectangular waveguide is loaded with a printed dipole-based FSS, and excited by a TE_0 mode. Two cases are taken into consideration: when the guide is completely closed (Fig. 2.3.4(a)) and when the guide is open-top (Fig. 2.3.4(b)). As we can see in Fig. 2.3.4, the TEN is made up of the equivalent admittance of the FSS (Y_{FSS}, found in the previous step), and segments of transmission lines which characteristic impedance is the one associated to a TE_0 mode (Z_0^{VAC} ó Z_0^{DIE}, in case the guide is empty or filled with dielectric). In the case of a closed waveguide (Fig. 2.3.4(a)), the upper transmission line is ended by a shortcircuit. When dealing with top-open waveguides (Fig. 2.3.4(b)), the opening is characterized by the equivalent radiation impedance of Marcuvitz (Z_{RAD}), which models the radiating discontinuity under TE incidence [Marcuvitz 1951], [Gómez 2006-I and II]. The expressions of the impedances which appear in Fig. 2.3.4 are the following ones:

$$k_z^{VAC} = \sqrt{k_0^2 - k_y^2} \tag{2.3.2}$$

$$k_z^{DIE} = \sqrt{k_0^2 \varepsilon_r - k_y^2} \tag{2.3.3}$$

$$Z_0^{VAC,DIE} = \frac{\omega\mu_0}{k_z^{VAC,DIE}} \tag{2.3.4}$$

$$Z_{DOWN}^{(a),(b)} = jZ_0 \tan(k_z H) \tag{2.3.5}$$

$$Z_S^{(a)} = jZ_0 \tan(k_z S) \tag{2.3.6}$$

$$Z_S^{(b)} = Z_0 \frac{Z_{RAD} + jZ_0 \tan(k_z S)}{Z_0 + jZ_{RAD} \tan(k_z S)} \tag{2.3.7}$$

$$Z_{SY}^{(a),(b)} = \frac{Z_S^{(a),(b)}}{Y_{FSS} Z_S^{(a),(b)} + 1} \tag{2.3.8}$$

$$Z_{UP}^{(a),(b)} = Z_0 \frac{Z_{SY}^{(a),(b)} + jZ_0 \tan(k_z^{DIE} D)}{Z_0 + jZ_{SY}^{(a),(b)} \tan(k_z^{DIE} D)} \tag{2.3.9}$$

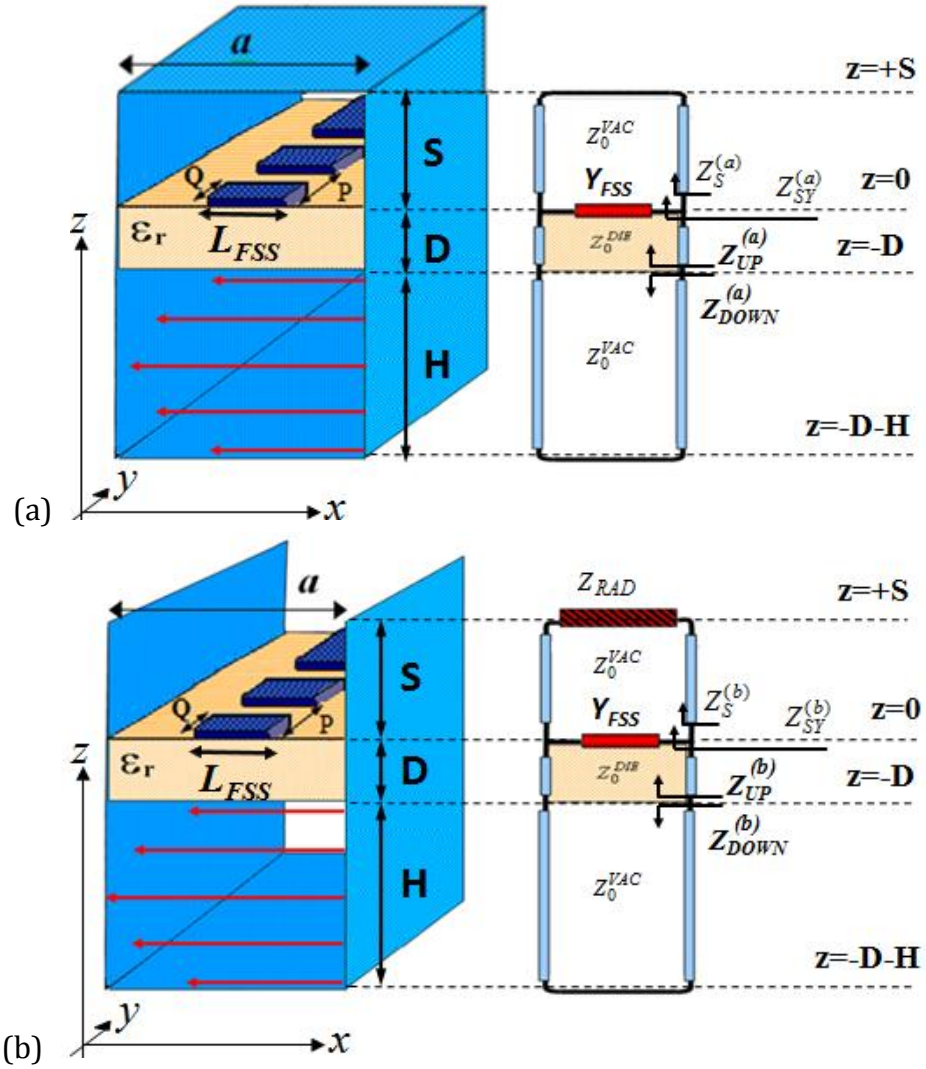

Fig. 2.3.4 Rectangular waveguide loaded with a printed dipole-based FSS and its transverse equivalent circuit.

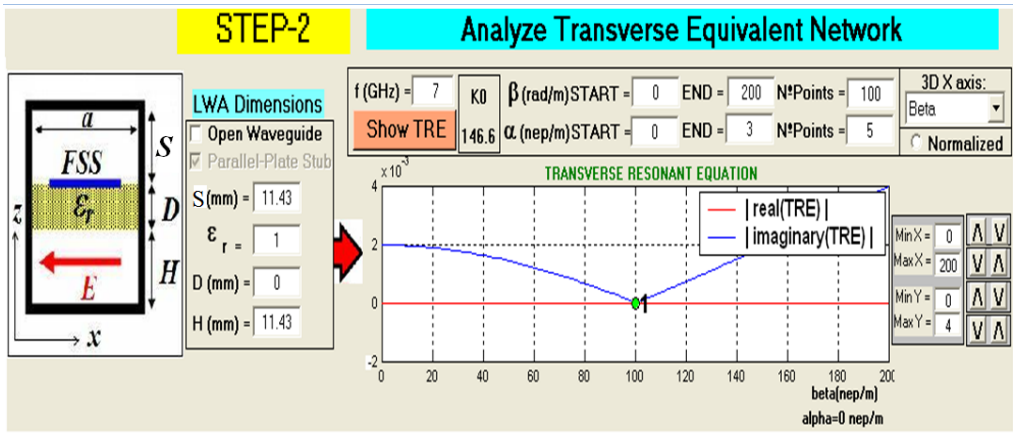

Fig. 2.3.5 Part of the graphical interface that analyzes the transverse equivalent network.

It is worth appreciating that every element included in the TEN is a function of k_y (Eq. 2.3.2-Eq.2.3.9), which is the unknown propagating constant in the longitudinal axis of the waveguide (y axis, Fig. 2.3.4). The part of the graphical interface which is associated to this step is shown in Fig. 2.3.5. When pushing the button "Show TRE", our tool also represents the Transverse Resonant Equation (TRE, [Maci 2005],[Zhao 2004 and 2005-I]) at a certain frequency. This equation can be expressed as (2.3.10), where Y^{UP} and Y^{DOWN} are the admittances shown in Fig. 2.3.4. The TRE is a function the unknown wavenumber k_y, and frequency or geometry (depending on the pole-zero expansion employed for the characterization of the FSS). To study the dispersion of the structure, we should find the values of k_y that make the TRE equal to zero for a fixed frequency and geometry (L_{FSS}).

$$\Psi(\omega, k_y, L_{FSS}) = Y^{UP}(\omega, k_y, L_{FSS}) + Y^{DOWN}(\omega, k_y) \qquad (2.3.10)$$

In Fig. 2.3.5 is also displayed an example of a TRE (module of its real and imaginary part) which corresponds to a design with closed waveguide at 7GHz. As it can be seen, there is a certain value of k_y which makes the TRE equal to zero.

STEP 3: Solving the TRE.

In the third step, our tool obtains the modal solutions of the structure at a specific frequency and for a given geometry. For that purpose it is necessary to find the values of k_y that satisfy the TRE ($\Psi(\omega, k_y, L_{FSS}) = 0$, Eq. 2.3.10), obtained in the previous step. In order to find these values, the tool solves the TRE by the Newton-Raphson method when pushing the button "Find ky" (Fig. 2.3.6). The application then plots the found solution in the graph of the TRE (green circle in Fig. 2.3.5). In general, this solutions will be of complex nature, $k_y = \beta_y\left(\frac{rad}{m}\right) + j\alpha_y\left(\frac{nep}{m}\right)$. In case we are dealing with a lossless and closed structure (Fig. 2.3.4(a)), real k_y solutions will correspond to its propagating modes, since they suffer no attenuation [Gomez 2006-II] ($\alpha_y = 0, k_y = \beta_y$).

On the contrary, if our structure is open at the top (Fig. 2.3.4(b)), if we introduce losses, or if the mode is at cutoff or at a bandgap, the TRE's solution won´t be real, and the values of k_y will be found in the complex plane. For the case of an open structure, the tool will perform an iterative search which is based on the one proposed in [Gomez 2006-II]. Specifically, it starts from the real solution of the closed waveguide and searches the complex solution opening the top of the structure gradually (in a number of steps fixed by the user). At each iteration, the opening of the top will have influence in the value of Z_{RAD} in the TEN (Fig. 2.3.4(b)). This impedance will now be called Z_{RAD}^{i}, which expression is the one in (2.3.11). The parameter ξ is defined in (2.3.12); its value will start being zero and will end being one. In the first iteration $Z_{RAD}^{1} = 0$, which means that the waveguide is closed (Fig. 2.3.4(a)), while in the last iteration $Z_{RAD}^{end} = Z_{MARCUVITZ}$, which means that the waveguide is totally top-open (the scenario we are interested on, Fig. 2.3.4(b)). In each step, the solution of the TRE associated to each TEN will be found following the opposite direction of the function´s gradient.

$$Z_{RAD}^{i} = \xi * \mathrm{Z_{MARCUVITZ}} \tag{2.3.11}$$

$$\xi = \frac{i}{Nº Steps} \tag{2.3.12}$$

An example of the evolution of the solution value through the iterations is illustrated in Fig. 2.3.6 (the complex solution is found in 6 steps in this case). This search starts at the real solution of the closed waveguide (ξ =0, Eq. 2.3.11). It is worth appreciating that, as the top of the waveguide opens, a negative imaginary component appears in the propagating constant (the radiation constant of the structure, α_y). In the last iteration, when the structure is completely open (ξ =1), the wavenumber (k_y) of the complex mode is found.

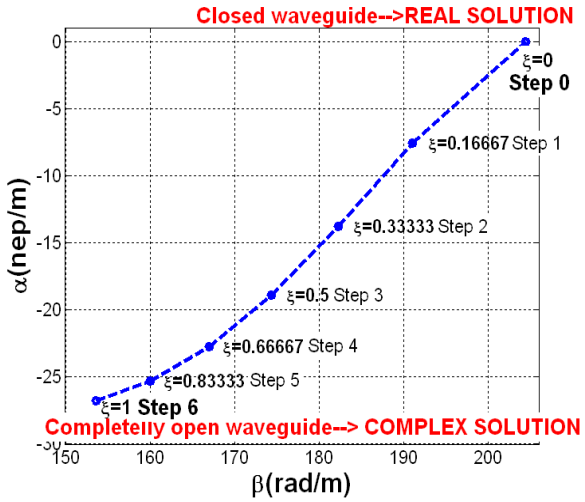

Fig.2.3.6 Evolution of TRE´s solution (through 6 steps).

Once the propagating constant (at a specific frequency and geometry) of a mode in the structure has been found, it is possible to obtain different interesting results, such as the dispersion curves or the near electric field inside the structure. It is also possible to have a physical insight into the structure based on the resonance of the mode in the transverse axis of the structure.

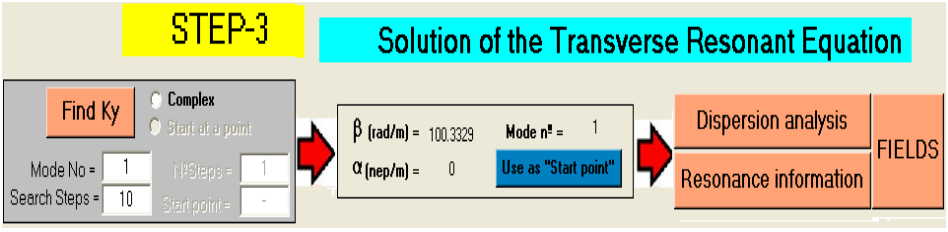

Fig. 2.3.7 Part of the graphical interface that finds the solutions of the TRE.

The **restrictions** of this tool should be now clarified:

- The structure must work under the condition of single mode propagation. This is due to the fact that both the pole-zero technique and the transmission lines employed in the TEN are only valid under the previous assumption.
- In order to employ the pole-zero technique, it must be assured that we are working in the non grating lobes regime of the periodic layers. This way, it is assured that the equivalent admittance is accurate.
- In the case of characterizing a radiating structure, as the open discontinuity is modeled by Marcuvitz´s expressions, it should be assured that $a<\lambda_0$ (as it is stated in [Marcuvitz 1951]).
- In the case of considering more than one periodic layer, the accuracy of the approach may be reduced as they are put closer. This effect is due to the fact that the interaction between the evanescent harmonic of the two layers is not considered in this approach.

Different structures based on rectangular waveguides loaded with FSS will be next analyzed in order to prove the efficiency of the proposed pole-zero technique and the implemented tool. The button “Dispersion analysis” in Fig. 2.3.7 will provide the dispersion curves, and pushing on “Fields” the graph of the transverse electric field will appear.

2.3.2 Analysis of HIS-loaded waveguide

The efficiency of the proposed pole-zero technique is proven by being applied in the **analysis of a HIS-loaded rectangular waveguide**. The miniaturization effect provided by the FSS that was reported in [Caiazzo 2004] and [Goussetis 2007-II] will also be proven in this section. In this section, the structure shown in Fig. 2.3.8(a) will be analyzed using the TEN illustrated in Fig. 2.3.8(b). As Fig. 2.3.8(a) shows, an empty rectangular waveguide (width a and height H) is loaded with a HIS, which consists of a periodic dipole-based FSS

(dipoles length L_{HIS}, width Q and periodicity P) over a cavity backed dielectric substrate of thickness D and relative permittivity ε_r.

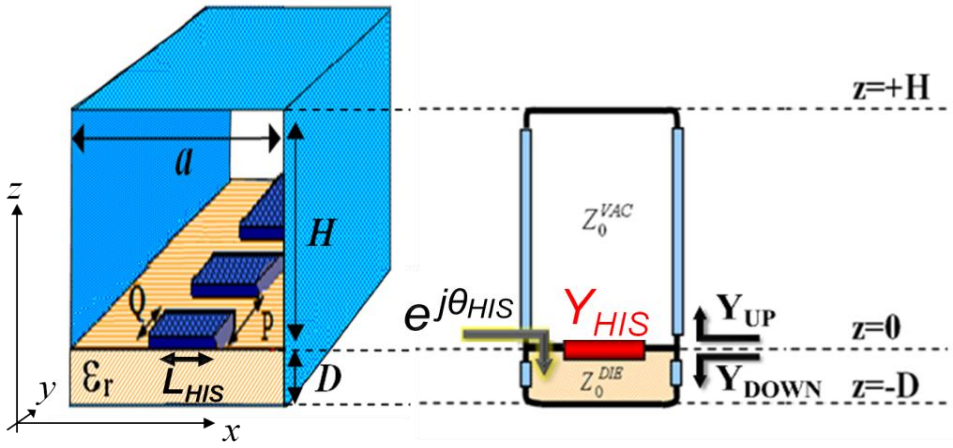

(a) (b)

Fig. 2.3.8 (a) Rectangular waveguide loaded with a dipole-based HIS (H = a = 11mm, D = 1.13 mm, ϵ_r = 2.2, L_{HIS} = 9 mm, P = 1.5 mm, Q = 0.5 mm). (b) Transverse equivalent network of the structure.

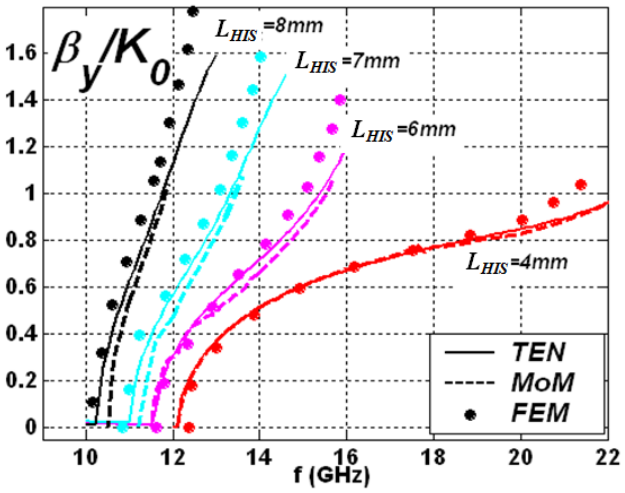

Fig. 2.3.9. Frequency dispersion curves for different lengths of the HIS dipoles.

To analyze this structure, the following TRE associated to the TEN shown in Fig. 2.3.8(b) must be solved:

$$Y_{UP}(\omega,k_y)+Y_{DOWN}(\omega,k_y)+Y_{HIS}(\omega,k_y,L_{HIS})=0 \qquad (2.3.13)$$

where Y_{HIS} represents the equivalent admittance of the dipole-based FSS, while Y_{UP} and Y_{DOWN} are the input admittances of the two sections of short-circuited transmission lines (the first of length H and the second of length D and dielectric

constant ε_r, see Fig. 2.3.8(b)). The two main variables involved in the TRE (2.3.13) are the analysis frequency ($\omega = 2\pi f$) and the unknown longitudinal propagation constant k_y (see axes in Fig. 2.3.8(a)), which must be numerically solved to obtain the dispersion curves with frequency. However, we have explicitly added the length of the HIS dipoles (L_{HIS}) as a variable in Y_{HIS}, since we are also interested in obtaining dispersion curves as a function of this design variable for a given fixed frequency of design.

The frequency dispersion analysis of the structure will be first performed. Using the pole-zero technique presented by Maci in [Maci 2005], the HIS with a fixed geometry can be analytically modeled with frequency by the admittance $Y_{HIS}(\omega,k_y)$. Introducing this expression in the TEN (Fig. 2.3.8(b)) and solving the associated TRE (2.3.13), the frequency dispersion curves shown in Fig. 2.3.9 are obtained. In particular, Fig. 2.3.9 shows the normalized propagation constant (β_y/k_0) curves derived from the TEN (continuous lines), which are compared to those obtained with a full-wave EBG modal analysis technique based on the Method of Moments [Gómez 2006-II] (MoM, dashed line), and with full-wave modal results obtained from commercial Finite Element Method [HFSS 2011] (FEM, circles). Different frequency-dispersion curves have been obtained for four different values of the HIS dipoles length (L_{HIS} = 4, 6, 7 and 8 mm). Good agreement is observed between the three techniques for all values of L_{HIS} in all the fast-wave frequency range ($\beta_y/k_0 < 1$, where the values for the angles of incidence θ given by $\sin\theta = k_y/k_0$ are real). Good agreement is observed even in the surface-wave region ($\beta_y/k_0 > 1$), validating the effectiveness of the frequency-pole-zero approach presented in [Maci 2005]. However, this technique does not allow for a direct derivation of the dispersion with the length of the FSS dipoles. As a result, if we want to study how L_{HIS} affects the performance of the HIS loaded waveguide, the pole-zero technique must be repeated for every single value of L_{HIS}, as it has been done to obtain the curves shown in Fig. 2.3.9. This is not as efficient as the modified pole-zero technique described in the previous section.

Following the modified pole-zero method proposed in Section 2.2 we can directly obtain dispersion curves varying the length of the dipoles in the HIS for a fixed frequency. In particular, the equivalent admittance $Y_{HIS}(k_y,L_{HIS})$ is derived

following (2.2.2), and is then introduced in the TEN of Fig. 2.3.8(b) in order to solve (2.3.13) for any value of L_{HIS}. Figure 2.3.10(a) shows the normalized phase constant (β_y/k_0) for the perturbed TE_{01} mode of the HIS-loaded waveguide of Fig. 2.3.8(a), varying L_{HIS} from 2 mm to 6 mm at the design frequency of 15 GHz. As expected, the longitudinal phase constant of the perturbed TE_{01} mode is enlarged as L_{HIS} increases from 2 mm to 6 mm, producing the aforementioned miniaturization effect [Caiazzo 2004], [Goussetis 2007-II]]. The results obtained with the proposed approach are very accurate, since they match those derived from different full-wave techniques such as MoM [Gómez 2006-II] and FEM [HFSS 2011], while being much more efficient in terms of computational cost, as will be described later (table 2.3.1).

Moreover, physical insight can be easily extracted from the TEN. For instance, Fig. 2.3.10(b) shows the reflection phase of the HIS (θ_{HIS}, Fig .2.3.8) seen by the perturbed TE_{01} mode when varying L_{HIS} at 15 GHz. As it can be seen in Fig. 2.3.10(b), the FSS is almost transparent for dipoles lengths below 4 mm, presenting a value of θ_{HIS} around 120° due to the dielectric slab of thickness D = 1.13 mm and ϵ_r = 2.2. When the dipoles length increases, the resonance of the HIS appears, obtaining magnetic-wall boundaries (θ_{HIS} = 0°) for L_{HIS} = 5.9 mm, which creates an effective waveguide of double height. Beyond this value, θ_{HIS} becomes negative, allowing for higher miniaturization, until the modes gets into the surface-wave regime.

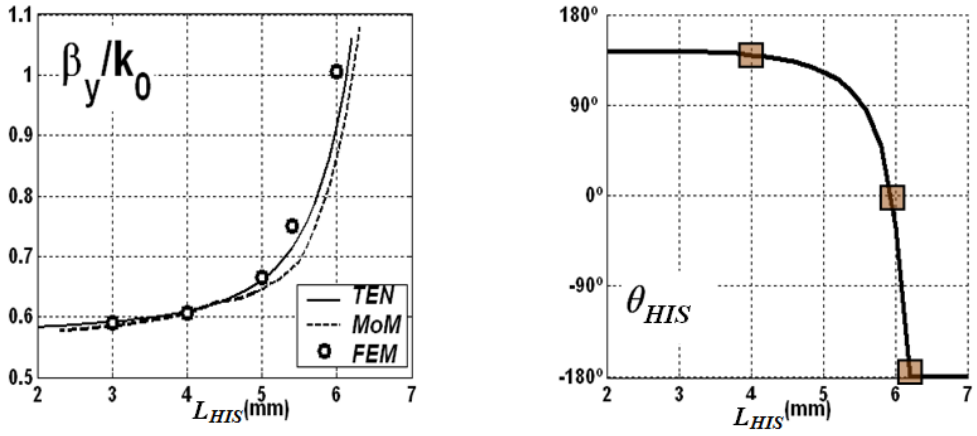

(a) (b)

Fig. 2.3.10 Dispersion curve for the structure of Fig. 2.3.8 varying L_{HIS} at 15 GHz.

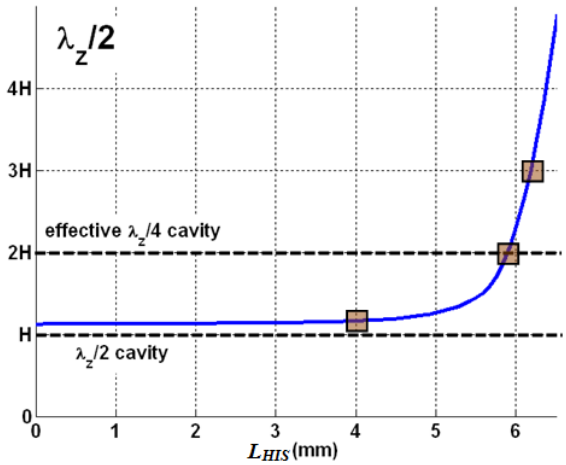

Fig. 2.3.11 Dispersion curve showing the effective waveguide height $\lambda_z/2$ as a function of L_{HIS}, at *15GHz.*

This profile reduction process can be equivalently appreciated by studying the wavelength of the propagating mode in the transverse plane (λ_z, Fig. 2.3.11). In a waveguide with no FSS, this wavelength is approximately twice the height of the cavity ($\lambda_z/2=H$). This occurs when the FSS in our structure is almost transparent (L_{HIS} < 4 mm, see Fig. 2.3.11). As L_{HIS} increases, the FSS perturbs the propagating mode, increasing its λ_z, which is equivalent to dealing with an unperturbed TE_{01} mode in a bigger waveguide. Particularly, when L_{HIS} = 5.9 mm we can see that $\lambda_z/2=2H$, which means we are working with an effective waveguide of double height due to the magnetic boundary condition presented by the HIS. In this situation, it is achieved a reduction of the resonant cavity to a half. Increasing L_{HIS} more, we can obtain further effective cavity heights, as it is shown in Fig. 2.3.11.

This process can be illustrated by plotting the transverse electric field lines of the perturbed TE_{01} mode in the structure, as shown in Fig. 2.3.12. Again, very good agreement is observed between the fields obtained with the simple TEN model (Fig. 2.3.12(a)), and the full-wave fields obtained using a full-wave MoM technique [Gómez 2006-II] (shown in Fig. 2.3.12(b)). However, it must be noticed that the TEN is very simple and it only represents a single Floquet-mode, losing all the visual information given by evanescent higher-order Floquet-modes in the proximity of the printed dipoles. Nevertheless, the boundary condition of the HIS is perfectly depicted from the simple TEN model, showing transparency at L_{HIS} = 4

mm, AMC (Artificial Magnetic Conductor) boundaries at L_{HIS} = 5.9 mm, and surface-wave regime at L_{HIS} = 6.3 mm.

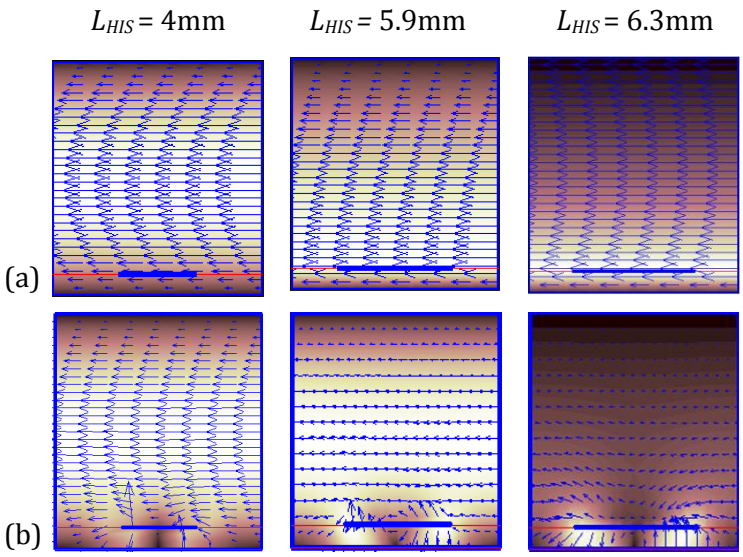

Fig. 2.3.12 Transverse electric field inside the HIS-loaded waveguide, obtained (a) from TEN (b) from MoM [Gómez 2006-II]

2.3.3 Analysis of open waveguide loaded with PRS (1D LWA)

In this section, a one dimensional (1D) leaky-wave antenna (LWA) is analyzed with the developed tool. Although a brief explanation on the behavior of this kind of antennas is now provided, they are presented in detail in Section 3.

As it was explained in Section 2.1, FSS can also be used to synthesize partially reflective surfaces (PRS) in resonant antennas [Trentini 1956]. As it is well-known, the radiation from a punctual source can be enhanced by placing it between a metallic screen and a Partially-Reflective Sheet (PRS) [Trentini 1956], [Jackson 1988], [James 1989], [Feresidis2001]. The electromagnetic waves that arise from the feeding point are bounced back and forth between the two sheets, becoming leaky-modes of the guiding structure. This type of LWAs has been referred as Fabry-Perot (FP) antennas due to their analogy with optical resonant cavities. Here, it is analyzed a 1D configuration of FP LWA created with an open rectangular waveguide loaded with a dipole-based FSS that acts as a PRS. The scheme of the structure and the main dimensions are shown in Fig. 2.3.13, together with its TEN.

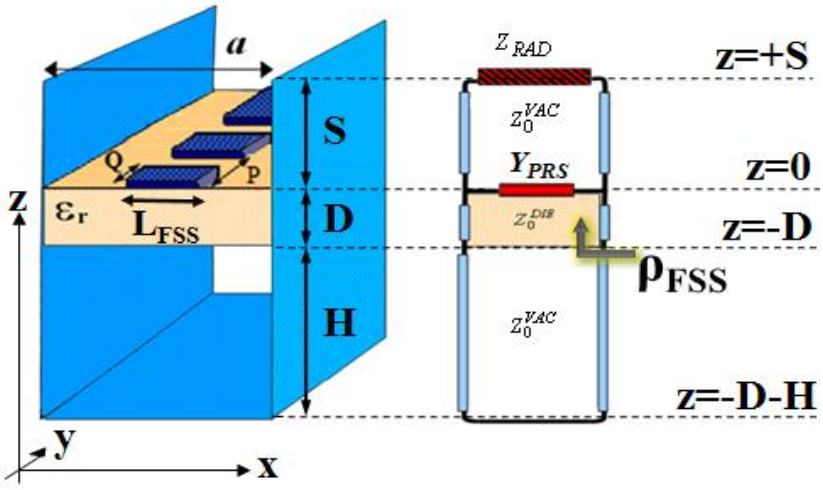

(a) (b)

Fig. 2.3.13 (a) 1D Fabry-Perot leaky-wave antenna formed by a parallel-plate waveguide loaded with a dipole-based FSS acting as a PRS (b) Transverse equivalent network of the structure. ($a = H$ = 11 mm, S = 5 mm, D = 1.13 mm, ϵ_r=2.2, L_{FSS} = 10 mm, P = 1.5 mm, Q = 0.5 mm).

Leaky-modes are characterized by a complex propagation constant along the longitudinal direction of the waveguide (y axis in Fig. 2.3.13(a))

$$k_y = \beta_y - j\alpha_y \tag{2.3.14}$$

where β_y stands for the propagation or phase constant, and α_y is the attenuation rate, due to the radiation or leakage induced by the leaky-wave [Oliner 1993]. To analyze and design a LWA, the dispersion curves of the constituent leaky-mode are of much help ([Guglielmi 1991], [Oliner 1993], [Gómez 2006-III], [Kosmas 2007] and [Goussetis 2007-I]). Particularly, β_y determines the pointing or radiating angle of the LWA in the elevation plane (zy plane in Fig. 2.3.13(a)), θ_{RAD}, which is approximately expressed as [Oliner 1993]:

$$\sin\theta_{RAD} = \frac{\beta_y}{k_0} \tag{2.3.15}$$

and the leakage rate α_y is related to the radiation efficiency of the LWA of length L_A, η_{RAD}, which in the lossless case is [Oliner 1993]:

$$\eta_{RAD} = 1 - e^{-2\alpha_y L_A} = 1 - e^{-4\pi \frac{\alpha_y}{k_0} \frac{L_A}{\lambda_0}} \tag{2.3.16}$$

The main beamwidth is determined by the length of the antenna and the aperture illumination, which for a uniform LWA (exponential illumination) can be expressed as [Oliner 1993]:

$$\Delta\theta \cong \frac{1}{\frac{L_A}{\lambda_0}\cos\theta_{RAD}} \tag{2.3.17}$$

In many cases, 90% radiation efficiency LWAs are desired, in these cases, Eqs.(2.3.16-17) provide the following approximate expression for the antenna beamwidth:

$$\Delta\theta \approx \frac{\alpha_y / k_0}{0.183 \cdot \cos\theta_{RAD}} \tag{2.3.18}$$

The admittance of the dipole-PRS-FSS can be analytically expressed as a function of frequency and the unknown leaky-propagation constant, k_y, following Eq.(4) of Maci's pole-zero procedure [Maci 2005]. This function $Y_{PRS}(\omega,k_y)$ can then be introduced in the TEN (Fig. 2.3.12(b)), and the associated TRE can be numerically solved to obtain the unknown complex k_y (2.3.14) in the desired frequency band. The pole-zero matching procedure [Maci 2005] should be performed for every single desired value of the PRS-FSS dipoles length (L_{FSS}). Figure 2.3.14 shows the family of frequency dispersion curves obtained in this way. The results obtained with the TEN are plotted together with those given by a full-wave analysis tool for leaky-modes based on MoM [Gómez 2006-II]. Curves from 3D full-wave simulations using FEM commercial software [HFSS 2011] are also plotted. Good agreement is observed between these three techniques for all frequencies and different values of L_{FSS}, for both the pointing angle curves (θ_{RAD}, Fig. 2.3.14(a)), and the normalized leakage rate curves (α_y/k_0, 2.3.14(b)).

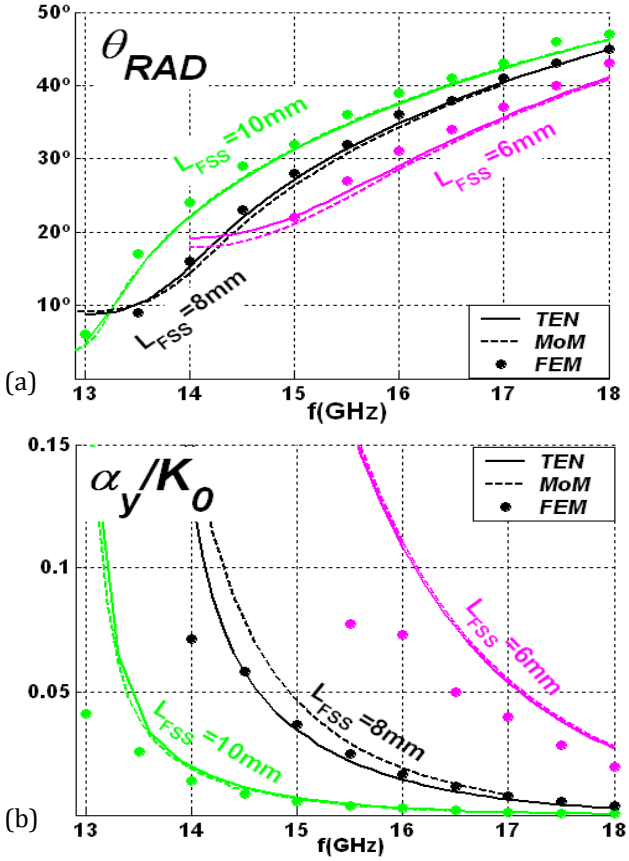

Fig. 2.3.14 Frequency dispersion curves for the 1D-PRS-LWA in Fig. 2.3.13 for different lengths of the FSS dipoles (L_{FSS}) (a) Pointing angle (b) Normalized leakage rate.

The PRS-FSS must be properly engineered to design the LWA [Feresidis 2001], [Maci 2003], [Zhao 2005-I], [Kosmas 2007]. Particularly, for a fixed pointing angle θ_{RAD} (2.3.15), we can synthesize a certain leakage rate α_y which will determine the radiation efficiency (2.3.16) and directivity (2.3.17) of the LWA [Oliner 1993]. In our case, we choose a pointing angle of 30° for a design frequency of 15 GHz. As shown in Fig. 2.3.14(b), L_{FSS} strongly affects the radiation rate of the leaky-mode due to the fact that L_{FSS} controls the transparency of the FSS [Vardaxoglou 1997], [Munk 2000], [Feresidis 2001], [Kosmas 2007]. However, the pointing angle is also affected by the FSS, and this must be taken into account for an accurate design. For this purpose geometry-dispersion curves at the frequency of design should be obtained. This will be next efficiently achieved.

Following the process described in Section 2.2, an analytical expression for the admittance of the FSS as a function of L_{FSS} and k_y, $Y_{PRS}(L_{FSS},k_y)$, can be derived

using (2.2.2). In this way the TRE can be solved for the unknown leaky-mode complex k_y, as a function of L_{FSS}, for a fixed design frequency. Figure 2.3.15 shows the results obtained at 15 GHz for the PRS-LWA of Fig. 2.3.13, sweeping L_{FSS} from 4 mm to 10 mm. Again, the results obtained by this procedure are compared to full-wave results obtained with 2D-MoM [Gómez 2006-II] and 3D-FEM [HFSS 2011], showing very good agreement. This analysis is very efficient, since it allows direct derivation of dispersion curves with the geometrical variable of interest, L_{FSS}. As it can be seen in Fig. 2.3.15(b), the leakage rate increases as L_{FSS} is lowered. This is a simple procedure to control the radiation efficiency (2.3.16) and directivity (2.3.17) of the LWA [Feresidis 2001], [Kosmas 2007], [Gómez 2005-I], [Gómez 2006-III].

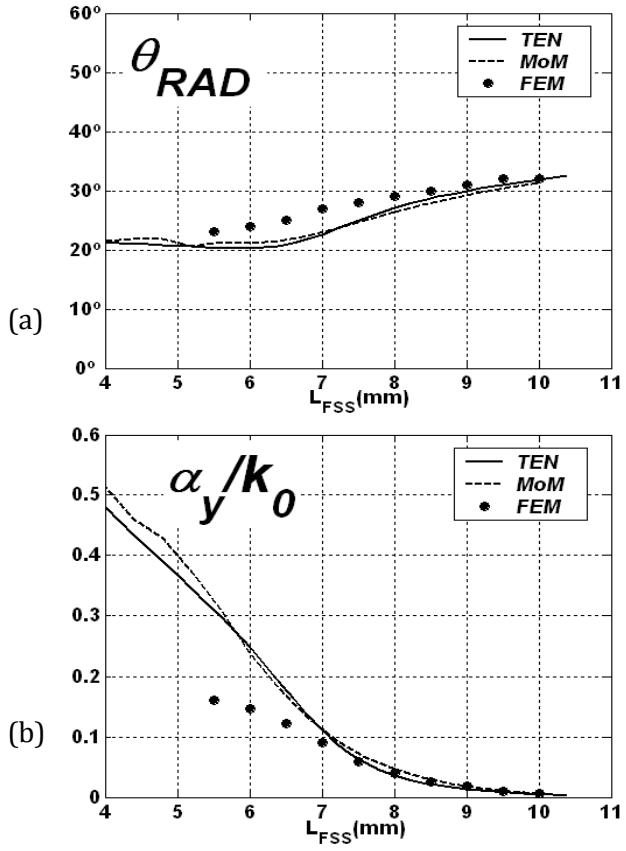

Fig. 2.3.15 Dispersion curves for the 1D-PRS-LWA in Fig. 2.3.13 with the length of the FSS dipoles (L_{FSS}), at 15bGHz (a) Pointing angle (b) Normalized leakage rate.

The TEN of Fig. 2.3.13(b) allows to obtain physical insight in this phenomenon, analyzing the reflection coefficient (modulus and phase) seen by the TE-leaky-wave incident on the PRS (ρ_{FSS} in Fig. 2.3.13(b)). This reflection

coefficient can be analytically derived from the expression of $Y_{PRS}(L_{FSS},k_y)$, once the dispersion curves are obtained using simple microwave relations. These results are shown in Fig. 2.3.16, where it can be observed that the PRS-FSS becomes more transparent as L_{FSS} decreases, which explains the increase of α_y/k_0 for lower values of L_{FSS} in Fig. 2.3.15(b). This can also be easily checked by inspecting the fields of the TE-leaky-mode inside the PRS-loaded cavity. The plots of the fields are shown in Fig. 2.3.17, and they are compared to those obtained with full-wave MoM [Gómez 2006-II]. Excellent agreement is observed, showing how the transparency of the PRS increases for lower values of L_{FSS}. Also, the field plots along the *zy* plane of the LWA (see reference axis in Fig. 2.3.13(a)), obtained with 3D-FEM [HFSS 2011] are shown in Fig. 2.3.18 for different values of L_{FSS}, confirming this phenomenon (see how more energy is radiated as L_{FSS} is decreased).

However, this control of the leakage rate with L_{FSS} has also some effects in the radiating angle of the LWA. The variation of θ_{RAD} with L_{FSS} observed in Fig. 2.3.15(a) is due to the dependence of the reflection phase of the PRS-FSS (θ_{FSS}) with L_{FSS}, shown in Fig. 2.3.16. Particularly, θ_{FSS} increases as L_{FSS} decreases, making θ_{RAD} decrease for lower values of L_{FSS}. This effect must be taken into account for an accurate design of the LWA.

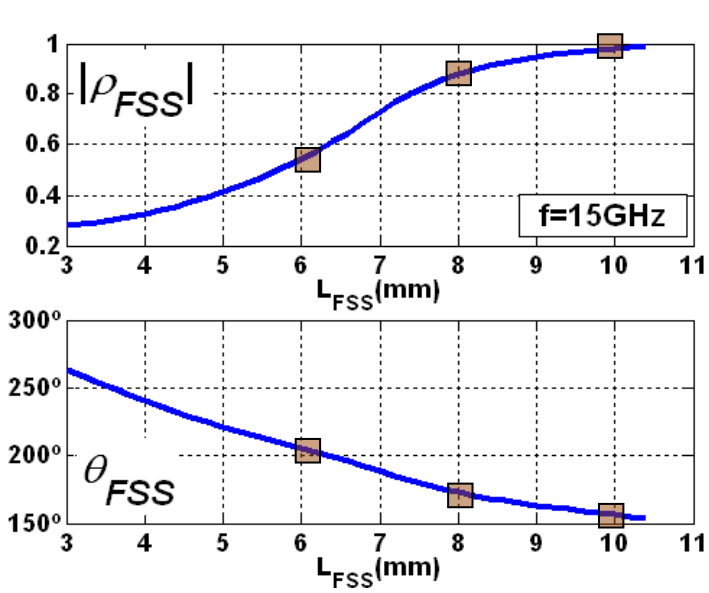

Fig. 2.3.16 Magnitude and phase of the reflection coefficient of the FSS-PRS (ρ_{FSS}), at 15 GHz, as a function of the length of the dipoles (L_{FSS}).

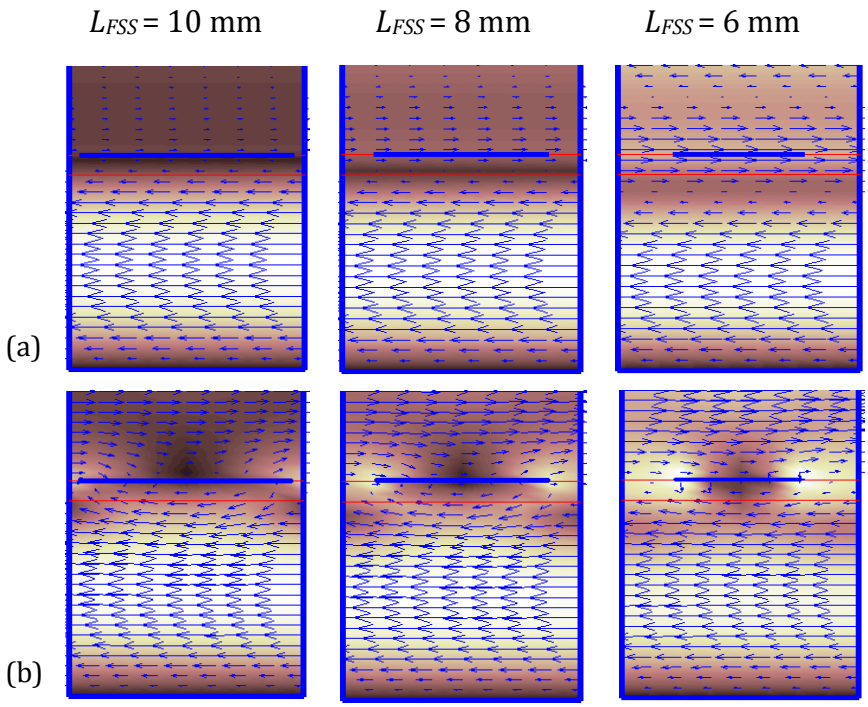

Fig. 2.3.17 Transverse electric field of the leaky-mode inside the PRS cavity obtained (a) from TEN (b) from MoM [22]

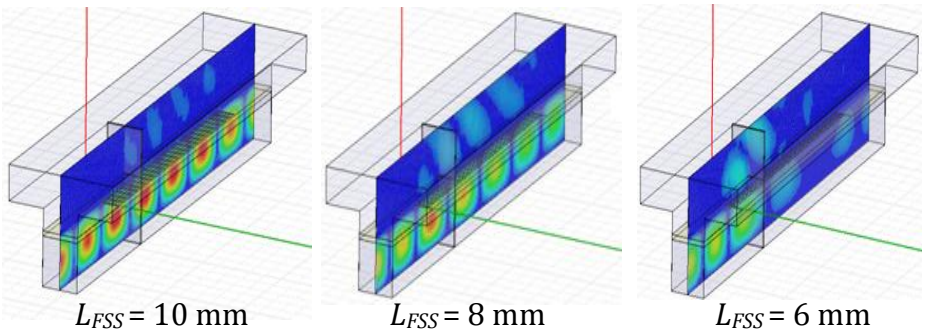

Fig. 2.3.18 Leaky-wave near field patterns obtained with 3D-FEM [HFSS 2011] for different values of L_{FSS}.

Finally, Fig. 2.3.19 shows the radiation pattern of the designed PRS-LWA at 15 GHz, with L_{FSS} = 8 mm and with an antenna length of L_A = 3.5 λ_0 = 61.2 mm. Acceptable agreement is observed between the far-field pattern calculated by Fourier transforming the leaky-wave aperture field obtained from the simple TEN, and the results given by 3D-FEM analysis of the LWA [HFSS 2011].

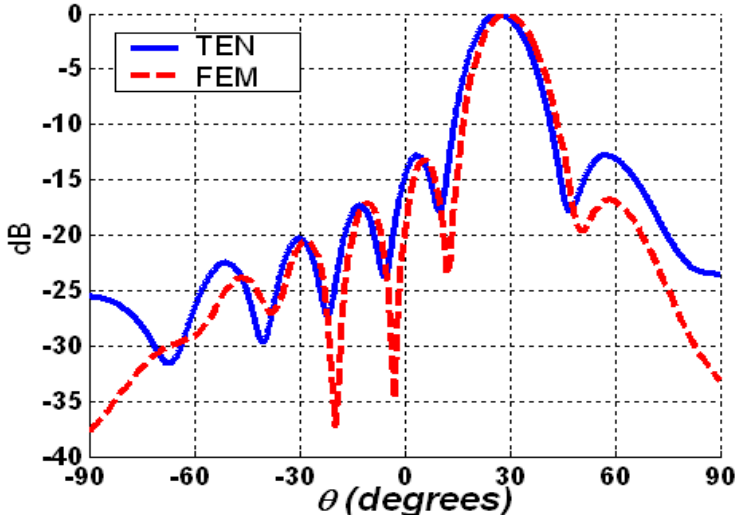

Fig. 2.3.19 Radiation pattern of the designed PRS-LWA (L_{FSS} = 8 mm, f = 15 GHz).

Table 2.3.1 compares computation times to analyse each point of the dispersion curves obtained in this paper. Computation times with the proposed technique based on TEN analysis are much lower than those needed with full-wave tools. A distinction has been made when dealing with complex leaky-modes, since the observed efficiency is even better in this case, due to the fact that the search of complex modes is more cumbersome. These computation times are obtained using an *Intel Centrino Duo T2400* processor, working at 1.83 GHz with 2GB *RAM*.

Real modes		***Complex modes***	
FEM 2D [16]	1800 s.	**FEM 3D [16]**	3600 s.
MoM EBG [15]	2 s.	**MoM EBG[25]**	6 s.
TEN	**.005 s.**	**TEN**	**.01 s.**

Table 2.3.1. Comparison of computation time per dispersion point.

Regarding the comparison of our results with full-wave simulations, a better agreement with MoM has generally been observed. This was expected, since MoM full-wave data were used for the rational fitting of the FSS.

2.4 Waveguide-discontinuity based approach

In this section, a quasi-analytical approach is presented to study the transmission/reflection of electromagnetic waves through 2-D periodic arrays of metallic dipoles. The approach is based on standard waveguide discontinuity theory, adopting the point of view proposed in [Medina 2008]. The equivalent circuit comes up after taking advantage of the periodicity of the structure, which allows the reformulation of the original problem as a certain equivalent waveguide scattering problem. Equivalent transmission lines are used to simulate the wave propagation whereas equivalent lumped circuit elements account for the effect of the evanescent fields excited in the discontinuity. However, the accuracy and reliability of the approach critically depends on the circuit topology employed in the model. The judicious choice of the equivalent circuit model simplifies considerably the original complex electromagnetic problem and gives a good physical insight into the parameters that are relevant in the phenomenon. It also provides a robust strategy that gives rise to surprisingly accurate results even for rather complex situations.

In comparison to the scenery of a metallic screen perforated with holes studied in [Medina 2008], the complementary structure of periodic arrangement of metallic dipoles is here characterized (shown in Fig. 2.4.1). However, the main novelty of the proposed approach resides in the fact that oblique incidence and the

presence of dielectric slabs are now considered. These aspects are essential for the application of the equivalent circuit to practical situations, since FSSs are normally printed over a dielectric substrate and work under arbitrary plane-wave incidence.

For the sake of simplicity, the case of oblique incidence of a TE polarized wave in H-plane will be firstly explained in **Section 2.4.1**, considering a free-standing FSS. Secondly, the presence of dielectric slabs will be studied in **Section 2.4.2.** This study commences from the case when the FSS is sandwiched between identical dielectric substrates, and extends to the case of arbitrary slabs. Later, oblique incidence of a TM polarized wave in E-plane is characterized in **Section 2.4.3**. Finally, the possibility of characterizing other shapes of the scatterers is discussed in **Section 2.4.4**.

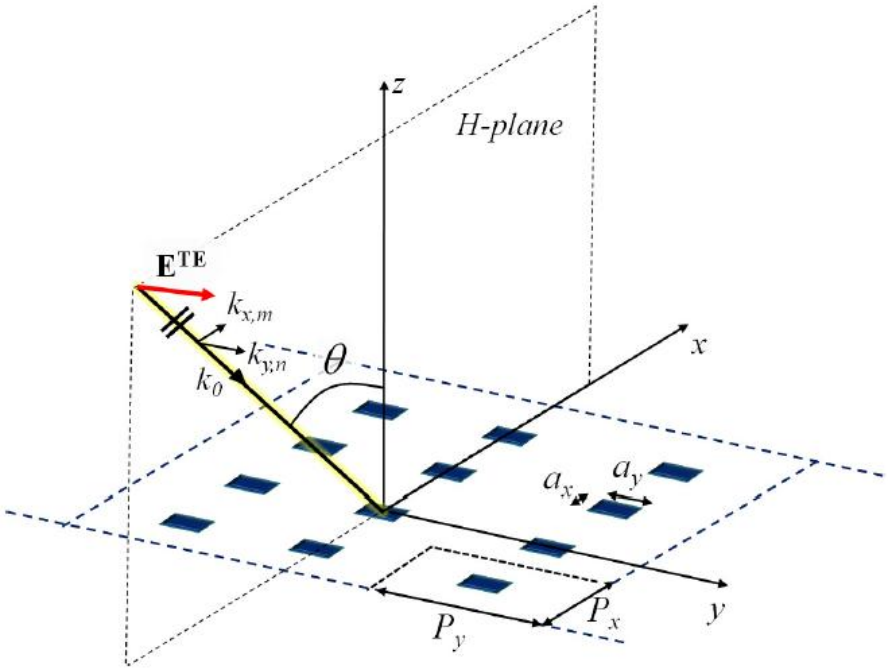

Fig. 2.4.1. Scheme of the free-standing array of metallic dipoles of zero thickness under oblique incidence in H-plane (P_x = P_y = 5 mm, a_x = 0.5 mm).

2.4.1 Circuit model for arbitrary TE incidence

In order to present the basic rationale underlying the proposed equivalent-circuit model, in this section it will be firstly considered the free-standing periodic surface shown in Figure 2.4.1, which is built from the periodic arrangement of conducting zero-thickness metallic patches (dipoles) of dimension $a_x \times a_y$. The array extends along the *x* and *y* axes, with periodicities P_x and P_y, respectively. The periodic surface is located at $z = 0$ and a plane wave impinges on this surface from the direction defined by θ. As can be seen in Fig. 2.4.1, the plane of incidence is *xz* (with azimuthal angle $\varphi = 0^o$), and the wave is TE polarized (*i.e.*, directed along the *y* axis). Therefore, in the scanned H-plane the impinging field is always parallel to the metallic dipoles, having a strong interaction with them. Due to periodicity, Floquet (space) harmonics are excited by the incident plane wave as it reaches the array [Guglielmi 1989-I], [Maci 2005], [Varela 2012]. These scattered waves can be either TE or TM polarized. The wavenumbers in the *x* and *y* axes associated with the space harmonics are given by

$$k_{x,m} = k_0 sin\theta + \frac{2m\pi}{P_x} \tag{2.4.1}$$

$$k_{y,n} = \frac{2n\pi}{P_y} \tag{2.4.2}$$

where m, n = 0, ±1, ±2 … and $k_0 = 2\pi f/c$ is the free-space wavenumber, with f being the frequency and c the speed of light in vacuum. Each excited space harmonic is defined by a pair of integers, *mn*, with the following associated complex wavenumber along the *z* direction:

$$k_{z,mn}^{(\varepsilon_r)} = \sqrt{k_0^2\varepsilon_r - k_{x,m}^2 - k_{y,n}^2} = \begin{cases} \beta_{mn} = \sqrt{k_0^2\varepsilon_r - k_{x,m}^2 - k_{y,n}^2}\,, & \text{if } f \geq f_{c,mn}^{(\varepsilon_r)} \\ -j\alpha_{mn} = -j\sqrt{k_{x,m}^2 + k_{y,n}^2 - k_0^2\varepsilon_r}\,, & \text{if } f < f_{c,mn}^{(\varepsilon_r)} \end{cases} \tag{2.4.3}$$

where $f_{c,mn}^{(\varepsilon_r)}$ is the cutoff frequency of the *mn*-th harmonic; namely, the frequency that satisfies

$$\gamma_{mn}^2 = k_{x,m}^2 + k_{y,n}^2 - k_0^2 \varepsilon_r = 0 \tag{2.4.4}$$

and that can be expressed as

$$f_{c,mn}^{(\varepsilon_r)} = \frac{1}{\varepsilon_r - sin^2\theta} \left\{ \frac{mc}{P_x} sin\theta + \sqrt{\varepsilon_r \left[\left(\frac{mc}{P_x}\right) + \left(\frac{nc}{P_y}\right) \right] - \left(\frac{nc}{P_y} sin\theta\right)^2} \right\}. \tag{2.4.5}$$

The above cutoff frequency is determined by the array periodicities (P_x and P_y), the angle of incidence (θ) and the medium dielectric constant (ε_r), but it is independent on the dipole dimensions. For convenience, the cutoff frequency is here formulated in the presence of a homogeneous dielectric medium with permittivity ε_r. This fact is represented by the superscript (ε_r), although free space is assumed in the present subsection (ε_r = 1), which will be denoted by the superscript (1). Note that, for the case of normal incidence (θ = 0º), Eq. (2.4.5) reduces to the well-known expression of the modal cutoff frequencies in a rectangular waveguide of dimensions P_x x P_y.

At a given frequency, as (2.4.3) reveals, $k_{z,mn}^{(1)}$can be purely imaginary or real, defining evanescent (slow) or grating (fast) waves, respectively [Munk 2000]. Specifically, each harmonic is an evanescent wave that decays along the z direction below its cutoff frequency $f_{c,mn}^{(1)}$. Above this frequency, $k_{z,mn}^{(1)}$ is no longer imaginary and the associated harmonic becomes a (grating) plane wave that propagates along a direction parallel to the vector $\boldsymbol{p}_{mn} = k_{x,m}\hat{\boldsymbol{x}} + k_{y,n}\hat{\boldsymbol{y}} + k_{z,mn}^{(1)}\hat{\boldsymbol{z}}$. In our analysis, the incident plane wave in Fig. 2.4.1 corresponds to the dominant *mn* = 00 Floquet harmonic. This wave propagates at any given frequency along the direction defined by θ (note that $k_{z,00}^{(1)}$is always real). In most of microwave, engineering and antenna applications, the working frequency regime is set within the so-called *no grating lobes regime* [Munk 2000]; i.e., only the dominant Floquet harmonic is propagating while the remaining harmonics are evanescent. Certainly, for practical purposes, only a finite number of these evanescent space harmonics are significant. Therefore, only the fast waves and the lowest few harmonics below cutoff are the relevant contributions to the field at the transverse plane.

In general, each Floquet harmonic can be either TE or TM polarized and has the following associated characteristic impedance [Munk 2000], [Pozar 2005]:

$$Z_{TE,mn}^{(\varepsilon_r)}(\omega) = \mathrm{j}\omega\mu_0/\gamma_{mn} \tag{2.4.6}$$

$$Z_{TM,mn}^{(\varepsilon_r)}(\omega) = -\mathrm{j}\gamma_{mn}/(\omega\epsilon_0\epsilon_r). \tag{2.4.7}$$

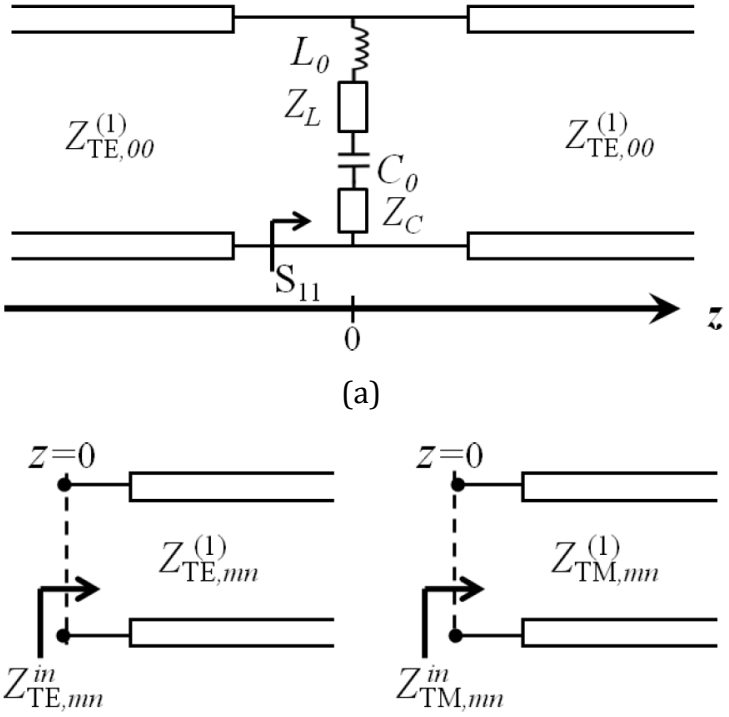

Fig. 2.4.2. Proposed transverse equivalent network for Fig. 2.4.1.

Depending on the nature of the harmonic, its associated impedance is real or purely imaginary. In particular, inductive/ capacitive impedances correspond to TE/TM evanescent waves. Due to the assumed impinging TE wave polarization and plane of incidence, the problem under consideration can be reduced to a single unit cell with electric walls in the *xz* plane and Floquet walls (periodic boundary conditions) in the *yz* plane (see Fig. 2.4.1). This is equivalent to a parallel-plate transmission line formed by two paralell-to-*xz*-plane electric walls separated by a distance P_y and two paralell-to-*yz*-plane Floquet walls separated by a distance P_x. It should be noted that the family of excited Floquet harmonics corresponds to the modal solutions of this transmission line. In addition, TM_{m0} harmonics do not

satisfy the specified boundary conditions and are not excited in the structure under consideration.

According to the above discussion, the structure in Fig. 2.4.1 can be modeled by the Transverse Equivalent Network (TEN) shown in Fig. 2.4.2(a). The propagation of the incident, reflected, and transmitted TE plane wave is modeled by the infinite transmission lines placed at both sides of the discontinuity. The characteristic impedance associated to these lines is real and corresponds to

$$Z_{TE,00}^{(\varepsilon_r)}(\omega) = \omega\mu_0 / k_{z,00}^{(\varepsilon_r)} \ . \tag{2.4.8}$$

The lumped elements in the series configuration shown in Fig. 2.4.2(a) model the excitation of all other mn harmonics excited in the discontinuity [Munk 2000, Ch. 5]. Specifically, the inductive elements (L_0 and Z_L) account for the excitation of TE harmonics, whereas the capacitive components (C_0 and Z_C) account for the TM contribution. The impedances

$$Z_L(\omega) = \sum_{h=1}^{N_{TE}} A_h^{TE} Z_{TE,h}^{in}(\omega) \tag{2.4.9}$$

$$Z_C(\omega) = \sum_{h=1}^{N_{TM}} A_h^{TM} Z_{TM,h}^{in}(\omega). \tag{2.4.10}$$

characterize the excitation of a certain number of TE and TM harmonics with lowest cutoff frequencies (which are represented by N_{TE} and N_{TM}, respectively). In these expressions each considered harmonic h is associated with certain *mn* pair, and $A_h^{TE/TM}$ is a complex constant that accounts for the degree of excitation of each TE/TM *h*-th harmonic. The contribution of each TE/TM wave in (2.4.9)-(2.4.10) is proportional to the input impedance of its corresponding equivalent transmission line, which here corresponds to an infinite transmission line of impedance $Z_{TE/TM,mn}^{(1)}$ as shown in Fig. 2.4.2(b). The higher-order TE and TM harmonics that were not considered in (2.4.9)-(2.4.10) are highly evanescent waves whose dependence with frequency is almost insignificant. For this reason, their effect in the discontinuity can be accounted for by a frequency independent inductance, L_0, and capacitance, C_0, in Fig. 2.4.2(a).

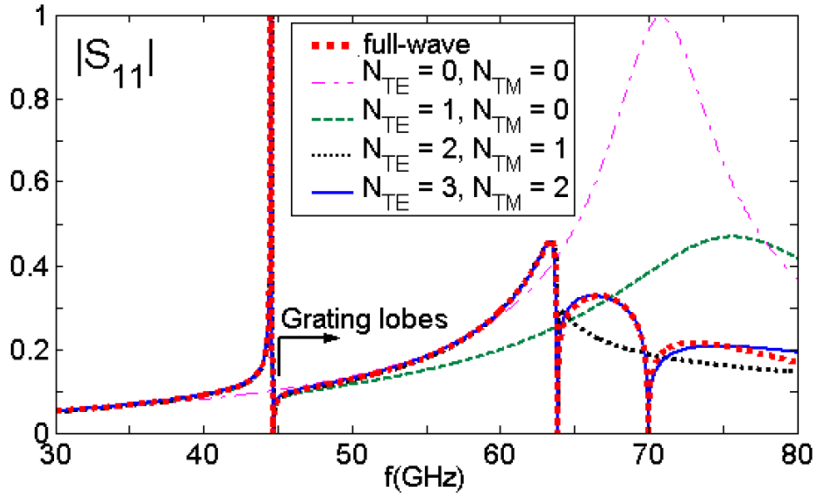

(a)

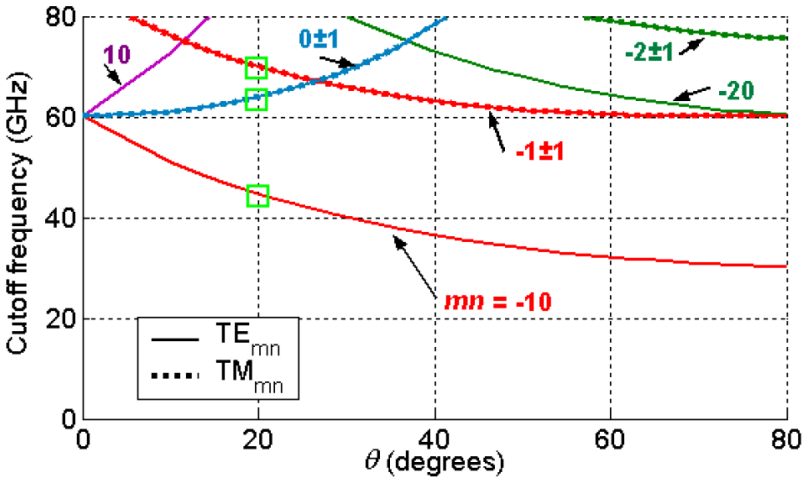

(b)

Fig. 2.4.3. (a) Magnitude of the reflection coefficient for the structure in Fig. 2.4.1 under 20º incidence and dipoles with a_y = 2 mm. (b) Cutoff frequencies associated with the higher-order *mn*-th harmonics excited in the structure as a function of the exciting wave angle of incidence.

Taking into account the circuit of Fig. 2.4.2(a), in order to calculate the quasistatic parameters of the structure [Tretyakov 2003], it is just necessary to compute the next expressions

$$C_{quas} = C_0 + \lim_{\omega \to 0} \frac{1}{j\omega Z_C} \tag{2.4.11}$$

$$L_{quas} = L_0 + \lim_{\omega \to 0} j\omega Z_L. \tag{2.4.12}$$

As a general rule, in order to achieve an efficient characterization of the dipole array until a certain frequency, the values of N_{TE} and N_{TM} should be set to one plus the number of TE and TM harmonics above cutoff (which depends on the angle of incidence, as can be deduced from (2.4.5)).). The values of the lumped components (L_0 and C_0) and the excitation coefficients ($A_h^{TE/TM}$) can be computed from a few full-wave simulations of the reflection coefficient S_{11}. For this purpose it should be considered that the S_{11} parameter in Fig. 2.4.2(a) can be related to the lumped-element parameters in this circuit in the following way:

$$\mathrm{j}\omega L_0 + \frac{1}{\mathrm{j}\omega C_0} + Z_L(\omega) + Z_C(\omega) = -Z_{TE,00}^{(1)}(\omega)\frac{S_{11}(\omega)+1}{2S_{11}(\omega)}. \tag{2.4.13}$$

If the above equation is written for a set of frequency values, we can write a linear system of equations whose solution is the set of unknown parameters of our equivalent circuit model. The minimum number of full-wave computations of the S_{11} parameter should be equal to the number of unknowns: N_{TE} + N_{TM} + 2 (typically no more than four or five for freestanding periodic surfaces). In order to assure that the system of equations is well-conditioned, our experience suggests that two of the evaluated frequency values should be low (in order to characterize the two quasi-static parameters) and the rest must be near the onset of the N_{TE} and N_{TM} modeled harmonics (in order to characterize each excitation coefficient). Following the Fabry-Pérot condition, every zero-thickness metallic dipole in the array resonates at a frequency where its length is approximately half a wavelength [Trentini 1956] (the fringing fields make the Fabry-Pérot condition only approximate). If this condition occurs at a frequency below the grating lobe regime, the array only presents total reflection at this frequency. However, if the Fabry-Pérot dipole resonance does take place in the grating lobe regime, an extraordinary total reflection is still expected to occur before the onset of the first grating lobe; as it was reported in [Ebbesen 1998] for total transmission in a dual structure. Moreover, the extraordinary reflection can be related to the appearance of Fano resonances [Fano 1961], *i.e.*, a peak of total reflection (transmission) which precedes a very close null of reflection (transmission). Therefore, depending on the length of the dipoles, the periodic surface can present either conventional or extraordinary reflection; or, in other words, either Fabry-Pérot or Fano type

resonance. Thus, in order to check the validity of our proposed equivalent circuit, the particular dipole array described in Fig. 2.4.1 with a_y = 2mm is studied in Fig. 2.4.3(a). This figure shows the reflectivity under plane wave oblique incidence (θ = 20º) computed with a full-wave Method of Moments approach [Goussetis 2006-I] and with the proposed TEN of Fig. 2.4.2. Figure 2.4.3(a) shows an extraordinary resonance (total reflection, $|S_{11}|$ = 1) at approximately 44.5 GHz (the expected dipole Fabry-Pérot resonance should be around 75 GHz). Three nulls can also be observed in the reflection coefficient at approximately 44.7 GHz, 63.9 GHz, and 70 GHz. These nulls can be associated with Wood's anomalies that appear at the onset of higher-order harmonics [Medina 2008]. Specifically, at the cutoff frequency of TE harmonics, their associated TE impedance diverges to infinite (see Eq. (2.4.6)), which makes Z_L behave as an open circuit in Fig. 2.4.2. Therefore, perfect impedance matching is experienced by the incident wave ($|S_{11}|$ = 0) at these TE cutoff frequencies [Medina 2008], [Munk 2000].

The above fact is illustrated in Fig. 2.4.3(b), where the higher order harmonic cutoff frequencies for the considered array are plotted as a function of the angle of incidence. These frequencies have been analytically computed using (2.4.5), and are identical for both TE and TM polarization. As mentioned above, no TM_{m0} harmonic can be excited. The squares in Fig. 2.4.3(b) point out the onset of the first harmonics when θ = 20º, which occur at 44.7 GHz, 63.9 GHz, and 70 GHz (harmonics mn = −10; 0$\pm$1, and -1$\pm$1, respectively) and correspond to the reflectivity nulls in Fig. 2.4.3(a). If only the elements L_0 and C_0 are considered in the circuit model (curve N_{TE} = 0, N_{TM} = 0 in Fig. 2.4.3(a)), the array response is only accurately predicted for low frequencies and the aforementioned reflectivity nulls are not obtained. In this case, the lumped elements are expected to account accurately for the quasistatic behavior of the metallic dipoles (considering that Z_c and Z_L are zero in (3.4.11) and (3.4.12)), and thus, they predict the aforementioned conventional total reflection (Fabry-Pérot type resonance) at 71 GHz. When the impedance of the first higher-order TE harmonic is considered in the TEN (curve N_{TE} = 1, N_{TM} = 0 in Fig. 2.4.3(a)), the total reflection peak at 44.5 GHz and the first null at 44.7 GHz are accurately obtained. It can then be concluded that the peak at 44.5 GHz is mainly caused by the inductive impedance associated with the first TE

higher harmonic in the circuit model, $Z^{(1)}_{TE,-10}$. This impedance strongly diverges to infinity close to the onset of the mode, causing that, at certain frequency below and near the cutoff frequency, Z_L provides the needed inductance to resonate with the lumped capacitance C_0 (Z_C = 0 since N_{TM} = 0). This makes the branch of series impedances in the equivalent circuit behave as a shortcircuit, thus causing total reflection ($|S_{11}|$ = 1). The Wood's anomaly associated to the onset of this harmonic (null at 44.7GHz) is also accurately predicted. Successive incorporation of the second and third TE higher-order harmonics impedances (with respective resonances at 63.9 GHz and 70 GHz in Fig. 2.4.3(b)), provides accurate description of the second and third nulls, which exactly appear at the cutoff frequency of each TE harmonic.

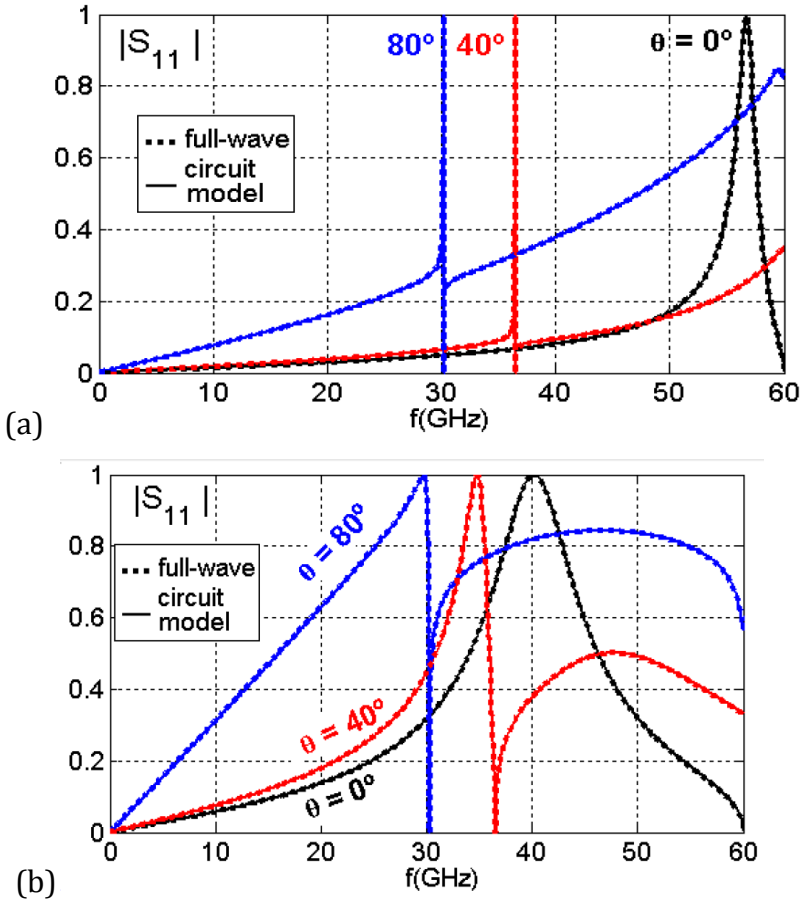

Fig. 2.4.4. (a) Magnitude of the reflection coefficient for the structure in Fig. 2.4.1 under 20º incidence and dipoles with a_y = 2 mm. (b) Cutoff frequencies associated with the higher-order *mn*-th harmonics excited in the structure as a function of the exciting wave angle of incidence.

It should be noted that the higher-order impedances become real after the onset of their corresponding harmonics, resulting in radiation losses in the TEN of Fig. 2.4.2(a). The onset of the first higher-order harmonic sets the beginning of the grating lobe regime. Therefore, above the frequency of the first reflectivity null (44.7 GHz), total reflectivity peaks ($|S_{11}| = 1$), *i.e.*, perfect mirror reflectance, cannot occur anymore. Nevertheless, local maxima in the reflection coefficient are observed between every two consecutive nulls, as it can be seen in Fig. 2.4.3(a). The capacitive impedances associated with TM higher-order harmonics are also needed to accurately predict the array response, although they do not produce nulls in the reflection coefficient since their characteristic impedance does not diverge at their cutoff frequency (see Eq. (2.4.7)). In the case treated in Fig. 2.4.3(a), the number of higher-order harmonics needed by the circuit-model approach to accurately obtain the array response until 70 GHz is $N_{TE} = 3$ and $N_{TM} = 2$. The above results makes evident that the reflectivity response provided by the simple circuit model perfectly matches the full-wave results, and gives a good physical insight of this complicated response, even in the grating lobe region (diffraction regime). These results also prove the important reduction of computational effort that our approach provides. In the case of Fig. 3(a), around 500 full-wave points were needed to obtain the complete spectrum (red curve), whereas only 7 simulations were performed when applying our equivalent circuit approach (blue curve).

The effect of the angle of incidence can also be modeled and interpreted by the proposed circuit model. The reflectivity of the dipole array previously considered is shown in Fig. 2.4.4 for three different angles of incidence ($\theta = 0^o$; 40^o; 80^o). Following the proposed procedure, for each angle of incidence and in order to characterize our structure up to 60 GHz, it is necessary to select the appropriate values of N_{TE} and N_{TM} by looking at Fig. 2.4.3(b). Specifically, $N_{TE} = N_{TM} = 1$ was employed to obtain the $\theta = 0^o$ curve in Fig. 2.4.4, whereas $N_{TE} = 2$ and $N_{TM} = 1$ were needed to obtain the curves $\theta = 40^o$ and $\theta = 80^o$. Figure 2.4.4(a) shows the extraordinary reflection produced by dipoles of less-than-half length compared to the array periodicity ($a_y = 2$ mm, with Fabry-Perot resonance around 75 GHz) whereas conventional resonances are shown in Fig. 2.4.4(b) for the case of longer

dipoles (a_y = 3.5 mm, with Fabry-Perot resonance around 40 GHz). Again, excellent agreement is obtained between full-wave results and the circuit model. As a general comment, it can be seen in Fig. 2.4.4 that the reflectivity is strongly affected by the angle of incidence of the impinging wave. As this angle increases, the frequency of the reflectivity null reduces from 60 GHz for $\theta = 0^o$ to 36.52 GHz for $\theta = 40^o$, and to 30 GHz for $\theta = 80^o$. These values exactly coincide with the first TE higher-order harmonic cutoff frequency at each angle of incidence (see the *mn* = -10 curve in Fig. 2.4.3(b)). This effect appears both in Fig. 2.4.4(a) and Fig. 2.4.4(b) since the cutoff frequency does not depend on the dipole length. The frequency of the total reflection peaks also decreases as θ increases. In particular, Fig. 2.4.4(a) shows that the Fano (extraordinary reflection) resonances are displaced to lower frequencies with extremely sharp responses. This fact can be explained considering that the open-circuit and shortcircuit conditions in the branch of series impedances occurs in a very narrow frequency band; increasingly narrow with increasing incidence angle. The total reflection peaks in Fig. 2.4.4(b) (associated with Fabry-Pérot type resonances) also decrease with increasing θ, basically for the same reasons as in Fig. 2.4.4(a).

2.4.2 Dipole array in stratified medium

In this section it is considered the presence of dielectric substrates, which is commonly needed for mechanical purposes (to support the patterned metallic surface). Due to this reason, some authors have already paid attention to the analysis of metallic perforated screens printed over a dielectric slab ([Lomakin 2005 and 2007], [Moreno 2006] and [Ortuo 2010]). The presence of the dielectric substrate makes the transmission spectrum much richer than that of the free standing structures, as it will be seen in along this section. The scheme of the dipole array under study, sandwiched between dielectric slabs, is shown Fig. 2.4.5. The incident waves impinge obliquely on the array in the plane *xz* (H-plane) from an angle θ. The scenery described in Sec. 2.4.1 is a particular case of the present one. Since the generation of higher-order harmonics due to the presence of the dielectric slabs increases the complexity of the situation [Munk 2000], for the sake

of simplicity, the study commences from the case of identical slabs and extends to arbitrary dielectric slabs.

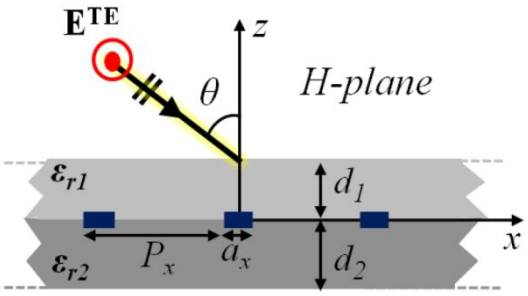

Fig. 2.4.5 Scheme of the TE-polarized incidence in H-plane in the dipole array of Fig. 2.4.1 when sandwiched between dielectric slabs.

A. Dipole Array Sandwiched by Identical Dielectric Slabs

This subsection deals with the case of a periodic dipole array sandwiched between two identical slabs, which corresponds to $d_1 = d_2 = d$ and $\varepsilon_{r1} = \varepsilon_{r2} = \varepsilon_r$ in Fig. 2.4.5. The proposed TEN that models this structure is shown in Fig. 2.4.6 following the guidelines reported in Sec. 2.4.1, although with some important changes.

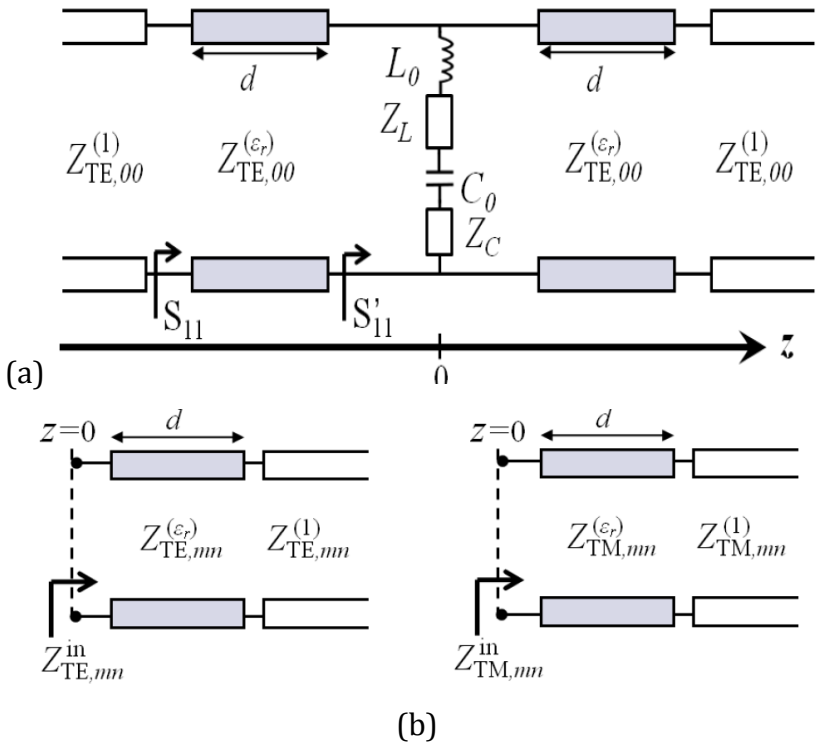

Fig. 2.4.6 Equivalent circuit for the scattering of an obliquely incident plane wave which impinges on a dipole array sandwiched by identical dielectric slabs.

First, the propagation of the incident, reflected, and transmitted TE plane wave should take into account the presence of the dielectric slabs, which is modeled by the transmission lines of length d and characteristic impedance $Z_{TE,00}^{(\varepsilon_r)}$ (which can be obtained from (2.4.8)). Also, the impedances associated with the excitation of higher-order harmonics, Z_L and Z_C (2.4.9), are now computed from the following equivalent input impedances seen by each TE/TM harmonic (as depicted in Fig. 2.4.6(b)):

$$Z_{TE,mn}^{in}(\omega) = Z_{TE,mn}^{(\varepsilon_r)}(\omega)\,\frac{Z_{TE,mn}^{(1)}(\omega) + \mathrm{j}Z_{TE,mn}^{(\varepsilon_r)}(\omega)\,tan\left(k_{z,mn}^{(\varepsilon_r)}d\right)}{Z_{TE,mn}^{(\varepsilon_r)}(\omega) + \mathrm{j}Z_{TE,mn}^{(1)}(\omega)\,tan\left(k_{z,mn}^{(\varepsilon_r)}d\right)}. \qquad (2.4.14)$$

Looking at the equation (2.4.14) it can be observed that the cutoff of higher-order harmonics in the dielectric medium (onset of the so-called "trapped" surface waves [Munk 2000, Ch.5]) plays an important and intricate role in the appearance of singularities in Z_L and Z_C as well as in the subsequent generation of reflectivity resonances and nulls. From the proposed TEN, the following equation can be written and solved for the unknown values of L_0, C_0, and $A_h^{TE/TM}$:

$$\mathrm{j}\omega L_0 + Z_L(\omega) + \frac{1}{\mathrm{j}\omega C_0} + Z_C(\omega) = \left(\frac{1-S_{11}'(\omega)}{[1-S_{11}'(\omega)]\,Z_{TE,00}^{(1)}(\omega)} - \frac{1}{Z_{TE,00}^{(in)}(\omega)}\right)^{-1} \qquad (2.4.15)$$

where $S_{11}'(\omega)$ is the reflection coefficient at the reference plane z = 0, as shown in Fig. 2.4.6(a), and Z_L, Z_C are given by (2.4.9). This reflection coefficient can readily be expressed in terms of the reflection coefficient S_{11} at z = -d [Fano 1961]. This latter coefficient is obtained from full-wave simulations [Goussetis 2006-I]. Thus, the parameters L_0, C_0, and $A_h^{TE/TM}$: can be obtained after solving the system of equations resulting of particularizing (2.4.15) at a few values of frequency. As for the case of freestanding dipoles, it is needed as many full-wave data points as the number of unknowns. The choice of the evaluated frequency values basically follows the same general rule suggested in the previous section. However, in the present case, it has been found to be very convenient to take the high frequency points near and below the onset of the higher order harmonics in the denser dielectric medium.

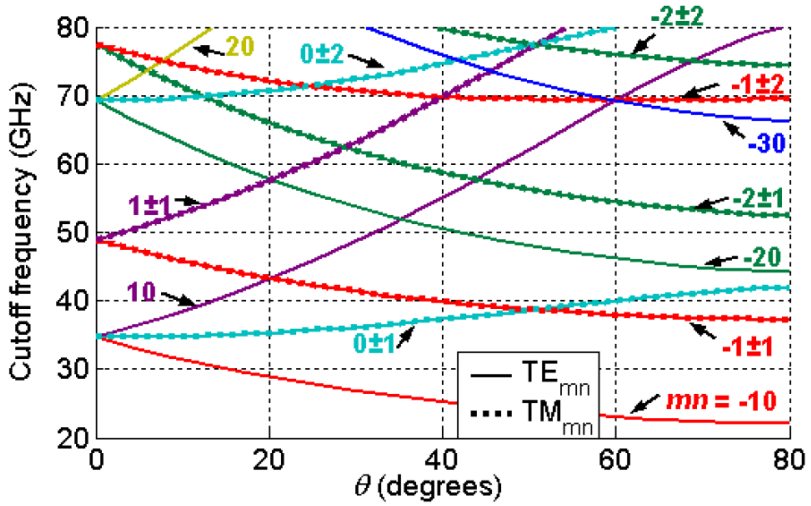

Fig. 2.4.7 Higher order harmonic cutoff frequency when ε_r = 3.

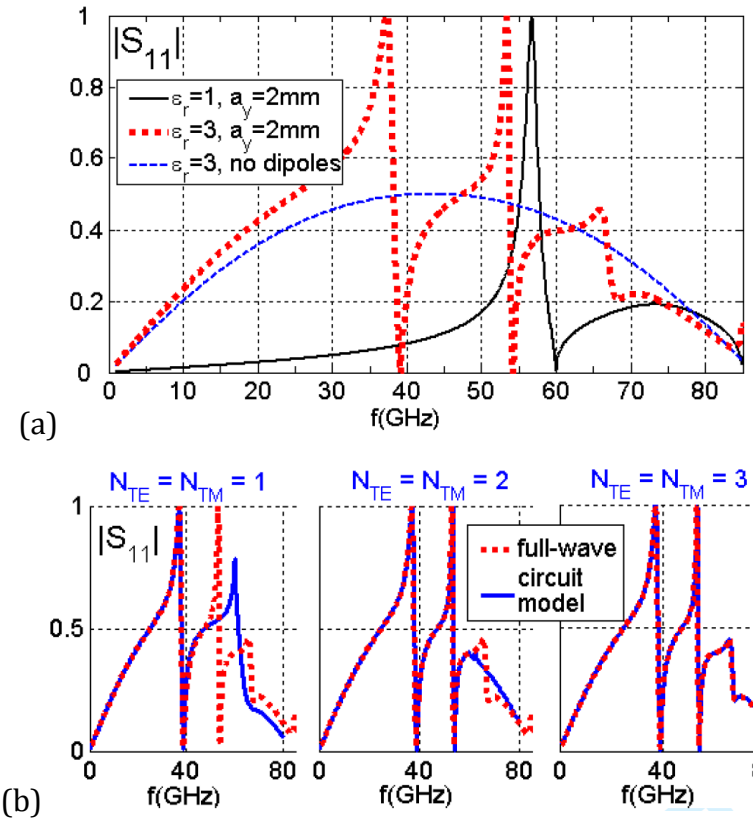

Fig. 2.4.8 (a) Magnitude of the full-wave reflection coefficient at normal incidence for the structure in Fig. 5 with $\varepsilon_{r1} = \varepsilon_{r2} = \varepsilon_r$, $d_1 = d_2$ = 0:5 mm, $P_x = P_y$ = 5mm and a_x = 0.5 mm. (b) For the case of the red dotted line in Fig. 2.4.8(a), comparison between full-wave and circuit model results (configurations: $N_{TE} = N_{TM}$ = 1, 2, and 3, respectively).

Since the cutoff frequency of higher-order harmonics is lower inside a dielectric medium, the frequency range satisfying $f_{c,mn}^{(\varepsilon_r)} < f < f_{c,mn}^{(1)}$ corresponds to

the existence of harmonics that are propagative in the dielectric slab but evanescent in free space. Thus, in this range there are trapped surface waves below the grating lobe regime [Munk 2000]. (The grating lobe regime is still determined by the frequency at which the first higher-order harmonic in free space becomes propagative; 60 GHz in the present case for normal incidence, as shown Fig. 2.4.3(b)). As a consequence, the total amount of higher-order harmonics that should be considered in the TEN (N_{TE} and N_{TM}) increases with respect to the free-standing case. Figure 2.4.7 shows the cutoff frequency chart vs. the angle of incidence in a dielectric medium with ε_r = 3, and the same array periodicity as in previous examples (P_x = P_y = 5 mm). For normal incidence it can be seen that the onset of the trapped surface waves occur at 35 GHz and 49 GHz, well below the starting frequency of the grating lobe regime (60 GHz). As a result, two singularities appear for $Z^{in}_{TE,mn}(\omega)$ at approximately 47.3 GHz and 62.5 GHz, where the denominator of Eq. (2.4.14) is zero (more specifically, at 47.3 GHz for the TE_{10} harmonic and at 62.5 GHz for the TE_{11} harmonic). At these frequencies, Z_L diverges causing an open circuit in the branch of series elements that account for the effect of the dipoles in Fig. 2.4.6(a). Since this open circuit makes irrelevant this branch, at the aforementioned frequencies, the complete structure should behave as if the dipoles were not present. This fact is corroborated in Fig. 2.4.8(a) at 47.3 GHz and 62.5 GHz where the dashed blue curve (which shows the behavior of the structure without dipoles) crosses with the dotted red curve (with dipoles). Figure 2.4.8(a) shows two reflectivity resonances below the grating lobe regime for the dielectric sandwiched array with dipole length a_y = 2mm. These two resonances are of the Fano type (characterized by a total reflection followed by a reflection null), in similarity with the free-standing case. However, in this latter case, only one Fano resonance can occur below the grating lobe regime, as it is plotted in Fig. 2.4.8(a) in solid black line. Once within the grating lobe regime, radiation losses prevent the appearance of additional total reflection peaks (see Fig. 2.4.8(a) above 60 GHz). Also, it is interesting to note that the array follows the frequency response profile of the bare dielectric slab (blue dashed line in the figure) out from the Fano resonances. The reflection nulls in Fig. 2.4.8(a) do not appear at the cutoff frequencies f the trapped surface waves (35 GHz and 49 GHz), as happened in the free-standing case (where the reflection nulls exactly coincide with the cutoff

frequencies of higher-order harmonics in free space; *i.e.*, with the divergence of Z_L). In the presence of dielectric, the impedance matching condition [Medina 2008] responsible for the reflection nulls requires that the input impedance at $z = -d$ equals that of the incident transmission line. Certainly this condition is not easily expressible in closed form, but it can be observed that it does not only depend on the unit-cell size but also on the characteristics of the dielectric slab as well as on the dipole geometry (this latter dependence comes through the excitation parameters $A_h^{TE/TM}$ appearing in Z_L and Z_C, which are certainly influenced by such characteristics). In order to investigate the role played by the higher-order harmonics in the dielectric slab on the behavior of the array reflectivity, Fig. 2.4.8(b) shows the profile of this magnitude when it is computed using different number of harmonics. If only the first TE and TM higher-order harmonics (TE_{10} and TM_{01}) are considered, the subplot $N_{TE} = N_{TM} = 1$ in Fig. 2.4.8(b) shows that the reflectivity response is accurately modeled up to the frequency of the first resonance and subsequent null ($f \leq 39$ GHz). The addition of extra harmonics is needed to retrieve the following nulls and associated maxima. The addition of a second TE and TM harmonics (TE_{11} and TM_{11}) implies that a second trapped surface wave inside the dielectric is now considered. The effect of these additional harmonics is depicted in the subplot $N_{TE} = N_{TM} = 2$, which shows now a good agreement for the two Fano resonances. Finally, the subplot $N_{TE} = N_{TM} = 3$ in Fig. 2.4.8(b) shows the effect of the addition of a third TE and TM harmonics (TE_{20} and TM_{02}). It can be seen that this addition helps to accurately reproduce the reflectivity local maximum at 66 GHz, which does not reach total reflection by being within the grating lobe regime. As the dielectric permittivity is increased, more surface waves are launched below the grating lobe regime, resulting in an increased number of higher-order resonances in the reflectivity response, as shown in Fig. 2.4.9. As in previous examples, the agreement between our circuit-model data and full wave data is excellent.

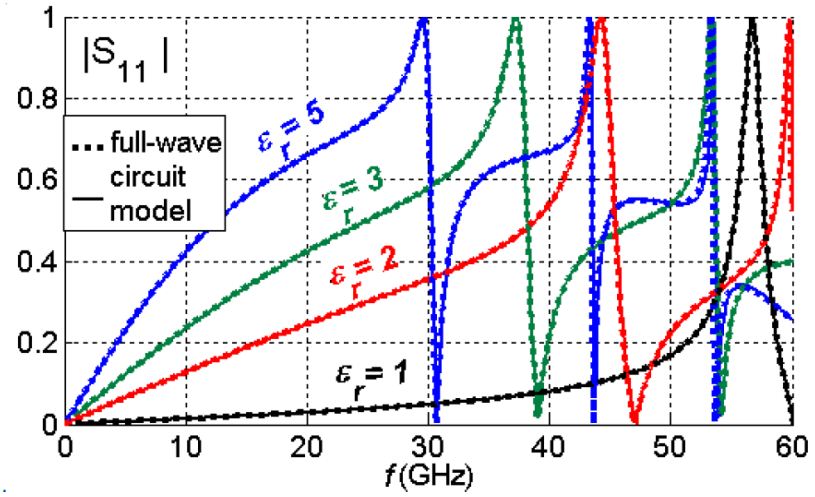

Fig. 2.4.9 Magnitude of the reflection coefficient at normal incidence for different values of the relative permittivity ($\varepsilon_{r1} = \varepsilon_{r2} = \varepsilon_r$) for the structure in Fig. 2.4.5 with $d_1 = d_2 = 0.5$mm (unit cell: $P_x = P_y = 5$mm and $a_x = 0.5$mm and $a_y = 2$ mm.)

In Fig. 2.4.10(a) it is shown the effect of increasing the angle of incidence. At normal incidence we can observe two extraordinary total reflection peaks but only one of these peaks remains for the other incidence angles here considered, which do show several non-total reflection peaks. As it can be seen in the cutoff chart for the dielectric medium with $\varepsilon_r = 3$ (Fig. 2.4.7), the cutoff of the first higher-order TE harmonic decreases from 35 GHz to 25 GHz as _ increases from 0o to 40o. Related to this fact, the lowest reflectivity resonance frequency also decreases in Fig. 2.4.10(a) from ~ 38 GHz at normal incidence to ~ 32 GHz at θ = 40o. However, it should also be observed that the grating lobe frequency (shown in the free-space cutoff chart in Fig. 2.4.3(b)) also decreases from 60 GHz at $\theta = 0^o$ to 36:52 GHz at $\theta = 40^o$. Consequently, no additional total-reflection peaks are observed in Fig. 2.4.10(a) for $\theta = 40^o$ since the grating lobe regime appears at 36.52 GHz before any extra higher-order harmonic has emerged from cutoff. At the onset of the grating lobes it is observed an inflection in the reflectivity response. This detail is amplified in the subplot $\theta = 40^o$ of Fig. 2.4.10(b). It is also interesting to note in Fig. 2.4.10(a) the appearance of several minima of reflectivity that are not null. They happen at those frequencies where the input impedance at z = -d reach a value close but not identical to $Z^{(1)}_{TE,00}$. The reflectivity response for $\theta = 80^o$ bears some similarities to that observed for $\theta = 40^o$. Thus Fig. 2.4.10(a) shows a unique extraordinary reflection peak that is shifted to lower frequencies (~ 27.5 GHz),

followed by a closer grating lobe onset now located at 30GHz (see Fig. 2.4.3(b)). A similar inflection point is also observed at 30GHz in the subplot θ = 80º of Fig. 2.4.10(b). It should be highlighted that the circuit-model approach perfectly matches the complicate spectrum given by the full-wave method, including all the fine details of very sharp resonances, inflection points, partial maxima and minima, etc.

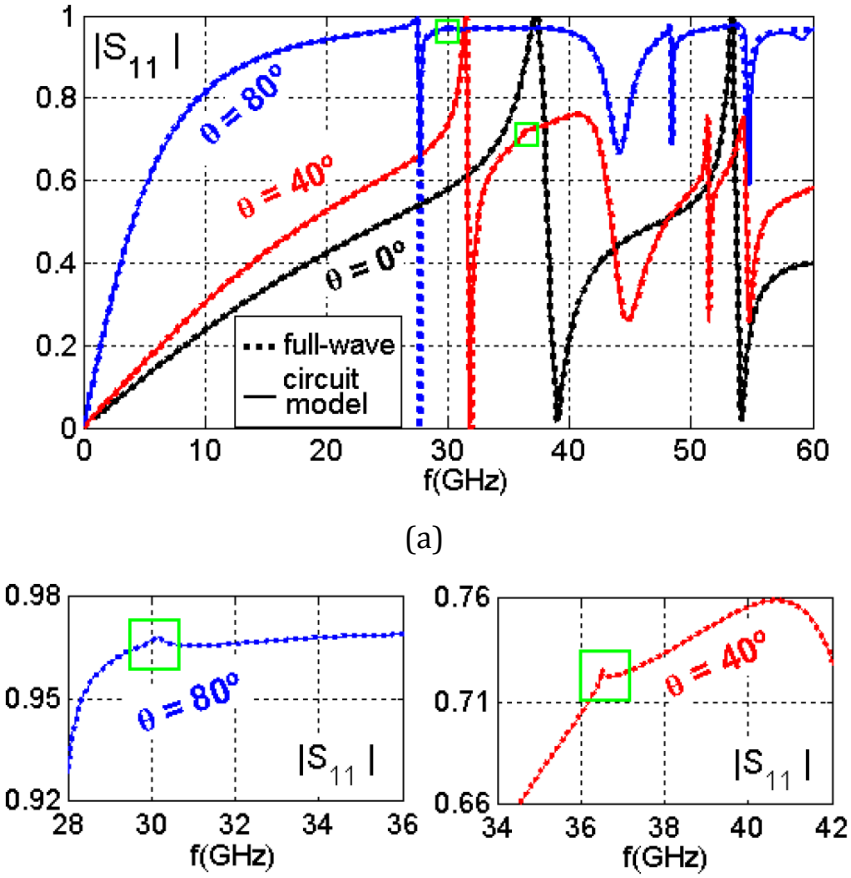

Fig. 2.4.10 Magnitude of the reflection coefficient for the structure in Fig. 2.4.5 with $d_1 = d_2$ = 0.5 mm, $\varepsilon_{r1} = \varepsilon_{r2} = \varepsilon_r$ = 3 and a_y = 2mm (unit cell: $P_x = P_y$ = 5mm and a_x = 0.5 mm). (a) Different angles of incidence. (b) Detail of the appearance of grating lobes.

Finally, Fig. 2.4.11 illustrates the reflectivity response for the sandwiched array with dipoles of length a_y = 3.5 mm. At normal incidence, and in contrast to the curve θ = 0º in Fig. 2.4.4(b), a first conventional dipole resonance is observed at 25 GHz followed by a higher-order resonance at 53 GHz, which is related to the appearance of a trapped surface wave in the dielectric below the grating lobe

frequency of 60 GHz. The conventional resonance can be identified as of Fabry-Pérot type whereas the sharp higher-order resonance is of Fano type. As the angle of incidence increases from θ = 0º to θ = 80º, the onset of the grating lobe decreases from 60 GHz to 30 GHz (as in Fig. 2.4.10(a)), which is reflected by a corresponding small inflection point. Once more, the proposed equivalent circuit accurately describes the complex behavior of this dipole array in the presence of a symmetrical dielectric slab, giving physical insight on the appearance of higher-order extraordinary resonances.

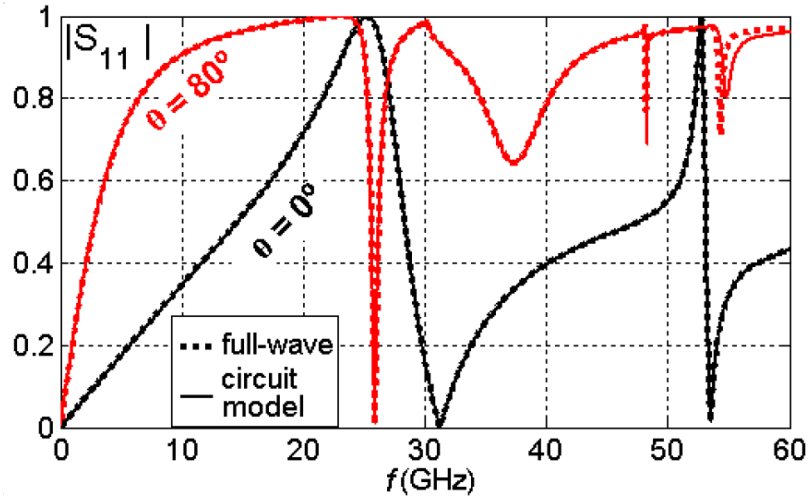

Fig. 2.4.11 Magnitude of the reflection coefficient for the structure in Fig. 2.4.5 with $d_1 = d_2$ = 0.5 mm, $\varepsilon_{r1} = \varepsilon_{r2} = \varepsilon_r$ = 3, $P_x = P_y$ = 5 mm, a_x = 0.5mm and a_y = 3.5 mm.

B. Dipole Array Sandwiched by Arbitrary Dielectric Slabs

The general scenario shown in Fig. 2.4.5 is characterized in this section. The proposed circuit model for this situation is shown in Fig. 2.4.12. Note that the cases studied in previous sections are particularizations of the general scenario now considered. Thus, in analogy with Fig. 2.4.6, the propagation of the incident plane wave through the dielectric slabs is modeled in Fig. 2.4.12(a) by the finite transmission lines placed at both sides of the discontinuity with characteristic impedances $Z_{TE,00}^{(\varepsilon_{r1})}$ and $Z_{TE,00}^{(\varepsilon_{r2})}$ (obtained using (2.4.8)). However, in order to account for different dielectric slabs, it is necessary to introduce the following impedances defined in Fig. 2.4.12(b):

$$Z_{TE,mn}^{left}(\omega) = Z_{TE,mn}^{(\varepsilon_{r1})}(\omega)\,\frac{Z_{TE,mn}^{(1)}(\omega) + \mathrm{j}Z_{TE,mn}^{(\varepsilon_{r1})}(\omega)\,tan\left(k_{z,mn}^{(\varepsilon_{r1})}d_1\right)}{Z_{TE,mn}^{(\varepsilon_{r1})}(\omega) + \mathrm{j}Z_{TE,mn}^{(1)}(\omega)\,tan\left(k_{z,mn}^{(\varepsilon_{r1})}d_1\right)}. \tag{2.4.16}$$

$$Z_{TE,mn}^{right}(\omega) = Z_{TE,mn}^{(\varepsilon_{r2})}(\omega)\,\frac{Z_{TE,mn}^{(1)}(\omega) + \mathrm{j}Z_{TE,mn}^{(\varepsilon_{r2})}(\omega)\,tan\left(k_{z,mn}^{(\varepsilon_{r2})}d_2\right)}{Z_{TE,mn}^{(\varepsilon_{r2})}(\omega) + \mathrm{j}Z_{TE,mn}^{(1)}(\omega)\,tan\left(k_{z,mn}^{(\varepsilon_{r2})}d_2\right)}. \tag{2.4.17}$$

Note that for the case of identical slabs the above expressions reduce to just half the input impedance $Z_{TE,mn}^{in}$ used in Fig. 2.4.6. In similarity with the rationale followed in [Munk 2000, Ch. 5], the contribution of each TE/TM *mn*-th harmonic to the total impedance $Z_L(\omega)$ or $Z_C(\omega)$ is accounted for by the parallel connection of $Z_{TE,mn}^{left}(\omega)$ and $Z_{TE,mn}^{left}(\omega)$, which can be written as

$$Z_L(\omega) = \sum_{h=1}^{N_{TE}} A_h^{TE}\left(\frac{1}{Z_{TE,mn}^{left}(\omega)} + \frac{1}{Z_{TE,mn}^{right}(\omega)}\right) \tag{2.4.18}$$

$$Z_C(\omega) = \sum_{h=1}^{N_{TM}} A_h^{TM}\left(\frac{1}{Z_{TM,mn}^{left}(\omega)} + \frac{1}{Z_{TM,mn}^{right}(\omega)}\right) \tag{2.4.19}$$

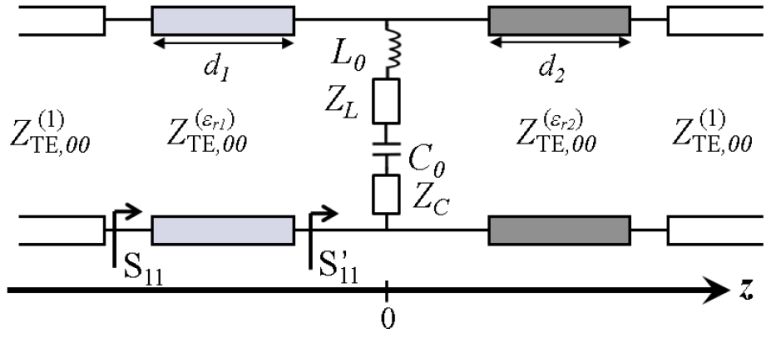

(a)

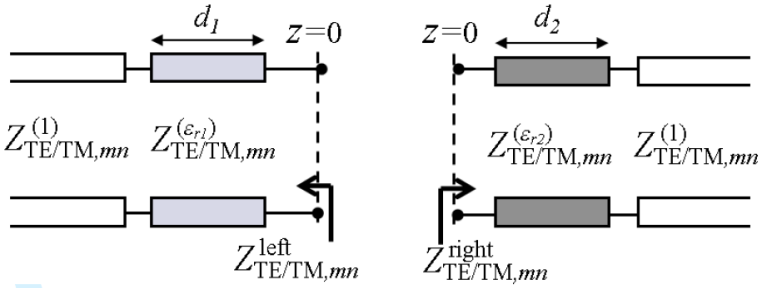

(b)

Fig. 2.4.12 Equivalent circuit for the scattering of an obliquely incident plane wave in the periodic array shown in Fig. 2.4.5.

The expressions (2.4.18) and (2.4.19) clearly show the combined influence of both dielectrics in the response of the array. Here it should be emphasized the capital relevance of setting up the appropriate connections between the different elements in order to make the equivalent network actually useful. Certainly, unless the equivalent network reflects accurately the underlying physics of the problem, the TEN would be no more than a smart fitting numerical procedure valid in certain frequency region.

As in the previous section, the cutoff of higher-order harmonics in both dielectric slabs is again related to the appearance of singularities in Z_L and Z_C. Therefore, the same discussion about the launch of trapped surfaces waves can now be applied. However, since in the present case of electric dipole arrays (2.4.18) and (2.4.19) show that the dielectric slabs contribute as a whole [Munk 2000], the number of higher-order harmonics to be considered (N_{TE} and N_{TM}) should correspond, at least, to the number of launched trapped surface waves in the denser slab. The influence of the slab thickness in the response of the array is expected to be similar to the permittivity effect, due to the fact that it also controls the amount of energy coupled into surface wave modes excited in the substrates [Munk 2000], [Katehi 1983]. In this regard our numerical experience suggests that we should increase the aforementioned number of higher-order harmonics to be explicitly accounted for if the thickness of the slab is similar to or larger than the slab wavelength. In order to calculate the unknown parameters L_0, C_0, and $A_h^{TE/TM}$, we proceed as in the previous section, solving (2.4.15) for a set of frequency values after expressing S'_{11} in terms of the reflection coefficient S_{11} at $z = -d_1$ (as shown in Fig. 2.4.12(a)).

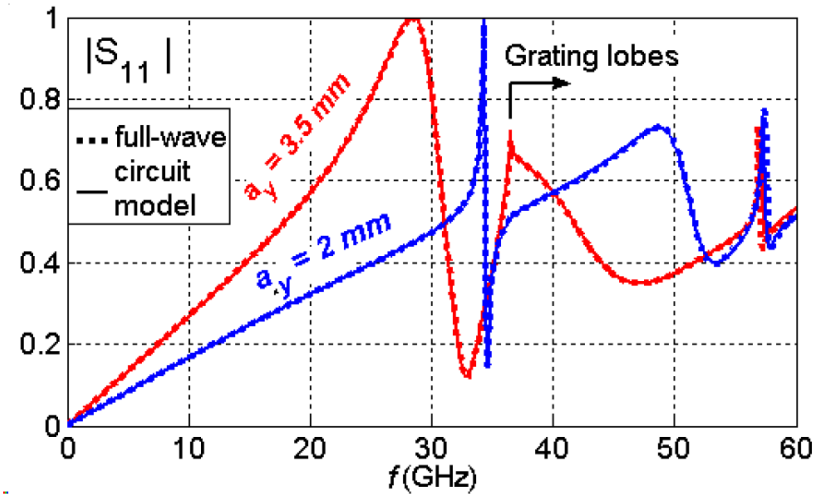

Fig. 2.4.13 Magnitude of the reflection coefficient under 40º incidence for the structure of Fig. 2.4.5 with ε_{r1} = 1, ε_{r2} = 3, d_1 = 0 mm, d_2 = 0.5 mm, $P_x = P_y$ = 5 mm and a_x = 0.5 mm.

In many practical situations, metallic arrays of dipoles are not embedded in the dielectric slab but printed on it ([Vardaxoglou 1997], [Beruete 2011], [Caiazzo 2004], [Goussetis 2006-I], [Lee 2000], [Feresidis 2001], [Tretyakov 2003], [Maci 2005]…). In this case, the dielectric is not only necessary to support the metallic dipoles but, as it has been discussed in the previous section, it also plays a key role in the shaping of the reflectivity response. Therefore, in order to validate our TEN in the present situation, the same unit cell previously studied and described in the caption of Fig. 2.4.1 is now modeled it is assumed that the upper dielectric in Fig. 2.4.5 is free space (d_1 = 0 mm and ε_{r1} = 1) whereas the lower supporting substrate has d_2 = 0.5 mm, ε_{r2} = 3. The study of this structure is shown in Fig. 2.4.13, which shows the reflectivity under plane wave oblique incidence (θ= 40º) for both electrically small and long dipoles (a_y = 2 mm and a_y = 3.5 mm, respectively). Apart from the excellent agreement again observed between our equivalent circuit approach and the full-wave simulations, the physics underlying these results can once more be explained by the circuit model. Most of the discussions in previous sections can readily be extended to the present situation although some new effects should now be highlighted. Thus, the a_y = 2 mm curve in Fig. 2.4.13 is similar to the θ = 40º curve in Fig. 2.4.10(a). Only one total reflection peak ($|S_{11}|$ = 1) is found in both curves below the grating lobe regime, with this regime being reached at 36.53 GHz in both cases and clearly manifested as an inflection in the

$|S_{11}|$ curves. However, instead of the reflectivity nulls below the grating lobe regime in Fig. 2.4.10(a), only local minima are found in Fig. 2.4.13. In fact, total transmission ($|S_{11}| = 0$) are not expected to occur easily when the dielectric slabs are not identical (the conditions to have impedance matching at $z = -d_1$ are now much harder to obtain owing to the parallel connection of the "left" and "right" impedances). The same cutoff frequency chart of Fig. 2.4.7 is now employed to set the values of the significant TE and TM harmonics (N_{TE} and N_{TM} in (2.4.18) and (2.4.19)). In particular, the results plotted in Fig. 2.4.13 have been obtained with $N_{TE} = 7$ and $N_{TM} = 4$, which are equal to one plus the number of TE and TM harmonics under cutoff below 60 GHz, respectively.

2.4.3 Dipole array under TM incidence

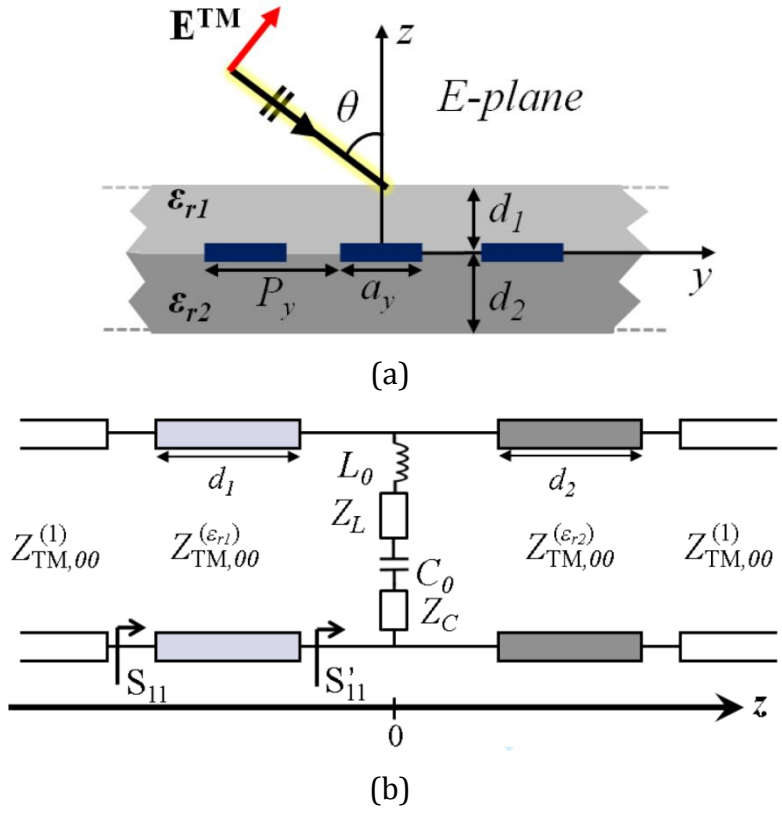

Fig. 2.4.14 (a) TM-polarized wave excitation in E-plane of a dipole array sandwiched between dielectric slabs. (b) Proposed circuit model.

The methodology previously used in the study of the TE incidence case can equally be applied when the exciting plane wave is TM polarized or it impinges in

other planes. In practice, partially reflecting sheet arrays are normally illuminated by a single central feed with the feeding element oriented so that the excited polarized electric field has a strong interaction with the dipoles ([Trentini 1956], [Vardaxoglou 1997], [Beruete 2011], [Caiazzo 2004], [Goussetis 2006-I], [Lee 2000], [Feresidis 2001], [Tretyakov 2003], [Maci 2005]…). Therefore, the characterization of the periodic array under TM polarization becomes relevant when the scan plane of incidence is *yz* (E- plane). An equivalent network can also be proposed for TE polarization in E-plane or TM in H-plane, although these cases are less relevant from a practical point of view since the dipoles are almost invisible for the impinging wave. Thus, in this section, the incidence of a TM-polarized plane wave in the E-plane of a dipole array (illustrated in Fig. 2.4.14(a)) is modeled by the circuit model shown in Fig. 2.4.14(b). The only difference between this TEN and the one in Fig. 2.4.12(a) is found in the transmission lines at both sides of the discontinuity; the transmission lines now model the propagation of the incident, reflected and transmitted TM_{00} harmonic instead of the TE_{00}. As a consequence, the same procedure explained in the previous section can be employed. The impedances Z_L and Z_C in Fig. 2.4.14(b) are again defined by (2.4.18) and (2.4.19), while (2.4.15) can also be solved for the unknown values of L_0, C_0, and $A_h^{TE/TM}$ considering that S'_{11} is the reflection coefficient plotted in Fig. 2.4.14(b). Due to the change in the plane of incidence, the excited harmonics now propagate along the *x* and *y* axis with the following wavenumbers (*m* and *n* are integers):

$$k_{x,m} = \frac{2m\pi}{P_x} \tag{2.4.20}$$

$$k_{y,n} = k_0 sin\theta + \frac{2n\pi}{P_y} \tag{2.4.21}$$

The cutoff frequencies associated with higher order harmonics can now be computed as

$$f_{c,mn}^{(\varepsilon_r)} = \frac{1}{\varepsilon_r - sin^2\theta}\left\{\frac{nc}{P_y}sin\theta + \sqrt{\varepsilon_r\left[\left(\frac{mc}{P_x}\right) + \left(\frac{nc}{P_y}\right)\right] - \left(\frac{mc}{P_x}sin\theta\right)^2}\right\}. \tag{2.4.22}$$

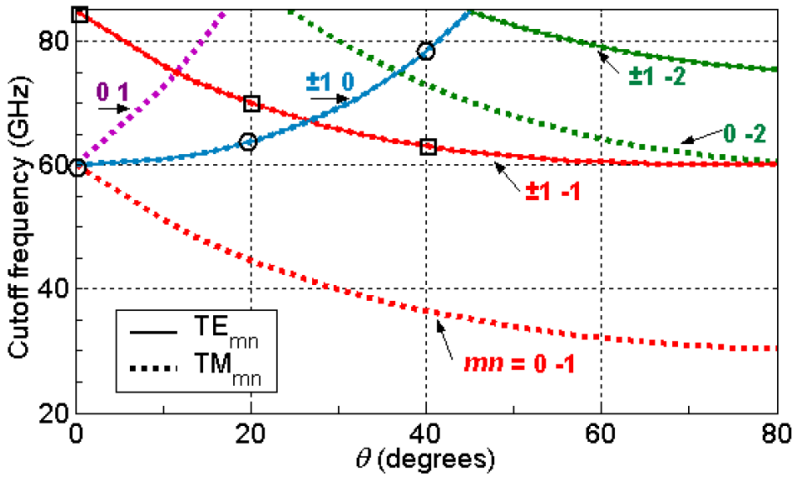

Fig. 2.4.15 Higher order harmonic cutoff frequency in free-space (unit cell with periodicities $P_x = P_y = 5$ mm).

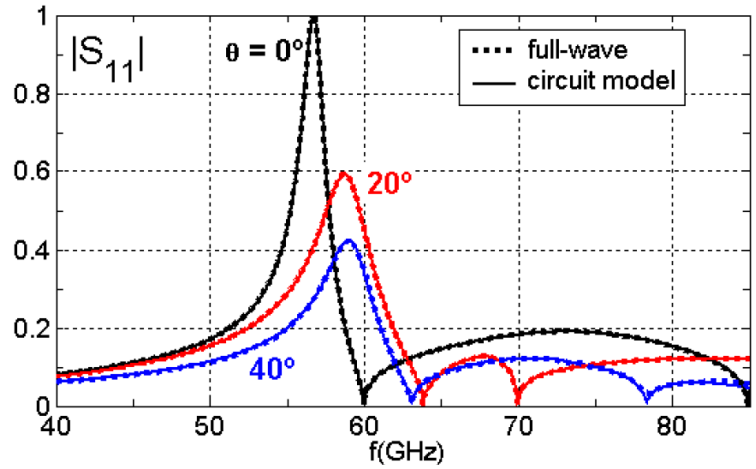

(a)

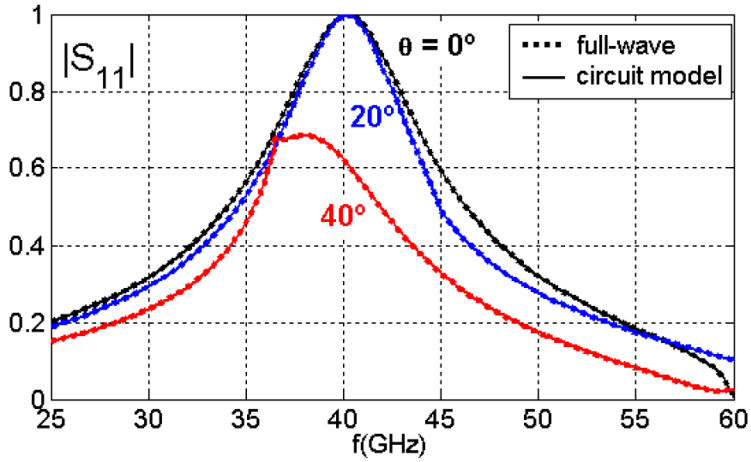

(b)

Fig. 2.4.16 Magnitude of the reflection coefficient of the structure described in Fig. 2.4.1 under oblique E-plane TM incidence. (a) Dipole length $a_y = 2$ mm. (b) $a_y = 3.5$ mm.

The problem under consideration can be reduced to a single unit cell with magnetic walls in the *yz* plane and Floquet walls (periodic boundary conditions) in the *xz* plane. Therefore, TE_{0n} harmonics do not satisfy the boundary conditions, and are not excited by the TM polarized impinging wave. This fact is illustrated in Fig. 2.4.15, which shows the higher-order cutoff frequencies computed for free space in a unit cell with periodicities $P_x = P_y = 5$ mm. In contrast to Fig. 2.4.3(b), the first grating lobe is now produced by the harmonic TM_{0-1}, instead of TE_{-10}. Our first study case for TM incidence is the free-standing case shown in Fig. 2.4.16(a), where the reflectivity of a dipole array with dimensions $P_x = P_y = 5$ mm, $a_x = 0.5$ mm and $a_y = 2$ mm is shown. Normal TE incidence in H-plane and TM incidence in E-plane are equal and, therefore, the $\theta = 0^o$ curves in Fig. 2.4.4(a) and Fig. 2.4.16(a) are identical. As it was explained in Sec. II, for normal incidence, an extraordinary transmission peak appears at 56.7 GHz, before the onset of the first TE harmonic. For each angle of incidence, the Wood's' anomalies (reflection nulls) found in Fig. 2.4.16(a) exactly appear at the onset of TE harmonics, analytically predicted in Fig. 2.4.15. Specifically, the reflectivity null associated to the onset of the harmonic TE10 increases from 60 GHz at 0^o to 63.9 GHz at 20^o and 78.4 GHz at 40^o (as marked with black circles in Fig. 2.4.15). In contrast, the onset of the harmonic TE_{1-1} decreases from 85 GHz at 0^o to 70 GHz at 20^o, and 63.1 GHz at 40^o (marked with black squares in Fig. 2.4.15). It must be highlighted that, for oblique TM incidence, the cutoff of the first TM harmonic is produced before any TE harmonic appears. Thus, the beginning of the grating lobes regime is now set by a TM harmonic (see TM_{0-1} curve in Fig. 2.4.15), which does not diverge at its cutoff, and therefore, it does not produce a singularity in the reflection coefficient. The consequence of this is the suppression of the extraordinary total reflection for oblique incidence, as shown in Fig. 2.4.16(a). The divergence of the first TE harmonic occurs in the grating lobes regime, where (as it was explained in previous sections), no total reflection can be produced. Yet, a peak of maximum reflectivity can still be found before the onset of the first TE harmonic, whose level decreases as θ increases. Figure 2.4.16(b) also shows the reflectivity response of the previous unit cell when $a_y = 3.5$ mm. The $\theta = 0^o$ curve again coincides with the one in Fig. 2.4.4(b), and as it was explained in Sec. 2.4.1, conventional total reflection appears at 40 GHz. This resonance may also be suppressed when the

onset of the $TM_{0\text{-}1}$ harmonic is lower that the quasistatic resonance of the dipole, as it is illustrated by curve θ = 40º in Fig. 2.4.16(b) ($TM_{0\text{-}1}$ cutoff frequency is 36.53 GHz, lower than 40 GHz). The onset of the first TE harmonic is not directly responsible for the appearance of the conventional reflection peak, and therefore, the resonance does not disappear for every incidence greater than zero. For example, Fig. 2.4.16(b) shows that total reflection still occurs when θ = 20º, due to the fact that the onset of the $TM_{0\text{-}1}$ harmonic is greater than 40 GHz (45 GHz as shown in Fig. 2.4.15). In Fig. 2.4.16(b), an inflection in the reflectivity response can be observed at the onset of the grating lobes.

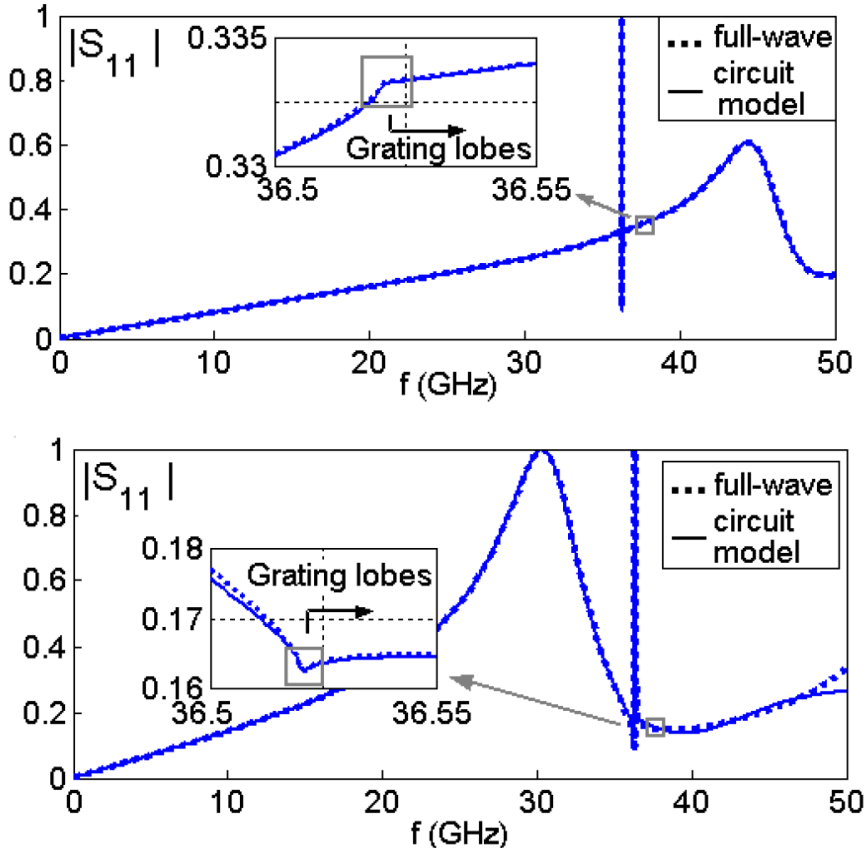

Fig. 2.4.17 Magnitude of the reflection coefficient under θ = 40º TM incidence on H-plane for the structure of Fig. 2.4.14 with $P_x = P_y$ = 5 mm, a_x = 0:5 mm, ε_{r1} = 1, ε_{r2} = 3, d_1 = 0 mm and d_2 = 0.5 mm. (a) Dipole length a_y = 2 mm. (b) a_y = 3.5 mm.

The practical design studied in the previous section of a dipole array printed on a thin dielectric substrate (which corresponds to a unit cell with dimensions $P_x = P_y$ = 5 mm, a_x = 0.5 mm, ε_{r1}= 1, ε_{r2}= 3, d_1 = 0 mm, and d_2 = 0.5 mm) can again be modeled under TM incidence in H-plane using the TEN proposed in

Fig. 2.4.14(b). Figure 2.4.17 shows the reflection coefficient presented by this printed structure under oblique incidence (θ = 40º) for electrically small (Fig. 2.4.17(a)) and long dipoles (Fig. 2.4.17(b)), which is analogous to the TE response plotted in Fig. 2.4.13. The onset of the first higher order harmonic causes again an inflection at 36.53 GHz, which has been zoomed in on each figure. The shaping effect of the supporting substrate in the reflectivity response is clear when comparing Fig. 2.4.17 with the θ = 40º curves in Fig. 2.4.16. Particularly, the dielectric slab makes Z_C diverge close to the onset of the grating harmonic $TM_{0\text{-}1}$, and therefore, an extraordinary (Fano) resonance is produced before 36.53 GHz in Fig. 2.4.17. In addition, the conventional resonance peak has not been suppressed in Fig. 2.4.17(b), and appears at a lower frequency than in Fig. 2.4.16(b). The circuit-model results shown in Fig. 2.4.17 have been obtained using N_{TE} = 3 and N_{TM} = 4 in (2.4.18) and (2.4.19), which correspond to one plus the number of TE and TM harmonics that are respectively above cutoff inside the dielectric slab at 50 GHz. Once more, excellent agreement with full-wave simulations is obtained, and what it is even more important, all the needed physical insight to explain dipole array TM excitation is given by the proposed circuit model, even in the grating lobes regime.

2.4.4 Modeling other scatterers

Before finishing this study, it should be highlighted that the proposed equivalent-circuit model can also be used to characterize other FSS unit cells, with different geometries of the scatterers and useful for practical applications. As representative examples, three arrays of different printed elements (*i.e.*, a cross-dipole, a squared patch and a symmetric ring) are analyzed under normal incidence in Fig. 2.4.18. In the cross-dipole case, it has been studied the reflectivity response when the electric field of the exciting plane is polarized along the *x* or *y* axis. The cross-dipole scatterers are sensitive to both polarizations since they have long metallization along both the *x* and *y* directions, and therefore, they are used as dual polarized elements in frequency selective surfaces [Parker 2001]. As it can be inferred from the previous analysis with simple metallic dipoles, the total reflection peaks found at 48.5 GHz in the H-plane and 34 GHz in the E-plane in Fig. 2.4.18(a) are mainly related to the dimensions a_x and a_y, respectively. When dealing with a squared patch or a symmetric ring structure, the same results are obtained in both planes for normal incidence. The first total reflection peak in Fig. 2.4.18(b) is related to the length of one side of the square (a_x). However, as we are not dealing with a thin dipole, the width of the squared patch (a_y) makes the resonance frequency occur at a frequency higher than c/a_x (as happened in the previous sections with thin dipoles). In the case of Fig. 2.4.14(c), the total reflection peak at 28.6 GHz appears when the wavelength is approximately the perimeter of the ring [Parker 1981]. The good agreement with full-wave simulations proves the versatility of the developed approach.

These types of scatterers haves attracted much interest in recent years for practical applications. A recent and interesting example can be found in [Kiani 2011], where a bandpass aperture type cross-dipole FSS is proposed for the improvement of the transmission of useful signals through energy-saving glass. This type of glass attenuates infrared waves, and therefore, it is employed in building design for the shielding of its interior against heat entering (keeping it cooler in summer and warmer in winter). However, this resistive coating has an important drawback; it also attenuates useful microwave signals required for

communication systems. The FSS combined with this glass allows the transmission of useful signals while preserving IR attenuation as much as possible.

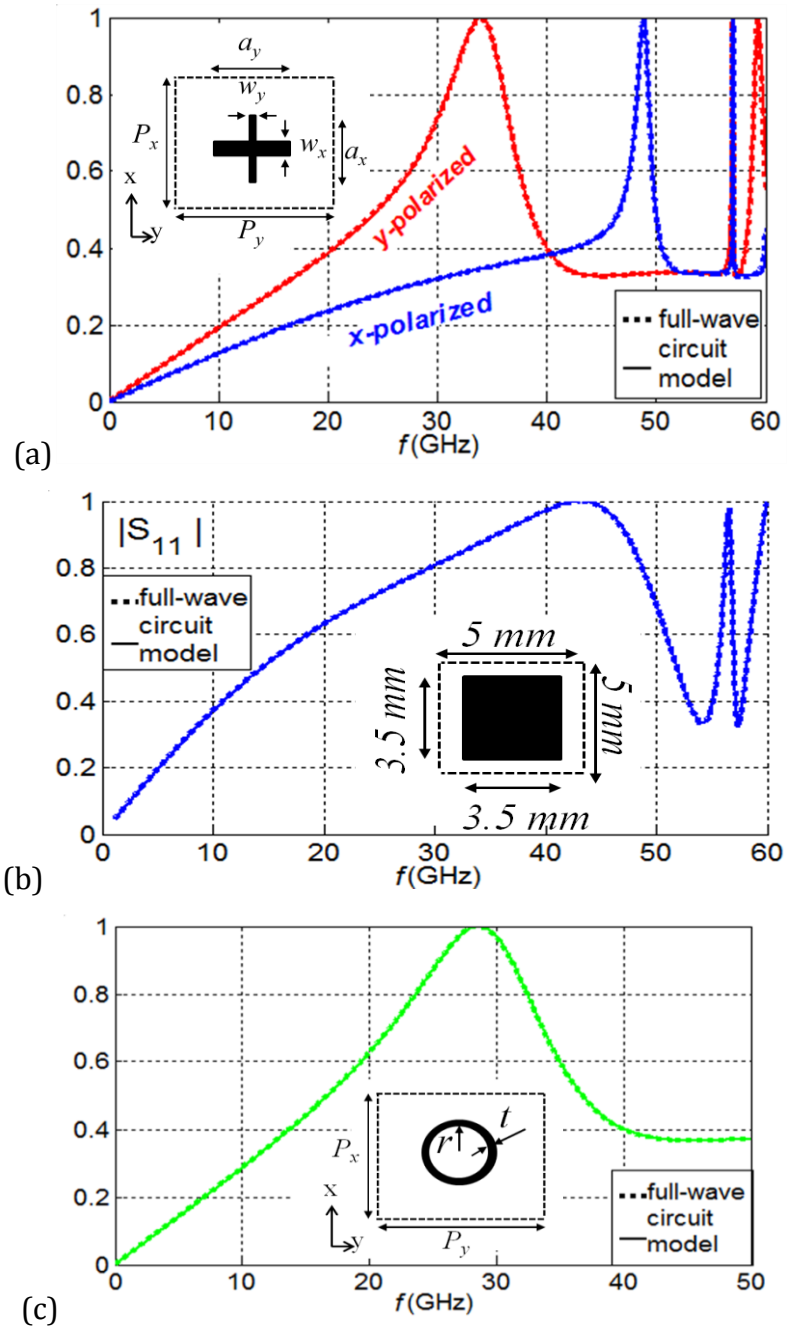

Fig. 2.4.18 Magnitude of the reflection coefficient normal incidence for periodic arrangements (P_x = P_y = 5 mm) of (a) cross-dipoles (a_x = 2 mm, a_y = 3.5mm and w_x = w_y = 0.5 mm), (b) patches and (c) circular rings (r = 3 mm, t = 0.5 mm). The arrays are printed on a substrate of ε_r = 2, d = 1 mm.

Here it should be highlighted an important limitation of the validity of the proposed equivalent circuit which is related to the shape of the scatterers. After this study and a detailed revision of the related literature, it has been found that there is no systematic methodology to build "simple" equivalent networks for arbitrary elements. In some specific 2D situations, we can find in the literature some simple *ad hoc* networks that seem to "match" the response of the FSS with complex elements (*i.e.*, [Capolino 2010]). These attempts are generally restricted to some limited range below the no-grating lobe regime and, furthermore, they require some *a priori* knowledge of the qualitative response of the FSS (since this information is key to choose the convenient lumped elements and connections required to build the corresponding equivalent network). The here developed approach is somewhat limited in its scope. The proposed topology comes directly from basic electromagnetic considerations under the assumption that the qualitative shape of the current profile on the scatterers does not change very much in the considered frequency range. In other words, the topology is not imposed by any *a priori* knowledge of the response of the structure. This limitation is the prize to pay for having a systematic way to build the network topology. In particular, multiresonant elements (*i.e.*, double concentric rings) cannot be systematically characterized with the proposed topology.

2.5 Conclusions

In this chapter it has been aimed the modelling of frequency selective surfaces (FSS) by equivalent circuit models. Due to the fact that FSS are employed in the next chapters in the conception of leaky-wave antennas, it is needed to find a pseudo-analytical equivalent expression of the FSS that can be later inserted in the transverse equivalent network which models the whole antenna structure. In addition, to perform the dispersion analysis of the whole complex structure, the elements in the TEN must analytically depend on the unknown mode wavenumber.

Two different approaches have been proposed in order to model dipole-based FSS by closed-form equivalent circuits, **fulfilling the first objective of this chapter** (O1). The first technique is presented in Section 2.2; it is based on a pole-zero method which provides an equivalent quasi-analytical admittance for the FSS. This expression is a function of the wavenumber and the length of the dipoles, and therefore, it allows the performance of dispersion analysis both with frequency and geometry of the FSS. The second approach, presented in Section 2.4, is based on the impedance matching concept proposed in [Medina 2008]. The FSS is now represented in terms of transmission lines and lumped-elements circuits, leading to a simple and computationally efficient approach that, in addition, allows for easy but accurate predictions on the transmission spectra.

The pole-zero technique presented in Section 2.2 is employed in Section 2.3 for the dispersion analysis of EBG structures conceived from the insertion of dipole-based FSS inside rectangular waveguides, **fulfilling the second objective of this chapter** (O2). As illustrative examples, the analysis of a rectangular waveguide loaded with a high impedance surfaces and an open waveguide loaded with a partially reflective surface, is performed in Section 2.3.

The last objective of this chapter (03) is achieved in Section 2.3, where it is presented the developed graphical user interface that has been implemented for the easy and systematic analysis of FSS-based EBG structures.

The work developed in this chapter has given rise to the publication of 3 peer-review international journal papers (IJ), 4 international conference papers (IC) and 3 Spanish conference papers (SC). These references are copied below; they have been extracted from the complete list of publications of Section 5.3.

IJ1. **M. García-Vigueras**, J.L. Gómez-Tornero, G. Goussetis, J.S. Gómez-Diaz, and A. Álvarez-Melcón, "A Modified Pole-Zero Technique for the Synthesis of Waveguide Leaky-Wave Antennas Loaded with Dipole-Based FSS", *IEEE Trans. Antennas Propag.*, June 2010. pp. 1971 - 1979, ISSN: 0018-926X.

IJ5. R. R. Berral, F. Medina, F. Mesa and **M. Garcia-Vigueras**, "Quasi-analytical Modeling of Transmission/Reflection in Strip/Slit Gratings Loaded with Dielectric Slabs*", IEEE Trans. Microw. Theory Tech.,* vol.60, no.3, pp.405-418, March 2012.

IJ6. **M. Garcia-Vigueras**, F. Mesa, F. Medina, R. R. Berral and J.L. Gómez-Tornero "Simplified Circuit Model for Metallic Arrays of Patches Sandwiched between Dielectric Slabs under Arbitrary Incidence, " *IEEE Trans. Antennas Propag.,* (in press).

IC1. **M. García-Vigueras**, J. L. Gómez- Tornero, G. Goussetis and A. Alvarez-Melcon “Software tool for the leaky-mode analysis of waveguides loaded with frequency selective surfaces”, *Proceedings of the 3rd European Conference on Antennas and Propagation*, Berlín, Germany, pp. 83-87, March 2009

IC9. F. Medina, F. Mesa, A.B. Yakovlev, R.R. Berral, and **M. García-Vigueras**, "*Overview on the Use of Circuit Models to Analyze Extraordinary Transmission and Other Related Phenomena*,'' 2010 IEEE AP-S/URSI-USNC International Symposium, (Toronto, Canada), 11-17 July 2010, (INVITED)

IC10. **M. Garcia-Vigueras**, F. Mesa, F. Medina, R. R. Berral and J.L. Gómez-Tornero “Equivalent Circuits for Conventional and Extraordinary Reflection in Dipole Arrays”, *2011 IEEE International Microwave Symposium, IMS 2011* (Baltimore, Maryland, USA),5-10 June 2011.

IC11. F. Mesa, F. Medina, **M. García-Vigueras**, R. Rodríguez-Berral and J. L. Gómez-Tornero, "Circuit Approach for a General Study of Frequency Selective Surfaces," *2001 International Conference on Electromagnetics in Advanced Applications (ICEAA'11)*, (Torino, Italy), pp. 122-125, 12-16 September 2011.

SC1. **M. García-Vigueras**, J.L. Gomez-Tornero, G. Goussetis, D. Cañete-Rebenaque and A. Álvarez-Melcón. “Herramienta para el análisis modal en guías de onda cargadas con superficies selectivas en frecuencia”, *XXIII Simposium Nacional de la URSI,* Madrid, 22-24 September 2008.

SC5. R. Rodríguez-Berral, F. Medina, F. Mesa, **M. García-Vigueras**, "Modelo analítico para rejillas de difracción metálicas cargadas con dieléctricos," *XXVI Symposium Nacional de URSI*, (Leganés, Madrid), 7-9 September 2011. (ISBN: 978-84-933934-4-1 (abstracts); 978-84-933934-5-8 (CD-ROM); in Spanish).

SC6. **M. García-Vigueras**, F. Mesa, F. Medina, R. Rodríguez-Berral, J.L. Gómez-Tornero, "Circuitos equivalentes para el modelado de la reflexión convencional y extraordinaria en arrays de dipolos," *XXVI Symposium Nacional de URSI*, (Leganés, Madrid), 7-9 September 2011. (ISBN: 978-84-933934-4-1 (abstracts); 978-84-933934-5-8 (CD-ROM); in Spanish).

Chapter 3:

Analysis and design of uniform double-layer Fabry-Perot LWA

In this chapter it is performed the analysis and design of uniform double-layer Fabry-Perot (FP) Leaky-Wave Antennas (LWAs). These antennas are conceived in a hybrid technology which results from the combination of metallic waveguides and periodic surfaces. The characterization of these surfaces is carried out taking advantage of the work developed in the previous chapter. The case of uniform antennas is here considered, both in one and two dimensional topologies (Chapter 4 will focus on the synthesis of non-uniform tapered antennas). Several one-dimensional LWA prototypes have been fabricated obtaining very good agreement between measurements and theory. From the general objectives enlisted in Chapter 1, these are the ones which are now pursued:

O4. Analysis and design of double-layer uniform one-dimensional Fabry-Perot leaky-wave antennas.

O5. Analysis and design of double-layer uniform two-dimensional Fabry-Perot leaky-wave antennas.

The first **Section 3.1** of this chapter mainly consists in summarizing basic concepts about leaky-wave antennas and reviewing the different proposed radiation mechanisms.

Next, in **Section 3.2,** it is described an original one-dimensional Fabry-Perot LWA in hybrid technology. The tool developed in Chapter 2 is here employed to analyze this structure and identify the role played by each of its components. Feeding and matching devices are also proposed and designed.

The possibility to control the pointing angle and beamwidth in this antenna is subsequently explained in **Section 3.3**. Next, **Section 3.4** shows how the frequency scanning behavior can also be successfully controlled and enhanced. Experimental results on fabricated prototypes operating at 15GHz are reported, demonstrating the versatile control of the LWA performance by changing the PRS and HIS parameters.

The analysis and design of two-dimensional FP LWAs is developed in **Section 3.5**. Here it is explained that it is possible to characterize these antennas in the H and E planes employing the tool developed in Chapter 2 by making an approximation towards one-dimensional structures.

Finally, in **Section 2.5** the main conclusions and results will be summarized, together with the discussion about the achievement of the aimed objectives.

3.1 Introduction

A leaky-wave antenna is basically a guiding structure that possesses a mechanism that allows a traveling wave [Walter 1965] leak its power all along the structure length. The basis on leaky-wave antennas can be found in excellent book chapters such as [Hessel 1969], [Tamir 1969], [Oliner 1993], [Jackson 2008]. A recent summary on the latest advances can be found in [Caloz 2010]. One of their biggest advantages is that they provide a simple mechanism to obtain highly-directive frequency scanned radiation patterns from a simple feed. The first leaky-wave antenna (shown in Fig. 3.1.1(a)) consists of a rectangular waveguide with a continuous longitudinal slot in its side; it was first proposed by Hansen [Hansen 1940] and later studied by Goldstone and Oliner [Goldstone 1959]. The hole in the waveguide allows the progressive leakage of energy out to free space, turning the waveguiding structure into a Leaky-Wave Antenna (LWA). Many other topologies of LWA have been proposed since Hansen´s proposal, an early example is shown in Fig. 3.1.1(b), where the waveguide is filled with a dielectric material and loaded with a periodic array of holes [Hines 1957]. These antennas are named as one-dimensional (1D) [Oliner 1993], due to the fact that the structure supports a wave traveling in a fixed direction, for example, along the *y* axis in the LWAs of Fig. 3.1.1.

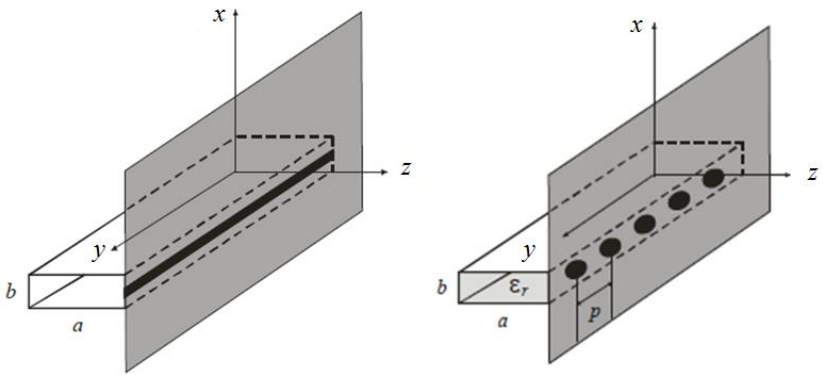

(a) (b)

Fig. 3.1.1 1D Leaky-wave antennas based on rectangular waveguides, with infinite ground plane surrounding the radiating aperture. (a)Empty rectangular waveguide with longitudinal slit in the narrow wall of the waveguide (b)Rectangular waveguide filled with dielectric material and loaded with a periodic array of holes. (Figs 7.1 and 7.2 in [Jackson 2008]).

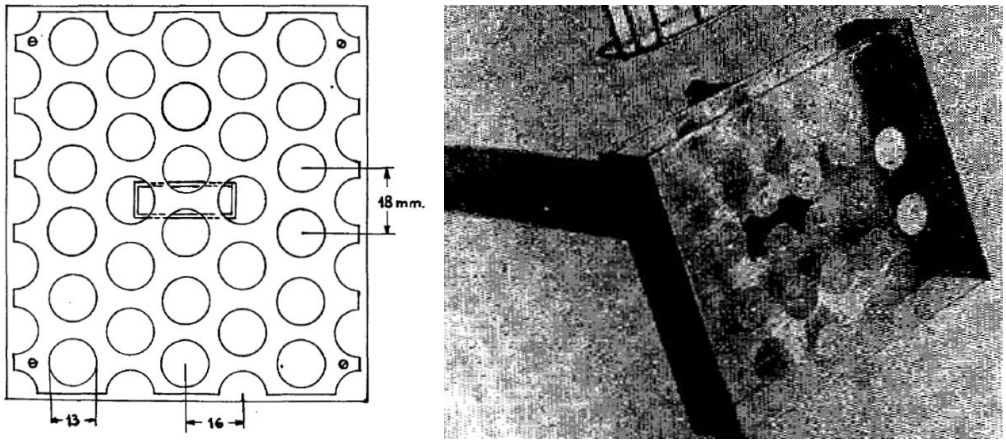

Fig. 3.1.2 2D Leaky-wave antenna (Figs 4 and 7 in [Trentini 1956]).

The concept of two-dimensional (2D) leaky-wave antenna was first introduced by Trentini in 1956, proposing a high directive antenna constituted by a periodic partially reflective screen over a ground plane (see [Trentini 1956]). The scheme of this antenna and a picture of it are shown in Fig. 3.1.2. Later, several other types of 2D LWAs were proposed (see [James 1989], [Alexopoulos 1984], [Jackson 1985-I, 1988, 1993], [Ip 1990], [Feresidis 2001], [Zhao 2005]…). The main advantage of these antennas is that they can provide pencil beams at broadside, as it will be later explained in detail. In contrast to 1D LWAs, 2D LWAs are fed by a source that, placed in the centre of the antenna, launches cylindrical leaky waves [Ip 1990].

3.1.1 Physics of leaky waves

Due to radiation, leaky-waves are characterized by a complex longitudinal propagation wavenumber [Oliner 1993]

$$k_y = \beta_y - j\alpha_y \tag{3.1.1}$$

Any field component of the leaky-wave propagating along the structure can be expressed as

$$\psi(x,y,z) = \psi(x,z)e^{-jk_y y} = \psi(x,z)e^{-j\beta_y y}e^{-\alpha_y y} \ . \tag{3.1.2}$$

Therefore, β_y and α_y stand for the phase (propagation) constant and the leakage (attenuation) constant, respectively. The phase constant represents the variation in the wave phase per meter (*rad/m*), whereas the attenuation constant is related to the decrease of the wave amplitude per meter (*nep/m*). The attenuation constant represents the loss of power along the structure as the wave propagates, and thus, it is also called radiation rate. If the guiding structure that supports the leaky wave has conductor and/or dielectric losses, then α_y accounts for these losses as well [Jackson 2008]. As it is explained in [Gomez 2006-III], the attenuation constant can be qualitatively split into three different contributions: reactive rate, losses rate, and leakage (radiation) rate:

$$\alpha_y = \ \alpha_y^{REAC} + \alpha_y^{LOSSES} + \alpha_y^{RAD} \tag{3.1.3}$$

This equation is just an approximation as it will be explained in detail along this section, together with the nature of these three contributions.

It would be quite complicated to give a general explanation of the leaky-wave dispersion which is valid for every possible case of LWA. Therefore, in this introduction we will focus on the case schemed in Fig. 3.1.3(a), which consists of a leaky wave propagating along a generic guiding one-dimensional uniform (or quasi-uniform) structure. It is worth noting that, for the sake of simplicity, this structure is considered to be short in the *x* axis, so that no surface waves are supported in the substrate along the *x* axis, and therefore, no energy is leaked into that direction. It is also assumed that the energy that reaches the end of the structure is absorbed by a matched load.

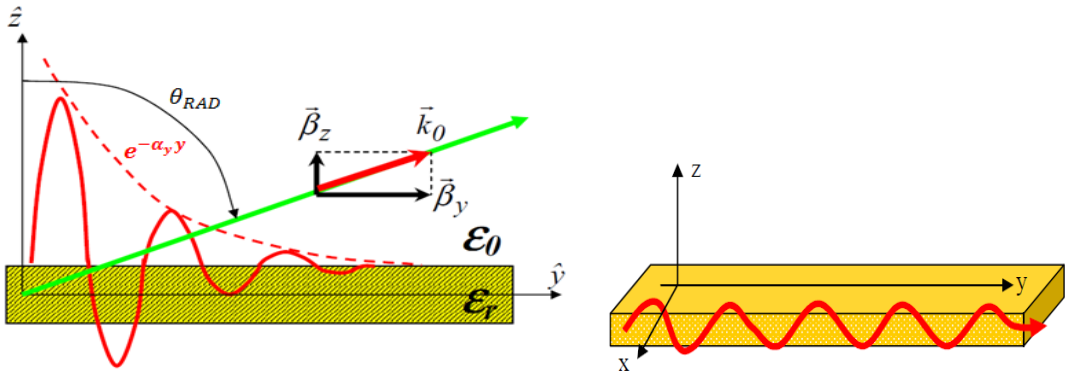

(a) (b)

Fig. 3.1.3 Scheme of a generic guiding one-dimensional uniform or quasi-uniform structure which supports a propagating (a) leaky-wave (b) surface-wave (Fig. 2.1.3 in [Gómez 2005-II]).

The distribution of the leaky-wave in the near field establishes the radiation pattern (far field). It is well known that the far fields can be obtained from the Fourier transform of the near fields in the radiating aperture of an antenna [Balanis 2005], [Tamir 1963-II]. In particular, the **phase constant β_y of the leaky-wave will determine the direction in which the energy is mainly radiated** (θ_{RAD}, the angle of the main beam in the radiation pattern, measured from broadside). As it can be seen in Fig. 3.1.3(a), the angle θ_{RAD} can be approximately obtained by ray optics from the longitudinal wavenumber (β_y) and the propagation constant in free space (k_0)

$$sin\theta_{RAD} \approx \frac{\beta_y}{k_0} \tag{3.1.4}$$

where

$$k_0 = \omega\sqrt{\varepsilon_0\mu_0} = \frac{2\pi f}{c_0} = \frac{2\pi}{\lambda_0}\ , \tag{3.1.5}$$

with f being the frequency and c_0 the speed of light in vacuum. In theory, th approximated equation (3.1.4) is valid when $\beta_y >> \alpha_y$, although in practice it is even valid when β_y is comparable to α_y. From (3.1.4) it can be easily deduced that radiation is produced when

$$\left|\frac{\beta_y}{k_0}\right| < 1 \,. \tag{3.1.6}$$

which is therefore called ***radiation condition***. If this condition is not satisfied, the wave propagates along the structure with a wavenumber β_y greater than the wavenumber of light in free space k_0. The radiation angle (θ_{RAD}) is positive in the case of forward leaky waves ($\beta_y > 0$), whereas it is negative when the wave is backward (β_y). Note that, by applying (3.1.3), radiation at forward end fire ($\theta_{RAD} = 90°$) occurs when $\beta_y/k_0 = 1$, backward end fire radiation ($\theta_{RAD} = -90°$) when $\beta_y/k_0 = -1$, and a broadside beam ($\theta_{RAD} = 0°$) will be produced when $\beta_y/k_0 = 0$. Thus, although the wave phase constant (β_y) may be either positive or negative, it must be noticed that the leaky-wave group velocity is always greater than zero, which means that the energy propagates away from the source. The waves that satisfy the condition (3.1.6) are also called ***fast waves*** due to the fact that their longitudinal phase velocity is greater than the one of light in vacuum [Gómez 2005-II]:

$$v_p = \frac{\omega}{\beta_y} = \frac{2\pi f}{\beta_y} = \frac{2\pi c_0/\lambda_0}{\beta_y} = \frac{c_0}{\beta_y/k_0} > c_0 \;\leftrightarrow\; \left|\frac{\beta_y}{k_0}\right| < 1 \,. \tag{3.1.7}$$

In contrast, when the phase constant is greater than k_0, the wave becomes a surface wave which is ***slow*** (case depicted in Fig. 3.1.3(b)); it is purely bound and does not radiate along the length of the structure (as it does not satisfy (3.1.6)). The energy associated to this ***surface wave*** ([Oliner 1993], [Tamir 1963-I], [Oliner 1979]) is confined within the guiding structure and it is only radiated at discontinuities (such as the very end of the waveguiding structure). In principle, surface waves do not appear in air-filled LWAs, but in partly dielectric-loaded configurations [Oliner 1993].

On the other hand, **the attenuation constant of the leaky wave (α_y) determines the illuminated area of the antenna radiating aperture L_A**, and therefore, the width of the radiation pattern main beam (**beamwidth**, $\Delta\theta$). The LWA beamwidth can be obtained by applying [Oliner 1993]

$$\Delta\theta \approx \frac{1}{\left(\frac{L_A}{\lambda_0}\right)\cos\theta_{RAD}} \tag{3.1.8}$$

The length of the antenna radiating aperture is usually selected for a given value of α_y, so that 90% of the power is radiated, with the remaining 10% absorbed by a matched load. In this case it is found the following relation ([Oliner 1993])

$$\frac{L_A}{\lambda_0} = \frac{0.183}{\alpha_y/k_0} \tag{3.1.9}$$

The **radiation efficiency** of the leaky-wave antenna (η_{RAD}) is defined as the power radiated into space divided by total power injected into the antenna, and it is related to the attenuation constant as ([Oliner 1993])

$$\eta_{RAD} = 1 - e^{-2\alpha_y L_A} \tag{3.1.10}$$

This equation is coherent with the fact that the energy that reaches the end of the antenna (which is supposed not to be radiated) corresponds to: $e^{-2\alpha_y L_A}$. Thus, the radiation efficiency is normally less than 100%, due to the power absorbed at the matched load placed at the end of the antenna. The LWA beamwidth associated to an antenna with 90% efficiency is

$$\Delta\theta \approx \frac{\alpha_y/k_0}{0.183\cos\theta_{RAD}} \tag{3.1.11}$$

As it can be observed in the expression of the near fields in the aperture (3.1.2) and in Fig. 3.1.3(a), the amplitude of a leaky wave is attenuated by the factor $e^{-\alpha_y y}$, which means that the aperture illuminated area increases as α_y is decreased. Thus, high directivity (low $\Delta\theta$) can be achieved in a long LWA with a low value of α_y, in coherence with (3.1.8) and (3.1.11).

Generally, β_y and α_y vary with frequency, and the functions $\beta_y(\omega)$ and $\alpha_y(\omega)$ are called the **dispersion and attenuation relations**. This dependence with frequency results in different propagation regimes. The definition of cutoff, radiation and bounded regimes of a leaky-wave antenna can be found in books such as [Oliner 1993], or other interesting papers such as [Tamir 1963-I], [Oliner

1979, 1986-I and II, 1987], [Song-Tsuen 1981], [Bagby 1993], [Lin 1997] or [Gomez 2006-III]. This literature leads to the following background knowledge necessary to work with leaky waves. As an illustrative example, Fig. 3.1.4 shows the evolution with frequency of the normalized phase and leakage constants (β_y/k_0 and α_y/k_0, respectively) which correspond to the first mode in a uniform one-dimensional dielectric-loaded LWA. For the characterization of the different propagation regimes we will first consider the lossless case.

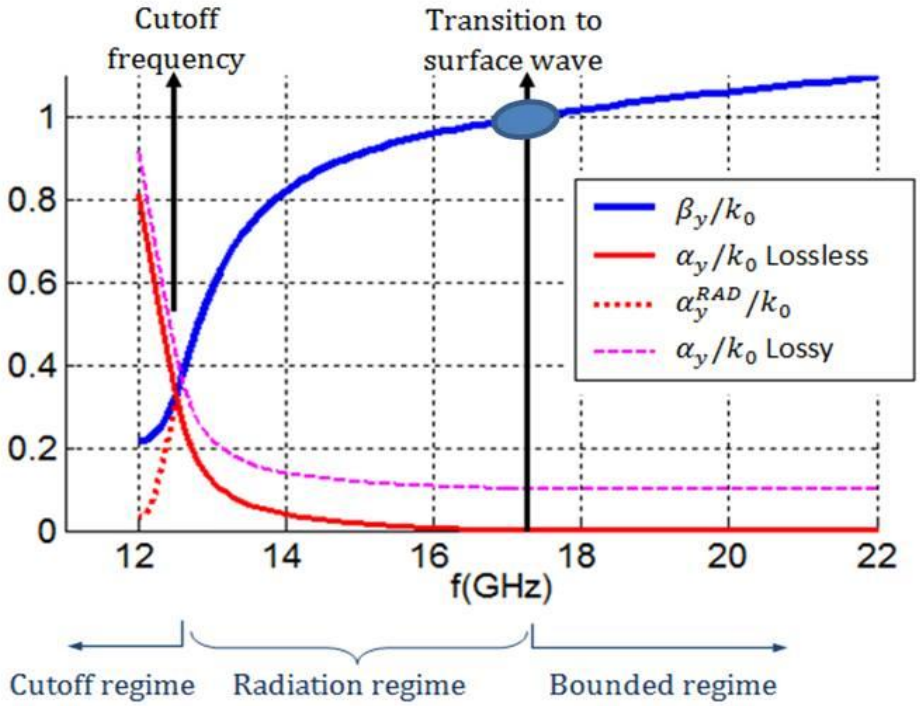

Fig. 3.1.4 Dispersion and attenuation relations in uniform 1D dielectric-filled LWA. Leaky mode propagation regimes.

In the particular case under study (one-dimensional LWA fed at one end), the frequency at which β_y=α_y is satisfied is named as the **cutoff frequency** of the leaky mode (LM). At this point, the active and reactive power densities associated with the leaky mode in the structure are equal. This fact is proven in Eq. (3.1.12), where the poynting vector of the LM is obtained ($S_y^{\mathrm{TE/TM}}$). In this expression, the LM is considered to be either a TE or a TM modal solution of the 1D waveguiding structure (depending on its polarization), characterized by a complex propagation constant k_y. In (3.1.12), the characteristic impedance associated to the TE/TM-

polarized guided LM ($Z_c^{\mathrm{TE/TM}}$) is obtained applying respectively (2.4.6) or (2.4.7) [Munk 2000], [Pozar 2005].

$$S_y^{\mathrm{TE/TM}} \approx \frac{|E|^2}{2Z_c^{\mathrm{TE/TM}}} \begin{cases} \dfrac{|E|^2}{2\omega\mu_0} k_y = \dfrac{|E|^2}{2\omega\mu_0}\left(\beta_y - j\alpha_y\right), & \text{TE case} \\ \dfrac{|E|^2}{2k_y}\omega\varepsilon_0\varepsilon_r = \dfrac{|E|^2}{2\left(\beta_y^2 + \alpha_y^2\right)}\left(\beta_y + j\alpha_y\right), & \text{TM case} \end{cases} \tag{3.1.12}$$

In this expression, the real and imaginary parts of the poynting vector correspond respectively to the active and reactive power densities associated with the TE/TM-polarized LM. It can be deduced that the active power is predominant at frequencies which satisfy $\beta_y > \alpha_y$ (the region which is above the cuttof frequency). The **cutoff regime** covers the frequencies which satisfy $\beta_y < \alpha_y$. At this frequency range, the 1D guiding structure acts similarly to a waveguide at cuttof: the reactive part of the power is the most significant, and the LM begins to be attenuated or reflected rather than propagative [Oliner 1993, Lin 1997, Gomez 2004-II and 2006-III]. Although still some radiation can be produced at the cutoff regime (due to the fact that the active power density is greater than zero), for convenience, and in analogy with the propagation of waves in closed 1D waveguides, it is considered that the leaky mode starts propagating through the structure at the cutoff frequency [Oliner 1993].

Above the cutoff regime, and when the radiation condition (3.1.6) is satisfied, the modal solution of the structure corresponds to a leaky wave whose energy is leaked from the angle θ_{RAD} (which in principle can be scanned between 0º and 90º); this regime is also called **space wave** region. The minimum value of θ_{RAD} is produced at the cutoff frequency, which is normally near broadside. The modal solution of the structure corresponds to a surface wave when $\beta_y/k_0 > 1$, this regime is named as **bounded**. As previously explained, the bounded regime is characterized by zero leakage ($\alpha_y/k_0 = 0$), in coherence with the solid red line in Fig. 3.1.4 (considering a lossless case). However, the cutoff regime (also named **reactive region**) is characterized by values of α_y greater than β_y. The sudden rise of α_y below the cutoff frequency does not represent an increase of the radiation rate, but the reactive attenuation of the fields previously explained [Oliner 1993,

Lin 1997, Gomez 2004-II and 2006-III]. In other words, below the cutoff frequency, the waves highly suffer from reflection losses and barely propagate along the structure. As a result, considering the definition of α_y in (3.1.3), it can be deduced that in the absence of losses, the main contribution to α_y below the cutoff frequency is α_y^{REAC}, whereas it is α_y^{RAD}in the radiation regime (as summarized in Table 3.1.3). The red dotted line in Fig. 3.1.4 corresponds to the radiation contribution (α_y^{RAD}) to the attenuation constant; in coherence with the previous conclusions, it can be seen that in the absence of losses, α_y^{RAD} decreases below the cutoff frequency while it is equal to α_y in the radiation regime. If losses are considered (pink dashed line in Fig. 3.1.4), they can be approximately regarded as a linear contribution to α_y (as it is expressed in (3.1.3)) [Gómez 2004-I, II and 2007]. Therefore, in the bounded regime, α_y corresponds to α_y^{LOSSES}. However, it should be noticed that equation (3.1.3) is a convenient approximation; in fact, the three considered contributions to α_y are in general coupled.

As it is marked with an elipse in Fig. 3.1.4, the transition between the radiation regime and the bounded regime is not continuous. At this transition between the leaky and bound regions there exists a small range in frequency within which the modal solution of the structure is non-physical. This transition range is called a **spectral gap**, its nature is now understood rather well and it was firstly described in [Shigesawa 1993 and 1995] and [Majumder 1997]. In this dissertation, this interesting phenomenon is not studied due to the fact that radiation at forward endfire is discarded in the particular case of our Fabry-Perot LWAs.

Propagation regime	$\boldsymbol{\alpha_y^{REAC}}$	$\boldsymbol{\alpha_y^{RAD}}$
Cutoff	Main contribution	Low
Radiation	zero	Main contribution
Bounded	zero	zero

Table 3.1.1 Contributions to the attenuation rate α_y in the absence of losses.

Leaky waves are characterized by a complex transverse wavenumber (*i.e.*, the vetical z axis in Fig. 3.1.3(a)), that can be obtained by ray optics from Fig. 3.1.3(a)

$$k_z = \sqrt{k_0^2 - k_y^2} \ . \tag{3.1.13}$$

The sign of this square root must be chosen carefully so as to obtain the solution that gives the correct wave physical behavior. This issue is very clearly explained in [Jackson 2008] and [Caloz 2011] and is next summarized. When considering a forward radiating leaky-wave (with $\beta_y > 0$ and $\alpha_y > 0$), the transverse wavenumber is of the form $k_z = \beta_z + j\alpha_z$ (being β_z and α_z positive real numbers). This field is termed as "**improper**" [Jackson 2008], due to the fact that the wave increases exponentially in the near transverse air region. This behavior can be clearly understood by looking at the power flow of the leaky-wave in the scheme of Fig. 3.1.4(a).

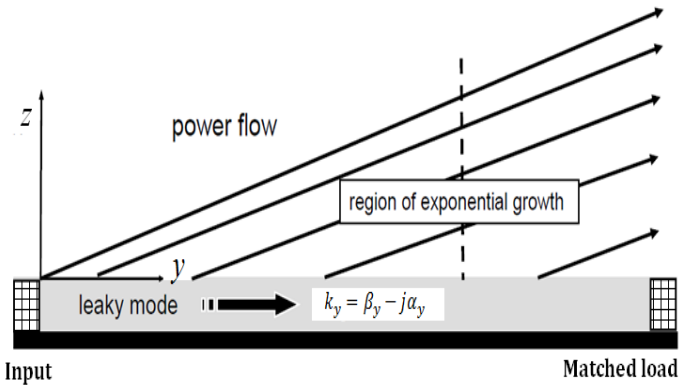

Fig. 3.1.5 Scheme of the near field created by a forward radiating leaky wave in a quasi-uniform 1D LWA (Fig. 7.8 in [Jackson 2008]).

3.1.2 Radiation properties of uniform 1D and 2D LWAs

The scheme of a 1D rectangular radiating aperture, which dimensions are $a\ x\ L_A$, is shown in Fig. 3.1.6. It is assumed that this aperture supports a leaky wave which propagates along the *y* axis, starting from one end, and its electric field is *x*-polarized. As the aperture is considered to be uniform or quasi-uniform (but non-modulated), the near fields that illuminate it can be expressed as

$$E_{LW}^{ILLUM}(x,y) = E(x)M(y)e^{+j\Psi(y)}; \qquad x\epsilon[0,a], \qquad y\epsilon[0,L_A] \tag{3.1.14}$$

where *E(x)* is the illumination along x and will assumed to be a constant *E(x)* = 1 (although in certain cases it can be a cosine function, depending on the type of resonance in *x*). The illumination in the *y* axis depends on the leaky-wave propagation constant $k_y = \beta_y - j\alpha_y$, and it corresponds to $E(y) = M(y)e^{j\Psi(y)}$, where

$$M(y) = \sqrt{\alpha_y}e^{-\int_0^y \alpha_y(\tau)d\tau} = \sqrt{\alpha_y}\, e^{-\alpha_y y} \tag{3.1.15}$$

$$\Psi(y) = -\int_0^y \beta_y(\tau)\, d\tau = -\beta_y y \tag{3.1.16}$$

Following the theory explained in [Balanis 2005], the fields radiated by the aperture can be written as

$$\mathrm{E_r} = 0 \tag{3.1.17}$$

$$\mathrm{E_\theta} = jE_0 a \frac{k_0 e^{-jk_0 r}}{2\pi r}\cos\phi \frac{\sin X}{X}\int_0^{L_A} M(y')e^{j\Psi(y')}\, e^{jy'\xi\sin\phi}\, dy' \tag{3.1.18}$$

$$\mathrm{E_\phi} = -jE_0 a \frac{k_0 e^{-jk_0 r}}{2\pi r}\cos\theta\sin\phi \frac{\sin X}{X}\int_0^{L_A} M(y')e^{j\Psi(y')}\, e^{jy'\xi\sin\phi}\, dy' \tag{3.1.19}$$

where E_0 is the wave amplitude, θ, ϕ and r denote the usual spherical coordinates with respect to the (x, y, z) axes,

$$\xi = k_0 \sin\theta \tag{3.1.20}$$

and $X = \frac{1}{2} k_0 a \sin\theta \cos\phi$. These far fields define fan-beam radiation patterns, which main beam is directive and frequency scanned in the H-plane, and wide in the E-plane. An example of this kind of radiation pattern is shown in Fig. 3.1.7, which corresponds to a 1D aperture which supports a fast leaky wave with k_y/k_0 = 0.6 + j0.01.

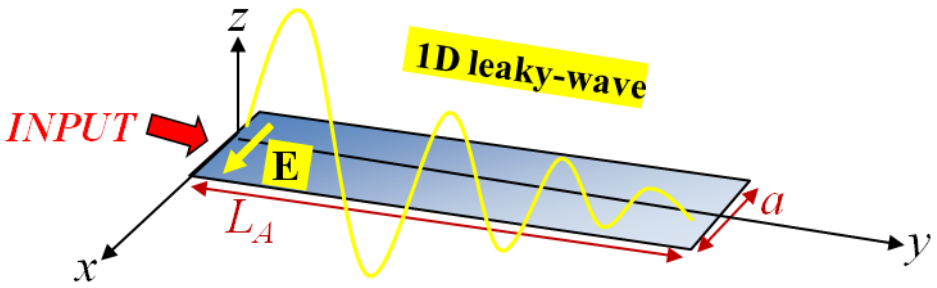

Fig. 3.1.6 Scheme of 1D radiating uniform or quasi-uniform (but non-modulated) aperture fed at one end.

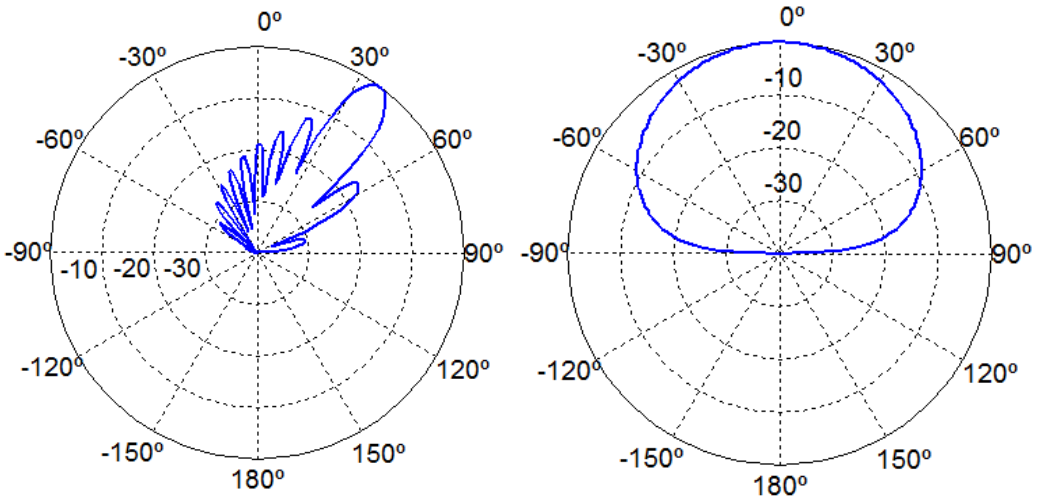

(a) (b)

Fig. 3.1.7 Normalized radiation pattern in dB of 1D LWA with dimensions: $a = 0.5\ \lambda_0$, $L_A = 6\ \lambda_0$, , fed at one end (k_y/k_0=0.6+j0.01). (a) H-plane (yz), (b) E-plane (xz).

Now it is considered that the 1D aperture supports a leaky wave which dispersion diagram is the one of Fig. 3.1.8(a). This figure corresponds to the typical behavior of the fundamental mode in a uniform or quasi-uniform (but non-modulated) LWA. It should be noted that broadside radiation ($\theta_{RAD} = 0$) will not be obtained from this antenna, due to the fact that the cutoff frequency is located at

a point where β_y is always greater than zero. Figure 3.1.9 shows how the radiation pattern associated to this aperture varies with frequency. In particular, Fig. 3.1.9(a) is obtained at the cutoff frequency (approximately located at 13 GHz), where k_y/k_0 = 0.1 + j0.1 (see Fig. 3.1.7), providing the lowest θ_{RAD} radiated from this LWA. Figure 3.1.9(b) corresponds to the radiation pattern at 14GHz, where k_y/k_0 = 0.39+j0.015.

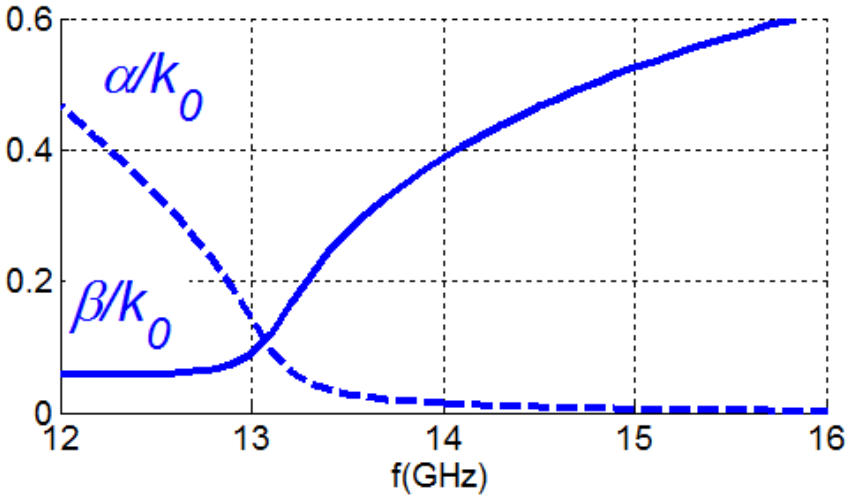

Fig. 3.1.8 Frequency dispersion diagram of fundamental leaky mode.

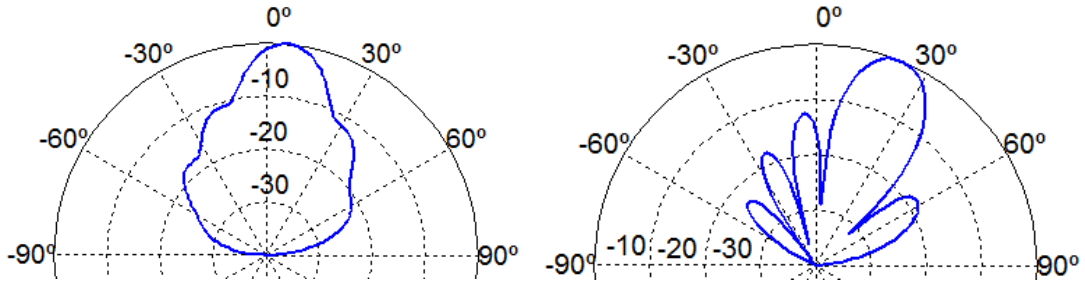

Fig. 3.1.9 Normalized radiation pattern in dB of 1D LWA with dimensions: $a = 0.5\ \lambda_0$, $L_A = 6\ \lambda_0$, fed at one end. (a) $k_y/k_0 = 0.1 + j0.1$, (b) $k_y/k_0 = 0.39 + j0.015$.

The scheme of a 2D circular aperture, which radio is L_A, is shown in Fig. 3.1.10. Cylindrical coordinates are now employed to describe magnitudes on the antenna aperture (z = 0). This scenario was studied in [Ip 1990], where it is explained that, when the aperture is fed by a horizontal electric dipole, a pair of leaky waves are launched, one TM_z and one TE_z. The vector potentials associated to this pair of waves are

$$\mathrm{A_z}(\rho,\phi) = \frac{1}{2}\cos\phi\, H_1^{(2)}\left(k_\rho^{\mathrm{TM}}\rho\right) \tag{3.1.21}$$

$$\mathrm{F_z}(\rho,\phi) = \frac{\omega\mu_0}{2k_z}\frac{1}{2}\sin\phi\, H_1^{(2)}\left(k_\rho^{\mathrm{TE}}\rho\right) \tag{3.1.22}$$

where $k_\rho^{\mathrm{TM/TE}} = \beta_\rho^{\mathrm{TM/TE}} - j\alpha_\rho^{\mathrm{TM/TE}}$ is the complex propagation wavenumber associated to the $\mathrm{TM_z}$ or $\mathrm{TE_z}$ leaky wave, and $H^{(2)}$ is the second kind Hankel function. As derived in [Ip 1990], the previous waves generate the following far fields:

$$\mathrm{E_\theta} = R(r)\cos\phi\cos\theta\left[AP_{\mathrm{TM}}(\theta) + BC_{\mathrm{TE}}(\theta)\right] \tag{3.1.23}$$

$$\mathrm{E_\phi} = -R(r)\sin\phi\left[AC_{\mathrm{TM}}(\theta) + BP_{\mathrm{TE}}(\theta)\right] \tag{3.1.24}$$

where

$$\mathrm{R(r)} = -\frac{j\omega\mu_0}{4\pi r}e^{-jk_0 r}, \tag{3.1.25}$$

$$P_{\mathrm{TM/TE}}(\theta) = \frac{2\pi k_\rho^{\mathrm{TM/TE}}}{\left(k_\rho^{\mathrm{TM/TE}}\right)^2 - \xi^2}\Big[k_\rho^{\mathrm{TM/TE}}\rho' H_1^{(2)}\left(k_\rho^{\mathrm{TM/TE}}\rho'\right)J_0(\xi\rho') - \xi H_0^{(2)}\left(k_\rho^{\mathrm{TM/TE}}\rho'\right)J_1(\xi\rho')\Big]_{\rho'=0}^{\rho'=L_A} - C_{\mathrm{TM/TE}}(\theta), \tag{3.1.26}$$

$$C_{\mathrm{TM/TE}}(\theta) = \frac{2\pi}{\xi}\left[H_1^{(2)}\left(k_\rho^{\mathrm{TM/TE}}\rho'\right)J_1(\xi\rho')\right]_{\rho'=0}^{\rho'=L_A} \tag{3.1.27}$$

A and B are the amplitudes of the $\mathrm{TM_z}$ and $\mathrm{TE_z}$ waves respectively and J_n is the $\mathrm{n^{th}}$ order Bessel function. As shown in [Ip 1990], when dealing with long apertures, the function $C_{\mathrm{TM/TE}}(\theta)$ of (3.1.27) is almost constant, and the function $P_{\mathrm{TM/TE}}(\theta)$ exhibits a sharp peak at an angle given by:

$$\theta_{RAD}^{\mathrm{TM/TE}} = \mathrm{asin}\left(\beta_y^{\mathrm{TM/TE}}/k_0\right) \tag{3.1.28}$$

Therefore, considering the far field expressions in (3.1.23) and (3.1.24), it can be deduced that the TM_z leaky wave mainly determines the E-plane pattern of the 2D FP LWA, while it is the TE_z leaky wave which mainly sets the H-plane pattern.

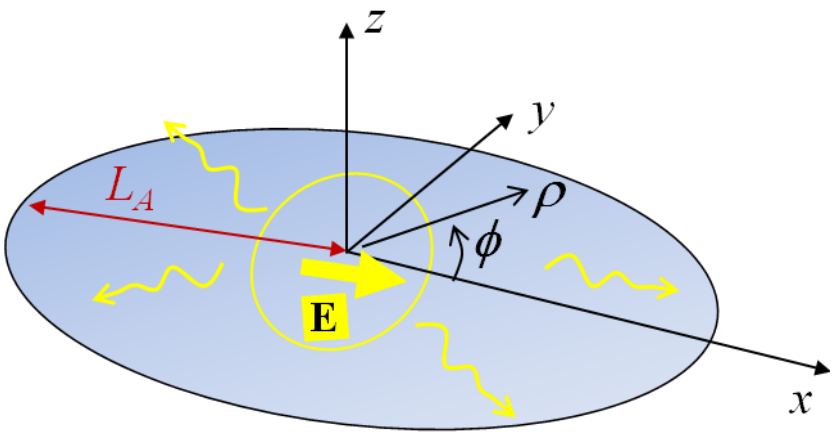

Fig. 3.1.10 Scheme of 2D radiating uniform or quasi-uniform (but non-modulated) aperture fed by a *x*-oriented electric dipole.

In the present case of 2D LWAs excited by a horizontal dipole, either a scanned beam ($\theta_{RAD} > 0$) or a broadside beam ($\theta_{RAD} = 0$) may be obtained. In particular, a broadside pencil beam is achieved when two beams, each one pointing slightly above broadside, combine to form one broadside beam. This effect occurs at frequencies which satisfy $\beta_\rho \leq \alpha_\rho$; particularly, maximum directivity at broadside is achieved at the so called *splitting condition*

$$\beta_\rho = \alpha_\rho \tag{3.1.29}$$

Good explanation, discussion and applications of this condition can be found in [Ip 1990], [Chien-Jen 1999], [Yamamoto 1999], [Lovat 2006], [Sutinjo 2008] and [Jackson 2008]. For greater frequencies, the previous two beams split, and the radiation pattern takes the shape of a conical beam. Recalling the dispersion diagram of Fig. 3.1.8, a 2D LWA which supports this leaky wave presents the pencil beam radiation patterns shown in Fig. 3.1.11 at 13 GHz (where the splitting condition is satisfied), and the conical beam patterns of Fig. 3.1.12 at 14 GHz.

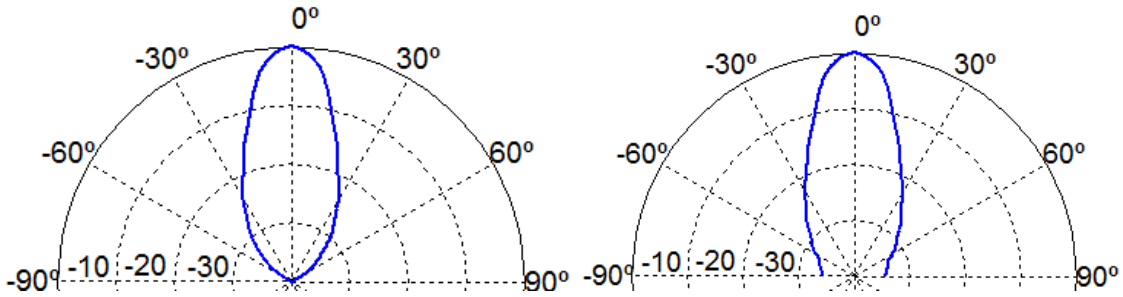

(a) (b)

Fig. 3.1.11 Normalized radiation pattern in dB of 2D LWA ($L_A = 6\ \lambda_0$) (k_y/k_0=0.1+j0.1). (a) H-plane (*yz*), (b) E-plane (*xz*).

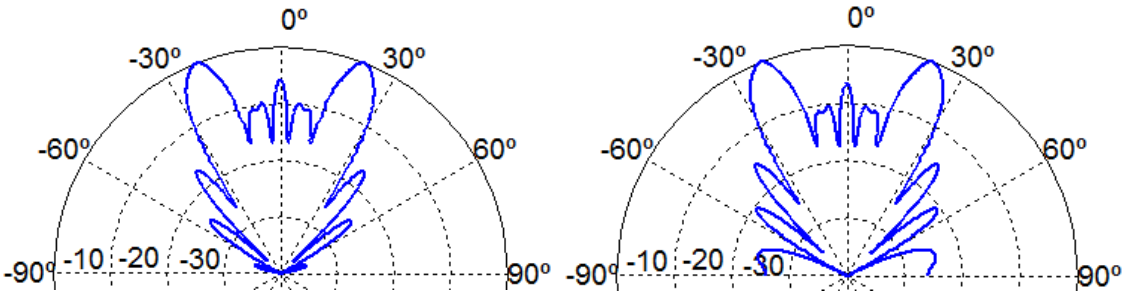

(c) (d)

Fig. 3.1.12 Normalized radiation pattern in dB of 2D LWA ($L_A = 6\ \lambda_0$) ($k_y/k_0 = 0.39 + j0.015$). (a) H-plane (*yz*), (b) E-plane (*xz*).

3.1.3 Dispersion of modes in complex transmission lines

In order to explain the different radiation mechanisms of leaky-wave antennas, it will be first briefly reviewed the dispersion of modes in general complex transmission lines. This study will start with the case of a uniform microstrip line. Periodic and metamaterials transmission lines will be subsequently considered, and finally, the specific case of empty waveguides is presented.

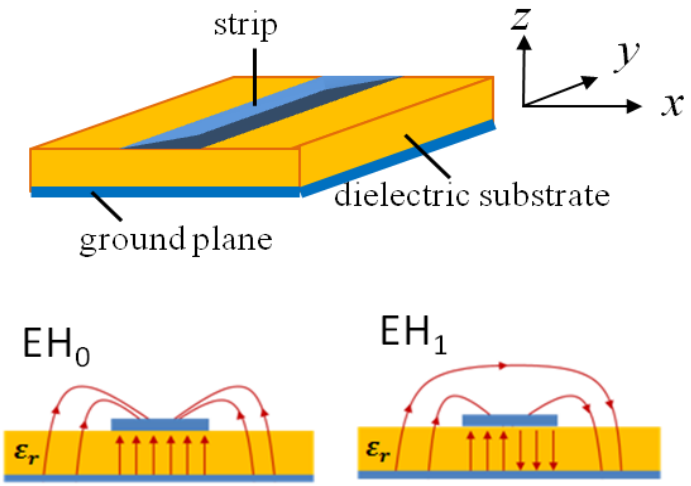

Fig. 3.1.13 Scheme of a microstrip line and the transverse field profile of the first two modes (EH_0 and EH_1).

A typical dispersion diagram of the modes existing in a microstrip line is shown in Fig. 3.1.14. It is worth noting here that, although the dispersion curves in Fig. 3.1.14 have been drawn with continuous lines, the transitions between leaky, surface or bounded waves may not be mathematically continuous, as it was firstly studied in [Mesa 2002-I and II]. The first mode (EH_0) in this inhomogeneous medium propagates with a velocity somewhere between the speed of light in air and inside the substrate with permittivity ε_r. The near fields associated to this mode are schemed in Fig. 3.1.13. The effective relative permittivity of the microstrip (ε_{ref}) is then defined as the dielectric constant of an equivalent homogeneous medium which presents the same propagation velocity as the inhomogeneous line. This mode propagates through the microstrip line at any frequency. The normalized phase constant of the EH_0 mode corresponds to:

$$\beta_y/k_0 = \sqrt{\varepsilon_{ref}} \tag{3.1.30}$$

which is always greater than one, tends to $\sqrt{\varepsilon_r}$ as the frequency is increased and is real in the absence of losses (as it can be seen in Fig. 3.1.14). Therefore, this mode propagates in the form of a bounded surface wave along the *y* axis, and all the energy associated to it is completely guided, and it is not leaked or radiated to free space.

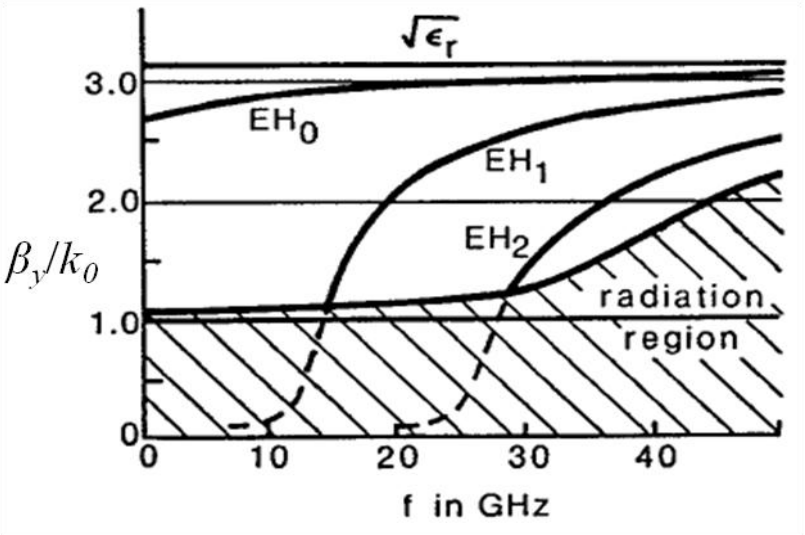

Fig. 3.1.14 Dispersion in a microstrip line (substrate with ε_r = 9.8). The solid lines represent real wavenumbers, whereas the dashed lines correspond to the real part of the leaky mode (complex) wavenumber in the leakage regime (Fig. 1 in [Oliner 1986-I]).

The dispersion properties of microstrip line higher modes have been the object of study over the past decades. In particular, the radiation of the first higher order mode has attracted much attention, the first attempts to achieve a microstrip LWA were proposed in [Ermert 1979] and [Menzel 1979]. However, it was not until 1986 that Oliner and Lee explained in detail their radiation mechanism [Oliner 1986-I and II, 1987] and [Lee 1986]. The first higher order mode, named EH_1, has an associated cutoff frequency from which it starts propagating along the *y* axis of the structure. In contrast to the fundamental EH_0 mode, the EH_1 mode has a cutoff frequency and enters the fast-wave regime. Thus, there is a frequency regime in which the phase constant associated to EH_1 is lower than k_0 (see Fig. 3.1.6), and therefore, as the condition (3.1.6) is satisfied, some power may be leaked at some angle which changes with frequency in the form of a space wave [Oliner 1986-I]. The transverse near field profile associated to this mode is shown

in Fig. 3.1.13. In contrast to the previous studied guiding structure of Fig. 3.1.2, the dielectric substrate now considered is long in the *x* axis (see Fig. 3.1.5), and therefore, some energy may be leaked away from the strip in the form of a surface wave on the dielectric layer outside of the strip region [Oliner 1986-I]. Although the modal field propagates along the *y* axis, there may be leakage into the surface wave, which propagates away on both sides of the printed dielectric substrate, which phase constant is k_s and satisfies

$$k_x = \sqrt{k_s^2 - k_y^2} \tag{3.1.31}$$

This equation makes clear that the condition for actual leakage to the surface wave is $k_x > 0$, or equivalently:

$$k_y < k_s \tag{3.1.32}$$

The radiation region highlighted in Fig. 3.1.14 considers the above two forms of leakage: the one produced in the form of a space-wave when $k_y < k_0$, and the one produced in the form of a surface wave when $k_y < k_s$. Therefore, the dashed lines which appear in this region in Fig. 3.1.14 correspond to complex solutions, and only the real part is plotted. Outside the radiation region, the mode is purely bound, and it decays both in the *x* and *z* axis.

By means of this example, it can be now concluded that the fundamental mode of a uniform microstrip line is a slow-wave that does not radiate. Antennas conceived from this media are normally based in the radiation of the first higher order mode. However, as it was proposed in [Grbic 2002], the fundamental mode of a coplanar waveguide can be turned into a fast-wave by periodically loading it with series capacitances.

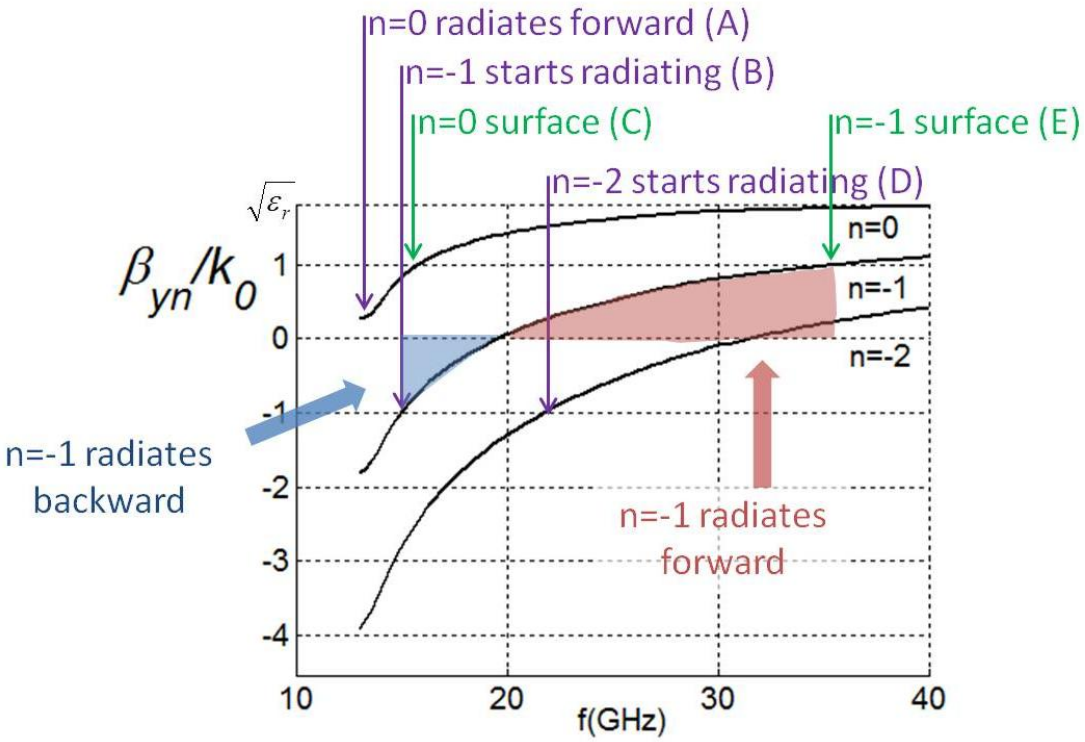

Fig. 3.1.16 Dispersion in periodic microstrip LWA (substrate with permittivity ε_r).

The previous antenna serves as well as an example of **periodic LWA** where, due to periodicity, an infinite number of space harmonics are excited [Walter 1965], [Oliner 1993]. This is also the case of the LWA shown in Fig.3.1.1(b), were the rectangular waveguide is periodically perforated by holes. When dealing with a periodic LWA, the leaky modes consist of an infinite number of Floquet harmonics, which wavenumber is $k_{y,n} = \beta_{y,n} - j\alpha_y$. The relation between the harmonics phase constants is

$$\frac{\beta_{y,n}}{k_0} = \frac{\beta_{y,0}}{k_0} + n\frac{\lambda_0}{P} \tag{3.1.33}$$

where n is an integer number, $\beta_{y,0}$ is the phase constant associated to the n=0 fundamental harmonic and P is the LWA periodicity. An example of the dispersion in periodic LWAs is shown in Fig. 3.1.15, where it has been plotted the phase constant associated to the n=0, n=-1 and n=-2 harmonics versus frequency. In this figure it is marked the frequencies at which each harmonic starts radiating (where $\beta_{y,n}/k_0 > -1$, points A, B and D), and the frequencies at which they become surface waves ($\beta_{y,n}/k_0 > 1$, points C and E). The first aspect that should be now

highlighted is that, in contrast to the previous examples of non-periodic LWAs, backward radiation can be now produced by the harmonics with n<0, due to the fact that they present a negative phase constant during a certain frequency range (as it has been marked in Fig. 3.1.16 in the case of the n=-1 harmonic). Thus, LWAs based in the radiation of the negative higher order harmonics can scan from backward to forward angles. Another relevant aspect is that radiation from more than one harmonic can be produced at certain frequencies (for example, n=0 and n=-1 radiate at different angles in the range [B,C]); appearing the so called grating lobes regimes (which were observed from another perspective in Section 2.4). Single radiation from the fundamental harmonic can be assured if the radiation of the n=-1 harmonic starts at a frequency higher than the one at which the n=0 harmonic becomes a surface wave (i.e., if B occurs at higher frequency than C). The proximity between the dispersion curves may be controlled by changing the value of P. Therefore, single radiation from the fundamental harmonic can be obtained if it is satisfied that

$$\frac{\beta_{y,-1}}{k_0} = \frac{\beta_0}{k_0} - \frac{\lambda_0}{P} = 1 - \frac{\lambda_0}{P} < -1 \Rightarrow P < \frac{\lambda_0}{2} \tag{3.1.34}$$

In the case of periodic LWAs, it is highly important to properly design the structure considering conditions such as the previous one. In this way, the overlap between the radiating space harmonic and the rest of them is avoided, and it is assured that no energy will be leaked to undesired angles.

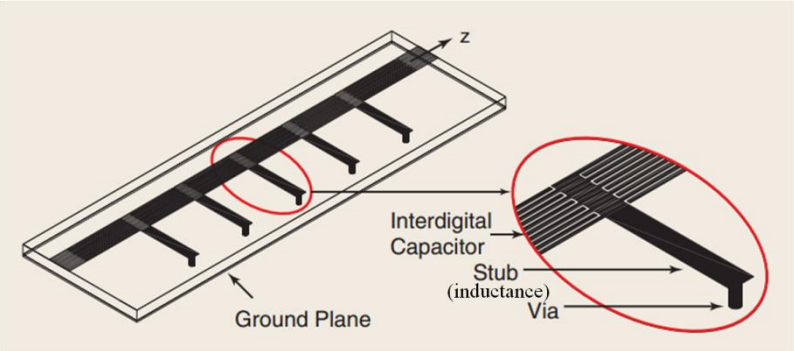

Fig. 3.1.17 CRLH microstrip line.

The fundamental harmonic of a LWA may also present a negative phase constant if it propagates along a media with simultaneously negative permittivity

and permeability ($\varepsilon < 0$ and $\mu < 0$, first described in [Veselago 1986]). This type of material is denoted as "Left-Handed" (LH), due to the fact that the electric field, magnetic field, and phase vectors build a left-handed triad, instead of the regular right-handed ("RH") one which materials in nature present. This LH materials are not readily available in nature, but effectively homogenous structures composed of a combination of discrete unit cells (whose size is much smaller than the guided wavelength at the frequencies of interest) were firstly proposed in [Caloz 2005] and [Eleftheriades 2005], been named Composite Right Left Handed (CRLH) materials or "**metamaterials**". In contrast to the previous periodic structures which used the -1 space harmonic to radiate from backfire towards the endfire directions as a function of frequency, LWAs which employ CRLH media allow their fundamental guided mode to perform that scanning, including radiation at broadside [Liu 2002] from a single leaky-wave propagation. CRLH LWAs are based on the periodic loading of a host transmission line with series capacitances (C_s) and parallel inductances (L_p). Figure 3.1.16 shows the case of a CRLH microstrip LWA. Typical CRLH leaky guides are microstrip lines [Liu 2002], [Lim 2004], coplanar waveguides [Grbic 2002], coplanar striplines [Antoniades 2008]... These concept may easily be extended in order to achieve a 2D CRLH LWAs [Oliner 2007], [Caloz 2011], one interesting example is the metallo-dielectric surface of the mushroom-type [Sievenpiper 1999], [Sievenpiper 2002]. An example of the dispersion of the first mode in a CRLH microstrip LWA is shown in Fig. 3.1.18. In coherence with the previous explanation, the fundamental harmonic presents both a LH and RH regimes, in which it radiates to backward and forward directions, respectively (see Fig. 3.1.18).

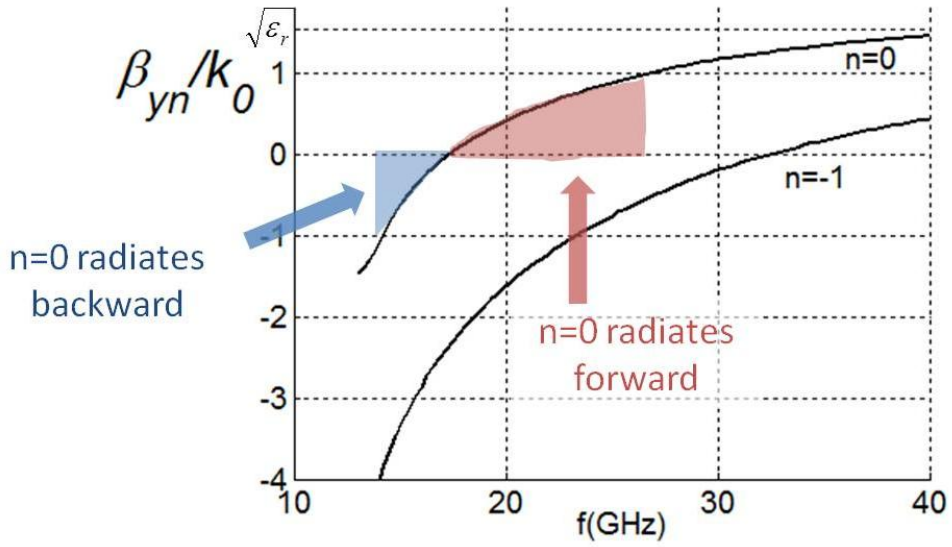

Fig. 3.1.18 Dispersion in a microstrip CRLH LWA (substrate with permittivity ε_r).

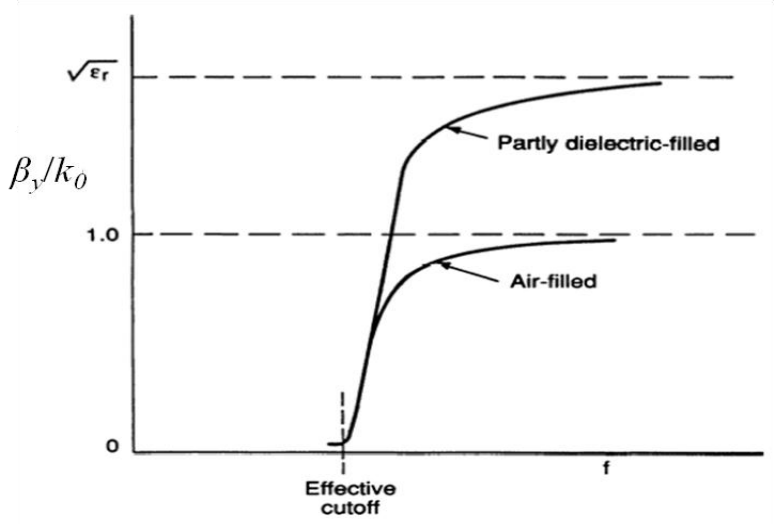

Fig. 3.1.19 Dispersion in a rectangular waveguide LWA (Fig. 11.3 in [Oliner 1993]).

Finally, the particular case of the dispersion in **empty guides** is studied by means of the example of rectangular waveguides**.** The case of the LWA shown in Fig. 3.1.1(a) is now considered. In contrast to the previously considered quasi-TEM lines, the fundamental mode in this waveguides is already dynamic. Figure 3.1.18 shows the dispersion diagrams of the fundamental mode in generic empty and dielectric-filled rectangular LWAs. As Fig. 3.1.19 shows, when the waveguide is air-filled, as the frequency is increased the normalized phase constant tends to one, but never reaching this value. Therefore, it can be concluded that in LWAs based in a conventional empty waveguide, the leaky wave never reaches the surface wave regime.

3.1.4 LWA radiation mechanisms

Depending on the application, the technology and the source polarization, LWAs are based on different radiation mechanisms. The main ones are now described, considering the case of 1D LWAs based on one-dimensional cavities perturbed on one side. Four types can be distinguished: radiation by asymmetry, proximity, periodicity and transparency. Some of them can also be found in 2D LWAs.

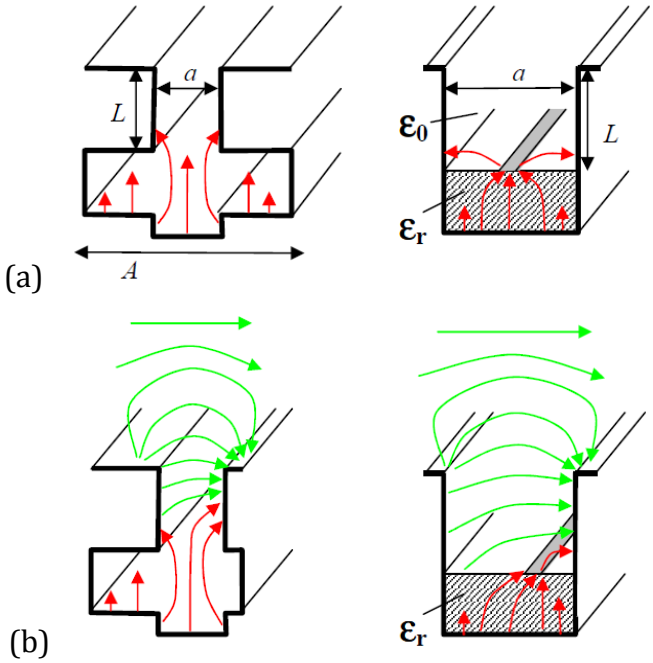

Fig. 3.1.20 Groove waveguide and printed-circuit stub-loaded waveguide fed by a vertical electric field. (a) Symmetric ,(b) asymmetric structure. (Fig. 3.16 in [Gómez 2005-II]).

As it is explained in [Schwering 1988] and [Oliner 1993], open waveguides fed by a source which electric field is aligned with the long Parallel Plate Waveguide (PPW) that connects the cavity with the radiating aperture (such as the ones shown in Fig. 3.1.20(a)) are normally non radiative. This is due to the fact that the modes generated are confined inside the cavity and do not propagate along the PPW towards the radiating aperture. However, by adding any asymmetric perturbation, radiation can be produced thanks to the horizontal electric field induced between the parallel plates (as Fig. 3.1.20(b) shows). Thus, in this case, leakage is controlled by the degree of asymmetry of the structure. Many examples of LWAs which **radiate by asymmetry** can be found in the literature. Hollow

waveguides designs were proposed in the form of groove guides [Lampariello 1985, 1987], [Ma 1987], slitted asymmetric ridge waveguides [Frezza 1994], stub loaded rectangular waveguides [Lampariello 1998] and stepped rectangular waveguides [Di Nallo 1995]. Examples of LWAs which use non-radiative dielectric guide (NRD) technology can also be found in [Oliner 1985], [Malherbe 1988], [Ma 1993], [Xu 1998], [Lee 2000]. More recently, radiation by asymmetry in hybrid technology was proposed in [Gómez 2005-II], where waveguides were combined with printed circuits.

In the previous cases, **radiation by proximity** can be produced (in the absence of asymmetry) if the parallel plates that connect the antenna cavity with the radiating aperture are short enough. The structure of Fig. 3.1.21 is an example of how a NRD guide can produce radiation without asymmetry, showing that leakage can be controlled by distance *d*. When *d* is small, the fields have not decayed to negligible values at the upper radiating end, and, therefore, some power is induced in the radiating aperture and it is leaked away. Some interesting examples of this mechanism can be found in [Yoneyama 1981], [Sánchez 1987], [Gómez 2005-II and 2008].

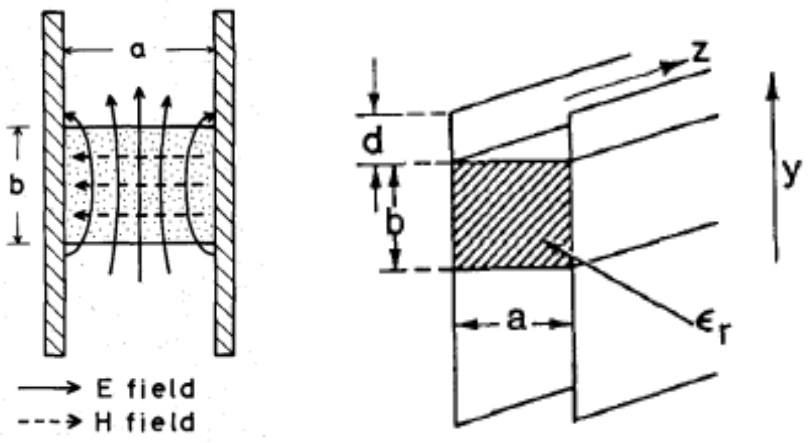

Fig. 3.1.21 Scheme of NRD waveguide where the leakage is controlled by distance *d*. (Fig. 4 in [Yoneyama 1981] and Fig. 2(a) in [Sánchez 1987]).

If the waveguide is fed by a horizontal electric field (perpendicular to the PPW) no asymmetry or proximity is needed for radiation to be produced. In this case, if the antenna is periodic (the value of the period is greater or comparable to

the wavelength) and the radiation is originated by the n=-1 Floquet harmonic, it is said that **radiation is produced by periodicity**. Two examples are depicted in Fig. 3.1.22, a dielectric grating LWA proposed in [Schwering 1983] and metal-strip-loaded inset LWA proposed in [Guglielmi 1991]. In these antennas, the leakage is not controlled by the value of the periodicity, but by the length of the perturbation inside a period (variable Q/P in Fig. 3.1.22). An early and interesting example where the radiation is produced by a sinusoidal periodicity can be found in [Oliner 1959].

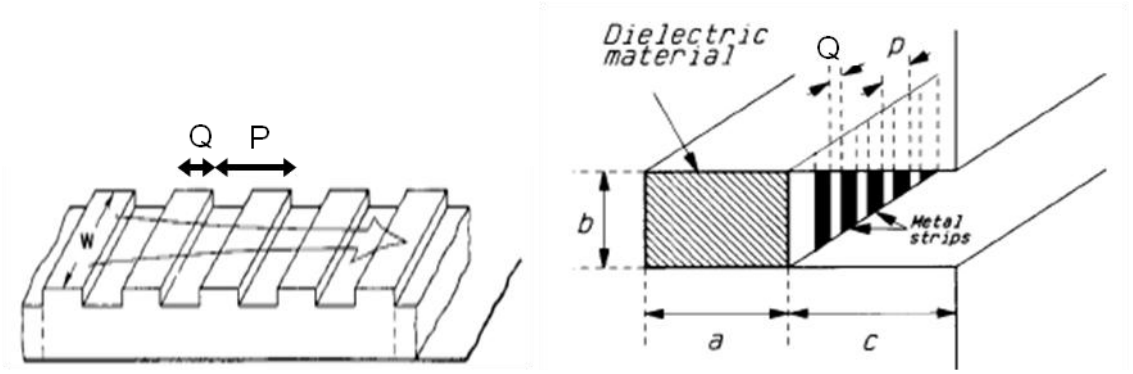

(a) (b)

Fig. 3.1.22 (a)Dielectric grating LWA (Fig. 12 in [Schwering 1983]. (b)Metal-strip-loaded dielectric inset LWA (Fig. 1 in [Guglielmi 1991]).

A different scenario is found when the electric field is perpendicular to the PPW but the perturbation in the waveguide is uniform or quasi-uniform (value of the periodicity much smaller than the wavelength). In this case, the fundamental mode is responsible for **radiation and it is produced due to the transparency** of the radiating aperture. The perturbed face of the waveguide that allows leakage can also be named as Partially Reflective Surface (PRS) due to its capability to control, with its reflectivity, the amount of energy which is leaked to free space. A clear example of these antennas is the slitted LWA proposed in [Hansen 1940], which was depicted in Fig. 3.1.1(a). The LWAs studied in this dissertation base their radiation in the transparency of a PRS, as it will be explained in the next section.

3.2 Description and analysis of novel 1D FP LWA

In this section it is proposed an original one-dimensional (1D) LWA which configuration is shown in Fig. 3.2.1(a), together with its main geometrical parameters. As it can be seen, the structure consists of a cavity backed parallel-plate waveguide (PPW) which is loaded with two printed circuit boards (PCBs) separated by distance *H*. Each PCB is formed from a periodic array of metallic dipoles. The cavity height *H* determines the operating frequency of the antenna; as in this case *H* = 11 mm, the antenna will operate around 15 GHz, which satisfies the resonance condition of the cavity: $H = \lambda_0/2 = c/(2f)$ [Trentini 1956]. The top PCB acts as a **Partially Reflective Surface** (PRS, [Trentini 1956]); with its transparency it controls de amount of energy which is leaked from the cavity to free space. Therefore, the PRS allows the modes of the cavity become leaky-waves, and determines the amount of energy that reaches the top aperture of the LWA. A metal-backed dipole-based FSS has been placed at the bottom of the antenna, acting as a **High Impedance Surface** (HIS). In this 1D LWA, the HIS strongly affects the dispersion of the leaky modes that propagate through the cavity.

This type of antennas is often referred to as Fabry-Perot (FP) cavity LWA due to its analogy with optical resonant cavities. The electromagnetic waves that arise from the feeding point are bounced back and forth between the two sheets, becoming leaky-modes of the guiding structure. Thus, highly directive radiation patterns are provided from a single low-directive source embedded inside the FP

cavity. This makes FP LWAs become a very attractive solution when compared to externally fed antenna systems (such as reflector, lenses or reflectarrays), and also when compared to arrays, which need much more complicated feeding networks. Two-dimensional PRS cavities were firstly introduced by von Trentini [Trentini 1956], and more recently, it was proposed to replace the bottom metallic screen by a High Impedance Surface (HIS) to reduce the cavity height [Feresidis 2001 and 2005]. An excellent review on these antennas can be found in [Jackson 2011].

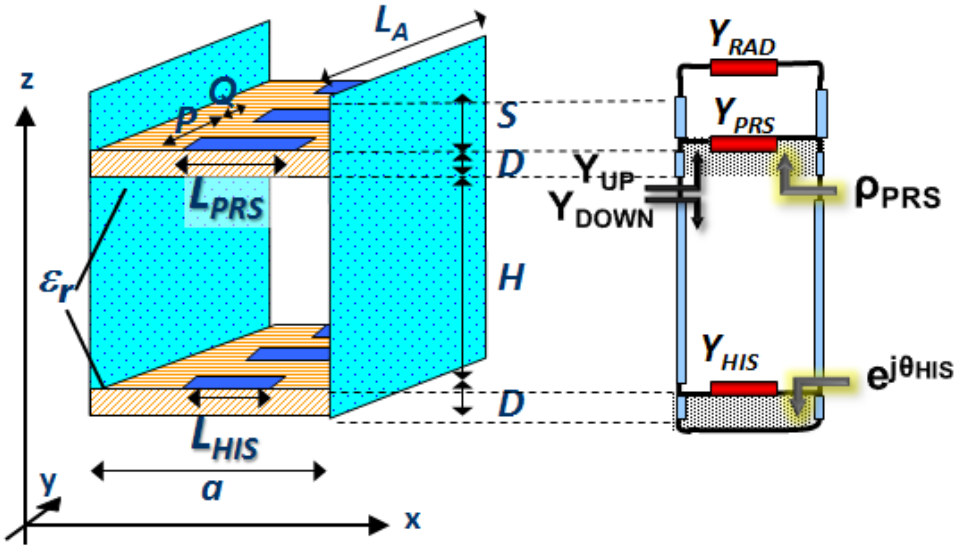

(a) (b)

Fig. 3.2.1 (a) Configuration of the proposed 1D FP LWA (b) Transverse Equivalent Network of the structure (a = H = 11 mm, S = 5 mm, D = 1.13 mm, ϵ_r = 2.2, L_{PRS} = 9 mm, L_{HIS} = 9 mm, P = 1.5 mm, Q = 0.5 mm).

A careful study of the natural modes in the LWA has been performed using a specific full-wave Method of Moments technique [Gómez 2006-II]. The leaky-mode dispersion results for the case L_{PRS} = L_{HIS} = 10 mm are plotted in Fig. 3.2.2. From this study, it can be concluded that three different modes are present in the present structure: the horizontally polarized channel-guide mode supported by the PPW (mode 1 in Fig. 3.2.2), and the perturbed horizontal TE_{01} and vertical TE_{10} modes of the cavity (modes 2 and 3 in Fig. 3.2.2). In the operating band (15 GHz), only modes 2 and 3 are in the fast-wave regime, while mode 1 is a nonradiative slow-wave [Oliner 1993]. Due to the symmetry of the structure, the vertically polarized mode 3 does not leak power to free space [Gómez 2006-II]. Also, single mode operation is assured by using a horizontally polarized feeding, as it is

explained at the end of this section. As a result, the proposed LWA operates with the perturbed TE_{10} leaky-mode (directed along the *x* axis in Fig. 3.2.1) in the operating frequency band. The elevation radiation angle θ_{RAD} is defined in the H-plane (*zy* plane in Fig. 3.2.1) and it is measured with respect to the *z*-axis. Thus, the dispersion characteristics are calculated considering TE polarization in the *zy* plane.

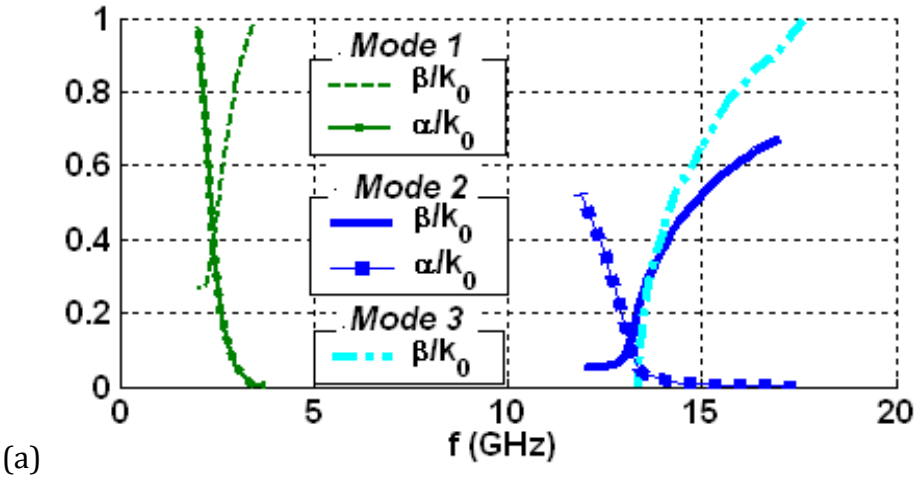

(a)

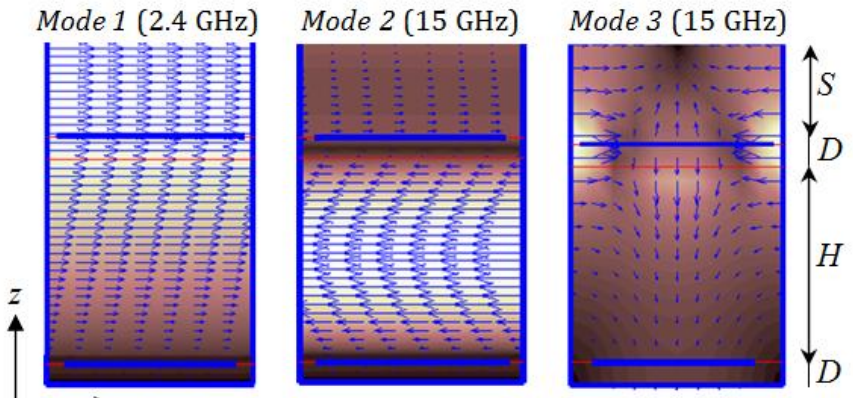

(b)

Fig. 3.2.2. (a) Dispersion of natural modes in the LWA (L_{PRS} = L_{HIS} = 10 mm) (b) Transverse electric fields in the cross-section of the LWA for each mode.

The dispersion of the TE_{01} leaky-mode in this 1D LWA can be analyzed with the software tool developed in the frame of this dissertation, and explained in Section 2.3. The proposed tool is based on the LWA Transverse Equivalent Network (TEN) shown in Fig. 1(b). As it is explained in Section 2.3, the complex propagation constant k_y (3.1.1) is obtained by solving the following Transverse Resonance Equation (TRE) associated to the TEN:

$$Y_{UP}(f, k_y, L_{PRS}) + Y_{DOWN}(f, k_y, L_{HIS}) = 0 \quad (3.2.1)$$

In the TEN, the PRS and HIS printed circuits are modeled by equivalent admittances, $Y_{PRS}(f, k_y, L_{PRS})$ and $Y_{HIS}(f, k_y, L_{HIS})$, which can be obtained employing pole-zero expansions, as described in Section 2.3. This enables one to efficiently obtain the dispersion curves of the TE leaky-mode as a function of frequency and the length of the PRS and HIS dipoles [L_{PRS} and L_{HIS}, see Fig. 1(a)]. In the next subsections, the effect of L_{PRS} and L_{HIS} on the pointing angle θ_{RAD} and normalized radiation rate α_y/k_0 is studied. All the leaky-wave dispersion results are obtained from this simple TEN, and they are validated with a Finite Element Method (FEM) full-wave simulator [HFSS 2011].

3.2.1 *Effect of the top PRS dipole length (L_{PRS})*

The transparency of the PRS determines the amount of energy that reaches the top aperture of the LWA, thus controlling the leakage rate. Figure 3.2.3 shows the leaky-mode frequency dispersion curves for different lengths of the PRS dipoles (the other dimensions of the LWA are summarized in the caption of Fig. 3.2.1). From Fig. 3.2.3, it is observed that L_{PRS} has a minimal effect on the pointing angle dispersion curves (θ_{RAD}), but it has a strong influence on the leay-mode normalized leakage curves (α_y/k_0). It is also shown that the analytical results agree well with the simulated ones using FEM shown in circles in the figure.

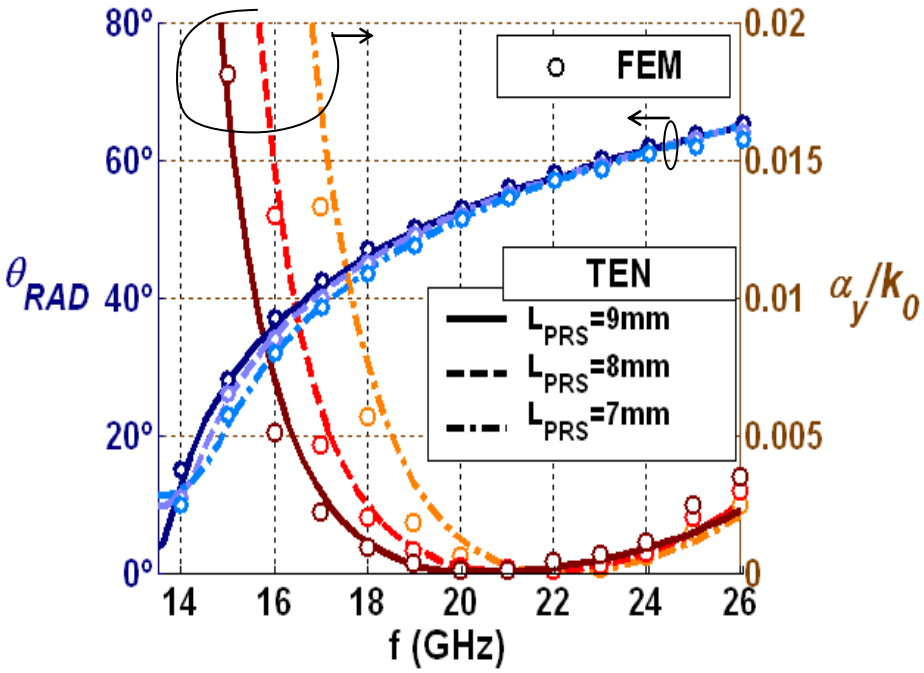

Fig. 3.2.3. Leaky-mode frequency dispersion curves for the LWA in Fig. 3.2.1 for different values of L_{PRS} (L_{HIS} = 9 mm)

At this point, it is worth noting that the frequency dispersion curves associated to this structure, which are of the form of the ones shown in Fig. 3.2.3, might seem unconventional at first sight. Figure 3.2.4(a) shows the well-known dispersion diagram of a conventional LWA, which can be compared to Fig. 3.2.4(b) which shows one particular case of our 1D PRS-HIS-LWA (L_{PRS} = 10 mm and L_{HIS} = 9 mm). As Fig. 3.2.4(b) shows, the cutoff frequency is located at 13.1GHz (β_y=α_y); as the frequency increases, the phase constant (β_y) increases and the leakage rate (α_y) decreases (this is equal to the conventional behavior due to the inherent dispersion nature of leaky-waves [Oliner 1993]).

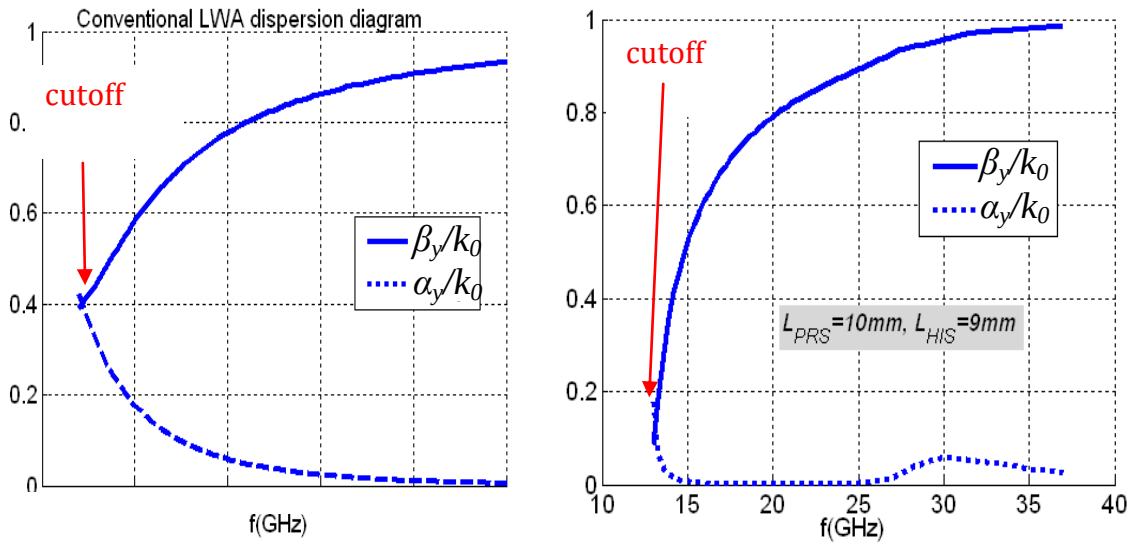

(a) (b)

Fig. 3.2.4. Dispersion curves of (a) conventional LWA (b) 1D PRS HIS LWA (L_{PRS} = 10 mm and L_{HIS} =9 mm).

The peculiar behavior of this LWA is found near 20 GHz, where the radiation rate becomes zero (α_y = 0), although the bounded regime hasn't been reached yet (it can be seen that $\beta_y/k_0 < 1$ and the pointing angle $\theta_{RAD} = asin(\beta_y/k_0) < 90^o$). For higher frequencies, the radiation rate increases for a while up to 30GHz. From 30 GHz α_y starts decreasing again until it becomes zero when $\beta_y/k_0 = 1$ (as it happens in the conventional case of Fig. 3.2.4(a), due to the approaching of the bounded region). It is important to highlight that the "same" leaky wave (same β_y and same α_y) is never found at two different frequencies. However, several leaky-mode solutions with the same radiation rate α_y but different phase constant β_y can exist, for example at 13.5 GHz, 27 GHz and 36GHz in Fig. 3.2.4(b).

The physics underlying this non conventional behavior of the radiation rate is related to the resonant nature of the top partially reflective surface (PRS). In particular, the null radiation frequency is found when the dipoles at the PRS resonate. This feature is illustrated in Fig. 3.2.5, where four different configurations of the proposed LWA (L_{PRS} = 4, 6, 8 and 10 mm, with L_{HIS} = 9 mm) have been analyzed. In addition, the 1D LWA has also been analyzed replacing the dipoles in the top PRS by a metallic plate (PEC) (with L_{HIS} = 9 mm). Figure 3.2.5(a) shows the reflection coefficient under the PRS (ρ_{PRS}, see Fig. 3.2.1(a)) associated to

each of the studied configurations, while Fig. 3.2.5(b) shows the frequency dispersion diagram. When the dipoles in the PRS resonate, this surface behaves as a PEC and $|\rho_{PRS}| = 1$. Therefore, for each of the studied cases the resonant frequency is located at the point in which their curves of ρ_{PRS} match the red curve in Fig. 3.2.5 (and thus, $|\rho_{PRS}| = 1$ is satisfied). Consequently, at these exact frequencies, the β_y/k_0 curves associated to each case match the red curve in Fig. 3.2.5, and $\alpha_y = 0$.

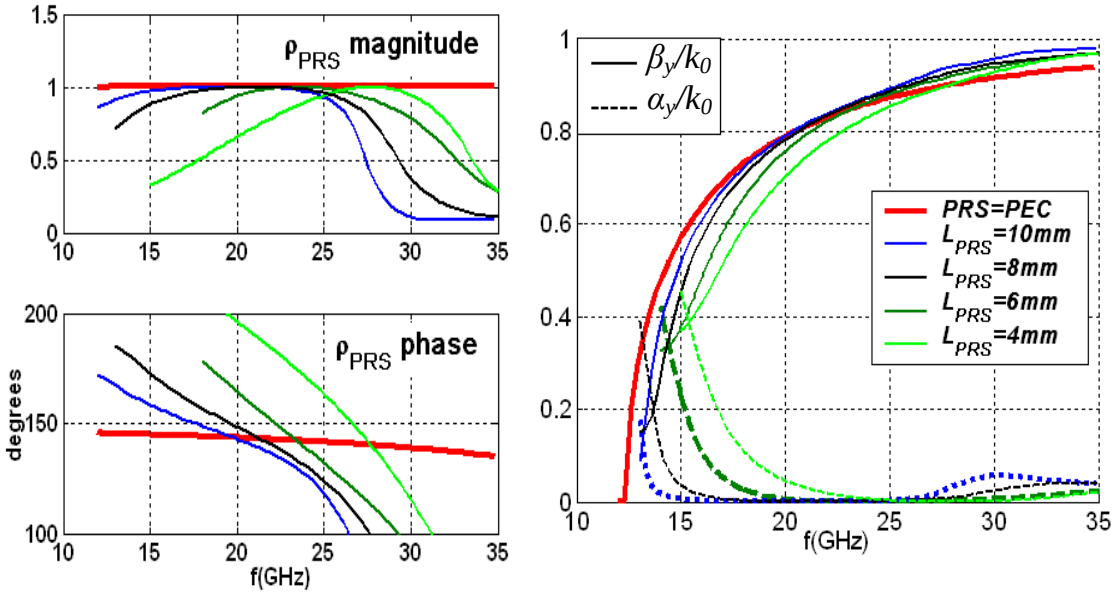

(a) (b)

Fig. 3.2.5. Dispersion curves of (a) conventional LWA (b) 1D PRS HIS LWA (L_{PRS} = 10 mm and L_{HIS} = 9 mm).

Therefore, it can be concluded that the PRS dipoles strongly affect the leakage rate of the modes in the proposed LWA. Thus, this feature can be applied to the control of the radiation rate of the LWA for a given design frequency. At a fixed frequency and according to the bouncing ray model for waveguide propagation [Pozar 2005], the PRS reflectivity experienced by the incident wave [ρ_{PRS} in Fig. 3.2.1(b)] is a function of the length of its resonant dipoles (L_{PRS}) [Feresidis 2001], as shown in Fig. 3.2.6(a) where the frequency is chosen as 15 GHz. The leaky-mode dispersion curves with L_{PRS} at 15 GHz are shown in Fig. 3.2.6(b). As can be seen in Fig. 3.2.6, the PRS dipoles resonate when L_{PRS} = 11 mm, being approximately half a wavelength at 15 GHz. At this length, the PRS behaves as a totally reflective sheet ($|\rho_{PRS} = 1|$), a FSS resonance occurs [Goussetis 2006-I]

and the leakage rate vanishes ($\alpha_y/k_0 = 0$). When L_{PRS} is decreased from 11 mm, the PRS becomes more transparent to the incident wave, thus leading to a progressive increase of the radiation rate.

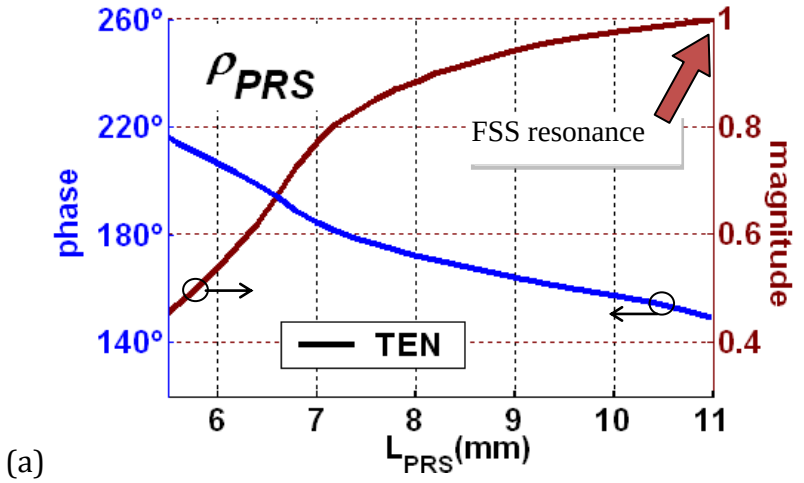

(a)

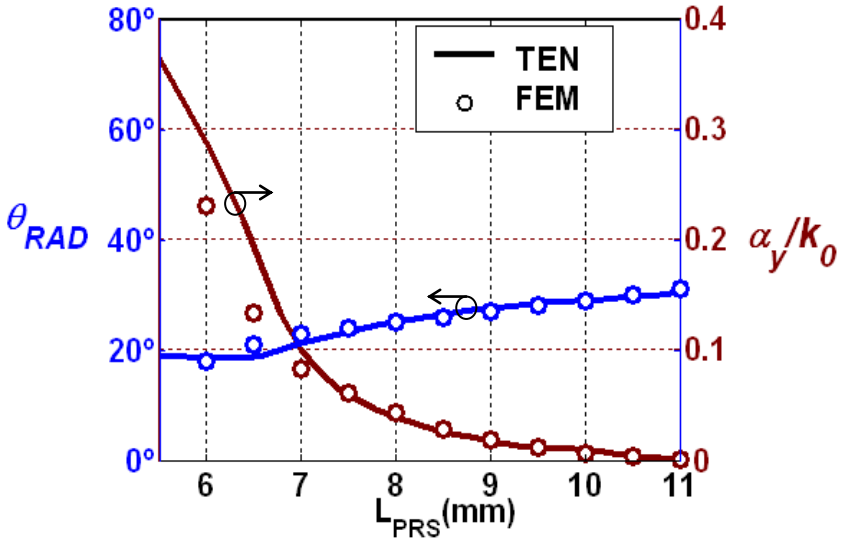

(b)

Fig. 3.2.6. Leaky-mode frequency dispersion curves for the LWA in Fig. 3.2.1 for different values of L_{PRS} (L_{HIS} = 9 mm).

This phenomenon is also illustrated in Fig. 3.2.7, where the leaky-mode electric field inside the LWA is plotted for different values of L_{PRS}. It is seen that as L_{PRS} is reduced from 11 mm, more energy illuminates the top aperture of the antenna, thus increasing the leakage level. Consequently, the possibility of controlling the radiation rate by varying the PRS dipoles length is verified. Yet, when L_{PRS} is varied, a second order effect occurs: the pointing angle θ_{RAD} is also

altered to some extent as shown in Fig. 3.2.6(b). This deviation is due to the dependence of θ_{RAD} on the phase of ρ_{PRS}, which also varies with L_{PRS} as illustrated in Fig. 3.2.6(a). This issue is addressed in the next sub-section.

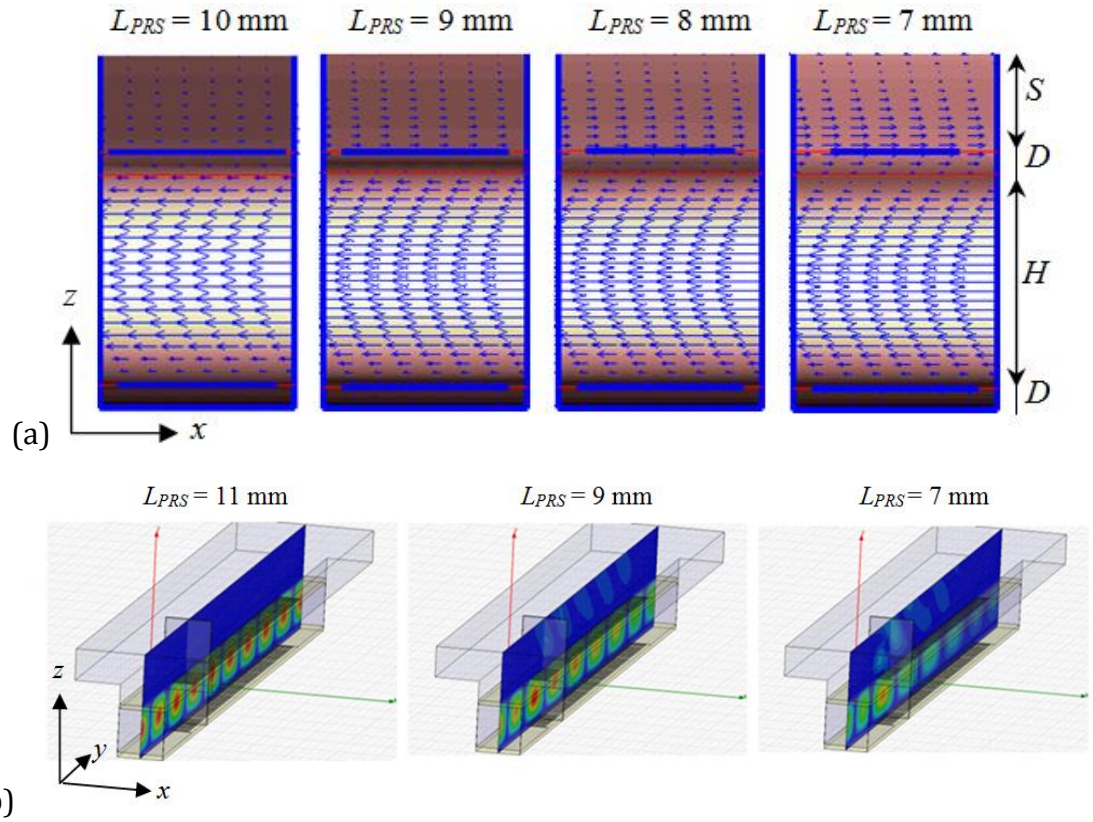

Fig. 3.2.7. Near electric field in the LWA of Fig. 3.2.1 at 15GHz (a) in the transverse plane (*xz*), obtained from the TEN (b) in the longitudinal plane (*yz*) obtained from a FEM-based tool [HFSS 2011].

3.2.2 Effect of the bottom HIS dipoles length (L_{HIS})

As previously mentioned, the bottom of the antenna is loaded with a HIS, which consists of a metal-backed dipole-based FSS. One of the first studies about these electromagnetic surfaces can be found in [Sievenpiper 1999], where it is explained that a HIS presents the interesting feature of exhibiting a variable input impedance. This is equivalent to say that the waves that impinge on a HIS can experience a variable reflection phase. In particular, this impedance varies with frequency, the angle of incidence and also with the geometry of the scatterers. In particular, it is said that the HIS is resonating when it presents a reflection phase of zero degrees, behaving as an Artificial Magnetic Conductor (AMC). This artificial surfaces are often employed for miniaturizing waveguides, due to the fact that they can modify the effective height of the cavity [Feresidis 2005], [Goussetis 2006-I]. In particular, in the 1D LWA under study, the HIS modifies the effective height of the resonant Fabry-Perot cavity formed by the two PCBs and therefore, it strongly affects the frequency dispersion curves of the TE_{01} leaky-mode, thus providing the control over the pointing angle at a fixed frequency. In a bouncing ray model for waveguide propagation, the length of the HIS dipoles (L_{HIS}), determines the reflection phase experienced by the waves propagating inside the waveguide [Feresidis 2005]. Figure 3.2.8(a) and (b) show respectively how L_{HIS} affects the LWA pointing angle and radiation rate, shifting the cutoff frequency from 11 GHz to 15 GHz. For a fixed frequency, the pointing angle is increased and the leakage rate is reduced when the cutoff frequency is decreased (higher effective cavities) [Oliner 1993]. Figure 3.2.8(c) shows the modes dispersion curves with L_{HIS} at the operation frequency of 15 GHz. In this figure it is clear that by changing L_{HIS} it is possible to scan the pointing angle in a wide range.

At this point it worth noting an interest effect that the HIS causes in the dispersion of the leaky modes that propagate along the cavity. As it was explained in Section 3.1.3, leaky modes in empty rectangular waveguides do not reach the surface wave regime (β_y/k_0). However, waveguides can be loaded with engineered surfaces to produce unusual dispersion characteristics [Collin 2000]. For example, in [Yang 1999] a photonic bandgap structure created a quasi-TEM waveguide when inserted inside a metallic rectangular waveguide. Another interesting

example can be found in [Marqués 2002], where left handed propagation inside a waveguide at cutoff was allowed by loading it with split rings. In the case of the 1D LWA under study, the HIS allows the leaky modes reach the surface wave regime inside the empty waveguide, as it can be seen in Fig. 3.2.8(a).

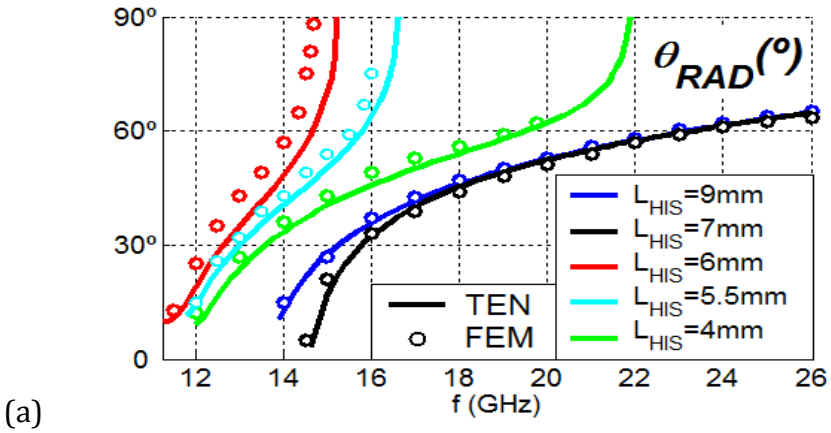

(a)

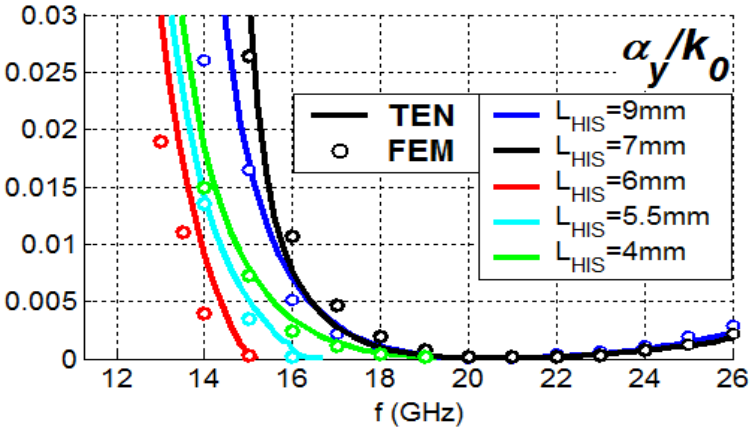

(b)

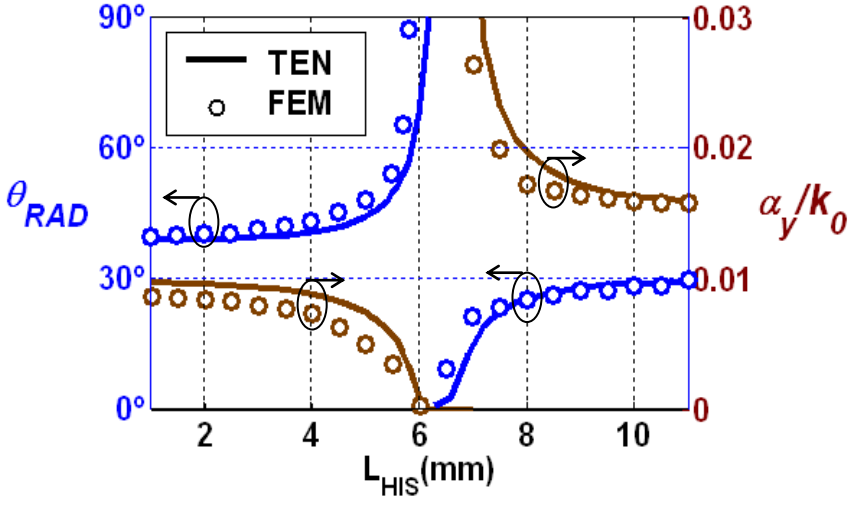

(c)

Fig. 3.2.8. Leaky-mode dispersion curves of the LWA in Fig. 3.2.1(a) for different values of L_{HIS} (L_{PRS} = 9 mm) (a),(b) Dispersion with frequency (c) Dispersion with L_{HIS} at 15 GHz.

In order to understand this effect, Fig. 3.2.9(a) shows the variation of the reflection phase seen by an incoming plane-wave at the HIS interface [θ_{HIS} in Fig. 3.2.1(b)] with L_{HIS} at 15 GHz, while Fig. 3.2.9(b) illustrates the near field patterns inside the LWA. When L_{HIS} = 11 mm (approximately half a wavelength at 15 GHz), a FSS resonance occurs and the HIS behaves as a Perfect Electric Conductor (PEC) [19] [θ_{HIS} = -180º in Fig. 3.2.9(a)], providing a given pointing angle of θ_{RAD} = 30º [see Fig. 3.2.8(b)]. As L_{HIS} is reduced, θ_{HIS} increases, producing a smaller effective resonant cavity [see L_{HIS} = 7 mm in Fig. 3.2.9 (b)], and reducing θ_{RAD} close to broadside [$\theta_{RAD} \approx 0°$ for L_{HIS} = 7 mm in Fig. 3.2.8(b)]. Maximum pointing angle at endfire ($\theta_{RAD} \approx 90°$) is reached for L_{HIS} = 6.1 mm in Fig. 3.2.8(b). When L_{HIS} = 6mm, the HIS provides a Perfect Magnetic Conductor (PMC) resonance [19] [θ_{HIS} = 0º in Fig. 3.2.9(a)]. In this case, the electric field is maximum at the HIS interface [see L_{HIS} = 6 mm in Fig. 3.2.9(b)], producing an effective cavity of double height and pointing angle of $\theta_{RAD} \approx 70°$. Further decrease of L_{HIS} continues increasing θ_{HIS} and reduces both the effective cavity height and the correspondent pointing angle θ_{RAD} [see L_{HIS} = 5.5 mm and 4 mm in Fig. 3.2.8(b) and Fig. 3.2.9].

The effect of L_{HIS} in β_y can be equivalently observed in Fig. 3.2.10, where it is plotted the near field in the longitudinal plane of the LWA. The distance between two consecutive field nulls in the *y* axis corresponds to $\lambda_y/2$, which is related to the longitudinal wavenumber of the leaky wave: $\beta_y = 2\pi/\lambda_y$. Therefore, taking into account the relation between θ_{RAD} and β_y (3.1.4), the evolution of β_y with L_{HIS} observed in Fig. 3.2.10 is coherent with the previous discussion. Therefore, one concludes that the pointing angle of the proposed LWA can be tuned by changing the length of the dipoles in the HIS.

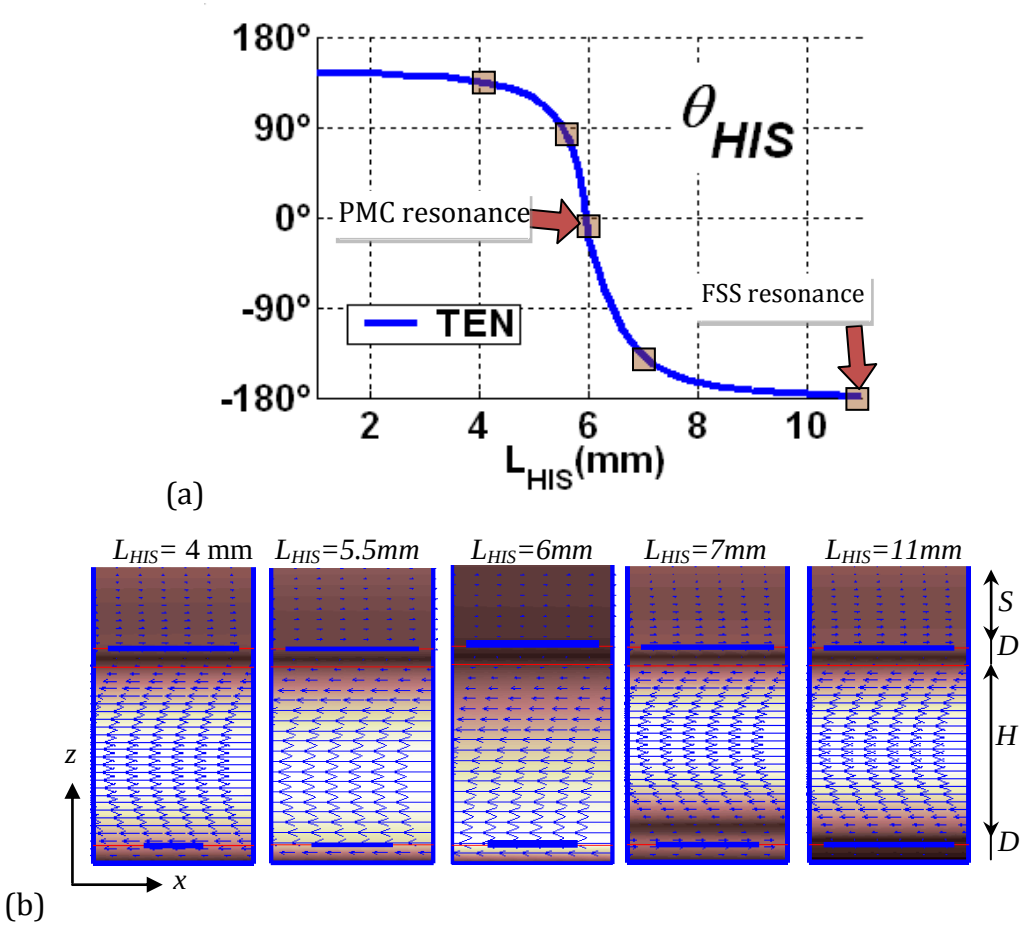

Fig. 3.2.9. Effect of L_{HIS} at 15 GHz (L_{PRS} = 9 mm). (a) Reflection phase seen by the incident leaky-wave at the HIS. (b) Near electric field in the transverse plane of the LWA in Fig. 3.2.1 obtained from the TEN at 15 GHz

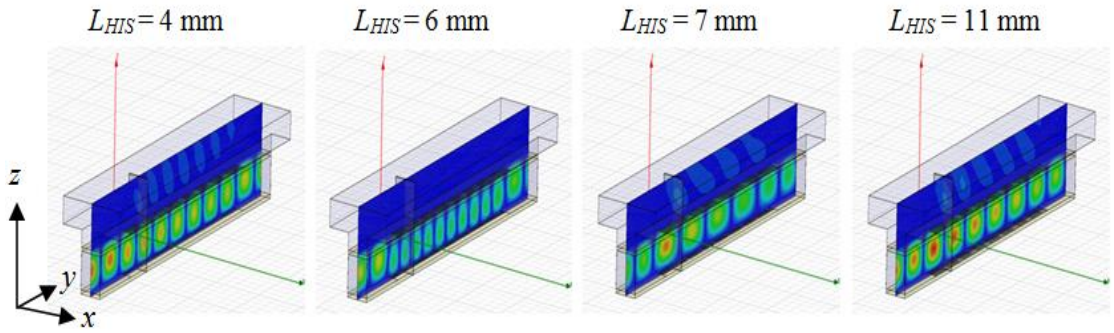

Fig. 3.2.10. Near electric field in the longitudinal plane of the LWA in Fig. 3.2.1 obtained from FEM-based tool [HFSS 2011] at 15 GHz (L_{PRS} = 9 mm).

The modification of the pointing angle also involves the inherent inverse variation in the leaky-mode radiation rate shown in Fig. 3.2.8. It is well known [Oliner 1993] that, as the pointing angle of a leaky-wave is increased, the associated leakage rate decreases. This fact is illustrated in the ray picture of Fig.

3.2.11, where it can be easily understood that higher radiation rates are naturally associated to lower radiation angles because the leaky wave reaches the top radiating surface more times per unit length.

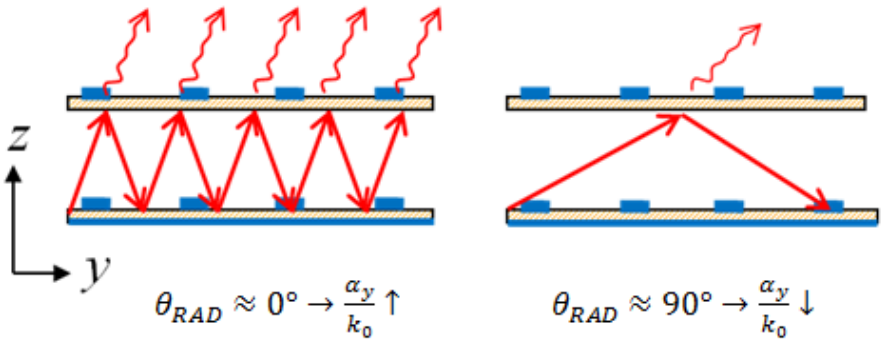

Fig. 3.2.11. General relation between the pointing angle and radiation rate of a leaky-wave.

3.2.3 Feeding and matching of the antenna

The previous results have been obtained considering an ideal feeding of the TE_{01} mode of the cavity created between the PRS and the HIS (see Fig. 3.2.1), and perfect matching at the input and output ports of the LWA. With the perspective of manufacturing the proposed 1D PRS-HIS LWAs, the goal in this section is to design a real feeding device which is capable of exciting the TE_{01} mode of the antenna cavity at the input port. This same device will be connected to the output port serving as a matched load which will absorb the remaining not-radiated energy which reaches the end of the LWA, thus, avoiding reflected radiated lobes [Oliner 1993]. Fig. 3.2.12(a) shows the scheme of this feeding/terminating circuit, which consists of a conventional metallic rectangular cavity with a coaxial probe. A tuning screw is also added to the feeding network in order to improve and readjust the matching. A couple of pictures of the fabricated device are shown in Fig. 3.2.12(b).

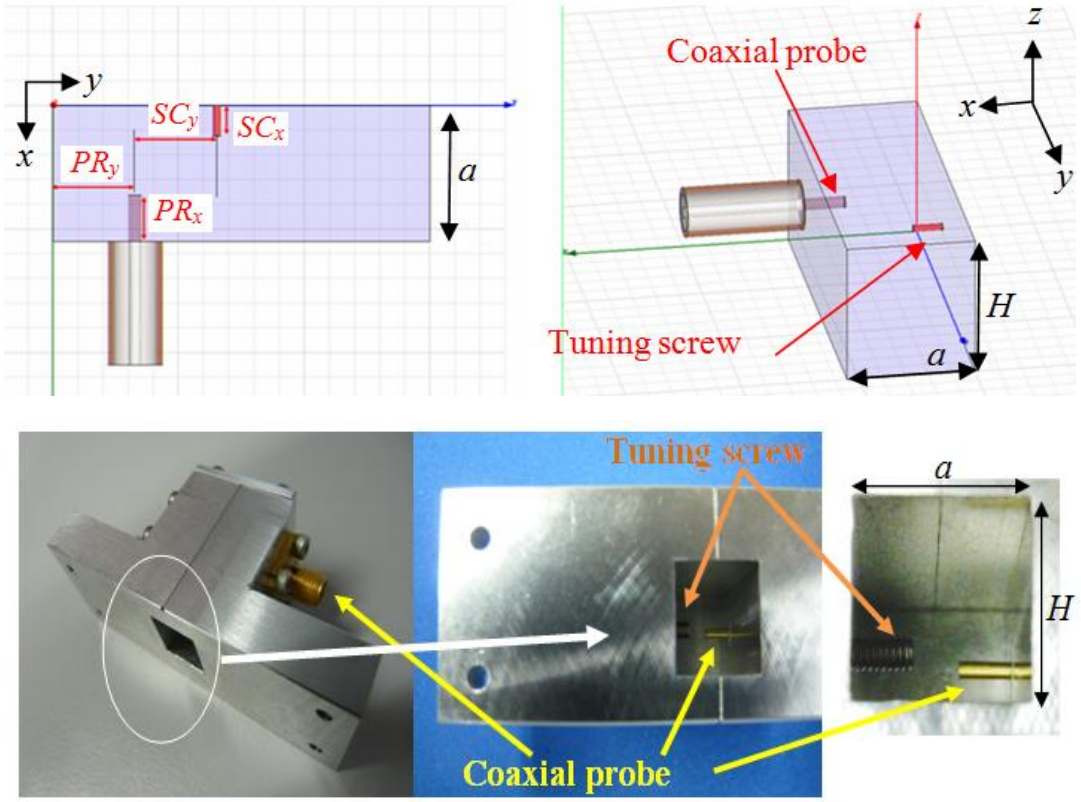

Fig. 3.2.12. Designed coaxial-to-waveguide transition. (a) Scheme. (b) manufactured.

The design of this coaxial-to-waveguide transition has been performed with a FEM-based commercial software tool [HFSS 2011], pursuing a value of the S_{11} parameter below -15 dB at the operation frequency (15 GHz, λ_0 = 20 mm), and below -10 dB at the frequency band [14 GHz – 16 GHz]. With this purpose, a parametric study of the size and the position of the probe and the screw is performed (named as *PRx*, *PRy*, *SCx* and *SCy* in Fig. 3.2.12(a)). The first study was performed without the screw, varying the position of the coaxial probe in the y axis (PR_y) across the range $\lambda_0/4 \pm \lambda_0/8$; the S_{11} parameter obtained is shown in Fig. 3.2.13(a). As this figure shows, the best results are obtained when the probe is positioned at 6.5 mm, providing a value of -4.3 dB for S_{11} at 15 GHz. Once PR_y is fixed to 6.5 mm, the study is next focused on the length of the probe which is inserted into the cavity (PR_x); Fig. 3.2.13(b) shows the values of S_{11} parameter obtained when this parameter is varied between $\lambda_0/8$ and $\lambda_0/2$. A notable matching improvement is observed when PR_x = 3.75 mm, obtaining the pursued value of S_{11} < -15 dB in the frequency band [14 GHz – 16 GHz].

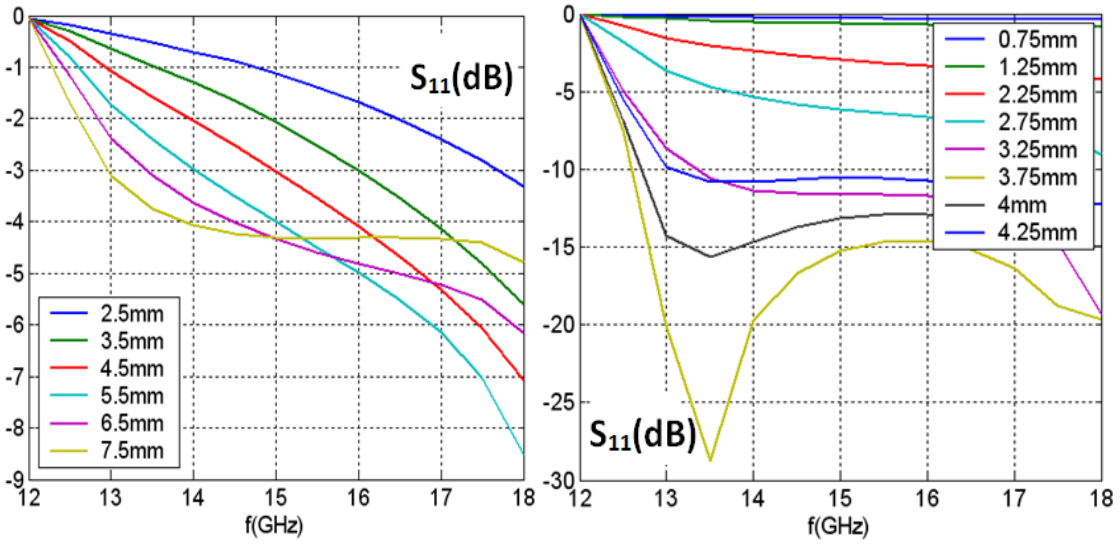

(a) (b)

Fig. 3.2.13 S_{11} parameter of the coaxial-to-waveguide transition without screw (a) Varying the position of the probe in the *y* axis, PR_y. (b) Varying the length of the probe, PR_x.

Although the requirements of the device are already met without the screw (as it can be seen in Fig. 3.2.13(b)), this latter element is added in order to improve the matching at 15GHz. The length of the screw, SC_x is fixed to $\lambda_0/4$, and its position

in the y axis, SC_y, is swept between $\lambda_0/4$ y $\lambda_0/2$ with respect to the probe; the obtained S_{11} parameter is shown in Fig. 3.2.14(a). Once more, it is chosen the value which provides the lower value of S_{11}, in this case SC_y = 7.5 mm. The resulting S parameters of the final designed device are shown in Fig. 3.2.14(b); at the operation frequency (15 GHz) the obtained matching is fairly good (S_{11} = -32.37 dB and S_{21} = -0.04 dB). A summary of the resulting dimensions of the transition is shown in Table 3.2.1.

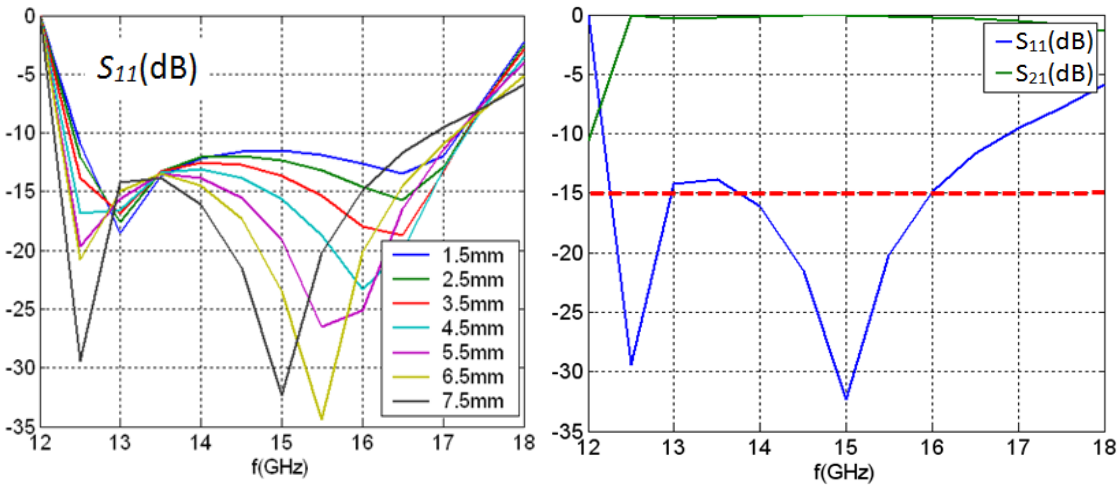

(a) (b)

Fig. 3.2.14. S_{11} parameter of the coaxial-to-waveguide transition with screw (a) varying the position of the screw in the *y* axis (PR_y), (b) final

Dimensions of the transition in Fig. 3.2.12 (f=15GHz, λ_0=20mm)	
a (waveguide width, see Fig. 3.2.1)	11mm
H (waveguide height, see Fig. 3.2.1)	11mm
Probe position *x* axis (***PR$_x$***)	3.75 mm
Probe position *y* axis (***PR$_y$***)	6.5mm(λ_0/4)
Probe position *z* axis	5.5mm(H/2)
Screw position *x* axis (***SC$_x$***)	2.5mm(λ_0/4)
Screw position *y* axis (***SC$_y$***)	14mm
Screw position *z* axis	5.5mm(H/2)
Coaxial, inner conductor radio	0.51mm
Coaxial, outer conductor radio	2.18mm
Coaxial, dielectric radio	1.68mm
Screw diameter	0.3mm

Table. 3.2.1. Dimensions of the designed coaxial-to-waveguide transition.

The electric field generated inside the transition is shown in Fig. 3.2.15(a), where it can be clearly seen that it is efficiently excited the TE_{01} mode of a cavity of dimensions H x a (which are the dimensions of the cavity created between the PRS and the HIS, see Fig. 3.2.1). The electric field at the end of the transition is linearly polarized along the x axis, as desired. The scheme of the complete structure (the LWA with one transition at the input and another one at the output port) is shown in Fig. 3.2.15(b).

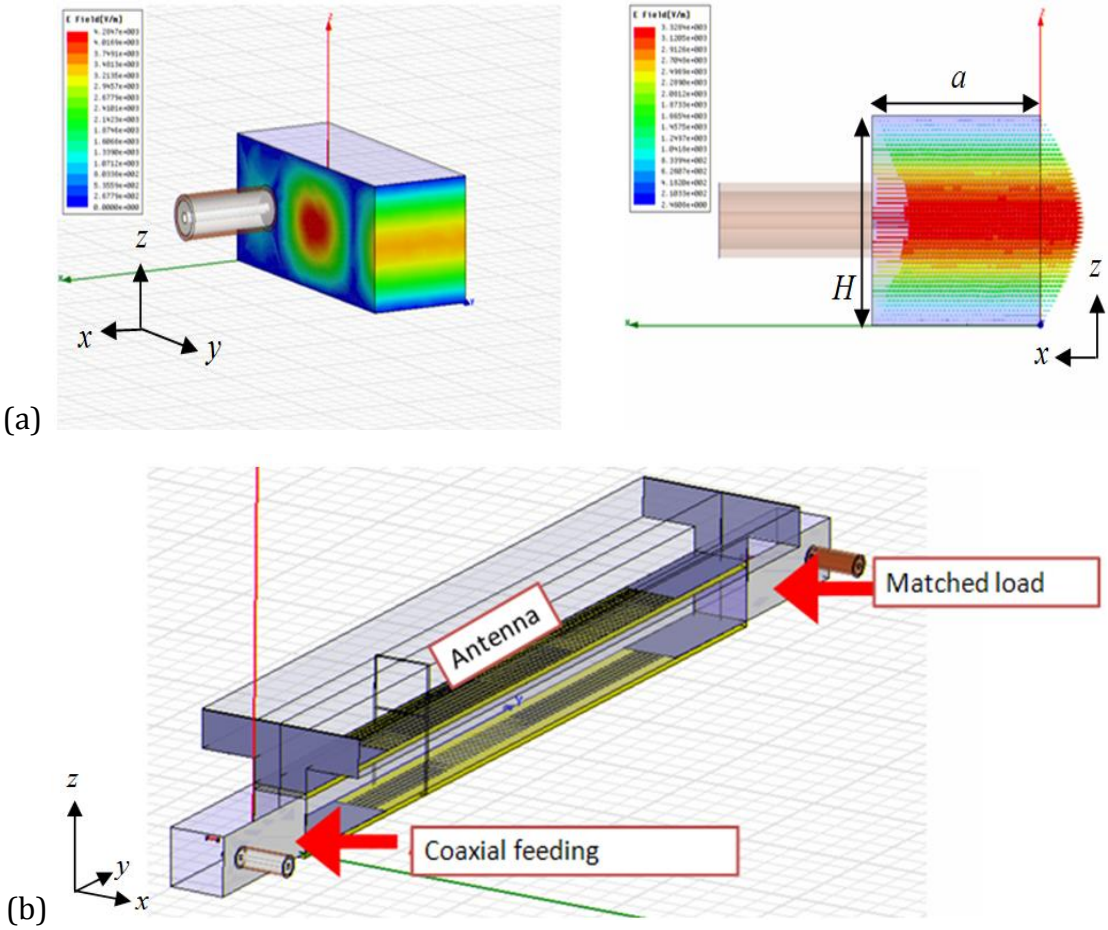

Fig. 3.2.15. (a) Simulated feeding device, generating the TE_{01} mode of the cavity. (b) Scheme of the complete structure.

As it was explained along this section, because of the boundary conditions presented by the PRS and the HIS, the leaky mode that propagates along the antenna is not exactly the TE_{01} mode of the physical H x a cavity. In particular, as it was shown in Fig. 3.2.9(b), the HIS strongly perturbs the cavity mode, and it can be equivalently appreciated by studying the wavelength of the propagating mode in the transverse plane (λ_z, Fig. 3.2.16). The metallic cavity of the feeding/matching

device provides a TE_{01} mode with $\lambda_z = 2H$, marked with a red line in Fig. 3.2.16. However, the value of λ_z inside the antenna radiating cavity may strongly differ from the previous value, depending on the value of L_{HIS}, as Fig. 3.2.16 shows.

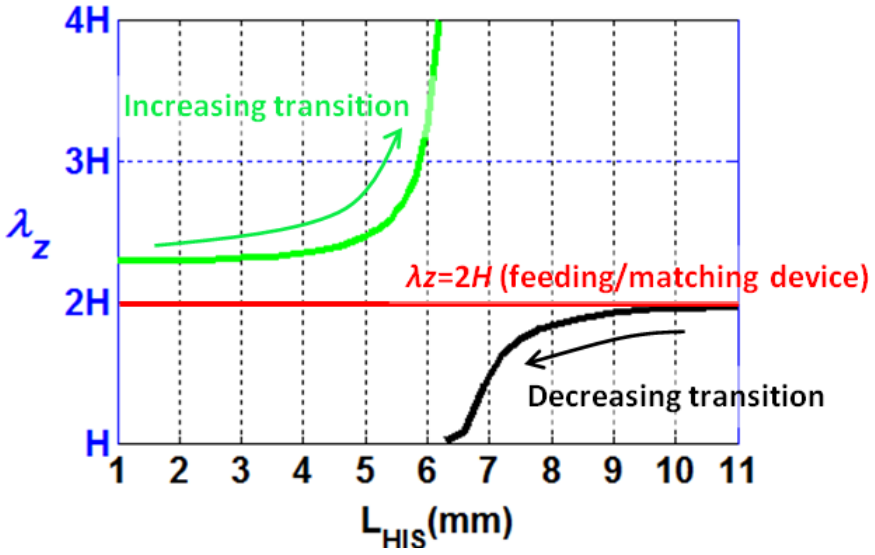

Fig. 3.2.16. Transverse wavenumber λ_z as a function of L_{HIS} at 15 GHz (L_{PRS} = 9mm).

Therefore, there may appear an undesired discontinuity in the connection between the feeding device and the antenna cavity. In order to improve this matching, a tapered transition [Gómez 2005-I] has been added at the bottom printed circuit, before and after the HIS, as depicted in Fig. 3.2.17. With this taper, the transition between the wavenumber of the feeding cavity and the one in the antenna will be smoother. It should be highlighted that, in order to prevent radiation from these tapered transitions, they are covered by metallic plates which are printed over the top PCB (located before and after the PRS), as it has been marked in Fig. 3.2.17. In order to efficiently change the value of λ_z, two types of matching can be applied, depending on the LWA associated value of L_{HIS}. In particular, if L_{HIS} corresponds to the green/black curve of Fig. 3.2.16, the taper applied will be of "increasing"/"decreasing" type. The tapered transition is named as "decreasing" (Fig. 3.2.17(a)), when the length of its dipoles starts being equal to a (11 mm), and then decreases linearly until it reaches the designed value of L_{HIS}. If, as shown in Fig. 3.2.17(b), the length of the dipoles in the transition starts being equal to 1 mm, and then increases until it reaches the value of L_{HIS}, the transition is named as "increasing". For example, considering a LWA design with L_{HIS} =7 mm, the applied transition will be of decreasing type. Thus, as depicted in Fig. 3.2.18(a),

the length of the dipoles in the HIS transition will decrease from 11 mm to 7mm, modulating the value of λ_z following the black curve in Fig. 3.2.16. This transition will smoothly decrease the transverse wavenumber provided by the feeding ($\lambda_z \approx 2H$) into the one that is propagating inside the radiating cavity ($\lambda_z \approx 3H/2$, see Fig. 3.2.16). This scenario is depicted in Fig. 3.2.18, where it can also be seen a picture of the manufactured PCBs. The decreasing taper transition would be applied, for example, in the case of a LWA design with L_{HIS} = 6 mm. The printed dipoles in the matching transition would increase from 1 mm to 6 mm, modifying λ_z accordingly following the green curve in Fig. 3.2.16. In particular, λ_z would be increased from approximately $\lambda_z \approx 2H$ (provided by the feeding) to $\lambda_z \approx 3H$ (propagating inside the radiating cavity, see Fig. 3.2.16). A picture of the manufactured PCBs which corresponds to this LWA is shown in Fig. 3.2.19.

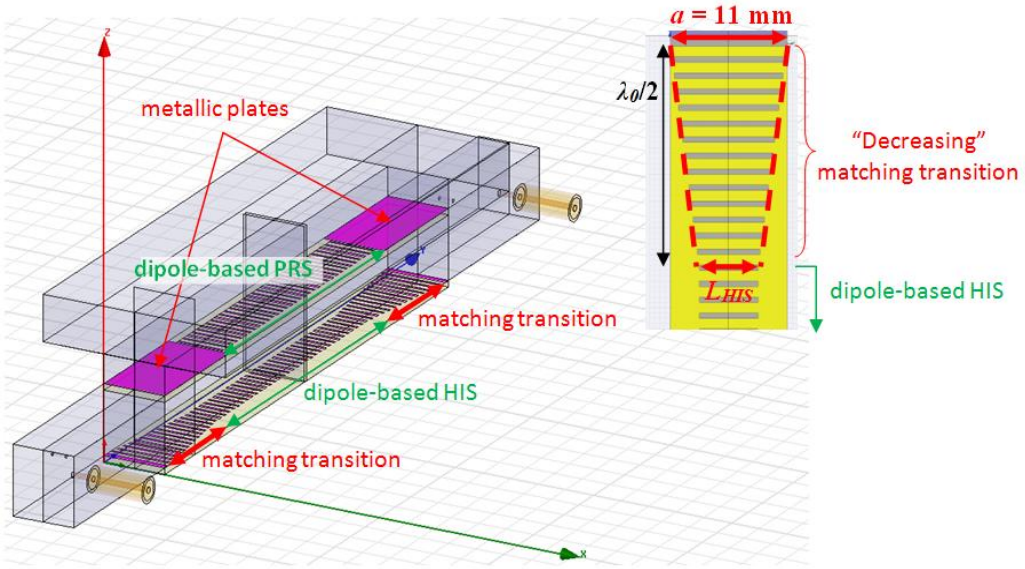

(a)

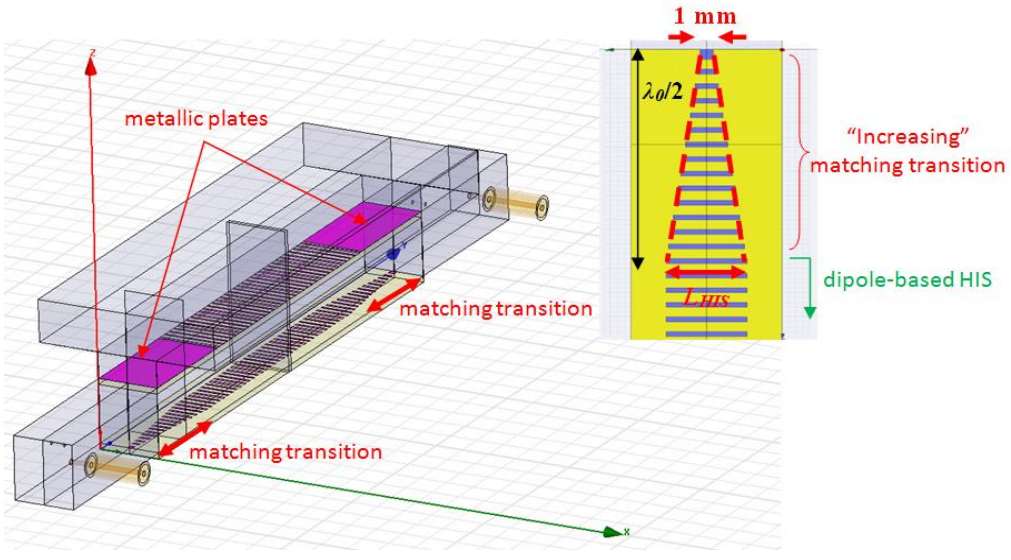

(b)

Fig. 3.2.17. Scheme of the whole structure with the matching transitions in the HIS.

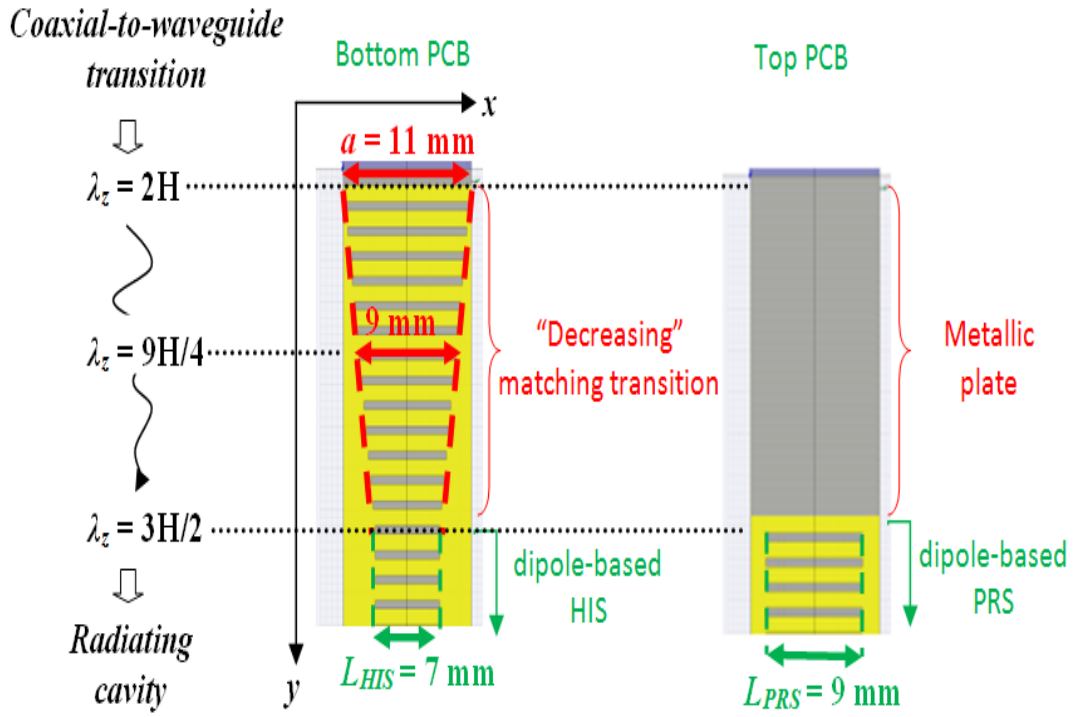

(a)

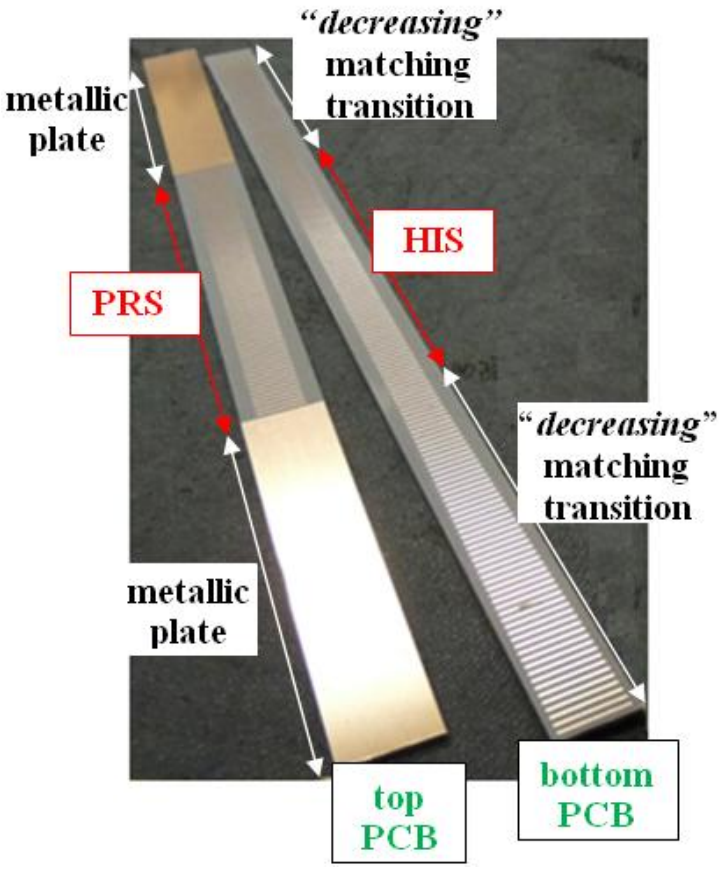

(b)

Fig. 3.2.18. PCBs for a designed LWA with "decreasing" transition (L_{PRS} = 9 mm and L_{HIS} = 7 mm) (a) Scheme (b) Manufactured.

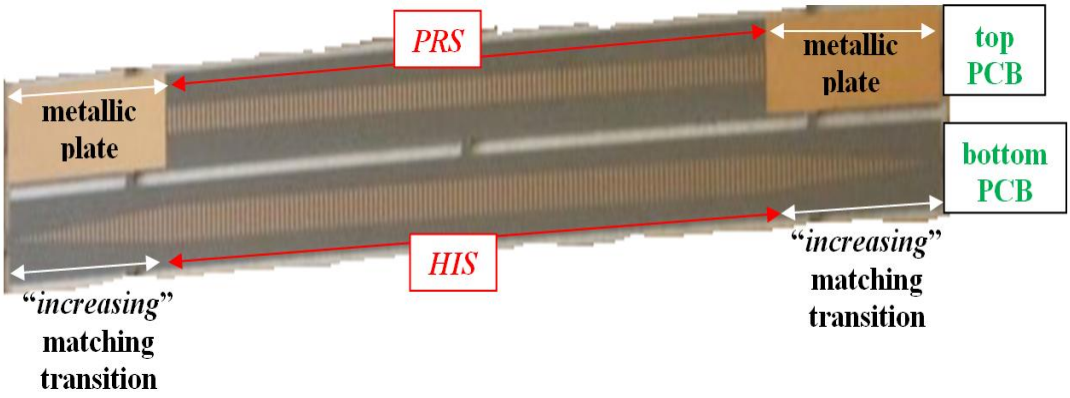

Fig. 3.2.19. Manufactured PCBs for a designed LWA with "increasing" transition (L_{PRS} = 4 mm and L_{HIS} = 6 mm).

3.3 Control of the pointing angle and beamwidth in 1D FP LWA

In the previous sections it has been demonstrated that changing the lengths of the printed dipoles of the PRS and the HIS allows the flexible variation of the leakage rate (α_y) and the phase constant (β_y) of the leaky-mode which propagates in the proposed 1D LWA. The independent control of these two parameters is of key importance for the synthesis and the flexible adjustment of the radiation pattern of a practical LWA. In this section we demonstrate that it is possible to independently and simultaneously vary β_y and α_y in the proposed 1D-PRS-HIS LWA. Experimental results of fabricated prototypes operating at 15 GHz are also reported to demonstrate this result.

The synthesis of a LWA consists in the selection of the antenna geometry (in our case, L_{PRS} and L_{HIS}) which provides the desired radiation pattern specifications: pointing angle θ_{RAD}, 3dB beamwidth $\Delta\theta$, and radiation efficiency η_{RAD}. All these parameters can be related to the LWA length L_A and the leaky-mode complex wavenumber ($k_y=\beta_y$-jα_y) considering the following well known equations:

$$\sin\theta_{RAD} = \frac{\beta_y}{k_0} \tag{3.3.1}$$

$$\eta_{RAD} = 1 - e^{-2\alpha_y L_A} \tag{3.3.2}$$

$$\Delta\theta \approx \frac{1}{L_A/k_0 \cos\ \theta_{RAD}} \approx \frac{\alpha_y}{k_0}\frac{1}{0.18\cos\ \theta_{RAD}}\,. \qquad (3.3.3)$$

As an example, seven LWAs with independent values of the pointing angle θ_{RAD} and beamwidth $\Delta\theta$, all of them presenting radiation efficiency η_{RAD} = 90%, are designed in this section as shown in Table 3.3.1. Four of these antennas point at a fixed angle θ_{RAD} = 20° while having different beamwidths $\Delta\theta$ from 25° to 5° (*LWA1*, *LWA2*, *LWA3* and *LWA4* in Table 3.3.1). Another set of four antennas have fixed 3 dB beamwidth $\Delta\theta$ = 10° and scan at different angles θ_{RAD} from 5° to 60° (*LWA5*, *LWA3*, *LWA6* and *LWA7* in Table 3.3.1). From each set of values of θ_{RAD}, $\Delta\theta$ and η_{RAD}, the corresponding values of α_y/k_0 and L_A can be extracted using (3.3.1)-(3.3.3), as summarized in Table 3.3.1.

η_{RAD}=90%	θ_{RAD}	$\Delta\theta$	α_y/k_0	L_A (mm)	L_{PRS} (mm)	L_{HIS} (mm)
LWA 1	20º	25º	0.08	47	7.58	8.06
LWA 2	20º	15º	0.05	75.5	8.3	7.64
LWA 3	20º	10º	0.034	111.5	8.75	7.42
LWA 4	20º	5º	0.017	221	9.64	7.19
LWA 5	5º	10º	0.0198	108.5	10.9	6.63
LWA 6	40º	10º	0.028	132.5	7.48	4.5
LWA 7	60º	10º	0.0215	180.5	5.79	5.84

Table 3.3.1. Electrical and geometrical parameters of the LWAs designed at 15 GHz.

The last step in the synthesis procedure involves the extraction of the pair of values L_{PRS} and L_{HIS} which provide the desired values of θ_{RAD} and α_y/k_0. For this purpose, a two-dimensional dispersion map similar to those used in [Gómez 2005-III and 2006-III] is obtained and shown in Fig. 3.3.1. L_{PRS} and L_{HIS} are simultaneously varied so that the functions $\theta_{RAD}(L_{PRS}, L_{HIS})$ and $\alpha_y/k_0(L_{PRS}, L_{HIS})$ are numerically obtained from the TEN. The required L_{PRS} and L_{HIS} for any pair of θ_{RAD} and α_y/k_0 can then be extracted from this dispersion map, where the contour curves of constant θ_{RAD} and constant α_y/k_0 are plotted as continuous lines and dashed lines in Fig. 3.3.1, respectively. Figure 3.3.1 also shows that θ_{RAD} and α_y are correlated in this antenna, so that in order to maintain θ_{RAD} constant and vary α_y/k_0

(or vice versa), it is necessary to simultaneous vary L_{PRS} and L_{HIS}. It must be noticed that the use of an efficient leaky-mode analysis technique is of essential importance to efficiently compute the 2D dispersion data shown in Fig. 3.3.1. As demonstrated in [Gómez 2005-III], the computational cost is dramatically reduced when the proposed TEN is employed, compared to the use of generic commercial full-wave simulators.

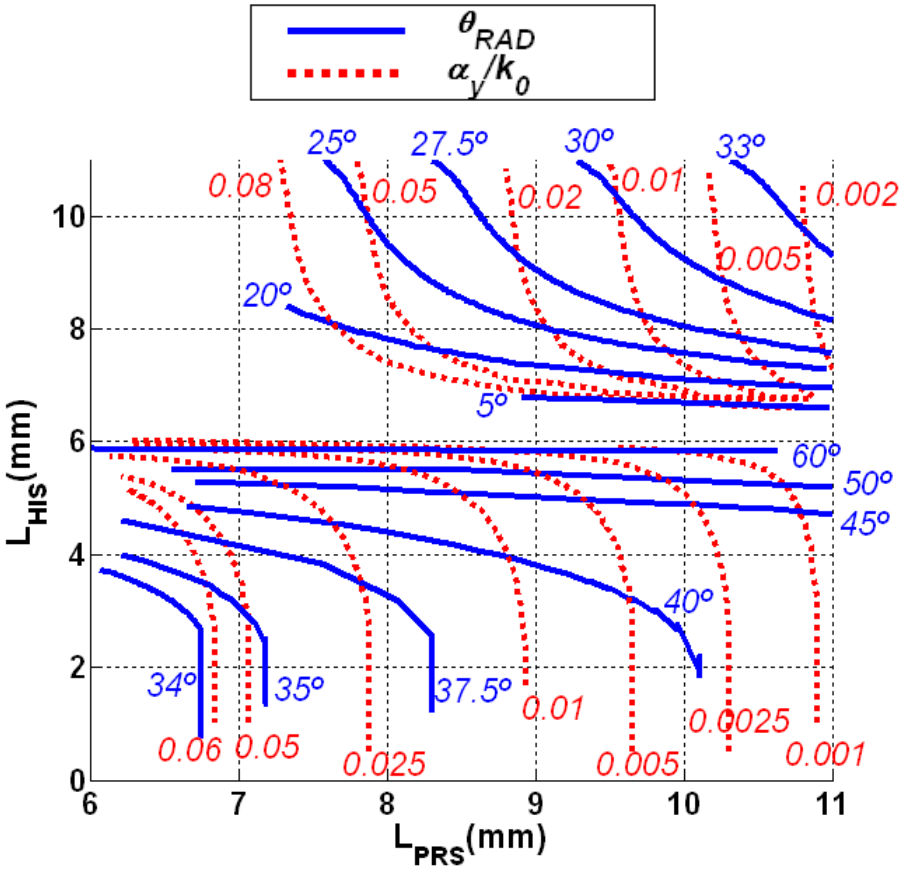

Fig. 3.3.1. 2D contour curve plots of θ_{RAD} and α_y/k_0 obtained at 15 GHz.

The dipole lengths L_{PRS} and L_{HIS} for each of the seven LWA designs were extracted using the described design procedure, resulting in the values summarized in Table 3.3.1. The rest of dimensions of the LWA are kept fixed to the values given in the caption of Fig. 3.2.1. In this way, no modification of the host waveguide structure is required, and standard photolithographic processes can be used to fabricate different PCB geometries that determine the LWA radiation features, as it is common in hybrid LWAs [Gómez 2005-I and 2006-III].

The seven designed LWAs were fabricated from Taconic TLY-5-0450 substrates. As can be seen in the photographs of Fig. 3.3.2, a single aluminum waveguide structure can be used to host all the PCB designs. The host waveguide is a cavity backed parallel-plate, which contains two pairs of slots to position the PRS and the HIS PCBs at the appropriate location. Two coaxial-to-waveguide transitions are used at the input and output of the LWA, to excite the TE_{01} mode of the resonant cavity and to match the antenna output, as can be seen in the photographs in Fig. 3.3.2 and Fig. 3.3.3(b). As described in Section 3.2, the feeding has been carefully designed to discard any direct radiation from the source, and discontinuities have been minimized to avoid diffraction. These facts ensure that the leaky mode is the main source of radiation from the antenna. The radiation pattern of the constructed prototype was measured in an anechoic chamber [see Fig. 3.3.3(a)] and also the S-parameters were measured using a vector network analyzer [see Fig. 3.3.3(b)].

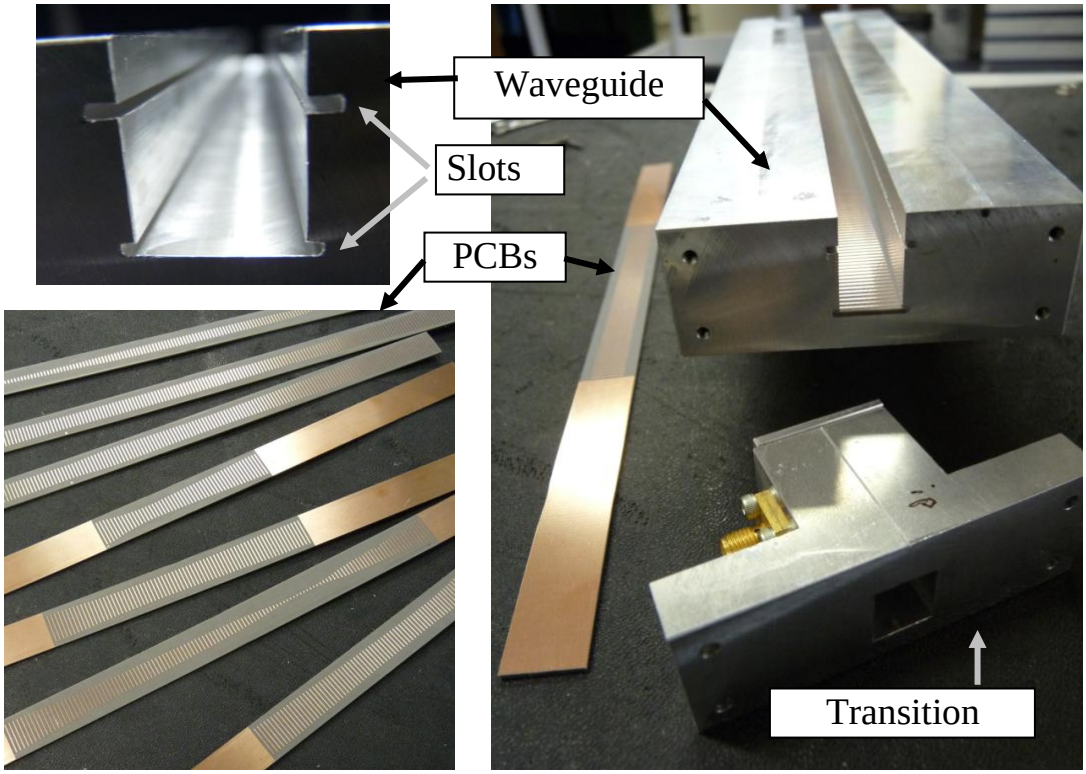

Fig. 3.3.2. Photographs of the manufactured LWA prototype.

(a)

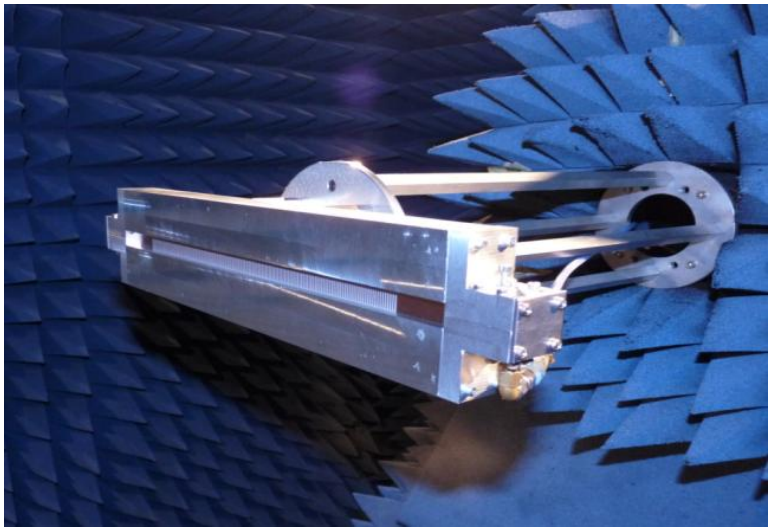

(b)

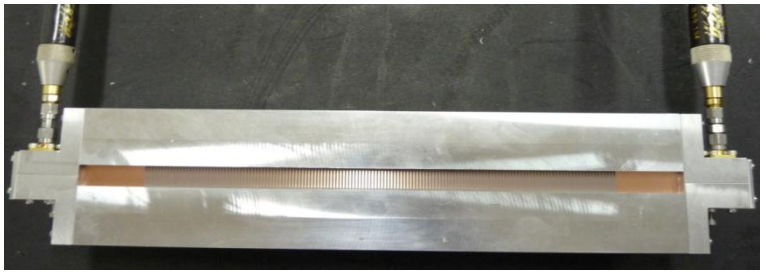

Fig. 3.3.3. Photographs of (a) Radiation pattern measurements (b) S-parameter measurements.

The normalized radiation patterns of the four LWAs presenting a constant pointing angle at θ_{RAD} = 20° and different beamwidths $\Delta\theta$ at the design frequency of 15 GHz, are plotted in Fig. 3.3.3. The theoretical radiation diagrams obtained from the corresponding leaky-mode propagation constant are compared to the measured results. Good agreement is observed between theory and measurements, showing the ability to control the beamwidth while keeping a constant pointing angle.

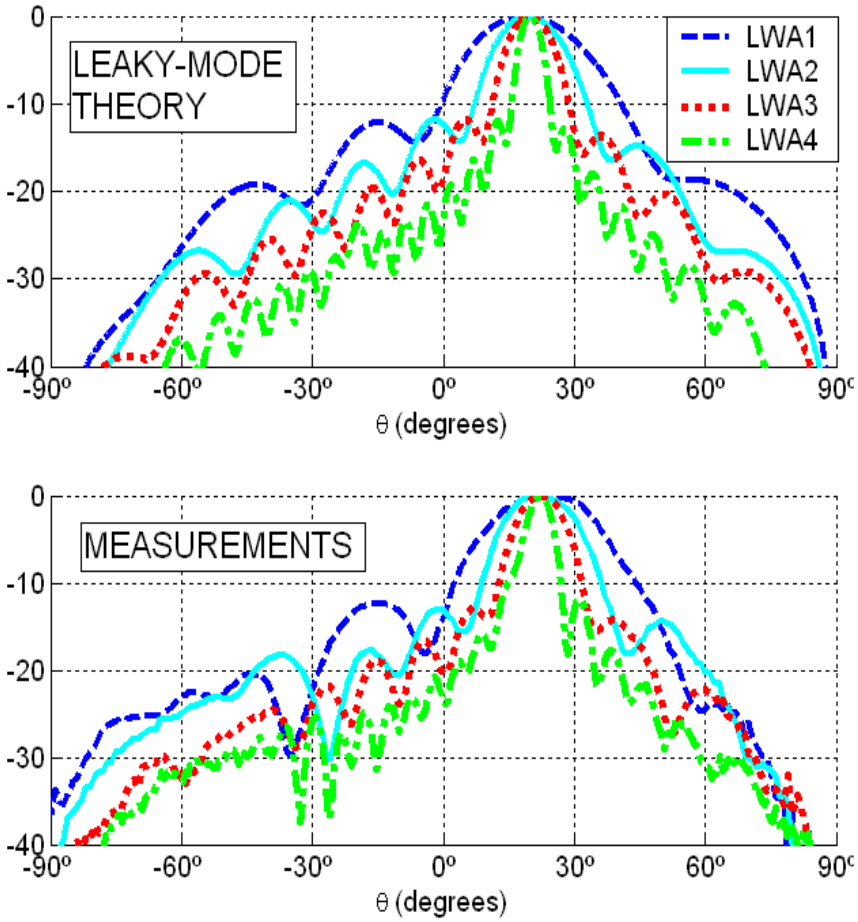

Fig. 3.3.3. Theoretical and measured normalized radiation patterns for the LWAs in Table I showing the control of the beamwidth $\Delta\theta$.

Figure 3.3.4 presents the theoretical and experimental radiation diagrams at 15GHz for the four LWAs with constant beamwidth $\Delta\theta$ = 10° and different scan angles θ_{RAD}. Again, good agreement is observed between leaky-mode theory and measurements, confirming the ability of the proposed LWA to control the pointing direction without affecting the directivity. It should be pointed out, however, that special care must be taken when radiation angles close to broadside θ_{RAD} = 0° or endfire θ_{RAD} = 90° are required. In the first case, the leaky-mode approaches the cut-off regime, decreasing both the efficiency and directivity of the antenna [Oliner 1993]. This can be observed in Fig. 3.3.5 for the case of *LWA5*, where the beamwidth has increased for scan angle θ_{RAD} = 5°. The maximum scanning angle of Fabry-Perot antennas is limited by the appearance of higher-order modes [Zhao 2005-I], which increase both the ripple and sidelobe levels of the radiation pattern, as can be seen in Fig. 3.3.5 for *LWA7* (which points at θ_{RAD} = 60°). This is a well-known disadvantage of hollow LWAs compared to dielectric filled LWAs, which

can scan to higher angles [Oliner 1993]. Finally, Fig. 3.3.6 compares the theoretical and measured scan angle and beamwidth obtained for the seven LWAs designed in Table 3.3.1. As shown in Figs. 3.3.4 - 3.3.6, the agreement between the specifications and the obtained measurement results is very good.

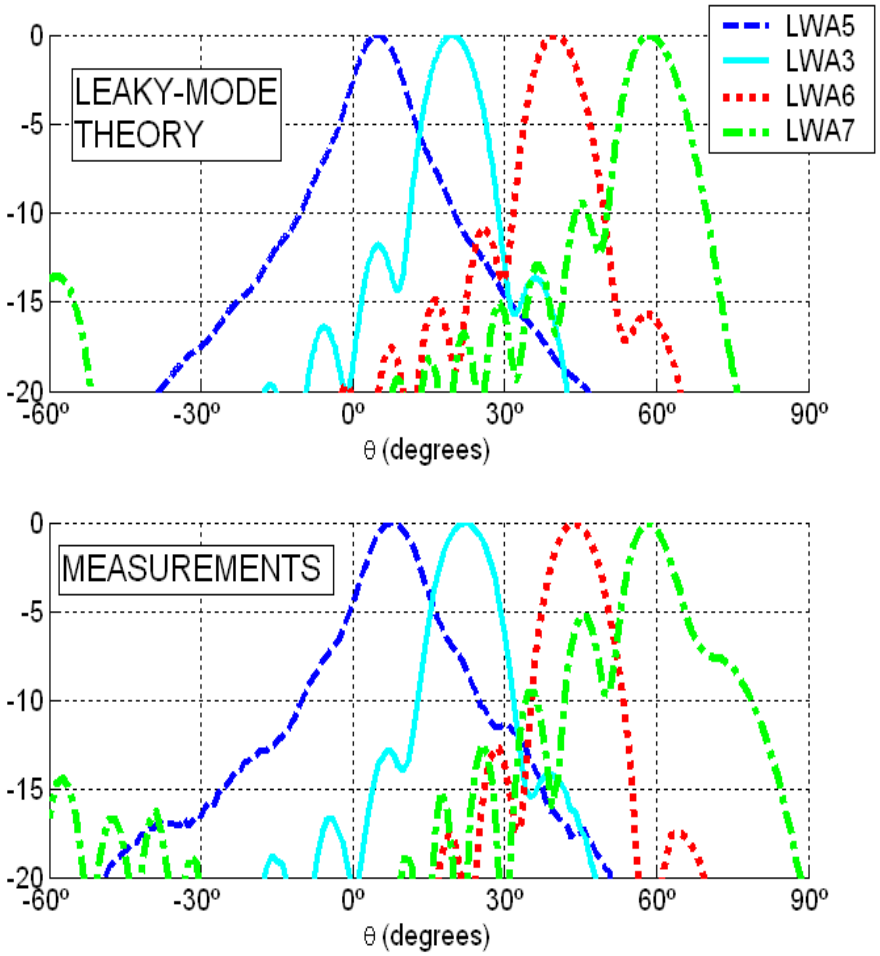

Fig. 3.3.5. Theoretical and measured normalized radiation patterns for the LWAs in Table I showing the control of the scan angle θ_{RAD}.

The measured S-parameters of one of the fabricated LWAs (all the LWAs present similar S parameters) are shown in Fig. 3.3.7. As can be seen, good input matching (S_{11} < -15 dB) and a transmission level of $S_{21} \approx$ -11.5 dB is observed at the frequency of design (15 GHz). The ohmic losses were evaluated by measuring the waveguide under no radiation conditions (closing its top aperture), obtaining a transmission value of -1.5 dB. These S-parameter values approximately correspond to a radiation efficiency η = 90%, as was requested for all the designs. The advantage of working with a hollow waveguide is clear when comparing these

losses with the ones associated with the dielectric-filled LWA proposed in [Gómez 2005-III and 2006-III]. In this case, the Teflon dielectric waveguide (ϵ_r = 2.2, $tan\delta$ = 0.005 [2006-III]) working at 15 GHz and the same length would introduce 6 dB losses. From the experimental results shown in Figs. 3.3.4 - 3.3.6, it is seen that the proposed PRS-HIS 1D LWA technology allows synthesis of high-gain radiation patterns with flexible control of scanning angle and directivity, whilst keeping high radiation efficiency in all the designs.

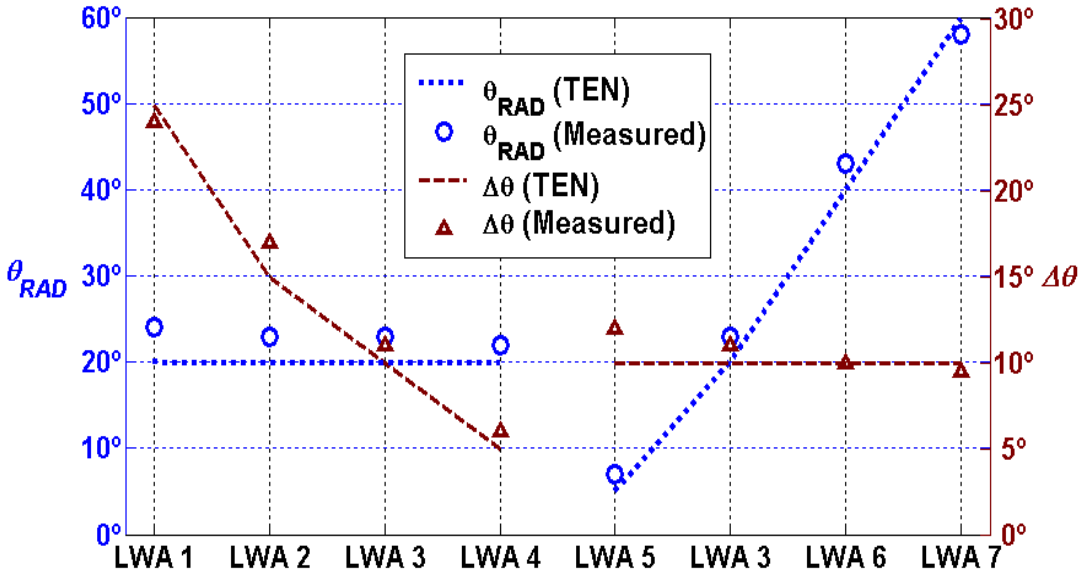

Fig. 3.3.6. Theoretical and measured scan angle and beamwidth for the LWAs designed in Table I.

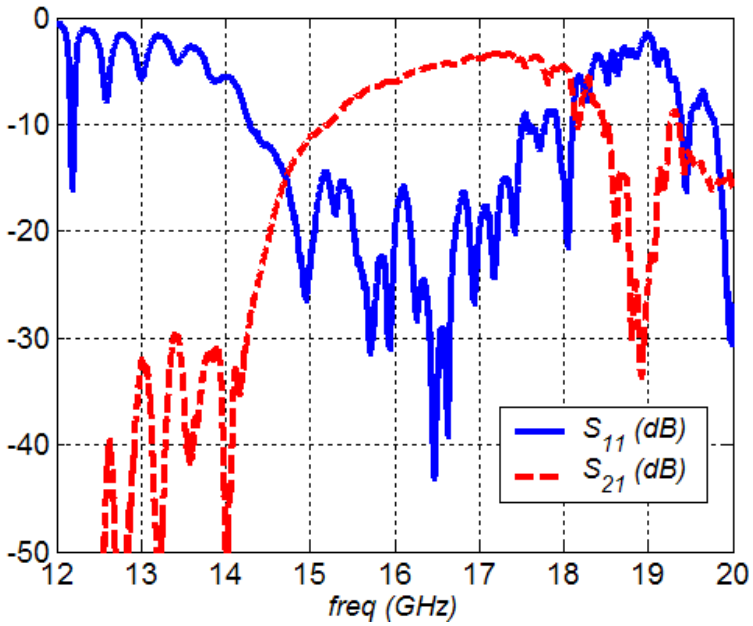

Fig. 3.3.7. Measured S-parameters of the LWAs.

3.4 Frequency scanning control in 1D FP LWA

Whereas the previous sections were centered in characterizing the dispersion of the proposed 1D PRS-HIS-LWA at a certain frequency, here it is aimed the detailed analysis of its frequency behavior. In particular, this section illustrates how the HIS placed at the bottom of the proposed structure can enhance its frequency sensitivity. Experimental results on manufactured prototypes are reported at the end of this section, validating the proposed mechanism to improve the LWA frequency-scanning response.

As it was explained in the introduction of this chapter, due to the dispersive nature of leaky waves, its complex propagation constant is frequency dependent and can be expressed in the following way:

$$k_y(f) = \beta_y(f) - j\alpha_y(f). \tag{3.4.1}$$

thus, the associated highly-directive main-beam elevation angle θ_{RAD} can be frequency scanned according to the next relation:

$$\theta_{RAD}(f) \approx arcsin\frac{\beta_y(f)}{k_0(f)} = arcsin\frac{c_0\beta_y(f)}{2\pi f}. \tag{3.4.2}$$

Frequency-beam scanning is a well-known property of leaky-wave antennas (LWAs) [Oliner 1993] with applications such as radar [Oliner 1993] or electrical prisms [Gupta 2009]. LWAs offer an attractive mechanism to frequency scan the

radiated beam of electrically large apertures by simply feeding a leaky-mode, thus avoiding more expensive feeding networks associated with array antennas. Frequency-scanned LWAs are also much simpler compared to electronically-scanned phased-arrays, which scan the radiated beam at a fixed frequency [Hansen 1998]. However, frequency scanned antennas may lead to higher front-end complexity due to the broader bandwidth needed to perform the scanning. Therefore, it is desirable to increase the antenna frequency sensitivity (*i.e*, how quickly the beam angle scans as the frequency is varied) in order to reduce the bandwidth of the circuitry associated with frequency-scanned LWAs.

The frequency-scan behavior of LWAs depends on the dispersive response of the associated leaky-mode phase constant $\beta_y(f)$, as stated by (3.4.2). Particularly, LWAs based on dielectric-filled waveguides [Gómez 2006-III] present higher frequency sensitivity and higher range of scanned angles [Oliner 1993] than LWAs based on hollow air-filled waveguides [Lampariello 1998] ,[Tsuji 2003]. For a rectangular waveguide of height H with relative permittivity ε_r operating in the perturbed TE_{01} leaky-mode, and assuming small perturbation conditions, the lower and upper frequencies of operation for broadside (θ_{RAD} = 0°) and endfire (θ_{RAD} = 90°) scanning can be approximated by:

$$f_{broadside} \approx \frac{c_0}{2H}\frac{1}{\sqrt{\varepsilon_r}} \tag{3.4.3}$$

$$f_{endfire} \approx \frac{c_0}{2H}\frac{1}{\sqrt{\varepsilon_r - 1}} \tag{3.4.4}$$

As can be seen in (3.4.4), the bandwidth needed to scan from broadside to endfire is reduced as ε_r is increased, while hollow waveguides (ε_r = 1) would require very large bandwidths to approach angles close to endfire, thus limiting the scanning range in practice. On the other hand, dielectric-filled LWAs have higher losses associated with the dielectric medium and they suffer from higher changes in the beamwidth as frequency is varied [Oliner 1993]. For these reasons, it would be desirable to create a LWA based on a hollow waveguide to minimize the dielectric losses and beamwidth dispersion, but with increased frequency sensitivity to perform the scanning in the minimum bandwidth. With this main

objective in mind, the 1D PRS-HIS LWA is proposed, which is based on a hollow rectangular waveguide with its top narrow wall replaced by a Partially Reflective Surface (PRS) and a High Impedance Surface (HIS) in the bottom narrow wall, as illustrated in Fig. 3.4.1(b) and described in Section 3.2.

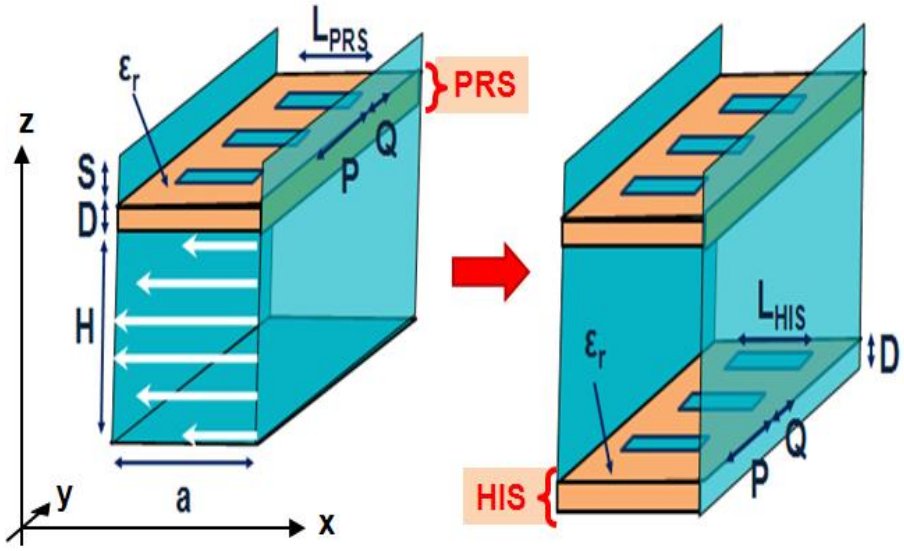

(a) (b) .

Fig. 3.4.1 (a) Hollow 1D PRS-LWA (b) 1D PRS-LWA loaded with HIS (a = H = 11 mm, S = 5 mm, D = 1.13 mm, ϵ_r = 2.2, L_{PRS} = 10 mm, L_{HIS} = 9 mm, P = 1.5 mm, Q = 0.5 mm).

Figure 3.4.1(a) shows the scheme of a PRS-loaded LWA, which is based on a hollow rectangular waveguide with a metallodielectric PRS formed by printed dipoles. The highly-reflective PRS allows the propagation of a TE_{01}-type leaky-mode with a weak leakage rate, providing a large radiating length and therefore high directivity. The dispersion with frequency of this leaky-mode can be analyzed by using the TEN and software tool presented in Chapter 2. The dimensions of the structure to operate in the 15 GHz frequency band are also shown in Fig. 3.4.1. Figure 3.4.2 shows how the pointing angle of this LWA is scanned from θ_{RAD} = 5° at 13GHz to θ_{RAD} = 65° at 26 GHz. If the waveguide is filled with a dielectric medium (for instance Teflon, with ε_r = 2.2), and the cavity height H is decreased from 11 mm to 9.5 mm in order to operate in a similar frequency band, a more sensitive scanning response is obtained, which is from θ_{RAD} = 5° at 11 GHz to θ_{RAD} = 90° at 15 GHz, thus increasing the range of scanned angles up to endfire and reducing the bandwidth, in accordance with (3.4.3) and (3.4.4).

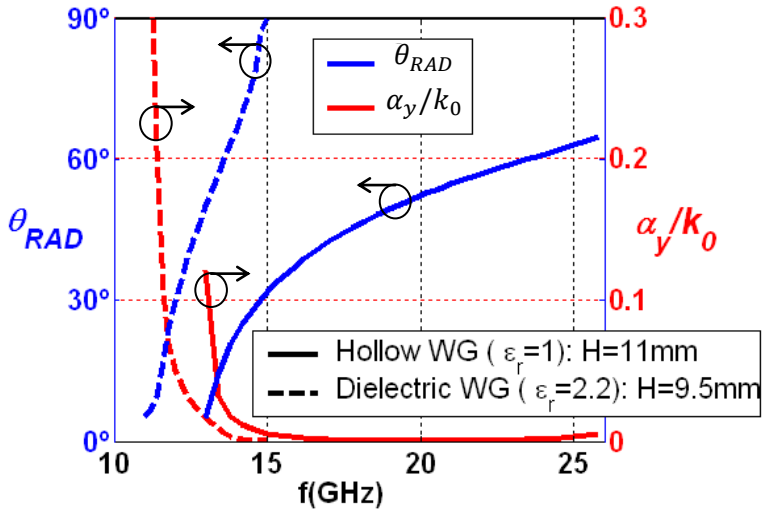

Fig. 3.4.2. Leaky-mode frequency dispersion of the LWA in Fig. 3.4.1(a), with and without dielectric filling.

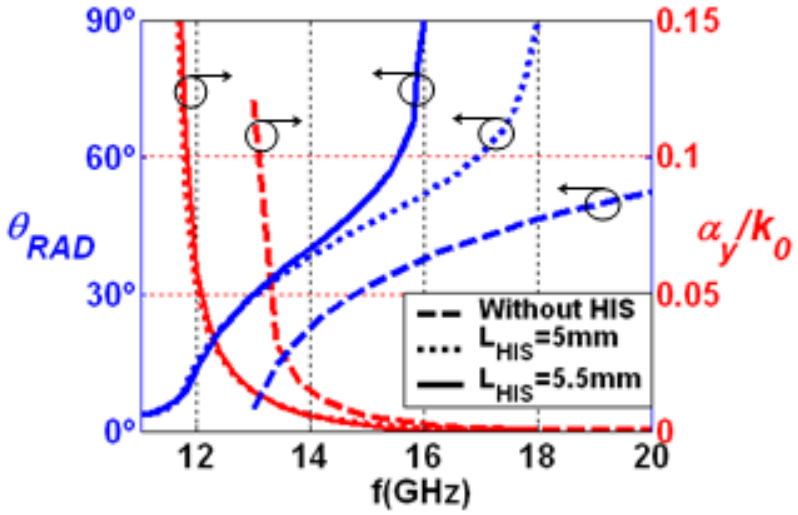

(a)

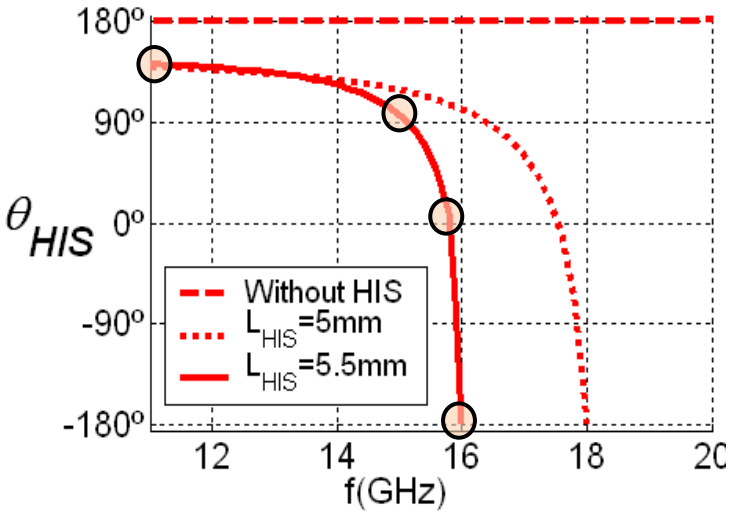

(b)

Fig. 3.4.3. (a) Leaky-mode frequency dispersion for the hollow LWA of Fig. 3.4.1(b) with different HIS dipoles length (b) Reflection phase presented by the HIS.

To avoid the use of dielectric and its associated losses, a metallodielectric HIS formed by a grounded array of printed dipoles is added at the bottom wall of the hollow leaky waveguide as shown in Fig. 3.4.1(b). The HIS strongly modifies the boundary conditions seen by the incident TE_{01}-type mode (as described in the previous section). Particularly, the length of the HIS dipoles (L_{HIS} in Fig. 3.4.1(b)) can be designed to create an Artificial Magnetic Conductor (AMC) condition which ultimately causes the leaky-mode to enter a surface-wave regime ($\beta_y/k_0>1$), thus increasing the LWA frequency scanning sensitivity up to endfire. This fact is shown in Fig. 3.4.3(a), where theoretical leaky-mode frequency dispersion results obtained using the TEN are given for different illustrative scenarios (without HIS and with L_{HIS} = 5 mm and L_{HIS} = 5.5 mm). As shown in Fig. 3.4.3(a), the beam-scanning curve becomes more sensitive to frequency change when the HIS is present. Moreover, by properly tuning the length of the HIS dipoles L_{HIS}, one can increase this sensitivity further. To understand this effect, we adopt the bouncing plane wave interpretation for waveguide propagation [Goussetis 2006-I] and plot the reflection phase (θ_{HIS}) experienced by the wave travelling along the leaky waveguide at the HIS plane. Figure 3.4.3(b) plots θ_{HIS} versus frequency for the different scenarios of Fig. 3.4.3(a). In the absence of the HIS, the boundary condition at this plane corresponds to a metallic wall and the reflection phase has a constant value of +180° for all frequencies and associated scanned angles θ_{RAD}. When the HIS is introduced, the reflection phase experienced at this boundary (θ_{HIS}), rapidly changes with frequency from θ_{HIS} = +140° to θ_{HIS} = -180°, as shown in Fig. 3.4.3(b). Particularly, the AMC condition (θ_{HIS} = 0°) can be tuned to lower or higher frequencies by modifying the HIS dipoles length L_{HIS} [Goussetis 2006-I]. As presented in Fig. 3.4.3(b), the AMC condition is set to 17.5 GHz for L_{HIS} = 5 mm and to 15.8 GHz for L_{HIS} = 5.5 mm. For clarity we note that the angle of incidence of the bouncing wave at the HIS plane, which is equal to the pointing angle of the radiated beam (θ_{RAD}), at these points is 68.5° and 67°, respectively. This AMC resonance condition establishes the frequency in which the leaky-mode pointing angle θ_{RAD} is pushed to high values (around θ_{RAD} = 70° in Fig. 3.4.3(a)), eventually obtaining the endfire direction (θ_{RAD} = 90°) when frequency is increased, and finally entering the surface-wave regime ($\beta_y/k_0>1$ with an imaginary value of θ_{RAD} [Oliner 1993]). In this way, by tuning the AMC resonance one can make the endfire radiation

frequency to be located close to the broadside radiation frequency (which is around 11 GHz for the HIS-loaded LWAs, as can be seen in Fig. 3.4.3(a)), hence reducing the bandwidth needed to scan the beam. This is the reason why the broadside to endfire frequency range is reduced to [11 GHz - 18 GHz] when L_{HIS} = 5mm, and to [11 GHz – 16 GHz] when L_{HIS} = 5.5 mm (see Fig. 3.4.3(b)). A HIS was also introduced inside a closed hollow rectangular waveguide in [Goussetis 2010], with the aim to reduce the dispersion suffered by short pulses propagating along the waveguide. In any case, it is shown that, by conveniently engineering the HIS dimensions, one can strongly modify the propagation and/or radiation properties of the host waveguide for improved performance.

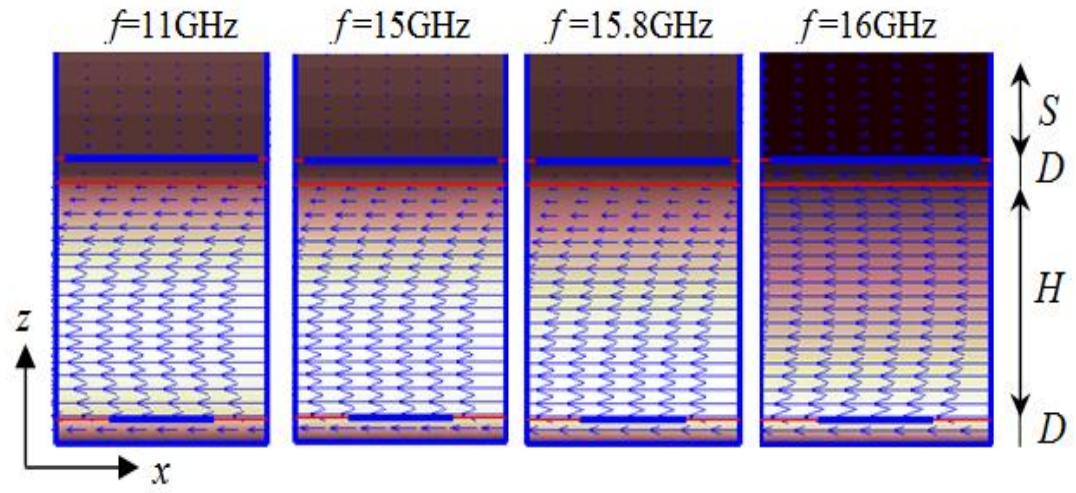

Fig. 3.4.4 Leaky-mode electric field distribution inside the 1D PRS-HIS LWA for different frequencies (L_{HIS} = 5.5 mm).

For the case L_{HIS} = 5.5 mm, Fig. 3.4.4 presents the leaky-mode electric field inside the LWA cavity at four frequencies of the scanning range, obtained with the software tool described in Chapter 2. The related values of θ_{HIS} are highlighted with circles in Fig. 3.4.3(b). At 11 GHz, the HIS behaves approximately as a grounded dielectric slab (θ_{HIS} = +140° in Fig. 3.4.3(b)) and a perturbation of the usual waveguide TE_{10} mode occurs in the LWA cavity (the cavity height H corresponds to half-wavelength of the resonant fields in the transverse direction, see Fig. 3.4.4). The hollow cavity height H is designed using (3.4.3) to provide near broadside radiation (waveguide close to cutoff) at this frequency ($\theta_{RAD} \approx 0°$ in Fig. 3.4.3(a)). The effect of the HIS starts to appear as frequency is increased, rapidly decreasing

θ_{HIS} and increasing θ_{RAD} due to the AMC resonance as shown in Fig. 3.4.3. At 15 GHz, θ_{RAD} has been increased to +48°. At 15.8 GHz, the HIS presents AMC resonance condition (θ_{HIS}=0° in Fig. 3.4.3(b)) which manifests in maximum average tangential electric fields intensity at the HIS interface (Fig. 3.4.4). As a result of the AMC condition the effective cavity height is increased, making the scanned angle rise suddenly ($\theta_{RAD} \approx 70°$ at 15.8 GHz in Fig. 3.4.3(a)) with respect to the case without HIS ($\theta_{RAD} \approx 40°$ in Fig. 3.4.3(a)). When frequency is augmented from this point, the leaky-mode passes by the endfire condition ($\theta_{RAD} \approx 90°$ at 16 GHz in Fig. 3.4.3(a)) and eventually transforms into a surface-wave (which does not radiate). As illustrated in Fig. 3.4.4, the field is confined in the AMC dielectric slab at 16 GHz with exponentially decreasing amplitude in the air-filled cavity region, as it corresponds to a surface-wave [Oliner 1993].

(a) 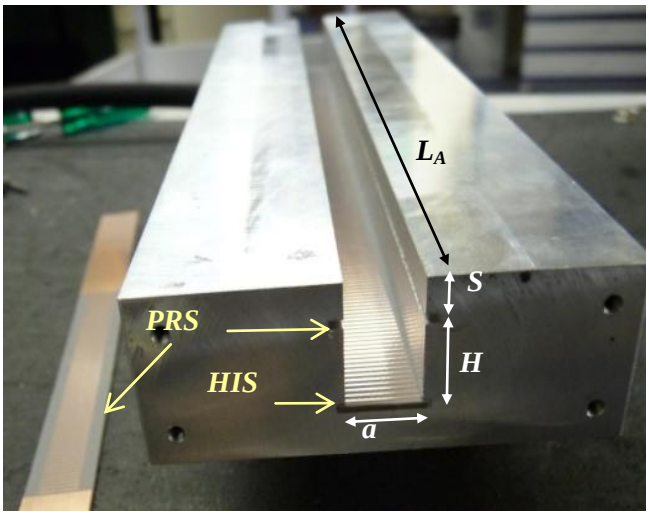

(b) 

Fig. 3.4.5. Photograph of manufactured LWA prototype, (a) Metallic waveguide hosting the printed-circuit dipole-based PRS (ready to be inserted at the top) and HIS (at the bottom) (b) Whole LWA structure at the anechoic chamber.

To experimentally confirm the effect of the HIS in the improvement of the leaky frequency-scanning response, three hollow LWAs were fabricated according to the dimensions of Fig. 3.4.5. The first of them does not use any HIS, while the other two LWAs were loaded with metallodielectric HIS with L_{HIS} =5 mm and L_{HIS} = 5.5 mm, respectively. A picture of the manufactured prototype is shown in Fig. 3.4.5. Figure 3.4.6 shows the frequency-scanning curves of the three manufactured LWAs, measured in the 10 GHz – 20 GHz frequency range. The leaky-mode results

from 10 GHz to 26 GHz obtained from the TEN are superimposed for comparison, showing good agreement between theory and experiments, and thus confirming the mechanism to enhance the scanning sensitivity and the range of scanned angles.

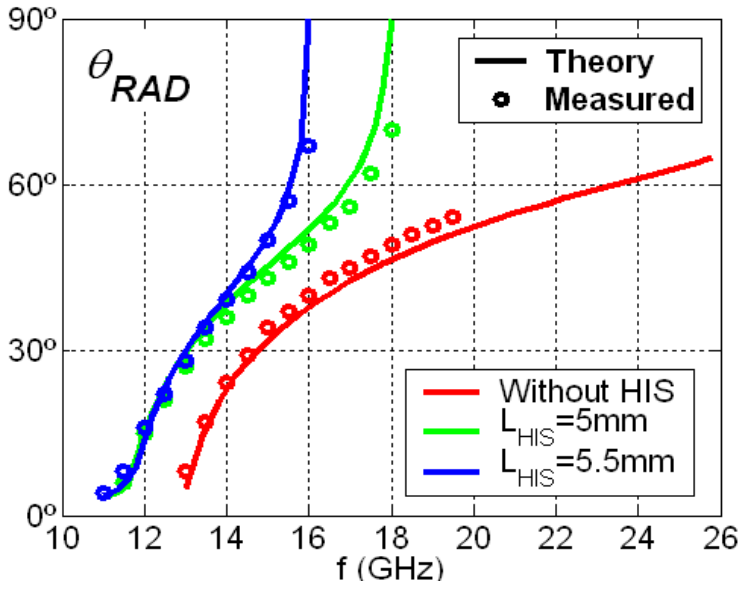

Fig. 3.4.6. Theoretical and measured frequency-scanning response of hollow LWAs showing the effect of the HIS.

Figure 3.4.6 shows that the HIS-loaded PRS LWA with L_{HIS} = 5.5 mm provides beam scanning from θ_{RAD} = 4° to θ_{RAD} = 67° in the frequency range 11 GHz-16 GHz, while the LWA without HIS has a poorer frequency sensitivity (from near broadside to θ_{RAD} = 65° in the frequency range 13 GHz - 26 GHz). The theoretical and measured normalized radiation patterns for the HIS-loaded LWA with L_{HIS} = 5.5mm and a radiating length L_A = 200 mm *(*9.2 λ_0 *at* 14 GHz*)* are plotted in Fig. 3.4.7(a) and Fig. 3.4.7(b), respectively. This radiating length provides a measured radiation efficiency of η_{RAD} = 90% at 14GHz. However, η_{RAD} is strongly dependent on frequency, decreasing to 80% and 20% at 15 GHz and 16 GHz respectively. The same behaviour is observed when measuring the LWA gain, which presents values from 12.2 dB at 14 GHz, to 11.1 dB at 15 GHz and 1.8 dB at 16 GHz. Good agreement between the theoretical and measured radiation patterns is observed, showing the scanning of the main beam elevation angle θ_{RAD}. The beamwidth broadens close to broadside (11 GHz in Fig. 3.4.7) due to the increase of the leakage rate (see α_y/k_0 curve in Fig. 3.4.3(a) for L_{HIS} = 5.5mm at 11 GHz). From

12GHz to 15GHz, the expected frequency-beam steering is obtained. At 16GHz, a secondary lobe appears in the angle $\theta \approx$ -67° as a result of the decrease in the leakage rate (see α_y / k_0 curve in Fig. 3.4.3(a) for L_{HIS} = 5.5 mm at 16 GHz), which reduces the LWA radiation efficiency and creates a reflected leaky-wave pointing at a mirrored angle with respect to the main beam [Oliner 1993]. Radiation to pointing angles higher than +70° is limited by the appearance of grating lobes due to higher-order modes [Oliner 1993], [Zhao 2005-I]. The measured ohmic losses of the fabricated hollow PRS LWA loaded with HIS are in the range of 1.5 dB for the entire frequency band, while for the case of a similar LWA based on a waveguide filled with Teflon (ε_r = 2.2, $tan\delta$ = 0.005) the losses are in the order of 6 dB, as demonstrated in [Gómez 2006-III].

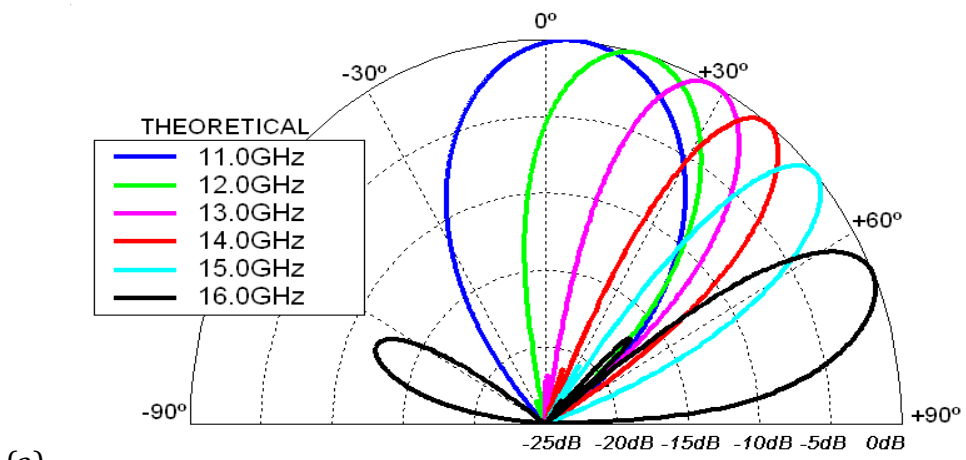

(a)

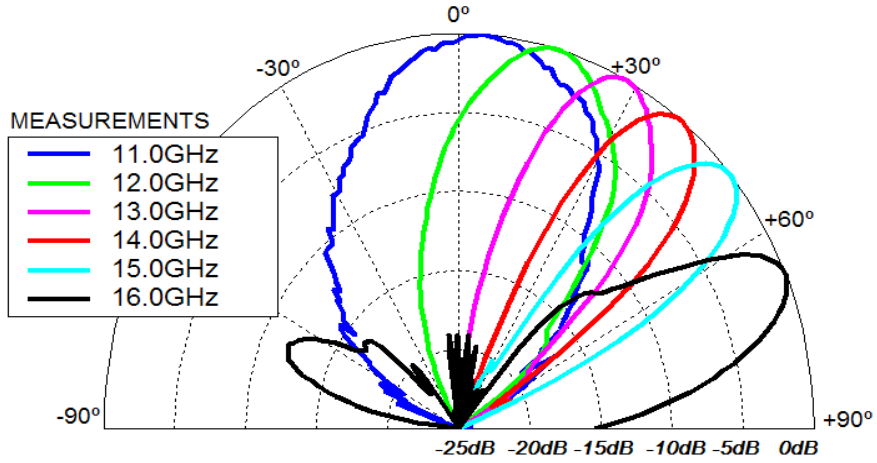

(b)

Fig. 3.4.7. (a) Theoretical and (b) measured radiation diagrams showing the frequency beam-scanning of the designed PRS-HIS LWA (L_{HIS} = 5.5mm).

3.5 Analysis and design of 2D FP LWA

Whereas the previous sections have employed the simple and efficient TEN-based technique presented in Section 2.3 in order to analyse double-layer one-dimensional Fabry-Perot (1D FP) LWAs, here it is shown how it also enables the analysis and design of double-layer two-dimensional (2D) FP LWAs. In this section, the TEN technique is firstly applied to the analysis of a 2D FP LWA with half-wavelength profile and subsequently extended to antennas with lower profile. The obtained dispersion diagrams are in good agreement with those derived by the technique proposed in [Mateo-Segura 2012], which is based on Method of Moments together with reciprocity as well as an array factor approach. One of the limitations of the TEN approach is shown at the end of this section, which appears when the FP cavity is very thin.

Figure 3.5.1 shows the scheme of a 2D FP LWA with generic printed top and bottom periodic layers and an ideal horizontal electric dipole source located in the centre of the cavity. As depicted in Fig. 3.5.1, the feeding element excites a two-dimensional cylindrical wave with its electric field oriented along the *x* axis, which propagates outward radially. As it is explained in [Ip 1990] and [Jackson 2008], a horizontal electric dipole source launches a pair of leaky waves, one TM_z and one TE_z. The TM_z leaky wave mainly determines the E-plane pattern of the 2D FP LWA while it is the TE_z leaky wave which mainly controls the H-plane pattern.

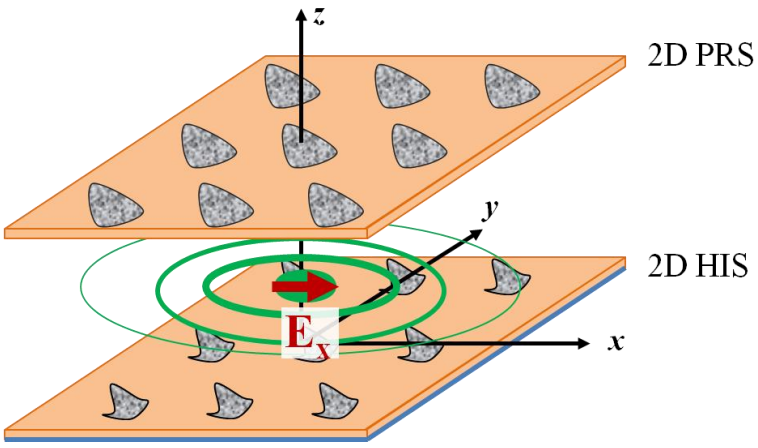

Fig. 3.5.1 Two-dimensional Fabry-Perot LWA with generic printed PRS and HIS.

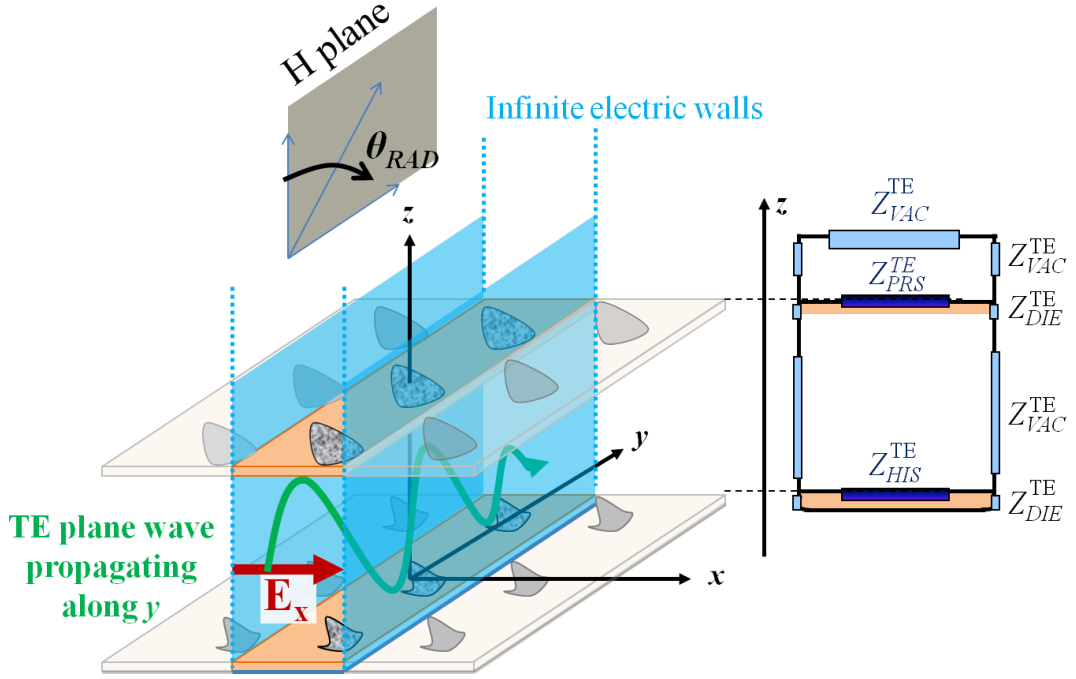

Fig. 3.5.2 (a) 1D equivalent model of 2D FP LWA in H-plane (b) Equivalent TEN.

Applying the method of images, the H-plane dispersion of the structure in Fig. 3.5.1 can be equivalently analyzed considering the 1D structure of Fig. 3.5.2(a). As this figure shows, a pair of infinite electric walls have been placed parallel to the *yz* plane and separated by a distance equal to the periodicity of the array in *x* axis. In this scenario, the feeding is a TE plane wave (with its electric field polarized along the *x* axis) which propagates along the *y* axis (as it can be seen in Fig. 3.5.2(a)). Considering this excitation, the metallic walls can be regarded as mirrors that effectively reproduce the behavior of the structure with infinite PRS and HIS

arrays of Fig. 3.5.1. This simplification allows us to characterize the structure of Fig. 3.5.1 in the H plane employing the Transverse Equivalent Network (TEN) of Fig. 3.5.2(b). As it was explained in Chapter II, the propagation of the leaky wave inside the empty cavity (ε_r=1) is modeled in the TEN of Fig. 3.5.2(b) by a transmission line with characteristic impedance

$$Z_{TE}^{VAC} = \frac{\omega\mu_0}{k_z^{(1)}} \tag{3.6.1}$$

whereas the propagation inside the PCB´s dielectric slabs, with permittivity ε_r, is modeled by transmission lines with characteristic impedance

$$Z_{TE}^{DIE} = \frac{\omega\mu_0}{k_z^{(\varepsilon_r)}} \tag{3.6.2}$$

In these expressions, $k_z^{(\varepsilon_r)}$ is the transverse wavenumber of the leaky wave

$$k_z^{(\varepsilon_r)} = \sqrt{k_0^2 - k_y^2} \tag{3.6.3}$$

where (ε_r) denotes the dielectric constant of the medium. The periodic surfaces are modelled by the impedances Z_{PRS}^{TE} and Z_{HIS}^{TE}, which are obtained following the pole-zero method described in Section 2.2, considering TE plane wave incidence in the H plane.

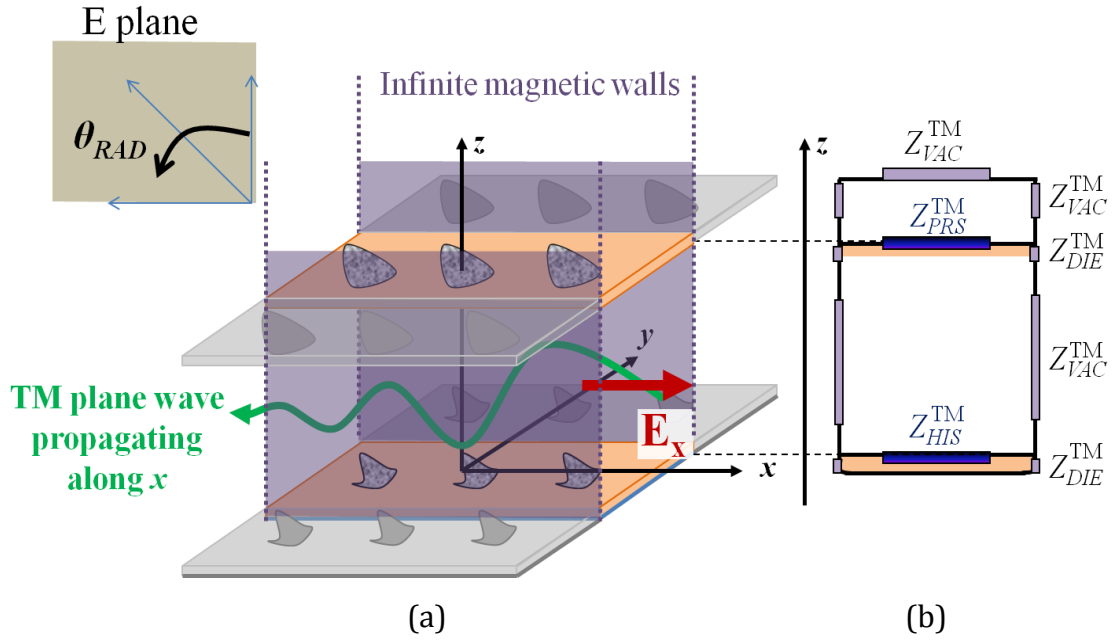

Fig. 3.5.3 (a) 1D equivalent model of 2D FP LWA in H plane (b) Equivalent TEN.

Analogously, when studying the dispersion of the 2D FP LWA of Fig. 3.5.1 in the E plane, the simpler scenario of Fig. 3.5.3(a) can be equivalently analyzed. As depicted in this figure, the feeding now is a TM plane wave (with its electric field polarized along the *x* axis) which propagates along the *x* axis. Two infinite magnetic walls have been placed parallel to the *xz* plane and separated by a distance equal to the periodicity of the arrays in the *y* axis. Considering the TM plane wave excitation, these magnetic walls allow the 1D structure of Fig. 3.5.3(a) to behave in the E-plane exactly the same way as the original one of Fig. 3.5.1. Thus, the structure of Fig. 3.5.1 can be characterized in the E-plane employing the Transverse Equivalent Network (TEN) of Fig. 3.5.3(b). In this case, the propagation of the leaky wave inside the empty cavity is modeled in the TEN of Fig. 3.5.3(b) by a transmission line with characteristic impedance

$$Z_{TM}^{VAC} = \frac{k_z^{(1)}}{\omega \epsilon_0 \epsilon_r} \tag{3.6.4}$$

and the propagation inside the PCB´s dielectric slabs is modeled by transmission lines with characteristic impedance

$$Z_{TM}^{(\varepsilon_r)} = \frac{k_z^{(\varepsilon_r)}}{\omega \epsilon_0 \epsilon_r} \tag{3.6.5}$$

The periodic surfaces are modelled by the impedances Z_{PRS}^{TM} and Z_{HIS}^{TM}, which are obtained following the pole-zero method described in Section 2.2, considering TM plane wave incidence.

Thus, it is now clear that considering these transformations, it is possible to characterize a two-dimensional structure by analyzing two one-dimensional scenarios. Then, the software tool described in Section 2.3 (which is highly efficient for the analysis of 1D FP LWA) can be now employed to obtain the dispersion characteristics of 2D FP LWAs in the E and H planes. In addition, it is worth noting that the TEN-base tool can also be employed in the design of these 2D antennas. Once the frequency of operation is fixed, the TEN enables the design of the two printed circuits together with the height of the cavity, in order to obtain broadside radiation. This will be proven in the next subsections, where three cases of 2D LWAs have been designed to point at broadside with different cavity heights.

Initially, it is considered a cavity antenna with a single periodic array and half-wavelength profile. Subsequently, the case of antennas with two periodic arrays and sub-wavelength profile is analyzed.

3.5.1 Half-wavelength antennas

The TEN approach is now applied to design a resonant cavity antenna with one periodic array that points at broadside at 14GHz, the layout of the structure is shown in Fig. 3.5.4. The LWA comprises a PRS consisting of square patches with edge L_{PRS} = 8.0 mm arranged in a square lattice with periodicity P = 9.0 mm and printed on a dielectric slab of thickness d_1 = 1.5 mm and relative permittivity 2.55. Using the TEN-based tool, it is designed that the PRS must be located at a distance $H = 9.82\,mm$ above a ground plane in order to satisfy the splitting condition ($\beta = \alpha$, as explained in Section 3.1.2) at 14GHz and therefore, point at broadside. This value corresponds to approximately half-wavelength at 14 GHz, which is the value at which an unperturbed TE_{01} mode starts propagating through a closed metallic cavity.

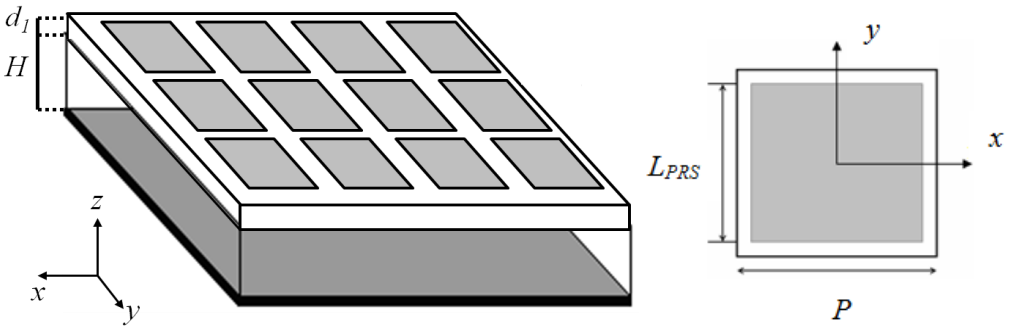

(a) (b)

Fig. 3.5.4 (a) Layout of the 2D FP LWA formed by a metallodielectric PRS placed over a ground plane (b) PRS unit cell.

Following the approach described at the beginning of this section, the H and E planes dispersion diagrams are obtained by analyzing respectively the two 1D scenarios of Fig. 3.5.5. The TEN-based technique presented in Section 2.3 is now employed in order to solve the associated transverse resonance equations, and the dispersion diagrams of Fig. 3.5.6 and Fig. 3.5.7 are obtained. In particular, when considering the H-plane scenario of Fig. 3.5.5(a), it is obtained the propagation constant $k_y = \beta_y - j\alpha_y$ of the 2D structure, which is plotted in Fig. 3.5.6. When the E plane is considered, the scenario of Fig. 3.5.5(b) is analyzed and the propagation constant $k_x = \beta_x - j\alpha_x$ of the 2D structure is obtained, which is plotted in Fig. 3.5.7.

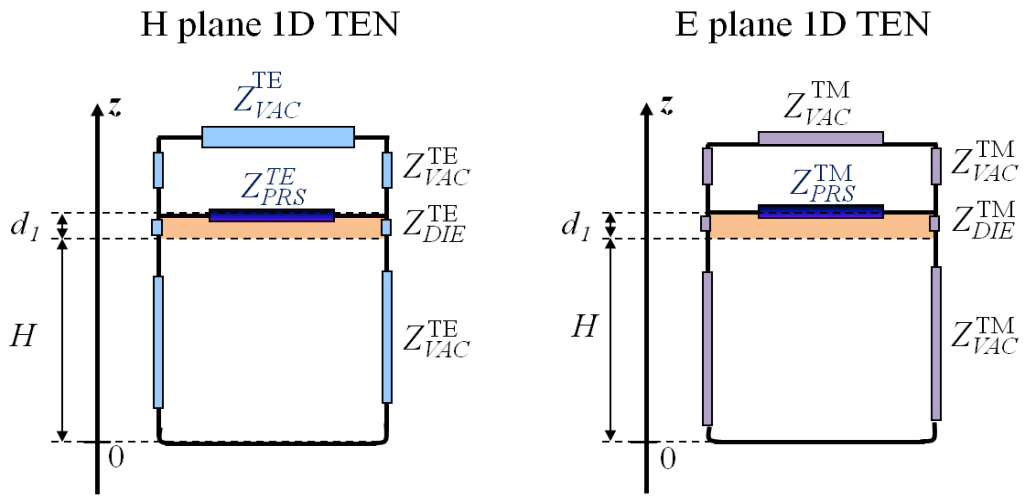

Fig. 3.5.5 One-dimensional TEN employed to analyse the two-dimensional structure of Fig. 3.5.4 in the (a) H plane, (b) E plane.

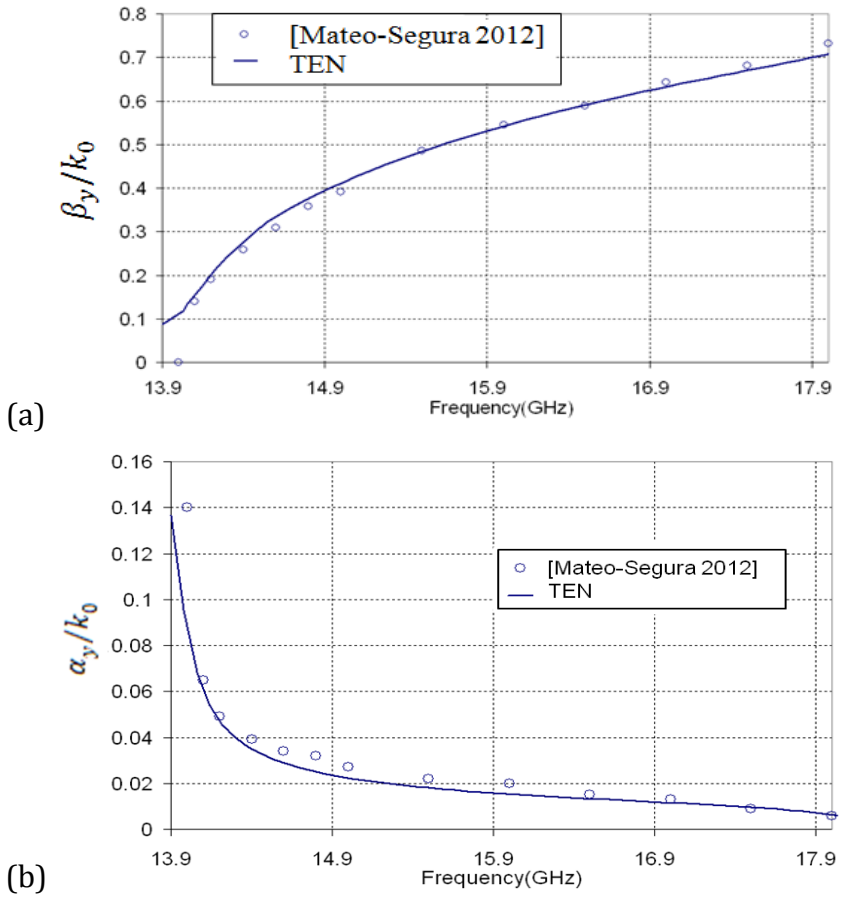

Fig. 3.5.6. Normalized propagation constant associated to the LWA of Fig. 3.5.4 in H plane. (a) Phase constant, (b) leakage rate.

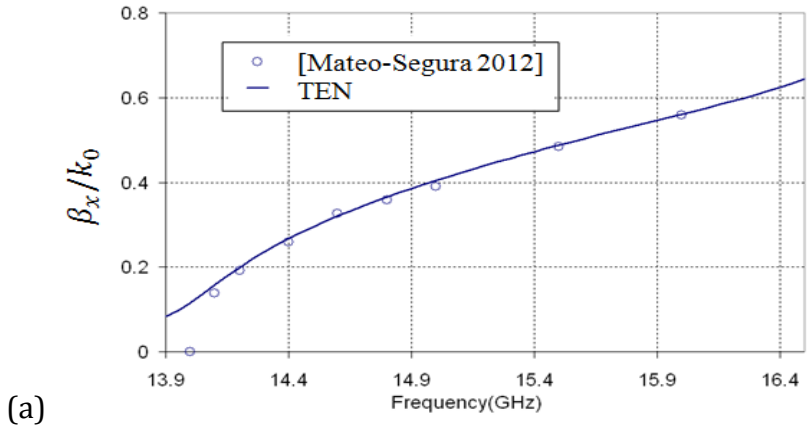

(a)

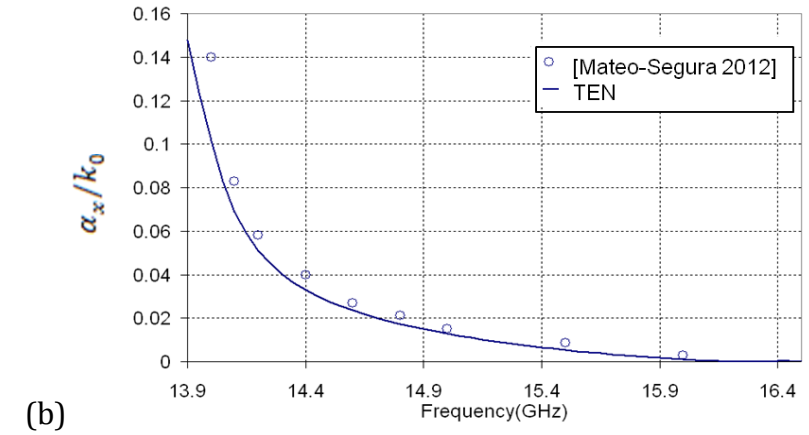

(b)

Fig. 3.5.7. Normalized propagation constant associated to the LWA of Fig. 3.5.4 in E plane. (a) Phase constant, (b) leakage rate.

The dispersion diagrams of Fig. 3.56 and Fig. 3.5.7 show the common LWA behaviour, the phase constant β increases with frequency and the leakage rate α decreases towards endfire direction. These figures also show superimposed the results obtained when using the technique presented in [Mateo-Segura 2012]. This full-wave approach makes use of method of moments and reciprocity to characterize the dispersion of 2D FP LWAs, thus being highly accurate but also computationally costly. Every space harmonic is considered by the previous technique, while the here employed TEN-based tool only accounts for the fundamental one. Therefore, the TEN-based tool can be accurately employed when the interaction produced by higher order harmonics is not relevant, taking advantage of its lower computational cost. The comparison of the values in Fig. 3.56 and Fig. 3.5.7 indicates very good agreement between the two techniques. Both of them differ when reaching the leaky-mode cutoff. In particular, [Mateo-Segura 2012] predicts null phase constant at approximately 13.91 GHz (see Fig. 3.5.6(a) and Fig. 3.5.7(a)), whereas the TEN approach predicts a value greater than

zero at this same frequency. This discrepancy is due to the fact that the technique presented in [Mateo-Segura 2012] estimates the phase constant from the pointing angle of the antenna, employing (3.1.4). As it was explained in the Section 3.1.2, at the leaky-mode cutoff frequency the splitting condition is satisfied, and due to the coalescence of the main radiated beams, the LWA points at broadside ($\theta_{RAD} = 0°$), although the phase constant is greater than zero. Thus, it must be highlighted that the TEN approach provides the most accurate result in this case.

3.5.2 Quarter wavelength antennas

As it was shown in Section 2.3.2, High Impedance Surfaces (HIS) may be used for miniaturizing purposes. In particular, FP LWAs with sub-wavelength profile can be produced loading the resonant cavity with a HIS [Goussetis 2007-II], [Feresidis 2005]. To a ray optics approximation, this can be attributed to the reduced reflection phase of the HIS-loaded ground plane. Here, it is analyzed a working example of an antenna such as the one shown in Fig. 3.5.8. The PRS employed in the previous example is now located above a HIS, which consists of patches with edge L_{HIS} = 4.1 mm, which is printed on a dielectric slab of thickness, d_2 = 1.15 mm and relative permittivity 2.2. The height of the cavity is H = 5.46 mm, which has been designed with the TEN-based tool for the antenna to produce a broadside pattern at 14GHz.

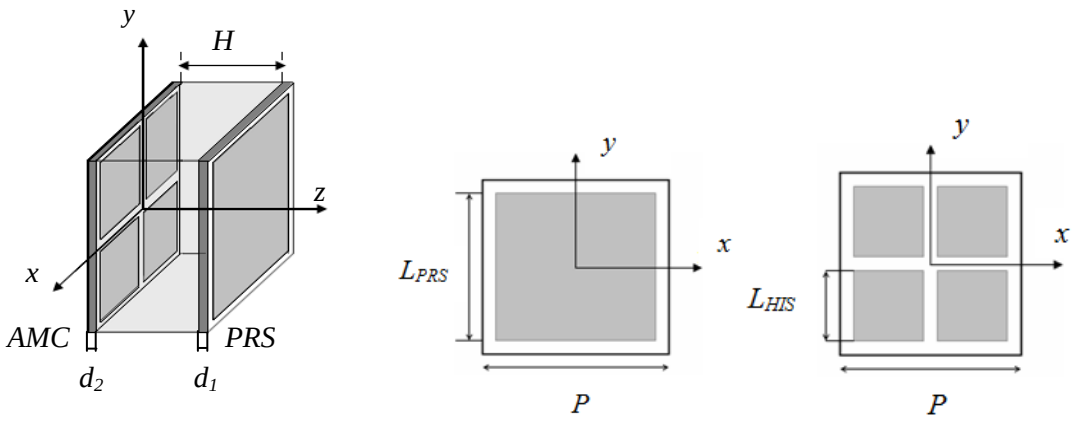

(a) (b) (c)

Fig. 3.5.8 (a) Layout of the resonant cavity leaky-wave antenna formed by metallodielectric PRS and HIS. (b) Unit cell of a square patch PRS array and (c) HIS array.

A similar study as the one performed for the half-wavelength antenna is now carried out. The 1D scenarios analyzed with the TEN are the ones in Fig. 3.5.2(b) and Fig. 3.5.3(b). The dispersion diagrams obtained are shown in Fig. 3.5.9 for a range of frequencies between 14 GHz and 15.6 GHz for the H plane and between 14 GHz and 16.5 GHz for the E plane. The results obtained employing the technique of [Mateo-Segura 2012] are also depicted in Fig. 3.5.9.

As the cavity is made thinner, the interaction between the two printed circuits starts becoming more and more relevant. This interaction is not accounted for by the simple TEN-approach, as it was explained in Section 2.2; whereas the full-wave method proposed in [Mateo-Segura] does. Consequently, as it is evident in Fig. 3.5.9, the agreement between the two methods for this antenna is reduced compared to the half-wavelength antenna, particularly in the H plane (*y*-direction).

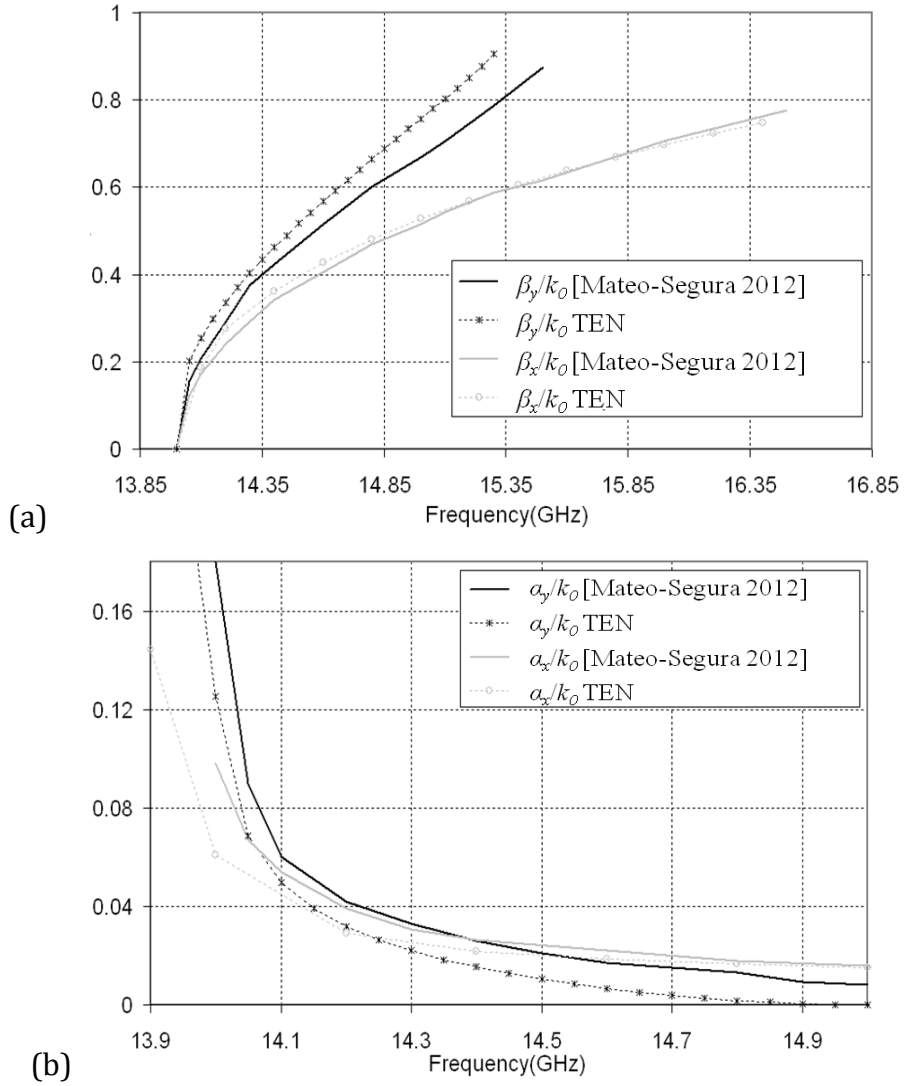

Fig. 3.5.9. Normalized (a) phase constant and (b) leakage rate versus frequency for the sub-wavelength antenna of Fig. 3.5.8, with dimensions (in mm) P = 9.0, H = 5.46, for the PRS: L_{PRS} = 8, d_1=1.5 and ε_r = 2.55 and for the HIS: L_{HIS} = 4.1, d_2 = 1.15 and ε_r=2.2.

This structure has been simulated with a commercial tool [HFSS 2011], using as source a Hertzian dipole polarized along *x* and placed in the middle of the

cavity (*i.e.*, z=*H*/2). The obtained radiation patterns are shown in Fig. 3.5.10, were it can be checked that broadside radiation is obtained at 14GHz, whereas for greater frequencies the beam becomes conical, as the splitting condition is no longer satisfied. The three-dimensional pattern at 14GHz is plotted in Fig. 3.5.11.

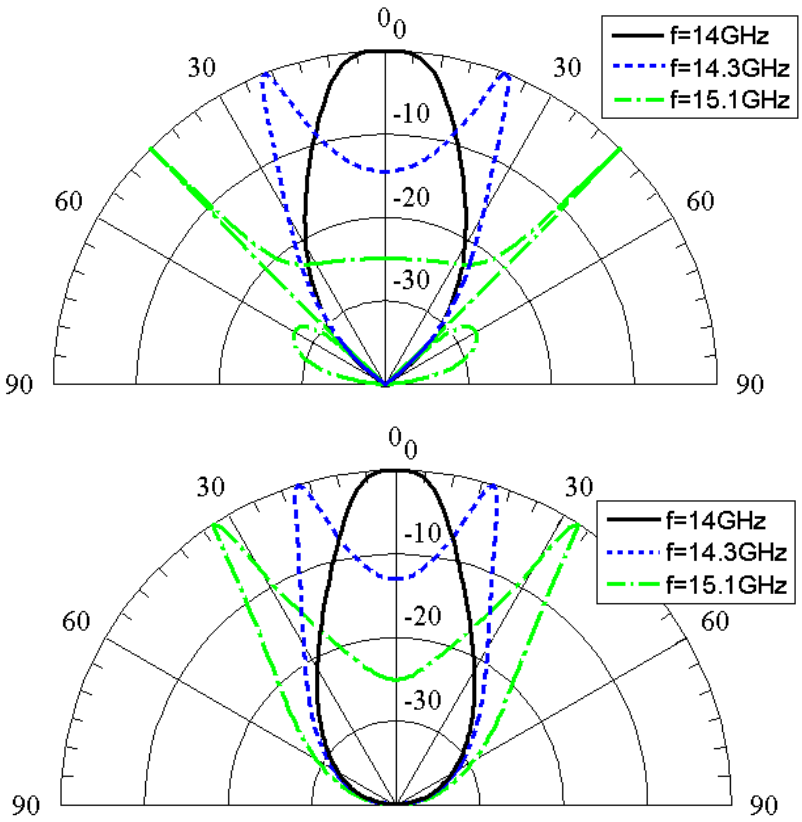

Fig. 3.5.10 (a) H- plane and (b) E-plane cuts of the antenna radiation pattern at different frequencies.

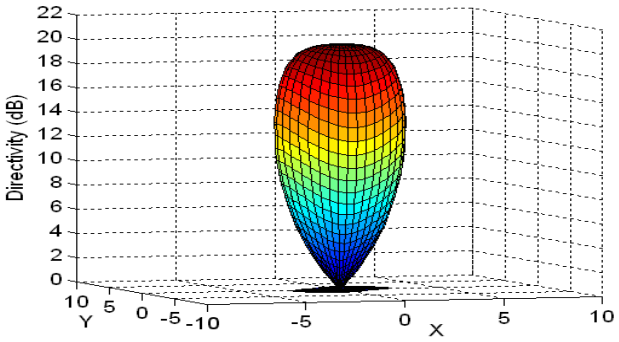

Fig. 3.5.11 3D radiation pattern at 14GHz.

3.5.3 Thin antennas

Very thin antennas with sub-wavelength profile can be produced employing a HIS with reflection phase lower than 0^o in the configuration of Fig. 3.5.8 [Feresidis 2005], [Kelly 2008], [Mateo-Segura 2011]. Due to the low profile, the interaction of higher order evanescent modes between the two arrays significantly increases. Here it is found one of the limitations of the TEN-based approach, and its accuracy gradually reduces compared to the half-wavelength profile LWA. In contrast, the technique proposed in [Mateo-Segura 2012] can be directly applied for thin antennas without loss of accuracy. This is next demonstrated by means of an example involving an antenna with profile $\lambda_0/7$ working at 14 GHz. The PRS is the same as in the previous studies and it is located at a distance H= 3.25mm ($\sim\lambda_0/7$) above a HIS array, which consists of patches with L_{HIS} = 4.3 mm printed on a dielectric slab of thickness, d_2 = 1.15mm and relative permittivity 2.2.

The obtained dispersion diagrams for the H- and E-plane are shown in Fig. 3.5.11 for frequencies between 14 - 14.6 GHz and 14 - 16.5 GHz, respectively. The interference of the side-lobes with the main lobe impedes the application of the employed techniques, in this case beyond 14.6 GHz for the H plane and beyond 16.5 GHz for the E-plane. This figure clearly shows how the accuracy of the TEN-based method has reduced even more for the $\lambda_0/7$ antenna, particularly at the H-plane. However, it must be highlighted that the proposed TEN-based approach is accurate for double-layer Fabry-Perot antennas with thickness over $\lambda_0/4$, and in this cases, it is much more efficient than full-wave based design tools such as [Carolina 2012]. Therefore, it can be used for the efficient design of novel double-layer 2D FP LWA, as it will be demonstrated in the next chapter.

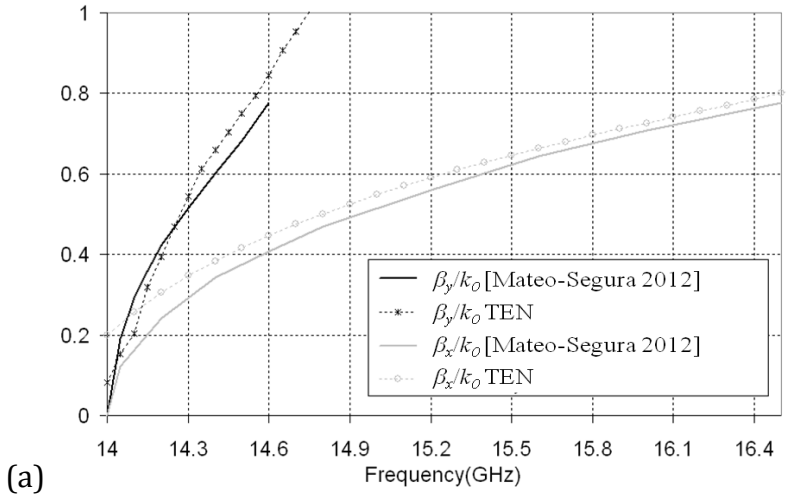

(a)

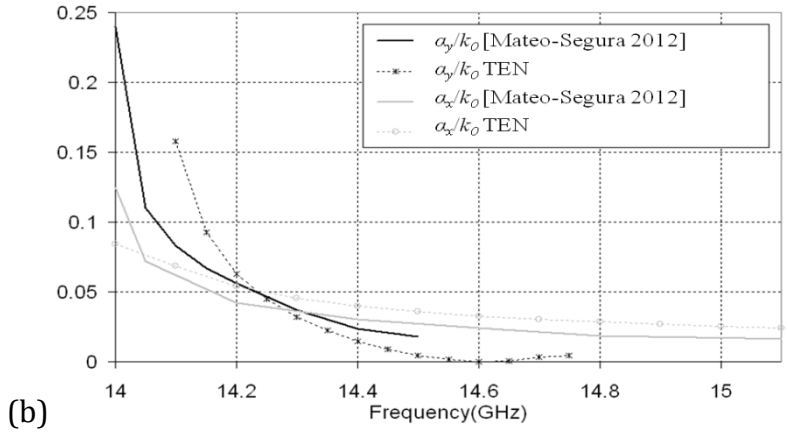

(b)

Fig. 3.5.12 Normalized (a) phase constant and (b) leakage rate versus frequency for the sub-wavelength antenna of Fig. 3.5.8, with dimensions (in mm) P = 9.0, H = 3.25, for the PRS: L_{PRS} = 8, d_1=1.5 and ε_r = 2.55 and for the HIS: L_{HIS} = 4.3, d_2 = 1.15 and ε_r=2.2.

3.6 Conclusions

In this chapter, it has been introduced an original one-dimensional double-layer Fabry-Perot LWA that enables the control over the radiation pattern main features. In Sections 3.2 and 3.3 it is explained that the new LWA is based on a hollow parallel-plate waveguide loaded with two periodic surfaces, which are formed by periodic arrays of printed metallic dipoles. One periodic array acts as a Partially Reflective Surface which can control the leakage rate by means of its transparency, while the second periodic array behaves as a High Impedance Surface which determines the scanning angle by means of its reflection phase. The TEN-based tool developed in Chapter 2 has been used for the analysis and design of this novel 1D LWA. It has been demonstrated that, once the cavity dimensions are chosen to operate at a desired frequency, the length of the dipoles allow the control of the leaky-mode propagation constant. This enables high-gain radiation patterns to be synthesized using standard photolithographic processes, without the need for modifying the waveguide structure. Compared to previous hybrid LWAs based on PCBs in dielectric waveguides, the proposed antenna avoids dielectric losses since a hollow waveguide is used as the host medium. To verify the concept and design theory, several LWA antenna prototypes operating at 15 GHz have been fabricated. Measured results agree with the predicted ones. It is demonstrated that it is indeed feasible to independently control the scanning angle and the directivity of the antenna at a fixed frequency, whilst keeping 90%

radiation efficiency. In addition, in Section 3.4 it has also been proven that the frequency scanning sensitivity of the novel antenna can also be controlled. The proposed topology increases the frequency scanning sensitivity, thus reducing the required bandwidth to scan the main beam from near broadside to near endfire. It avoids the use of dielectric-filled waveguides, thus minimizing the associated dielectric losses. Experimental results on fabricated prototypes have also been reported, showing very good agreement with theory. Thus **the first objective of this chapter (O4) has been accomplished**.

Double layered two-dimensional (2D) Fabry-Perot antennas have been subsequently studied in Section 3.5. In particular, three uniform LWAs are designed providing broadside radiation at 14GHz with different cavity profiles. In this section it is explained that the TEN-based approach developed in Chapter 2 can be employed for the analysis of 2D structures. The produced dispersion diagrams were in good agreement with those derived by a MoM-based technique. It is also shown that the validity of the single mode TEN is limited by the reactive interaction between the periodic layers due to evanescent higher-order Floquet harmonics. Therefore, very low-profile LWAs can not be accurately analyzed with the TEN technique. From these results it can be said that **the last objective of this chapter (05) has been fulfilled**.

The work developed in this chapter has given rise to the publication of 3 peer-review international journal paper (IJ), 5 international conference papers (IC) and 1 Spanish conference papers (SC). These references are copied below; they have been extracted from the complete list of publications of Section 5.3.

IJ2. **M. García-Vigueras**, J.L. Gómez-Tornero, G. Goussetis, A. R. Weily, and Y. Jay Guo, "Enhancing frequency-scanning response of leaky-wave antennas using high impedance surfaces," *IEEE Antennas and Wireless Propag. Lett.*, vol. 10, pp. 7–10, March 2011.

IJ3. **M. García-Vigueras**, J. L. Gómez-Tornero, G. Goussetis, A. R. Weily, and Y. J. Guo, "1D Leaky wave antenna employing parallel-plate waveguide loaded with PRS and HIS," *IEEE Trans. Antennas Propag*., vol.59, no.10, pp.3687-3694, Oct. 2011.

IJ4. C. Mateo-Segura, **M. García-Vigueras**, G. Goussetis, A. P. Feresidis, and J.L. Gómez-Tornero, "A simple technique for the dispersion analysis of Fabry-Perot cavity leaky-wave antennas", *IEEE Trans. Antennas Propag.*, vol.60, no.2, pp.803-810, Feb. 2012.

IC2. **M. García-Vigueras**, C. Mateo-Segura, J.L. Gómez-Tornero, G. Goussetis and A. Feresidis "Analysis and Design of 1D and 2D High-Gain Leaky-Wave Antennas using Metallodielectric FSS and AMC", *Proceedings of the 3rd International Congress on Advanced Electromagnetic Materials in Microwaves and Optics*, London, UK, 30-4 September, 2009 (INVITED).

IC3. J.L. Gómez-Tornero, **M. García-Vigueras**, G. Goussetis, Andrew R. Weily, Y. Jay Guo "Efficient Analysis and Flexible Design of 1D Leaky- Wave Antennas composed by a Parallel-Plate Waveguide loaded with two Metallodielectric FSS", *Proceedings of the International Symposium on Antennas and Propagation*, Bangkok, Thailand, 20-23 October, 2009.

IC4. Mateo-Segura, **M. García-Vigueras**, G. Goussetis, J.L. Gómez-Tornero and A. Feresidis"Analysis of Sub-wavelength Cavity Leaky-Wave Antennas with

High-Impedance Surfaces", *Loughborough Antennas & Propagation Conference*, Loughborough, UK, 16-17 November, 2009.

IC5. **M. García-Vigueras**, J.L. Gómez-Tornero, G. Goussetis, David Cañete, Fernando Quesada and A. Álvarez-Melcón, "Leaky-Mode Dispersion Analysis in Parallel-Plate Waveguides Loaded with FSS and AMC with Application to 1D Leaky-Wave Antennas", IEEE *AP-S Int. Symp*, Charleston, SC USA, June 1-5, pp. 1-4, 2009.

IC6. C. Mateo-Segura, **M. García-Vigueras**, G. Goussetis, J.L. Gómez-Tornero and A. Feresidis "Efficient dispersion analysis of 2D High-Gain Leaky-Wave Antennas",European Conference on Antennas & Propagation 2010, Barcelona, Spain, 12-16 April, 2010.

SC2. **M. García-Vigueras**, R. Guzmán-Quirós, J.L. Gómez-Tornero, J.S. Gómez-Díaz, and A. Álvarez-Melcón, "Estudio de la dispersión de modos Leaky en guías de onda de placas paralelas cargadas con FSS y AMC con aplicación en antenas Leaky-Wave", XXIV Simpósium Nacional de la Unión Científica Internacional de Radio URSI, 16-18 September 2009, Santander (Cantabria), Spain.

Chapter 4:

Synthesis of tapered double-layer Fabry-Perot LWA

In this chapter it is aimed the synthesis of tapered double-layer Fabry-Perot leaky wave antennas, both in one-dimensional and two-dimensional topologies. Thanks to the work carried out in the previous chapters, now we have a PRS-HIS LWA with the key feature of providing independent control over its propagation constant and that has been completely characterized with frequency and its geometry. Whereas the antennas proposed in the previous chapter are uniform (*i.e.*, with constant dimensions of the periodic unit-cell), tapered LWAs are here designed, where the unit cell dimensions are modulated in order to shape the radiated fields. At this point, it is possible to take full advantage of double-layer FP LWAs and perform the synthesis of desired aperture distributions. Thus, the following specific objectives will be pursued in this chapter:

O6. Analysis and design of double-layer tapered one-dimensional Fabry-Perot leaky-wave antennas.

O7. Analysis and design of double-layer tapered two-dimensional Fabry-Perot leaky-wave antennas.

This chapter is organized as follows:

Firstly, a state-of-the-art review on the tapering of one-dimensional and two-dimensional LWAs and its applications is explained in **Section 4.1**.

Secondly, in **Section 4.2,** it is described an original technique for the efficient synthesis of double-layer Fabry-Perot leaky-wave antennas. It is based on the study of the reflection characteristics presented by the two periodic surfaces that form the cavity. The synthesis technique avoids the search for modal solutions in the complex plane, which is typically needed to characterize the dispersion of the leaky modes associated with the antenna geometry. Instead it involves the solution of two simple equations, so that the desired aperture distribution (amplitude and phase) can be directly synthesized.

The previous synthesis equations are applied in **Section 4.3** in order to shape the near field patterns in 1D FP LWAs and reduce their sidelobes level for any desired scanning angle. Numerical and experimental results are shown in order to prove the efficiency of the synthesis approach

Later, the synthesis equations are also employed in **Section 4.4** and **Section 4.5** for the control of the illumination of 1D and 2D FP LWAs which point at broadside. A quasi-uniform taper is here proposed in order to achieve high aperture efficiency, while assuring high radiation efficiency and to minimize diffraction and standing waves.

Finally, in **Section 4.6** the main conclusions and results will be summarized, together with the discussion about the achievement of the aimed objectives.

4.1 Introduction

Uniform Leaky-Wave Antennas (LWAs) are those which geometry is invariant along their length (even if they are periodical, the periodic unit-cell dimensions remains constant along the whole antenna). In these structures, the complex propagation constant does not change along the radiating aperture. Therefore, the near field illumination has linear phase and exponential amplitude variation. By modulating the geometry of the antenna, such aperture distributions can be modified, resulting into a wide variety of new features and new applications for LWAs.

The control of the illumination aperture distribution in LWAs has been extensively dealt with by antenna engineers from early times. The first attempts were focused on 1D topologies, an early example can be found in [Honey 1959]. The underlying concept is the control of the leaky-mode longitudinal complex wavenumber along the LWA aperture. As it was convened in the previous chapter, in the case of one-dimensional antennas, the longitudinal wavenumber is defined in the y direction as

$$k_y = \beta_y(y) - j\alpha_y(y), \tag{1}$$

whereas in the case of two-dimensional LWAs, a radial wavenumber is defined

$$k_\rho(\rho) = \beta_\rho(\rho) - j\alpha_\rho(\rho). \quad (2)$$

In order to shape the radiation pattern of the antenna, both the phase constant (β) and the leakage rate (α), should be independently varied, as it was explained in [Oliner 1993]. To this end, the topology of the LWA must be properly engineered to support the requested tapering of the wavenumber at each point of the aperture.

The illumination synthesis has been classically applied in 1D LWAs to the **reduction of the sidelobe level** (SLL) while keeping a highly-directive main scanned beam. As sketched in Fig. 4.1.1(a), uniform 1D leaky waves decay exponentially in the near field, which translated to the far fields, results in a SLL of -13dB in the radiation pattern (see Fig. 4.1.1(c)). Tapering the magnitude of the radiating near fields by modulating the leakage rate (α_y) along the antenna aperture, the value of the SLL can be reduced. The value of the phase constant, or equivalently, the radiation angle (θ_{RAD}), should be maintained fixed to the same value so that the far-field radiation from all sections of the LWA is pointing to the desired direction [Oliner 1993]. As an example, a synthesized cosine near field pattern is shown in Fig. 4.1.1(b), which associated radiation pattern has a SLL of −23 dB (see Fig. 4.1.1(c)). This cosine illumination is provided by the modulated value of α_y at each point of the antenna length and constant θ_{RAD} shown in Fig. 4.1.1(d). The reduction of the sidelobe levels has been applied to different LWA technologies, such as inductive-grid-loaded cavities [Honey 1959], non-radiative dielectric waveguides [Sánchez 1987], [Schwering 1988], strip-loaded dielectric guides [Ghomi 1993], [Zong-Wen 1997], stub-loaded, stepped and rectangular waveguides [Di Nallo 1995, 1997-I and II], [Lampariello 1998], [Tsuji 2003 and 2007], corrugated dielectric-coated conducting cylinders [Chang-Won 2003], hybrid printed-waveguides [Gómez 2005-III and IV], ferrite-loaded waveguides [Kodera 2010], and more recently in Substrate Integrated Waveguide (SIW) LWAs [Cheng 2011]. Active tapering was proposed in [Casares-Miranda 2006] to distribute amplifiers along a metamaterial-type LWA. Although an interesting idea, the use of active circuits to taper the aperture would increase the antenna cost significantly. Pattern shaping has also been applied to design broadband tapered microstrip LWAs [Hong 2003], [Jin-Wei 2010]. Some examples are shown in Fig.

4.1.2, which show how the LWA geometry is modulated to taper the wave propagation constant, and therefore, achieve the SLL reduction.

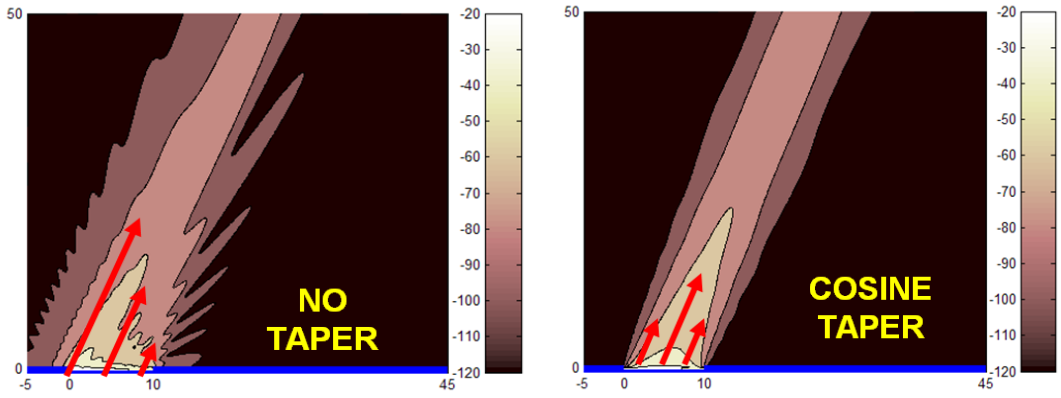

(a) (b)

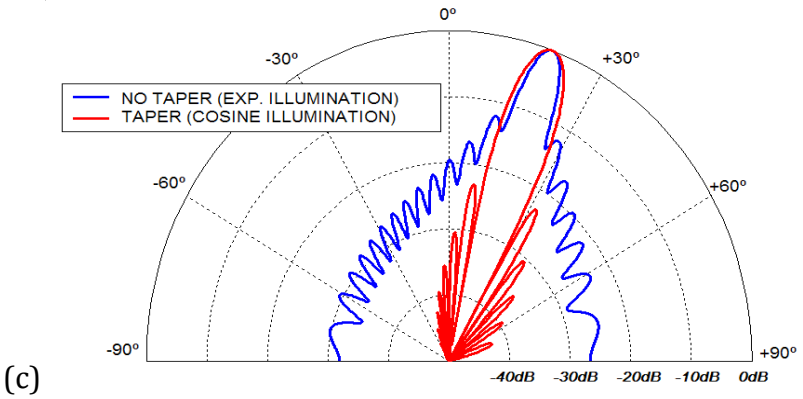

(c)

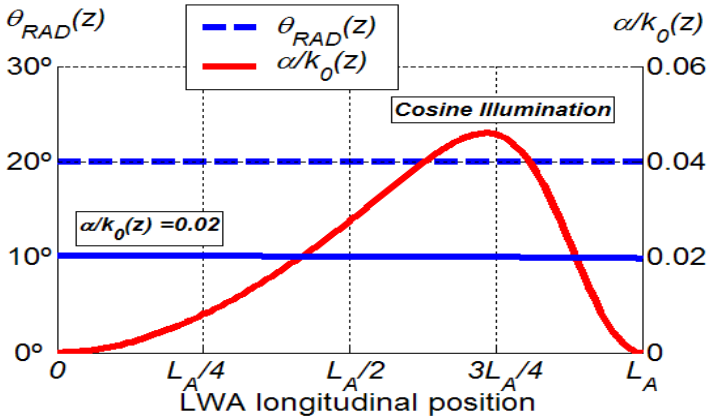

(d)

Fig. 4.1.1 SLL reduction in 1D LWAs. Longitudinal near fields above the 1D radiating apertures of (a) uniform (b) cosine-tapered LWAs. (c)Radiation patterns. (d) α/k_0 and θ_{RAD} at each point of the tapered antenna.

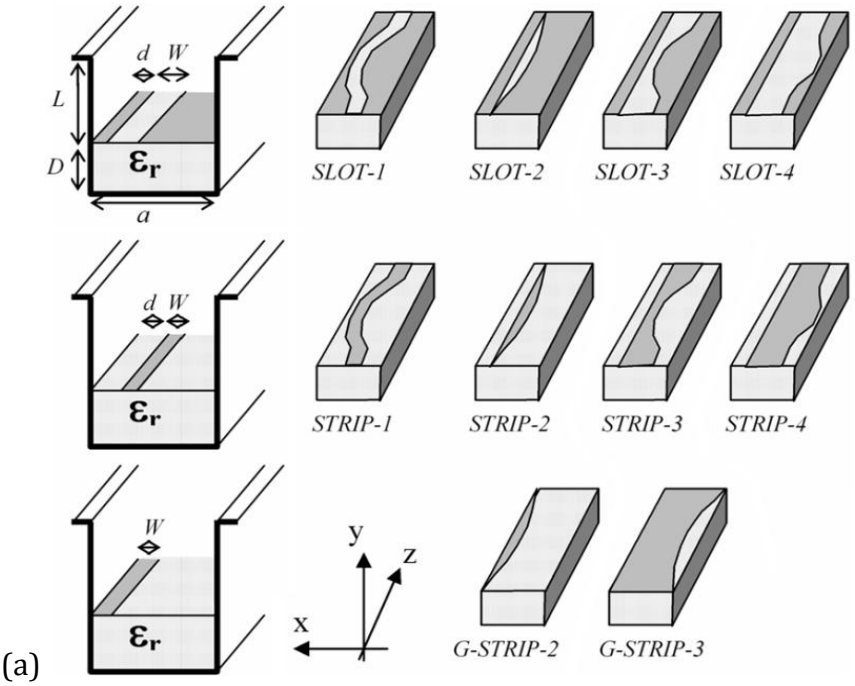

(a)

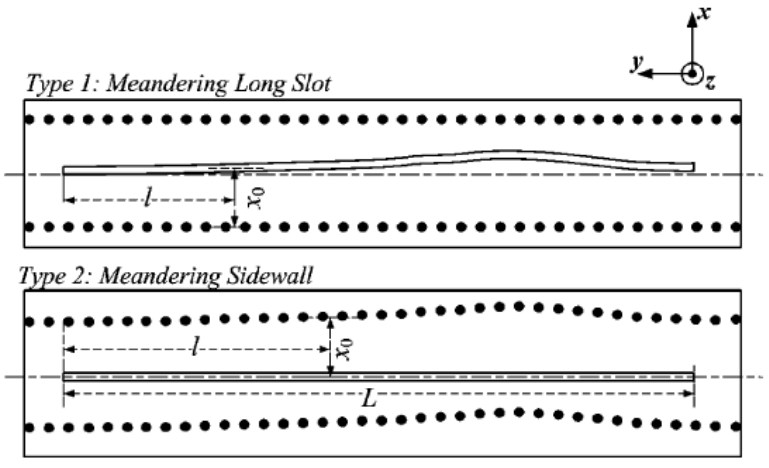

(b)

Fig. 4.1.2 Tapered 1D LWAs for SLL reduction, (a) hybrid waveguide-planar technology LWAs [Gómez 2005-III] (b) substrate integrated waveguide long slot LWAs [Cheng 2011].

More recently, new unconventional 1D LWA tapering procedures have been proposed, where not only the leakage rate (α_y), but also the phase constant (β_y) is varied along the aperture length. These techniques were firstly applied to the synthesis of **broad-beam patterns** [Burghignoli 2003], [Gómez 2011-II]. In order to obtain a broad main radiated beam, with high rejection out from the prescribed wide beam, the radiated leaky waves must diverge. Othera firstly proposed to curve a dielectric grating LWA to make the emitted rays converge/diverge and thus obtain the desired broad-beam patterns [Othera 1999, 2001 and 2002].

However, Burghignoli later proved that by applying nonstandard tapering techniques, broad-beam LWAs could be obtained without the need of curving the LWA [Burghignoli 2003]. In this way, the volume and manufacturing complexity of the structure is reduced. Gómez goes one step further in [Gómez 2011-II], where he examines practical design issues and validates this nonstandard tapering approach using the hybrid waveguide printed-circuit technology proposed in [Gómez 2005-II]. An example of this nonstandard tapering technique is shown in Fig. 4.1.3. The near field patterns of Fig. 4.1.3(a) and (b) illustrate the differences between uniform and divergent illuminations. It can be seen that in the second case, the beam angle is varied to make the emitted rays diverge in a specific fashion. Finally, Fig. 4.1.3(c) shows two examples of broad-beam patterns where the pointing angle along the antenna is diverged within the range $[0°, 40°]$ and $[-20°, 60°]$, respectively. For comparison purposes, that figure also shows the radiation pattern of an antenna were θ_{RAD} is kept fixed to 20°.

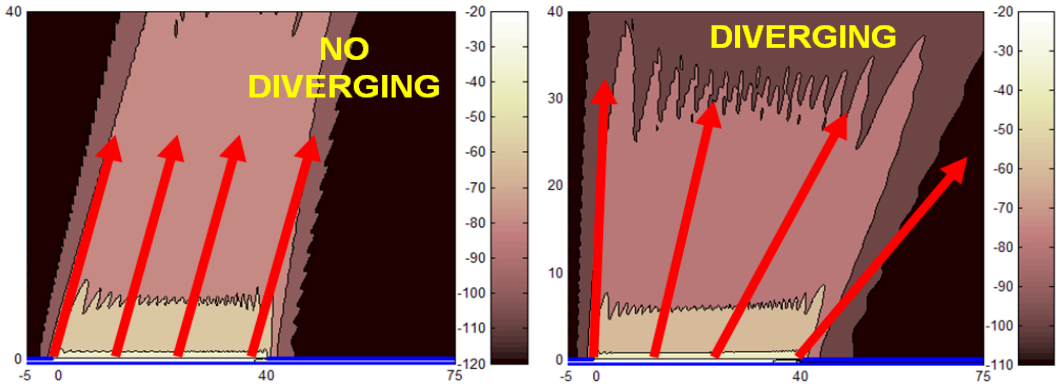

(a) (b)

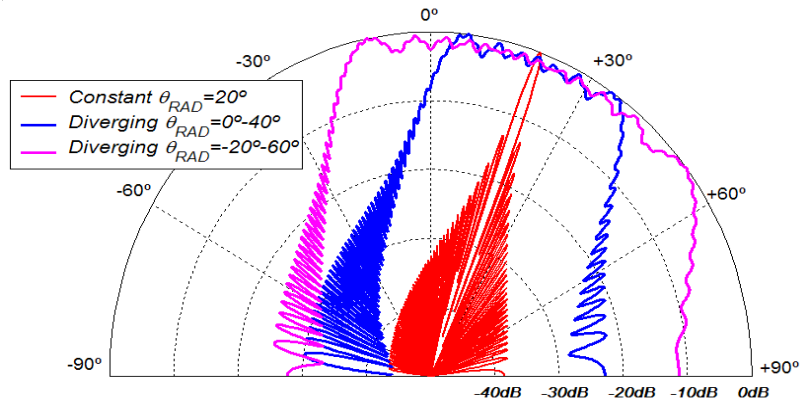

(d)

Fig. 4.1.3 Diverging broad beam synthesis in 1D LWAs. Longitudinal near fields above the 1D radiating aperture with (a) uniform/ (b) diverging illumination. (c) Broad-beam radiation patterns. (from [Gómez 2011-II])

Non-standard tapering procedures are also employed to design **conformal** 1D LWAs, were the tapering techniques amend the effect of the LWA curvature allowing the conformal structure to refocus its radiation main beam and have a comparable performance as the planar version. An example of the effects of conforming a LWA in the radiation pattern is shown in Fig. 4.1.4, which clearly shows the effectiveness of the tapering technique. Figure 4.1.5 shows the conformal metamaterial-based transmission-line proposed in [Hashemi 2008]. Other tapered conformal LWAs are also designed in [Losito 2007] and [Gómez 2011-III]. Gómez also proposed tapering techniques to produce **radiation diagrams with wide nulls** [Gómez 2010], an example shows in Fig. 4.1.6. Another recent contribution to unconventional pattern synthesis achieved in 1D LWAs is presented in [Martínez-Ros 2012]. Here, the LWA is designed in SIW technology and allows the independence control over β_y and α_y, as proven in [Martínez-Ros 2011].

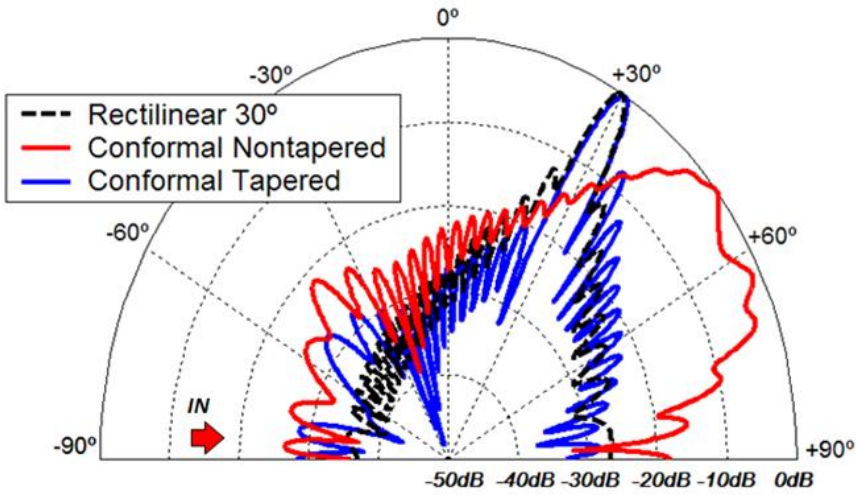

Fig. 4.1.4 Radiation pattern of 1D LWA.

Finally, converging **near-field focusing patterns** were proposed in [Gómez 2011-IV] and [Losito 2009] by modulating both the phase and leakage constant along 1D LWAs. These antennas could be extensively applied, for example in hyperthermia therapy systems and non-contact (remote) sensing or wireless power transmission. Figure 4.1.7 illustrates this case with an example. The near field patterns of Fig. 4.1.7(a) and (b) show how the radiated energy converges in a focus.

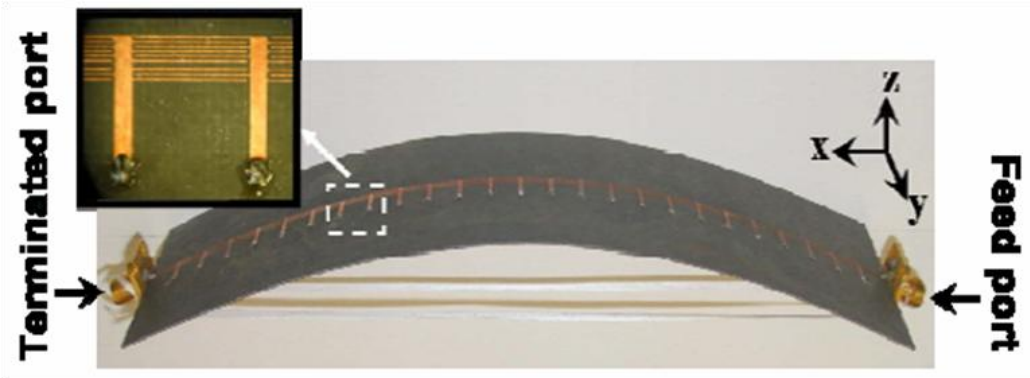

Fig. 4.1.5 Conformal metamaterial-based LWA proposed in [Hashemi 2008].

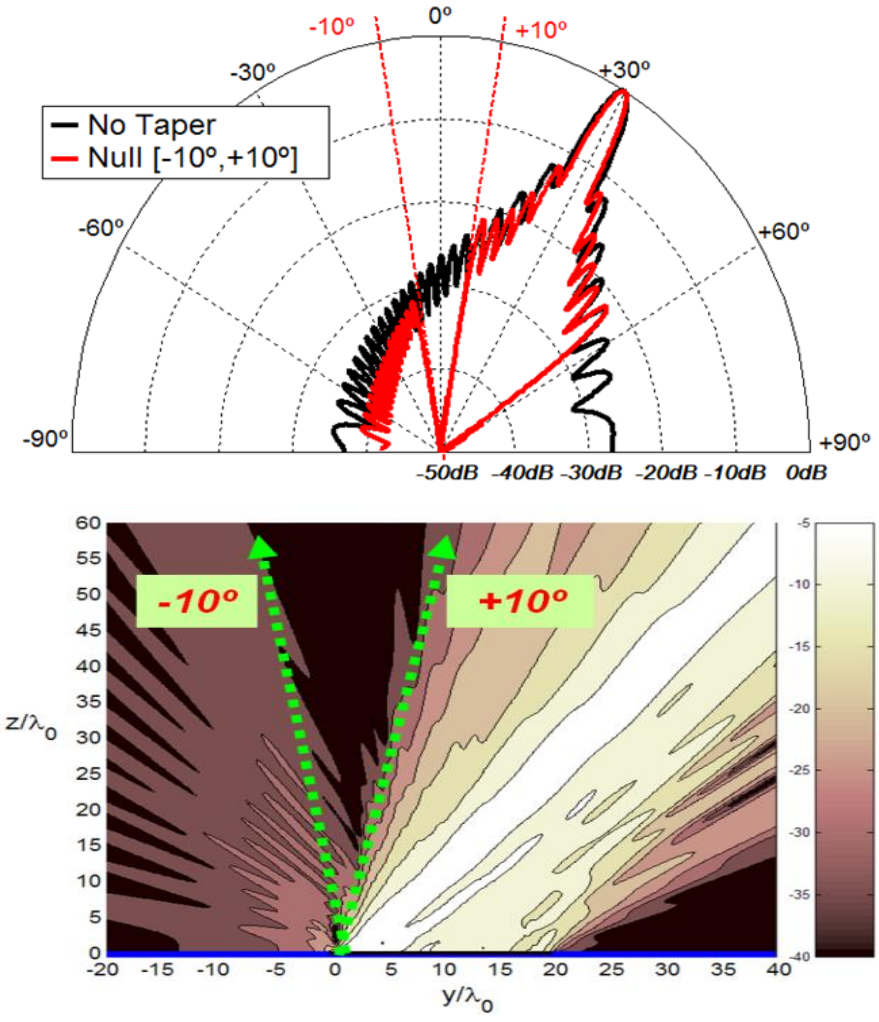

Fig. 4.1.6 (a) Radiation diagram with wide null between [−10°, 10°]. (b)Near field pattern in the tapered 1D LWA.

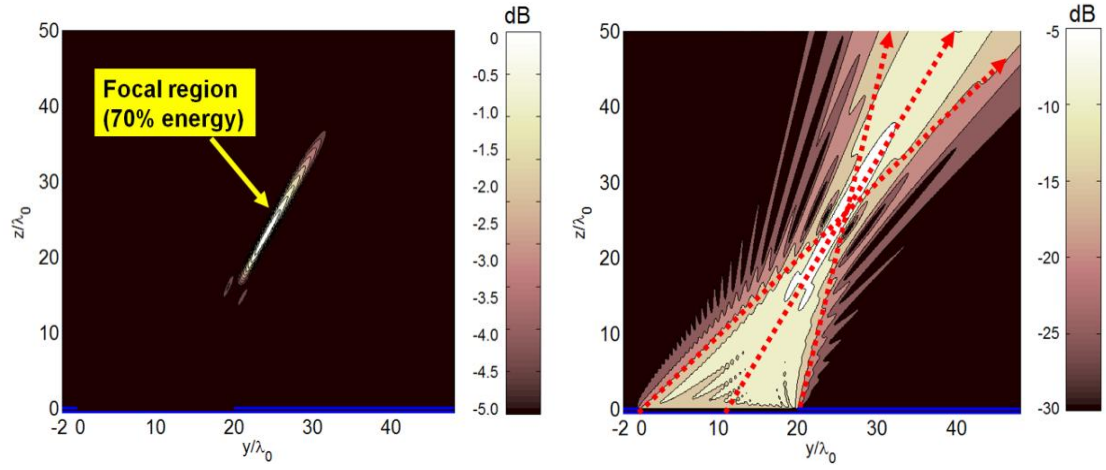

(a) (b)

Fig. 4.1.7 Near field focusing. Converging pattern with (a) -5dB/(b)-30dB scale.

With the development of two-dimensional LWAs, **tapering techniques have started to be also applied to 2D structures**. Normally, the purpose here is not the reduction of the SLL, due to the fact that the illumination in 2D LWAs is already quasi-cosine shaped [Jackson 2008]. The first attempts of 2D tapering were performed in Fabry-Perot cavity LWAs [Yeo 2009], [Wu 2010]. Their aim is to increase the antenna gain and bandwidth. An example of the obtained results is shown in Fig. 4.1.8. In these works, the bottom layer of the resonant cavity is physically modulated; the sketches of the proposed bottom layers are shown in Fig. 4.1.9. In contrast to the previous 1D tapering techniques, no accurate control over the propagation constant k_ρ is performed. Thus, it is not reported how β_ρ or α_ρ must be modulated along the structure in order to achieve their goal.

Later, when the synthesis of tapered 2D LWAs attracted more attention, research was focused on the accurate control over k_ρ and the concept of "**metasurfing**" was introduced [Maci 2011 and 2012]. Engineered artificial surfaces which allow the local modification of the propagation constant (at a constant frequency) can be considered as modulated reactance surfaces [Oliner 1959] or metasurfaces [Maci 2011 and 2012]. Therefore, metasurfing arises as a reinterpretation of tapering, which consists in the synthesis of an inhomogeneous surface impedance that provides a desired dispersion equation. In this way, the modulated surfaces of Fig. 4.1.9 can also be named as metasurfaces.

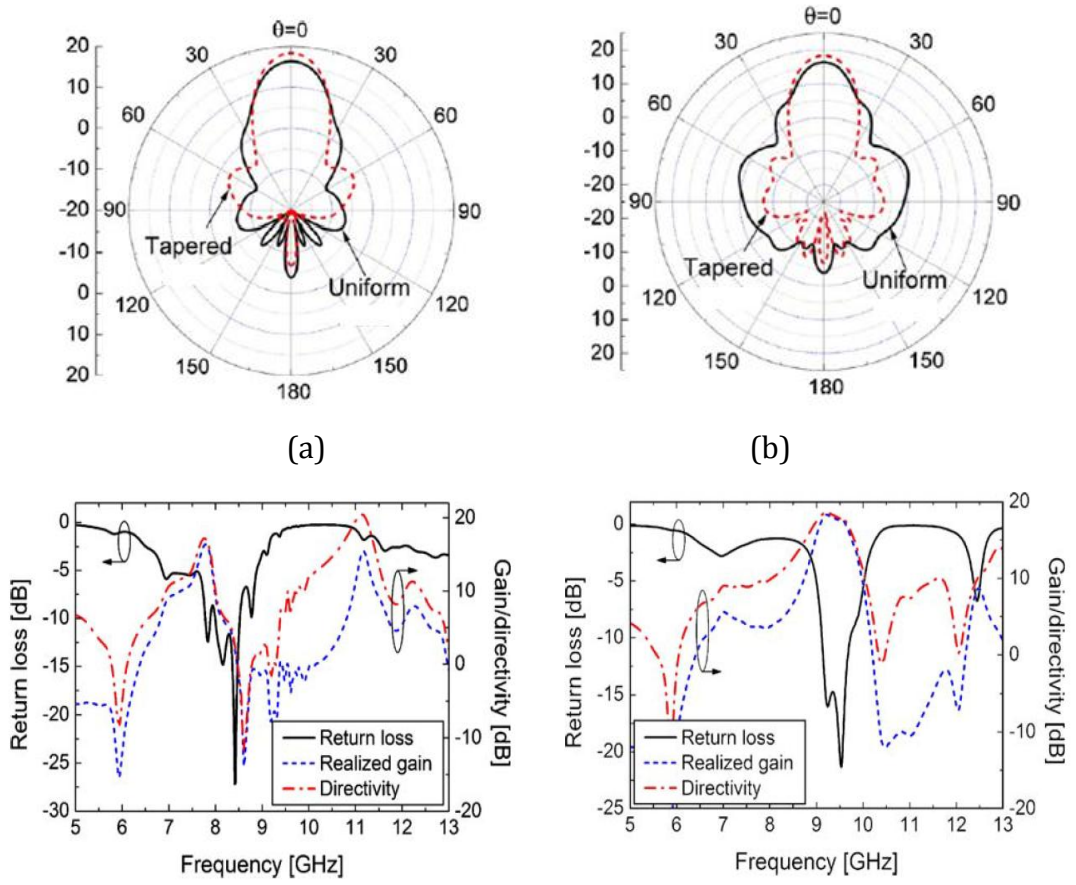

Fig. 4.1.8 Tapering of 2D FP LWAs. Realized gain in (a)H- (b)E-plane. (c) Return loss, gain and directivity in (c)uniform (d)tapered design.

(Figs. 2, 3 and 4 in [Yeo 2009])

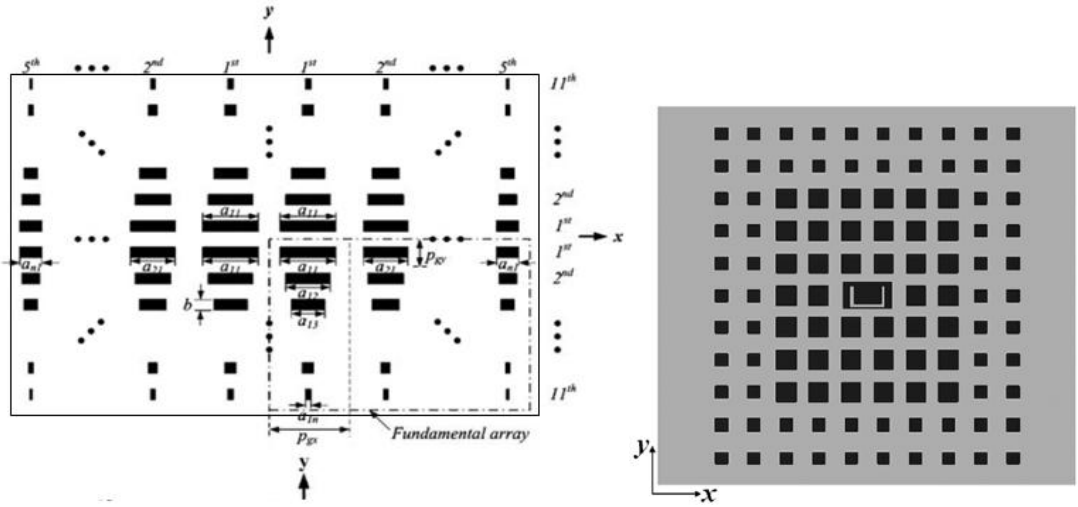

Fig. 4.1.9 Tapered surfaces employed as bottom layers of 2D FP LWAs in (a) [Yeo 2009] and (b) [Wu 2010].

Holographic-surface antennas [Sievenpiper 2005] can also be interpreted as tapered 2D LWAs, where a local modulation of the surface impedance leads to a transformation from a guided surface-wave to a radiative leaky-wave. The connection between holographic pattern and the leaky wave mechanism was clarified in [Nannetti 2007]. Thus, the concepts of artificial complex surfaces or metasurfaces [Kildal 2005], [Fong 2010], sheet impedances [Holloway 2009], and transformation electromagnetics [Pendry 2006],[Engheta 2006] are also related to the modulation of leaky waves and the design of holographic surface 2D LWAs. As an example, the modulated surface proposed in [Fong 2010] is shown in Fig. 4.1.10(a), which consists of an array of sub-wavelength metallic patches on a grounded dielectric substrate. The size of the patches is varied in order to achieve a desired dispersion of the input wave. In particular, they produce a scattered leaky wave with circular polarization (straight arrows in Fig. 4.1.9(b)) from a linearly polarized point source which excites a surface wave (undulating arrows in Fig. 4.1.9(b)).

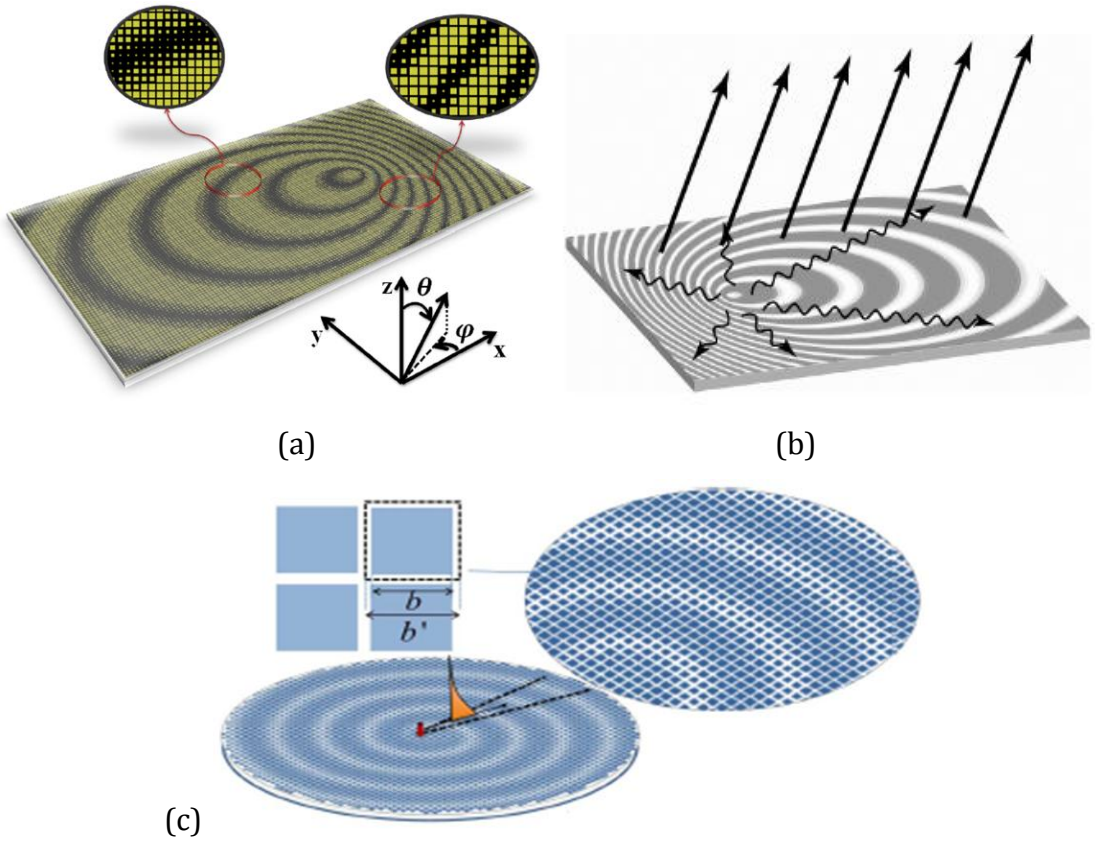

(a) (b)

(c)

Fig. 4.1.10 Holographic antennas proposed in (a)[Fong 2010], (b) [Minatti 2011-I and II].

Recently, holographic LWAs have been proposed to produce highly directive circularly polarized radiation patterns which radiate at broadside, from very flat structures which are simply fed by a single-point coaxial probe [Minatti 2011-I and II]. The scheme of this antenna is displayed in Fig. 4.1.10(c). The control over β_ρ or α_ρ is achieved employing the Oliner-Hessel method [Oliner 1959], able to predict the leaky-mode radial complex propagation constant k_ρ for a given surface modulation index and period.

Holographic printed-slot leaky-wave lenses have been also recently presented in [Gómez 2012]. In this case, focused near-field patterns are synthesized by modulating the radial separation between slots and the width of the slot unit-cell. Pictures of the proposed lens are depicted in Fig. 4.1.11. This low-profile structure provides high radiation and aperture efficiency, using a very simple coaxial probe feeding.

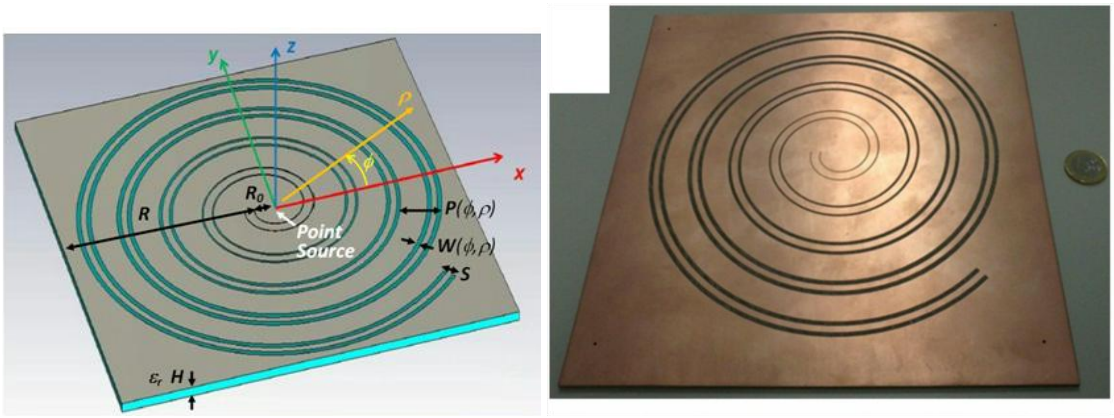

Fig. 4.1.11 Holographic lenses proposed in [Gómez 2012].

4.2 Synthesis equations

Once the technology that provides a flexible control over k_y has been chosen, the most intricate aspect of the pattern shaping is to find an appropriate geometry synthesis technique to determine the cross-sectional dimensions along the LWA length that produce the required complex wavenumber. Typically, this entails at least two geometrical degrees of freedom which are carefully selected to tune the phase constant (β) and the leakage rate (α) in Eq. (4.1.1) or (4.1.2). In practice, however, this is not trivial due to the fact that the geometrical degrees of freedom and the real and imaginary part of the complex wavenumber are coupled. In other words, the geometrical parameters of the LWA that have control over β_y also affect α_y, and vice-versa. Therefore, traditional synthesis approaches were based on iterative techniques to mitigate this inter-dependence [Oliner 1993], [Di Nallo 1995, 1997-I and II], [Hong 2003]. These techniques typically involve the solution of a large number of non-canonical eigenvalue problems in the complex plane, which is computationally costly. To avoid these costly iterations in the design, some authors chose to adjust α_y assuming small variation of β_y [Ghomi 1993], [Cheng 2011], [Casares-Miranda 2006]. However, this approximation might lead to undesired phase-aberration effects which would result in a loss of directivity as shown in [Gómez 2005-III]. Alternative techniques for avoiding the non-canonical complex eigenvalue problem involve reciprocity and pattern matching [Mateo-Segura 2012], but it request the expensive computation of full-

wave near fields inside the cavity. Finally, a simultaneous variation of the two design parameters can be performed to post-process the resulting two dimensional dispersion charts, as proposed in [Gómez 2005-III and 2011-II]. This approach allows the direct design of the tapered LWA (no iterations are requested), but a large set of dispersion data must be processed.

In this section it is proposed a direct non-iterative synthesis technique which does not need the computation of two-dimensional dispersion data, specifically suited to the design of tapered Fabry-Perot LWAs, and which accurately takes into account the coupling between the geometrical parameters and the complex leaky wavenumber. The proposed technique involves the solution of a set of two linear equations, one related to the design of the tapered PRS and the second related to the tapered HIS. The key feature of this approach lies in the fact that *it is based on the study of reflection rather than the study of leaky-mode dispersion* [Maci 2005]. As a result, this approach avoids the minimization of the transcendental equation that describes the homogeneous electromagnetic problem, which mathematically translates to a complicated task of zero finding for a complex function in the complex plane (β, α) to search for the leaky-mode solutions [Oliner 1993], [Maci 2005], [Cano 1995], [Gómez 2004-III]. Since this is not an iterative method, the antenna parameters can be directly extracted from the desired tapered aperture distribution, thus dramatically reducing the computational cost, which is very important for real-time synthesis of reconfigurable antennas. At the same time, the mutual dependence of the PRS and HIS geometry on β and α is automatically considered, thus avoiding any approximation which might lead to undesired phase and amplitude aberrations.

The proposed synthesis approach is presented in this section by means of an example involving the 1D PRS-HIS LWA configuration presented in the previous chapter (Section 2.3). The antenna is schematically depicted in Fig. 4.2.1(a) and it comprises a one-dimensional Fabry-Perot cavity formed between a PRS and a HIS placed in a parallel-plate waveguide. As explained in the introduction, it is essential to simultaneously control the phase constant (β_y) and the leakage rate (α_y) of the propagating leaky wave [Oliner 1993]. This control is flexibly provided by the proposed LWA topology as demonstrated in Section 2.3. In this structure, the

length of the metallic dipoles of the PRS and the HIS (L_{PRS} and L_{HIS} in Fig. 4.2.1(a)) can be adjusted to modify β_y and α_y over a wide range of values. The design goal of a tapered LWA is the determination of $L_{PRS}(y)$ and $L_{HIS}(y)$ along the antenna length that provides the desired tapering in the leaky-mode complex propagation constant β_y(y) and $\alpha_y(y)$ in Eq. (4.1.1).

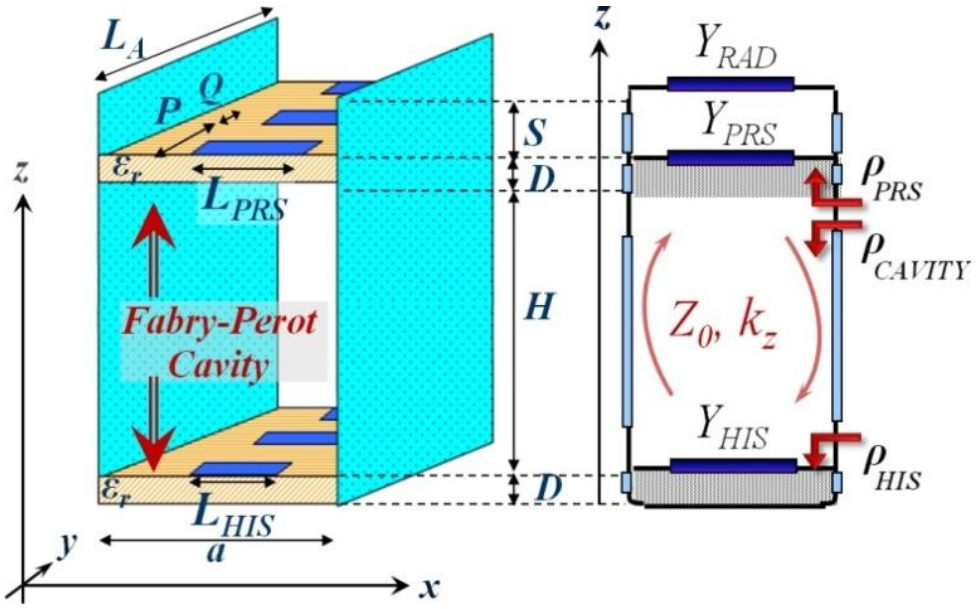

(a) (b)

Fig. 4.2.1 (a) Configuration of the 1D FP LWA (b) transverse equivalent network (a = H = 11 mm, S = 5 mm, D = 1.13 mm, ϵ_r = 2.2, P = 1.5 mm and Q = 0.5 mm).

As commented in the introduction of this chapter, one way to pursue the synthesis of the antenna radiation pattern is to employ two-dimensional leaky-mode dispersion charts as originally proposed in [Gómez 2005-III]. In our case, the dispersion of the leaky-mode phase and leakage rates for all potential values of L_{PRS} and L_{HIS} can be obtained from the Transverse Equivalent Network (TEN) shown in Fig. 4.2.1(b). To this end, as it was explained in Section 2.3, the Transverse Resonance Equation (TRE) associated with the previous TEN must be solved for the unknown leaky-mode complex propagation constant k_y, and for every possible pair of values (L_{PRS}, L_{HIS}). This is a very cumbersome task, since a zero search in the complex plane (β_y, α_y) must be performed for every pair (L_{PRS}, L_{HIS}) [Oliner 1993], [Cano 1995], [Gómez 2004-III]. Then, by post processing these data [Gómez 2005-III], one can plot contour curves and identify the dimensions (L_{PRS}, L_{HIS}) which provide certain requested values of β_y or α_y as shown in Fig. 4.2.2. As an example,

Fig. 4.2.2 illustrates with a black cross the dimensions required to synthesize a leaky wave with normalized complex propagation constant given by β_y/k_0 = 0.342 and α_y/k_0 = 0.05, leading to L_{PRS} = 8.23mm and L_{HIS} = 7.67mm (the rest of geometrical parameters of the LWA are kept constant to the values given in the caption of Fig. 4.21).

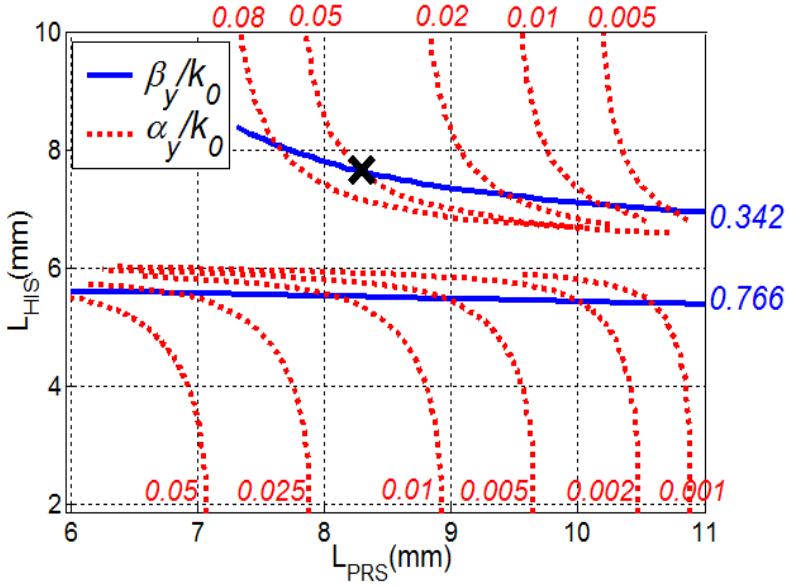

Fig. 4.2.2 Two dimensional dispersion plots for the design of 1D PRS-HIS LWA in Fig. 4.2.1 at 15GHz.

The earlier described LWA synthesis procedure is direct (in contrast to iterative design approaches [Oliner 1993], [Di Nallo 1995, 1997-I and II], [Casares-Miranda 2006]), but it needs to solve the leaky-mode $\beta_y - j\alpha_y$ dispersion for all possible values of L_{PRS} and L_{HIS}. A much more direct synthesis of the Fabry Perot LWA is proposed in this section by recalling the Transverse Resonance Equation (TRE) for the values of (β_y, α_y) which one wants to synthesize. To this end, we express the TRE using the equivalent reflection coefficients shown in Fig. 4.2.1(b):

$$\rho_{PRS}(L_{PRS})\rho_{HIS}(L_{HIS})e^{-j2k_zH} = 1 \tag{4.2.1}$$

where H stands for the FP cavity height, and the complex transverse wavenumber k_z is directly related to the desired leaky-mode longitudinal wavenumber k_y by:

$$k_z = \sqrt{k_0^2 - (\beta_y - j\alpha_y)^2} = \beta_z + j\alpha_z \tag{4.2.2}$$

As it was explained in Section 2.1, the improper nature of this forward leaky-wave is patent in this equation, with an amplitude that increases exponentially along the transverse z-direction [Oliner 1993], [Gómez 2004-III], [Jackson 2008]. As introduced in Section 2.2, due to the fact that the HIS is metal-backed, all the waves that impinge on it are fully reflected, and therefore it is satisfied that $|\rho_{HIS}| = 1$ [Feresidis 2005]. As a consequence, the complex Eq. (4.2.2) can be decomposed into the following magnitude and phase terms:

$$|\rho_{PRS}(L_{PRS})| = e^{-2H\alpha_z} \tag{4.2.3}$$

$$\theta_{HIS}(L_{HIS}) = 2H\beta_z - \theta_{PRS}(L_{PRS}) \tag{4.2.4}$$

where θ_{PRS} and θ_{HIS} are the reflection phases associated with ρ_{PRS} and ρ_{HIS}, respectively. Considering a fixed frequency and a desired propagation constant of the leaky wave (k_y), the synthesis approach proposed here is based on the solution of the two linear equations (4.1.3) and (4.2.4). In order to obtain the unknown values of L_{PRS} and L_{HIS}, the next three steps should be followed:

1) From the desired leaky-wave propagation constant $k_y = \beta_y - j\alpha_y$ and considering a fixed operating frequency, the transverse wavenumber $k_z = \beta_z + j\alpha_z$ is calculated by applying (4.2.2). For the example introduced at the beginning of this section, a leaky-wave with longitudinal $k_y = k_0$ (0.342-j0.05) presents an improper transverse wavenumber $k_z = k_0$ (0.941 + j0.018).

2) As it can be inferred from Eq. (4.2.3), the length of the dipoles in the PRS (L_{PRS}) must create a given transparency to the leaky waves inside the cavity with value $e^{-2H\alpha_z}$. As α_z is already defined in (4.2.2) and H is fixed, the only unknown in (4.2.3) is L_{PRS}. To obtain L_{PRS}, the reflection coefficient of the PRS (ρ_{PRS}) must be calculated as a function of L_{PRS} at the operating frequency, under plane-wave incidence and taking into account that the leaky wave impinges on it with a fixed angle of incidence given by [Oliner 1993], [Trentini 1956]:

$$\theta_{inc} = \text{asin}\left(\beta_y/k_0\right) \tag{4.2.5}$$

Once the function $\rho_{PRS}(L_{PRS})$ is numerically obtained, it is necessary to find the value of L_{PRS} that satisfies Eq. (4.2.3). This step is illustrated in Fig. 4.2.3 for the

case of the aforementioned example. For this case, the magnitude and phase of ρ_{PRS} as a function of L_{PRS} are plotted with continuous lines in Fig. 4.2.3(a) and 4.2.3(b), respectively. These results are obtained at 15 GHz, considering $\theta_{inc} = \text{asin}(0.342) = 20°$ (4.2.5) and employing the MoM-based approach presented in [Goussetis 2006-I]. As Fig. 4.2.3(a) shows, the PRS totally reflects all the incident waves ($|\rho_{PRS}| = 1$) when L_{PRS} = 11 mm (which is approximately half a wavelength at 15 GHz [Trentini 1956]). As the length of the dipoles is decreased, the transparency of the periodic sheet increases ($|\rho_{PRS}| < 1$). The value of L_{PRS} needed for the given LWA design is the one that satisfies Eq. (4.2.3). It is represented in Fig. 4.2.4(a) with a red rectangle, which corresponds to the point where the continuous blue curve (left term in (4.2.3)) coincides with the green dotted line (constant value given by the right term in (4.2.3)). In our example, the obtained design value is L_{PRS}^{design} = 8.23 mm. It is interesting to note that due to the improper nature of leaky waves [Oliner 1993], [Gómez 2004-III], the FP cavity of height H acts as an amplification medium for the leaky mode, so that the experimented amplifications (given by $e^{+2H\alpha_z}$) must balance the radiation losses given by the PRS sheet ($|\rho_{PRS}| < 1$). Indeed, the amplitude equation (4.2.3) is similar to the magnitude condition customarily used in the design of negative-resistance reflection oscillators [Pozar 2005].

3) The value of L_{PRS}^{design} found in the previous step provides the desired magnitude of ρ_{PRS} and a given associated phase, $\theta_{PRS}\left(L_{PRS}^{design}\right)$, which is marked with a red square in Fig. 4.2.3(b) (in our example θ_{PRS} =172º). Therefore, as β_z is also defined from (4.2.2), we can calculate the constant value taken by the right term of (4.2.4), which is plotted with a green dotted line in Fig. 4.2.3(c) (in this example $2H\beta_z$ - θ_{PRS} = -154º). As it is inferred from Eq. (4.2.4), this constant value must be equal to the reflection phase seen by the leaky-wave when it impinges on the bottom HIS, θ_{HIS}. Since θ_{HIS} depends on the length of its metallic dipoles L_{HIS}, and considering a fixed angle of incidence θ_{inc} (4.2.5) and a fixed frequency of operation, the numerical function $\theta_{HIS}(L_{HIS})$ can again be computed using a MoM-based analysis tool [Goussetis 2006-I]. In the case of the presented example, the HIS phase response $\theta_{inc}(L_{HIS})$ at 15 GHz and for θ_{inc} = 20° is plotted with a blue continuous line in Fig. 4.2.3(c). Equation (4.2.4) can now be solved by finding the

intersection between the continuous and the dotted curves in Fig. 4.2.3(c), obtaining the requested HIS dipoles (L_{HIS}^{design}= 7.67 mm, as it is marked with a red circle in Fig. 4.2.3(c)). Again, it is interesting to see that the phase equation (4.2.4) is similar to the phase condition that must be satisfied in the design of oscillators [Pozar 2005].

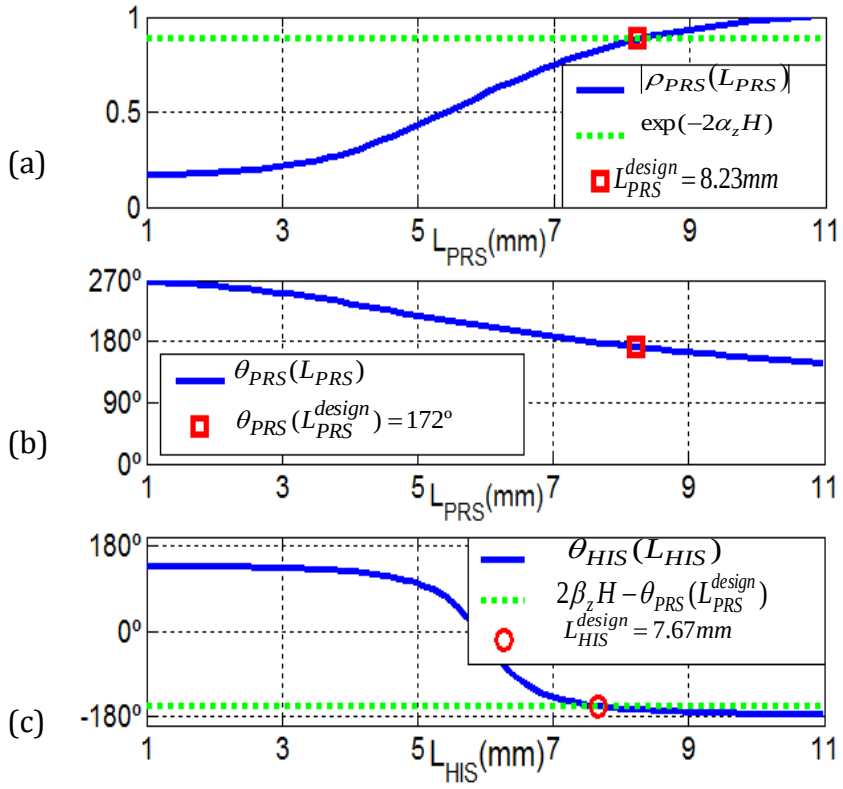

Fig. 4.2.3 Synthesis algorithm steps (a) Solving magnitude equation to obtain L_{PRS} (b) Obtaining the reflection phase of the designed PRS (c) Solving phase equation to obtain L_{HIS}.

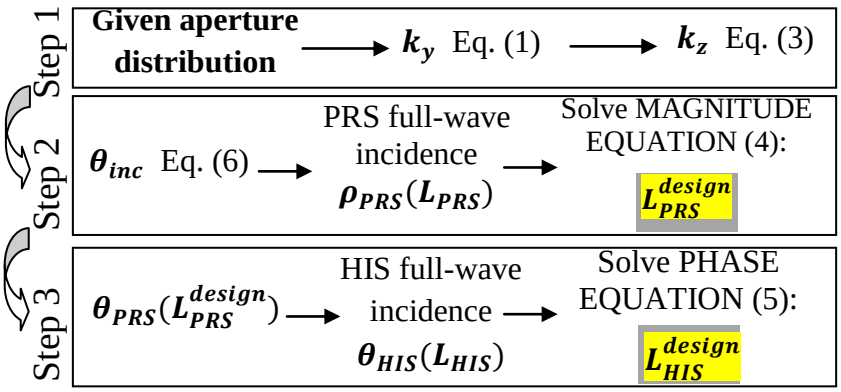

Fig. 4.2.4. Flow chart describing the steps of the proposed synthesis procedure.

Figure 4.2.4 summarizes in a flow chart the main steps involved in the proposed direct procedure. After these three steps, the geometrical values of L_{PRS} and L_{HIS} which provide the requested values of β_y and α_y have been found. The geometrical values obtained in our numerical example (L_{PRS}^{design} = 8.23 mm and L_{HIS}^{design}= 7.67 mm) are exactly the same as the ones previously obtained using the 2D dispersion analysis approach, and shown in Fig. 4.2.2.

In the next sections, the efficiency of this approach will be proven by the synthesis of 1D LWAs with low SLL (Section 4.3) and 1D and 2D LWAs with high aperture efficiency (Section 4.4 and 4.5, respectively).

4.3 Sidelobe level control of scanning 1D FP LWA

In this section, the previous synthesis approach is applied in the tapering of the 1D FP LWA presented in the previous chapter (Section 3.2) with the aim of reducing the sidelobe level (SLL). Uniform LWAs with constant leakage rate along their length have an associated SLL of -13 dB, as it corresponds to the exponential natural decay of non-tapered leaky waves [Oliner 1993]. By modulating the leakage rate along the antenna length so that a cosine aperture distribution is synthesized, this SLL can be theoretically decreased to -23 dB [Gómez 2005-III]. In order to prevent phase aberration and to perform an accurate taper, the phase constant of the leaky waves must be kept unchanged along the antenna [Oliner 1993].

A **first approximation to this design is performed in the case of the 1D PRS-loaded LWA presented in Section 2.3.3,** which is depicted in Fig. 4.3.1 together with its main geometrical parameters and its transverse equivalent network (TEN). The antenna can be recognized as a 1D Fabry-Perot cavity which consists of a grounded parallel plate waveguide (PPW) loaded with a periodic-dipole-based FSS acting as a partially reflective surface (PRS) [Trentini 1956]. The transparency of the FSS controls the amount of energy that reaches the top aperture of the antenna and therefore it determines the radiation rate of the leaky mode (α_y/k_0). The reflectivity of this kind of PRS mainly depends on the length of

its resonant dipoles (L_{FSS}, see Fig.3). In order to reduce the SLL, the FSS is properly tapered by engineering the variation of L_{FSS} along the LWA length.

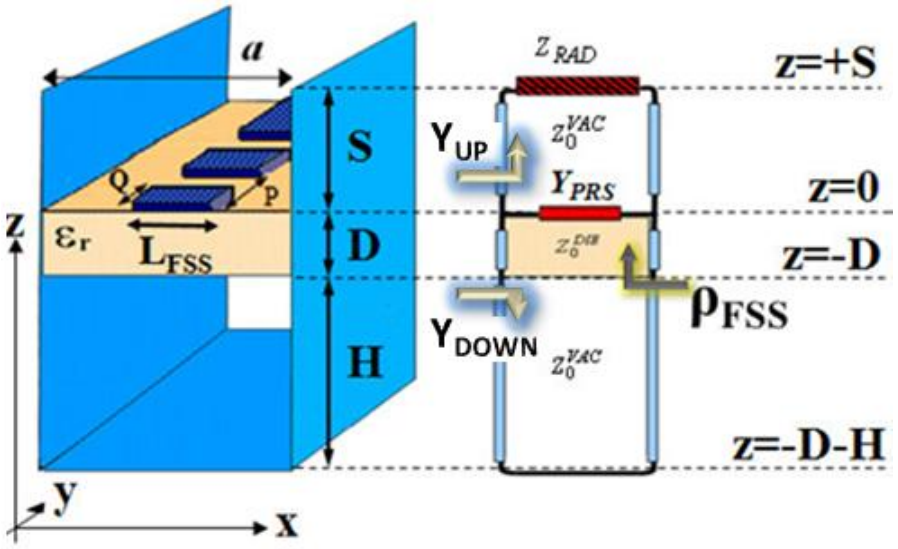

(a) (b)

Fig. 4.3.1 (a) 1D PRS-loaded FP LWA (b)TEN of the structure. ($a = H = 11$ mm, $S = 5$ mm, $D = 1.13$ mm, $\varepsilon_r = 2.2, P = 1.5$ mm and $Q = 0.5$ mm).

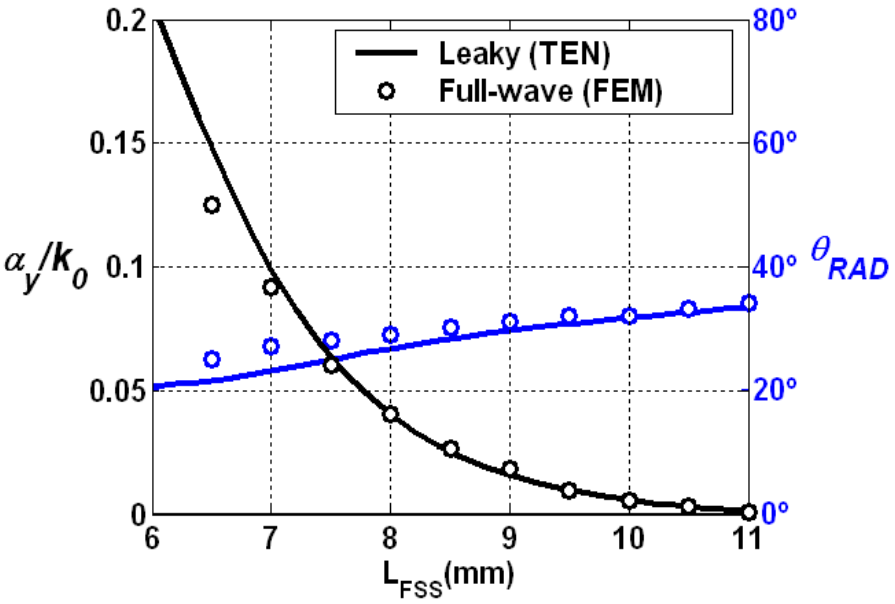

Fig. 4.3.2 Normalized radiation rate and pointing angle of the LWA shown in Fig. 4.3.1, as a function of the FSS dipoles length (frequency of operation 15GHz).

This LWA is analyzed with the software tool developed in Section 2.3, employing the TEN in Fig. 4.3.1(b). The results obtained are plotted in Fig. 4.3.2,

and they are compared with full-wave results based on Finite Element Method (FEM, [HFSS 2011]), showing very good agreement. In Fig. 4.3.2 we confirm that the radiation rate of the antenna α_y/k_0 can flexibly be controlled by modifying L_{FSS}, although the LWA pointing angle θ_{RAD} experiences only a small variation.

A uniform (non-tapered) LWA is designed, pointing at θ_{RAD} = 30º at 15GHz, with a η_{RAD} = 75% radiation efficiency and a radiating length $L_A = 3.5\ \lambda_0$, which provides a $\Delta\theta$ = 17º beamwidth. This performance can be achieved by using a uniform FSS with L_{FSS} = 8mm, which provides the required α_y/k_0 = 0.04 leakage rate (see curve of Fig. 4.3.2). The radiation diagram of this non-tapered LWA corresponds to the blue plots in Fig. 4.3.3 (FEM results are shown in continue line while leaky-mode results are shown in dashed line). It is seen that a *SLL* =-13dB is obtained, as it corresponds to the exponential illumination of the non-tapered LWA [Oliner 1993].

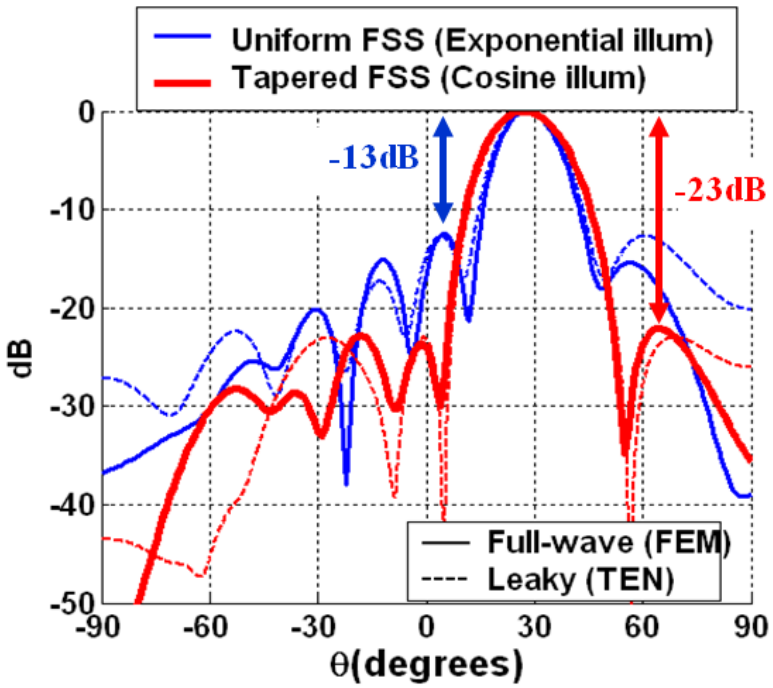

Fig. 4.3.3 Normalized radiation patter (L_a = 3.5 λ_0, η_{RAD} =75%, f=15GHz).

In order to obtain a desired illumination *M(y)*, the leaky-mode must radiate with a certain radiation rate at each point y_0 of the LWA length, and can be obtained from this known expression [Oliner 1993]:

$$\frac{\alpha(y)}{k_0} = \frac{\lambda_0}{4\pi} \frac{|M(y)|^2}{\frac{1}{\eta_{RAD}} \int_{y=0}^{y=L_a} |M(y)|^2 \partial y - \int_{y=0}^{y=y_0} |M(y)|^2 \partial y} \tag{4.3.1}$$

Fig. 4.3.4(a) shows the variation of α_y/k_0 along the LWA length needed to achieve a cosine illumination, together with the corresponding variation of the length of the dipoles, according to Fig. 4.3.2. The resulting tapered printed-circuit profile is shown in Fig. 4.3.4(b). The radiation diagram of this tapered LWA is also shown in Fig. 4.3.3, illustrating the clear reduction of the SLL to -23dB. Again, the leaky-mode results obtained from the TEN are in very good agreement with full-wave FEM simulations, while requiring a much lower computational time. A broadening of the main beam is also manifested, which is related to the cosine illumination [Balanis 1982]. However, it is possible to reduce the SLL of a radiation diagram while maintaining a desired directivity if we design a new antenna with a longer radiating aperture. Further reduction of the SLL could be achieved by performing a squared cosine illumination or other tailored functions [Balanis 1982].

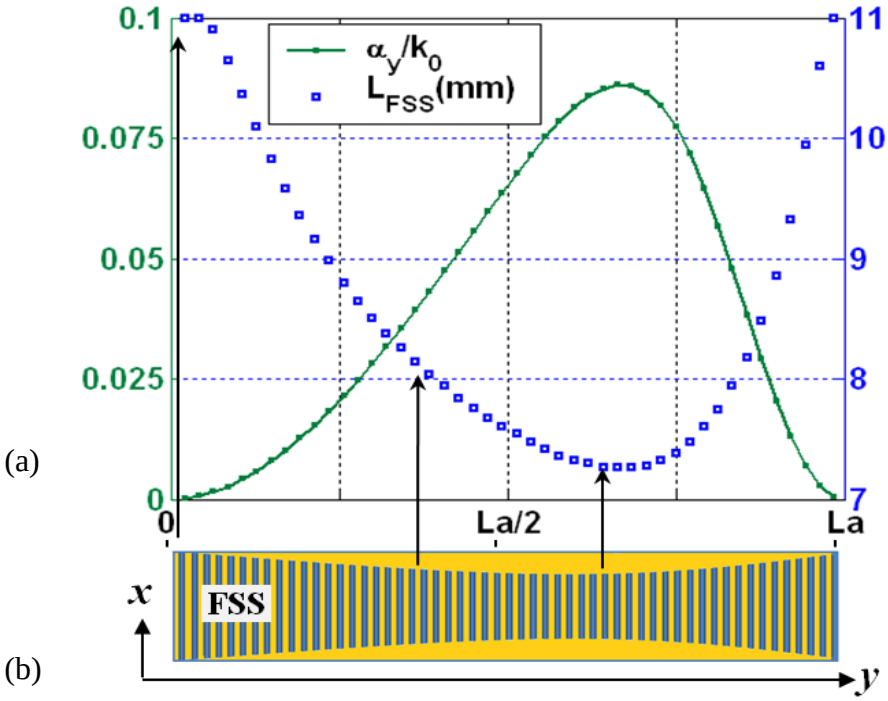

Fig. 4.3.4 (a) Radiation rate (α_y/k_0) at each point of the tapered LWA, and length of the dipoles in the FSS (L_{FSS}) that provide it. (b) Scheme of the tapered FSS.

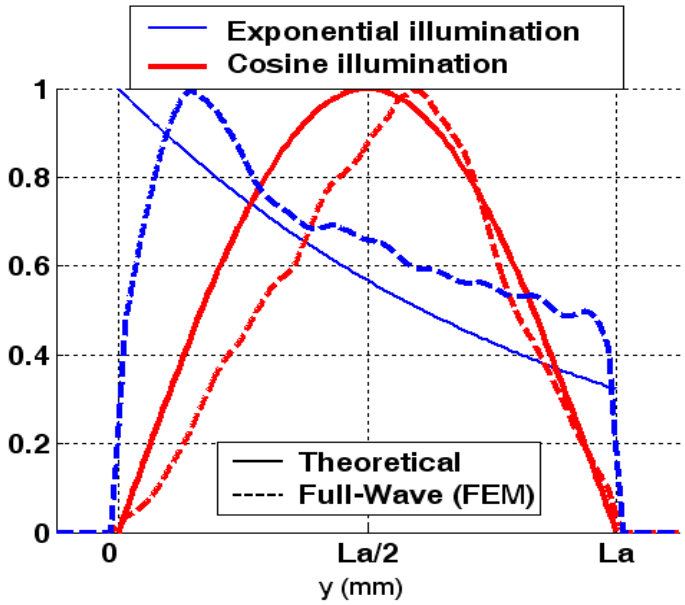

Fig. 4.3.5 Normalized illumination of the uniform and tapered LWA.

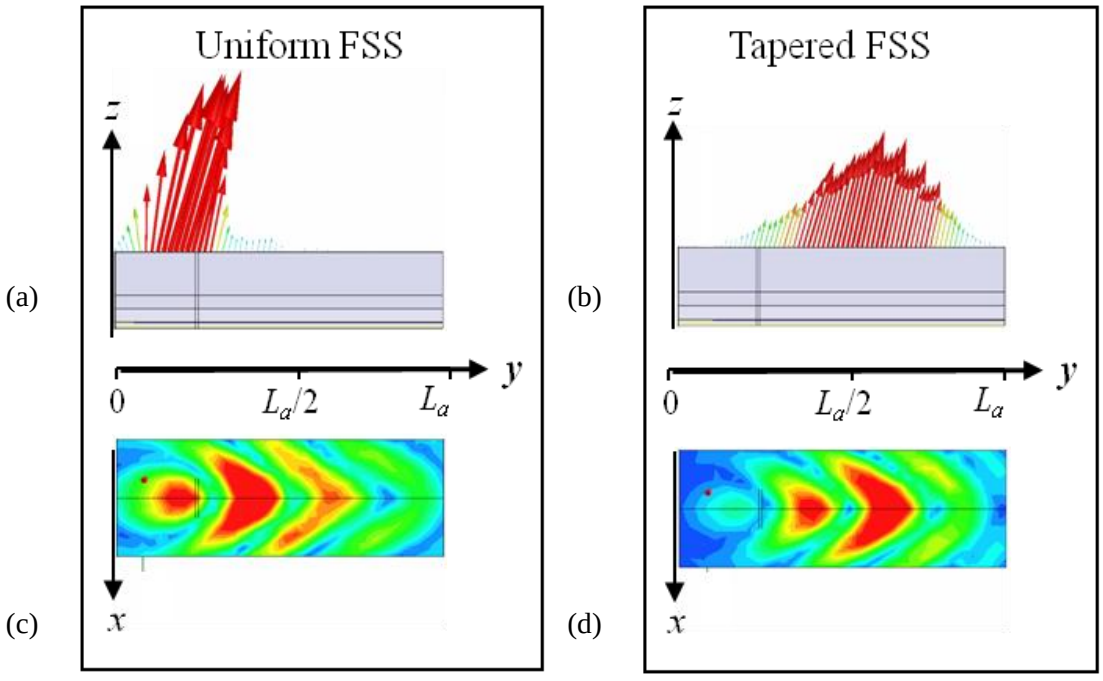

Fig. 4.3.6 (a,b)Poynting vector in the top aperture of the LWA. (c,d) Magnitude of the electric field in the aperture. (a,c) LWA with uniform FSS. (b,d) LWA with tapered FSS.

Figure 4.3.5 shows the aperture illumination of the designed antennas. The blue lines in this figure correspond to the uniform antenna, where we can easily check that the pattern is exponential. On the other hand, the red lines are

associated to the tapered antenna, where the cosine illumination is patent. Once more, the comparative between the theoretical and the full-wave results is reasonably good. The effect of the tapering can be also noticed in Fig. 4.3.6, where it is shown the poynting vector (Fig. 4.3.6(a) and (b)) and the magnitude of the electric field (Fig. 4.3.6(c) and (d)) in the top aperture of the antenna. Both Fig. 4.3.6(a) and (c) show that in the uniform antenna the energy is mostly radiated at the beginning, and decreases exponentially. However, in the tapered antenna (Fig. 4.3.6(b) and (d)) the maximum radiation is produced at the middle of the antenna while it is null at the edges.

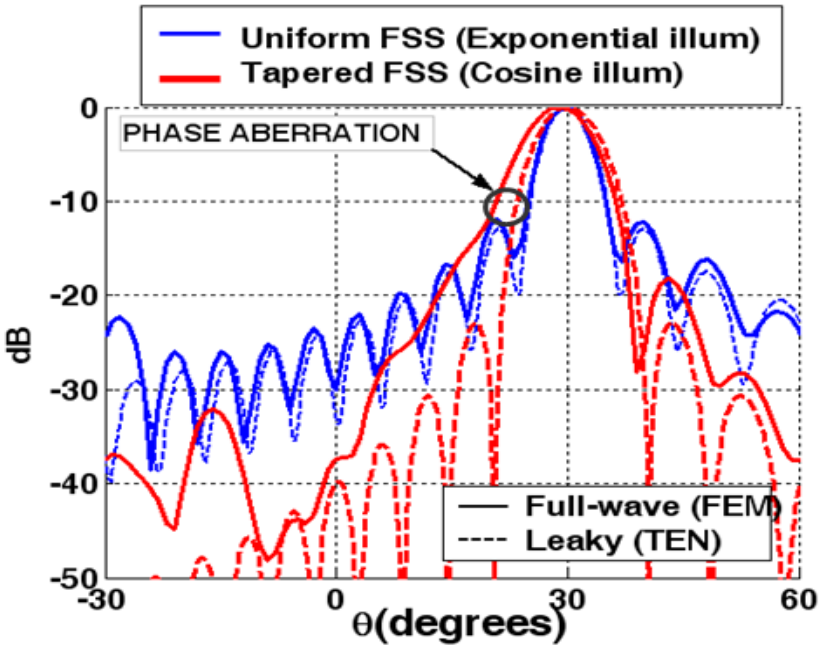

Fig. 4.3.7 Normalized radiation diagram (L_a = 10 λ_0, η_{RAD} = 75%, f = 15 GHz).

This tapering procedure not only produces a modulation of the radiation rate along the LWA length, but it also introduces variations in its radiation angle θ_{RAD} (see Fig. 4.3.2), which will result in phase aberration. In the previous design, this effect is not perceptible in the radiation pattern due to its wide beamwidth (see Fig. 4.3.3). However, some improvement will be required when dealing with more directive antennas. In these cases, it is needed to find the way to control α_y without affecting β_y, so that all parts of the aperture radiate to the same angle θ_{RAD}. An example that illustrates this necessity is shown in Fig. 4.3.7, where the proposed tapering procedure has been applied to a longer antenna (L_A = *10* λ_0, in contrast to the previous antenna which length was *3.5* λ_0,). The phase aberration

effect is clear in the tapered radiation diagram, where it is possible to see the distortion produced in the main beam. As it can be seen in Fig. 4.3.7, the main beam suffers a higher broadening and the reduction of the SLL is not successfully achieved. As it was explained in Section 3.3, **the 1D PRS-HIS LWA proposed in Section 3.2 overcomes this difficulty by loading the bottom side of the FP cavity with a HIS, allowing the simultaneous control over β_y and α_y.** This feature was proven in Section 3.4 by designing several uniform LWAs with variable pointing angle and beamwidth. However, when designing tapered LWAs, it is possible to take full advantage of the wavenumber independent control. Next, some tapered antennas are designed in order to prove the versatility of the 1D PRS-HIS LWA together with the efficiency of the synthesis equations proposed in Section 4.2.

Two tapered 1D PRS-HIS antennas are now designed, LWA1 and LWA2, with respective scanning angles θ_{RAD} = 20º and θ_{RAD} = 50º, operating at 15 GHz with radiation efficiency η_{RAD} = 90%, and Half Power BeamWidth (HPBW) $\Delta\theta$ = 10º. Another set of uniform antennas with exponential illumination are considered for comparison. The length of each LWA is respectively L_{A1} = 146 mm and L_{A2} = 214 mm (L_{A1} = 7.3λ_0 and L_{A2} = 10.7λ_0 at 15 GHz), needed to provide the specified HPBW $\Delta\theta$ = 10º for their particular scanning angles with cosine illumination [Oliner 1993]:

$$\frac{L_a}{k_0} = \frac{68.8^\circ}{\Delta\theta \cos(\theta_{RAD})} \tag{4.3.2}$$

The constant value of β_y which corresponds to the designs can be easily obtained from the pointing angle by applying the well-known expression $\beta_y = k_0 \sin\theta_{RAD}$ [Oliner 1993]. As it was explained in Section 3.1, for the non-tapered designs, the constant value of α_y can be readily obtained from the radiation efficiency η_{RAD} by applying [Oliner 1993]:

$$\frac{\alpha_y}{k_0} = -\frac{\lambda_0}{4\pi L_a} ln(1-\eta_{RAD}) \tag{4.3.3}$$

The reduction of the SLL is performed in both antennas by modulating the leakage rate along the radiating aperture. Employing the well-known expression in (4.3.1), we obtain the leakage rate tapering function at each longitudinal section y of the LWA for the desired cosine illumination $M(y)$. Note that equation (4.3.3) is a reduced form of (4.3.1) assuming an exponential illumination $M(y)$ (as it corresponds to non-tapered LWAs). Figure 4.3.8 shows the tapered leakage functions $\alpha(y)/k_0$ for LWA1 and LWA2 with cosine aperture distribution. The pointing angle θ_{RAD} remains constant along all the aperture length to optimize the aperture phase efficiency at the prearranged scanning angles θ_{RAD} = 20º and θ_{RAD} = 50º.

The desired leaky-mode tapering functions $\alpha(y)/k_0$ and $\theta_{RAD}(y)$ of Fig. 4.3.8 can then be used as the input of the synthesis technique presented in the previous section, which must be applied to all longitudinal positions y of the LWA. This way, the geometrical tapering of the PRS and HIS metallic dipoles lengths, $L_{PRS}(y)$ and $L_{HIS}(y)$, are obtained as plotted in Fig. 4.3.9. The dashed horizontal lines in Fig. 4.3.9 correspond to the non tapered antennas, with uniform PRS and HIS dimensions along the whole LWA length. For the case of the tapered designs, it must be noted that null radiation (α_y/k_0 = 0) is requested at the edges of the tapered antennas [Oliner 1993] (see Fig. 4.3.8). The PRS must present total reflection at these null-leakage points located at the antenna input and output: this is obtained for resonant PRS dipoles at the design frequency of 15GHz (L_{PRS} = 11 mm $\approx \lambda_0/2$) in Fig. 4.3.9(a). It can also be inferred from Fig. 4.3.8 that maximum leakage is demanded at a longitudinal point y which is right shifted from the center of the tapered LWAs [Oliner 1993]; here, the transparency of the PRS is the highest (lowest values of L_{PRS}), allowing high leakage from the FP cavity. It is easy to see from Fig. 4.3.8 and 4.3.9(a) that the tapering of L_{PRS} follows an inverse variation to the requested modulation of α_y/k_0. Notice that the tapered LWA2 presents lower values of L_{PRS} that LWA1, although LWA1 requests higher values of α_y/k_0. This is due to the fact that LWA2 operates at 50º, which is less perpendicular to the PRS sheet than LWA1 (operating at 20º). As it is well-known, the PRS transparency decreases as the incident angle is increased [Goussetis 2006], and therefore, the

PRS dipoles of LWA2 must be much shorter than those of LWA1 to provide the same of even lower leakage rates.

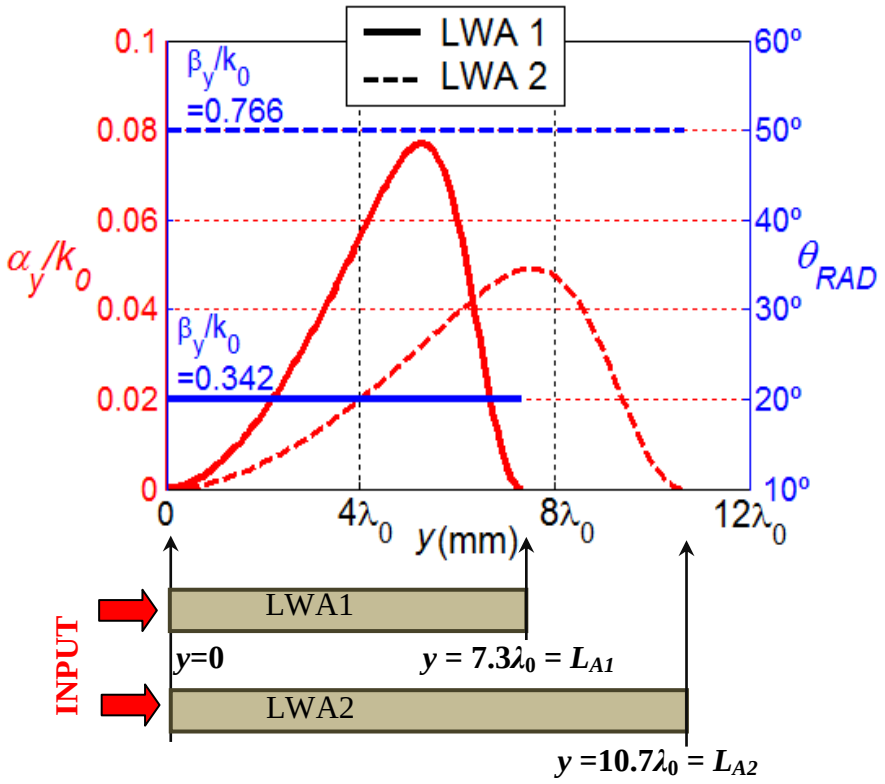

Fig. 4.3.8 Tapering of the leaky-mode pointing angle (θ_{RAD}) and normalized leakage rate (α_y/k_0) requested to achieve a cosine illumination with η_{RAD}=90%.

As it was explained in detail in Section 3.2, L_{PRS} not only modifies the radiation rate, but also affects the LWA pointing angle θ_{RAD}. Therefore, L_{HIS} must also be modulated in order to correct any deviation and to achieve the desired constant value of θ_{RAD} [Gómez 2005-III]. This variation of L_{HIS} is shown in Fig. 4.3.9(b): it is more pronounced for the case of LWA1 due to the fact that shorter LWAs need higher variations of α_y/k_0 for similar radiation efficiencies and aperture functions than longer LWAs (see Fig. 4.3.8). As a result, these stronger leakage modulations create higher distortion of the scanning angle θ_{RAD} which must be corrected with higher tuning of L_{HIS}.

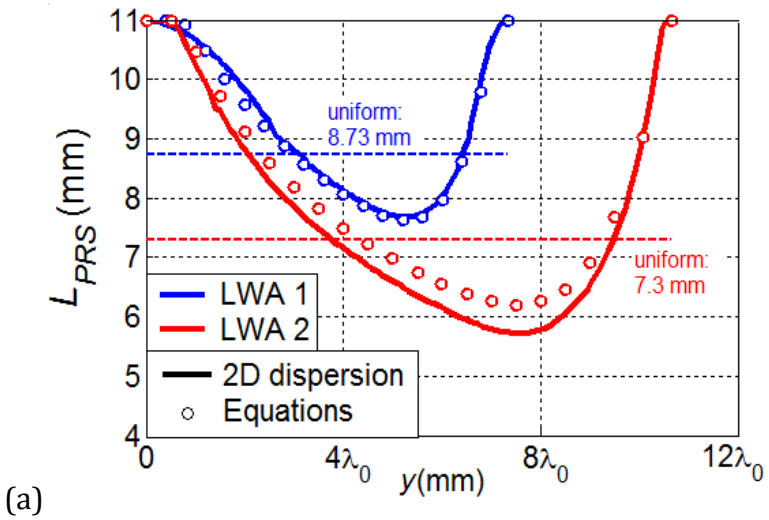

(a)

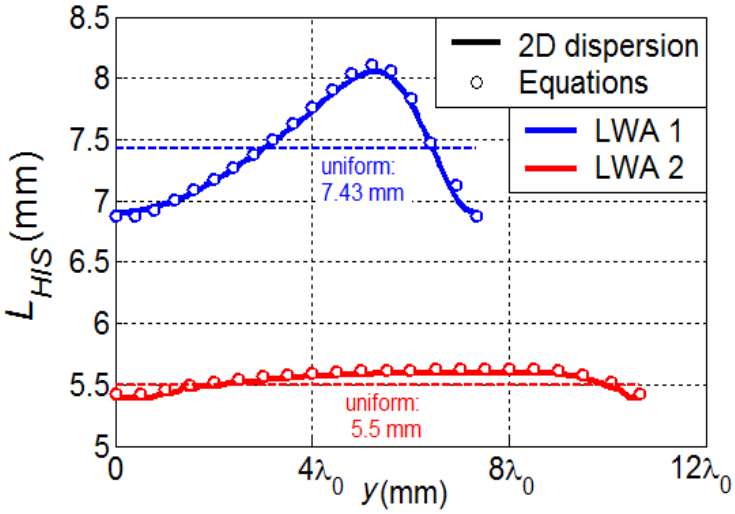

(b)

Fig. 4.3.9 Tapered length of the dipoles in the top PRS and bottom HIS.

Synthesis equations approach	2D dispersion charts	Full-wave optimization [HFSS 2011]
30 s.	10800 s	several days

Table 4.3.1. Comparison of computation time needed for the synthesis of LWA2.

Two sets of tapered dimensions $L_{PRS}(y)$ and $L_{HIS}(y)$ are plotted in Fig. 4.3.9 for each LWA. The first curves correspond to the synthesis equations proposed in this paper and they are plotted with circles, while the second set of dimensions are represented with continuous lines and they have been extracted from the 2D dispersion chart of Fig. 4.2.2, which is used as a look-up table. Good agreement is found between both techniques. Some discrepancies between these two approaches are attributed to numerical errors associated with interpolations in

obtaining the blue curves in Fig. 4.2.2: it must be highlighted that the direct synthesis equations are more accurate due to the fact that it avoids any interpolation of the dispersion data which is normally done in the post processing to complete all possible values of L_{PRS}, L_{HIS} (as explained in Section 3.3). In addition, the main advantage of the direct synthesis approach is the dramatic reduction in the computational cost associated to the design procedure, as shown in Table 4.3.1.

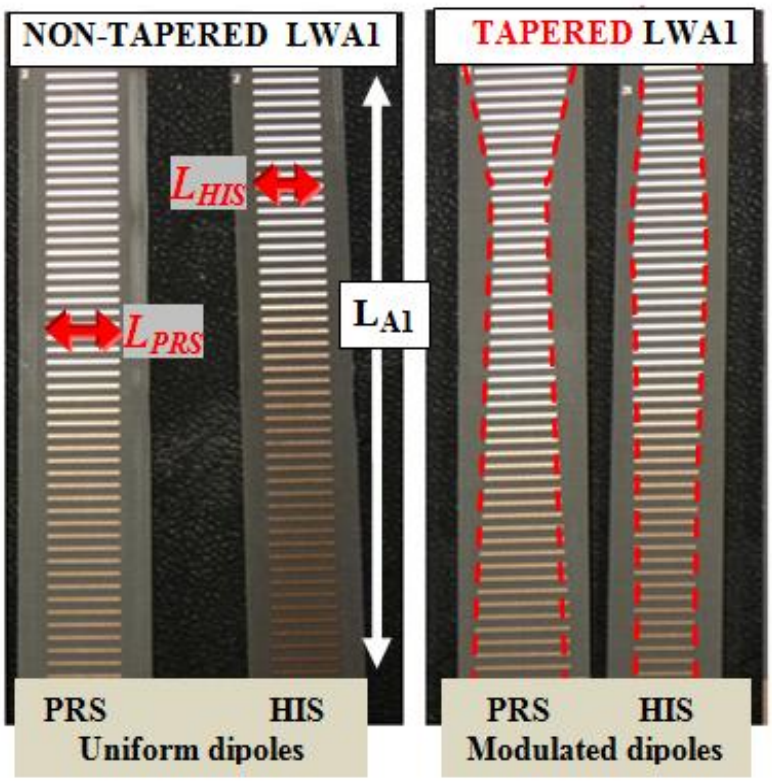

Fig. 4.3.10 Manufactured PCBs for LWA1 (a) Non-tapered (b) Tapered designs.

The accuracy of the proposed synthesis approach is proven in this section through the manufacture and measurement of the uniform and tapered LWAs designed in Section II (LWA1 and LWA2). These prototypes have been constructed and measured at CSIRO ICT laboratories. Taconic TLY-5-0450 substrates (D = 1.13 mm, ε_r = 2.2, $tan\delta$ = 0.0009) were used for the PRS and HIS printed circuits. Fig. 4.3.10 illustrates some pictures of the uniform and tapered PCBs of length L_{A1} which correspond to LWA1. The PRS and HIS shown in Fig. 4.3.10(a) belong to the non-tapered prototype, where the length of the dipoles (L_{PRS} and L_{HIS}) remains constant. As it can be seen in Fig. 4.10(b), the modulated PRS and HIS follow the tapering functions shown in Fig. 4.3.9, with the PRS dipoles shorter at the LWA far

center, while the HIS dipoles become longer at the same longitudinal position. These PCB designs are then placed inside the metallic 1D parallel-plate waveguide structure described in Section 3.3, where a TE_{01} leaky mode is fed by using a simple coaxial-to-waveguide transition.

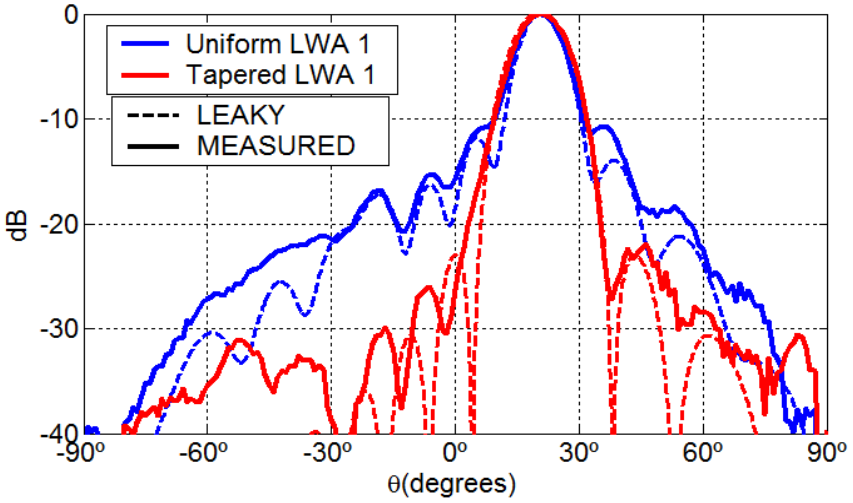

(a)

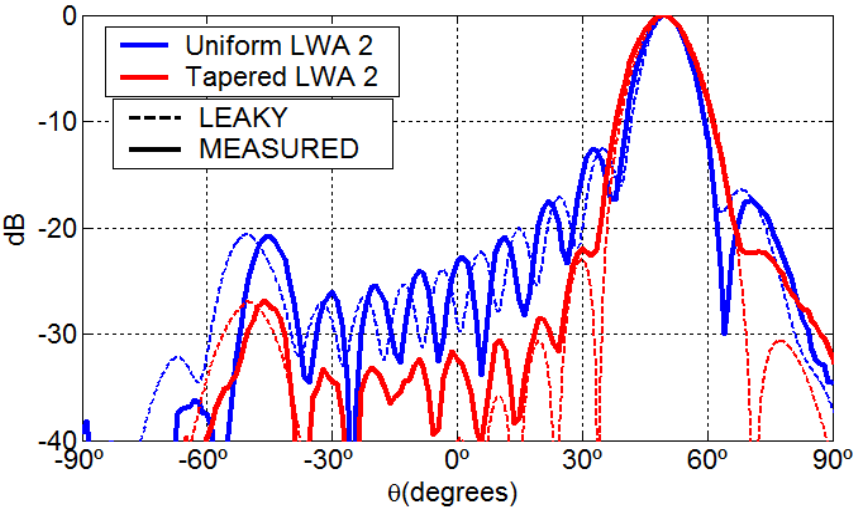

(b)

Fig. 4.3.11 Theoretical and measured normalized radiation patterns for the designed antennas, showing the reduction of the SLL achieved by the taper.

The radiation patterns of the uniform and tapered prototypes operating at 15 GHz are plotted in Fig. 4.3.11, for both LWA1 and LWA2. Measured results are compared with radiation patterns obtained from simple leaky-wave theory [Oliner 1993]. Good agreement is obtained for the major and the minor radiated lobes, even in the case of the reflected lobe at -50º shown in Fig. 4.3.11(b). The pointing angles in Fig. 4.3.11(a) and (b) are respectively 20º and 50º, which perfectly match

the specified scanning values. The SLL reduction is also proven in Fig. 4.3.11, which shows with blue lines that the SLL presented by the uniform designs (in the order of 11-13dB) can be effectively decreased below 20dB by properly tapering the LWA geometry patterns plotted with red lines (an ideal cosine illumination would provide -23 dB SLL [Oliner 1993]).

Finally, Fig. 4.3.12 shows measured radiation patterns for tapered LWA2 as frequency is shifted. It is observed that secondary lobes are kept below -20dB as the main beam is frequency scanned from 20º (12GHz) to 55º (16GHz). At higher frequencies, a side lobe emerges and degrades the SLL performance. This is due to the fact that θ_{RAD} increases and α_y/k_0 decreases as frequency is shifted to higher values (this is the normal dispersion of a leaky mode [Oliner 1993]). This makes the aperture distribution become much distorted for higher frequencies with respect to the cosine function synthesized at 15GHz, tending to a more uniform distribution which presents a higher SLL. On the contrary, a quasi cosine distribution is maintained at lower frequencies, due to the fact that α_y/k_0 increases as frequency decreases from 15GHz. This makes the SLL remain low at the expense of an increase in the HPBW $\Delta\theta$, as a result of the decreased effective illuminated length (observe the wide main beam at 12GHz in Fig. 4.3.12).

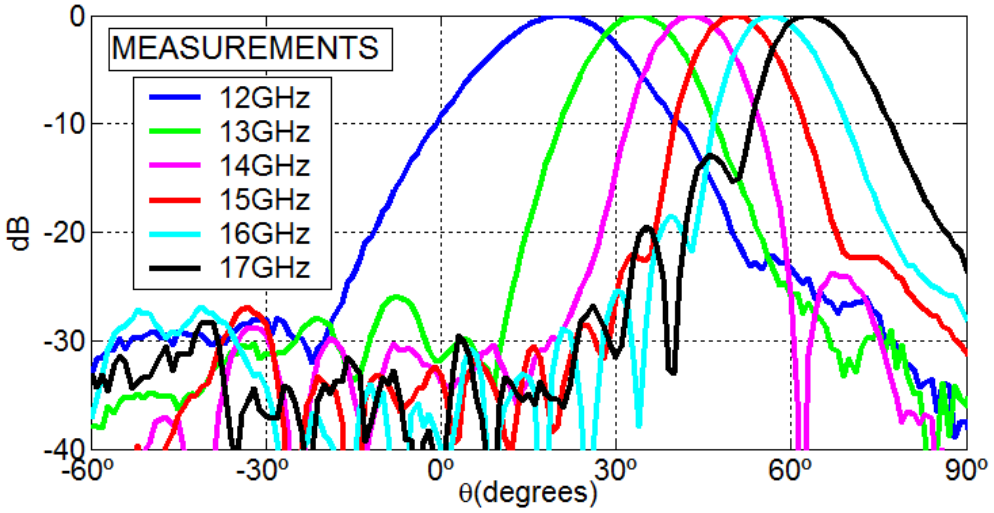

Fig. 4.3.12 Measured normalized radiation patterns of the tapered LWA 2 at different frequencies.

4.4 Control of the illumination at broadside of 1D FP LWA

In this section, broadside radiation from non-uniform 1D FP LWAs is studied; this time the source is placed at the middle of the antenna length. In contrast to the previous section, the illumination of this antenna will be tapered in order to improve the radiating aperture efficiency, while achieving broadside radiation and keeping high radiation efficiency (η_{RAD}) at a fixed operation frequency. Low sidelobes level (SLL) is also achieved due to the LWA quasi-cosine near field illumination resulting from the two opposite-directed exponentially-decaying leaky waves.

In recent years, it has been proven that broadside radiation is no longer a limitation to leaky wave antennas (LWAs), remarkable examples can be found in [Ip 1990], [Guglielmi 1993], [Chien-Jen 1999], [Caloz 2005], [Burghignoli 2006] and [Lovat 2006]. Particularly, interesting results have been lately published in order to achieve this feature in 1D LWAs. Considering periodic configurations, the radiation is produced by the leaky n=-1 spatial harmonic (SH) [Guglielmi 1993], [Burghignoli 2006]. In the case of using composite right-left-handed transmission lines, is the n=0 SH the responsible for the radiation [Caloz 2005]. Broadside radiation from homogeneous 1D LWAs can also be produced by the n=0 SH by satisfying the splitting condition in a symmetrically fed configuration [Ip 1990],

[Lovat 2006], [Chien-Jen 1999]. These papers show leaky-mode frequency results regarding the optimization of the splitting condition [Sutinjo 2008], the radiated power at broadside, -3dB beamwidth ($\Delta\theta$)…

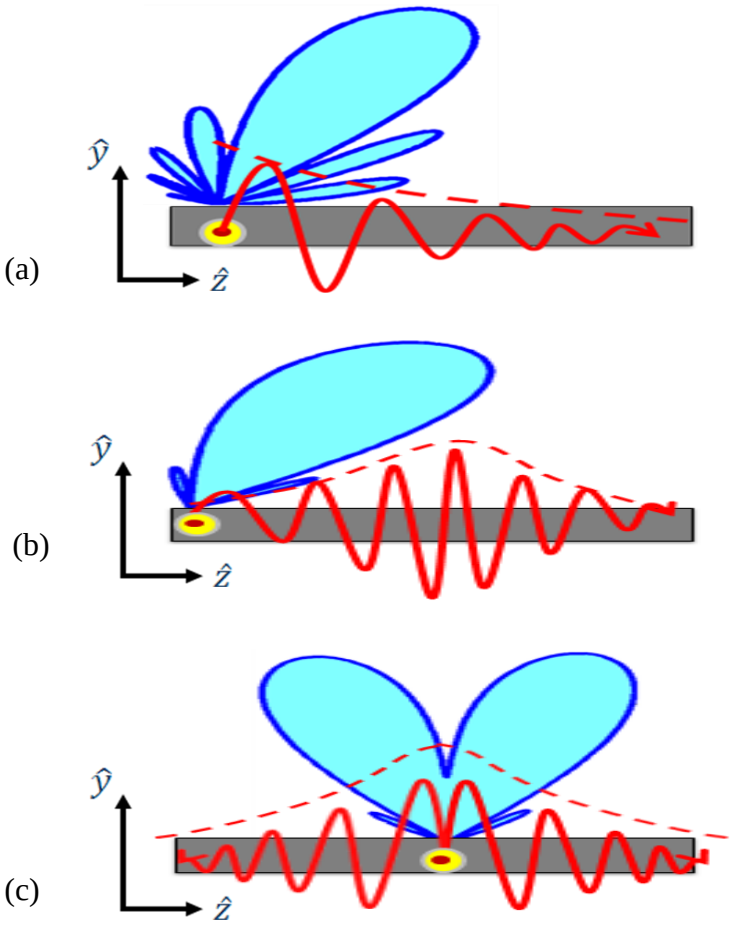

Fig. 4.4.1 Scheme of leaky-waves propagation along the *z* axis in three different 1D LWAs configurations: (a) Non tapered, unidirectional (b) Tapered, unidirectional (c) Non tapered and symmetrically fed (bidirectional).

1D LWAs are commonly fed at one end, and therefore are based in the propagation of leaky-waves in a single direction [Oliner 1993], [Balanis 1982], [Lampariello 1985]... The main advantage of this configuration is the single frequency scanned beam in the radiation pattern [Oliner 1993]. These LWAs are considered unidirectional, and are illustrated in the scheme of Fig. 4.4.1(a). As it was studied in the previous section, these LWAs have an associated exponential near field illumination to which corresponds a SLL of approximately -13dB. This SLL value may not be acceptable for some practical applications, and it is necessary

to shape the antenna near field patterns in order to reduce the SLL. Convenient illuminations such as cosine can be achieved by tapering the leakage rate associated to the leaky-mode (α). Fig. 4.4.1(b) shows the scheme of a 1D LWA with a cosine taper, which provides lower SLL than the non tapered antenna in Fig. 4.4.1(a). However, this amplitude taper can be avoided when the source is placed in the middle of the antenna [as illustrated in Fig. 4.4.1(c)]. In this situation, the uniform guiding structure supports propagation in both opposite directions, achieving a quasi-cosine near field illumination. As it can be seen in Fig. 4.4.1(c), the resulting radiation pattern is a superposition of the radiation contribution of both unidirectional waves. Particularly, as it was explained in Section 3.1, when the splitting condition $\beta_y = \alpha_y$ is accomplished; a single broadside beam is produced due to the coalescence of the two radiated beams [Sutinjo 2008]. Yet, this configuration is only attractive for broadside radiation, due to the fact that two main beams appear in the radiation pattern for other pointing angles [see Fig. 4.4.1(c)]. In order to clarify these aspects, three different scenarios of 1D LWAs that satisfy the splitting condition are illustrated in Fig. 4.4.2. In particular, the radiation patterns and near electric fields associated to each antenna are shown. The first case [Fig. 4.42(a)] corresponds to a unidirectional non tapered LWA. As it can be seen, the radiation is produced at a small angle greater than zero. A SLL of -13dB is achieved in this configuration, as corresponds to exponential illumination of the near field patterns. The second case corresponds to a unidirectional LWA in which a cosine taper has been performed. Thus, the SLL in Fig. 4.4.2(b) is lower than in the previous case, although the pointing angle is the same. The collimated illumination in this antenna (cosine shaped) can also be observed in the near field patterns. At last, the third case corresponds to a non tapered LWA which is symmetrically fed. As Fig. 4.4.2(c) shows, broadside radiation and low SLL is achieved with this configuration. The radiation pattern beamwidth is increased due to the aforementioned superposition of beams. The quasi-cosine illumination can also be observed in the near field patterns of Fig. 4.4.2(c).

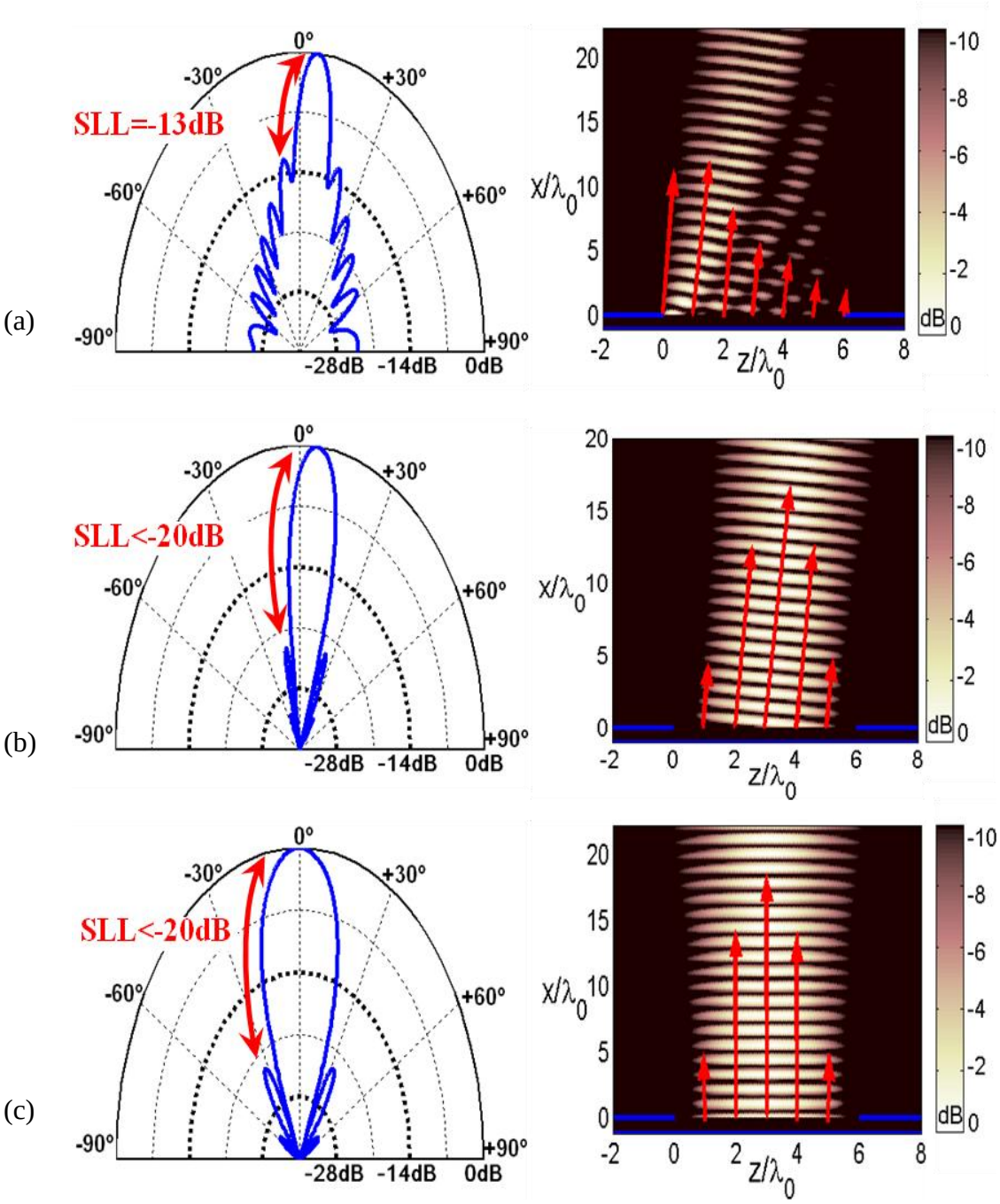

Fig. 4.4.2 Near longitudinal electric fields of 1D LWAs (a) Non tapered, unidirectional (b) Tapered, unidirectional (c) Non tapered and symmetrically fed (bidirectional).

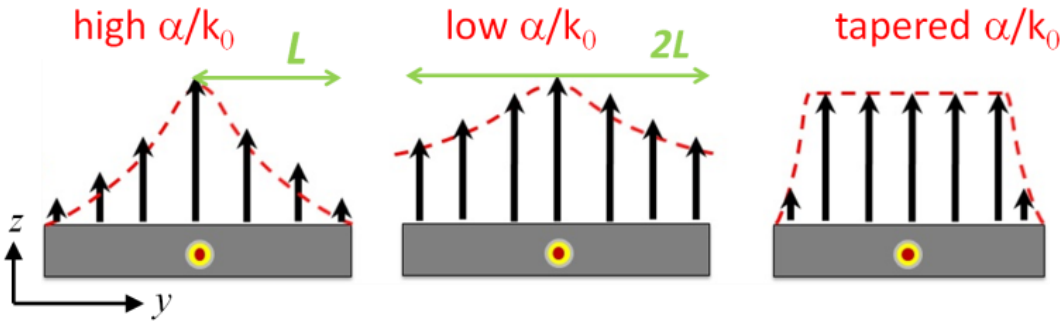

(a) (b) (c)

Fig. 4.4.3 Aperture illumination for 1D LWAs, (a) and (b) are non tapered, (c) is tapered.

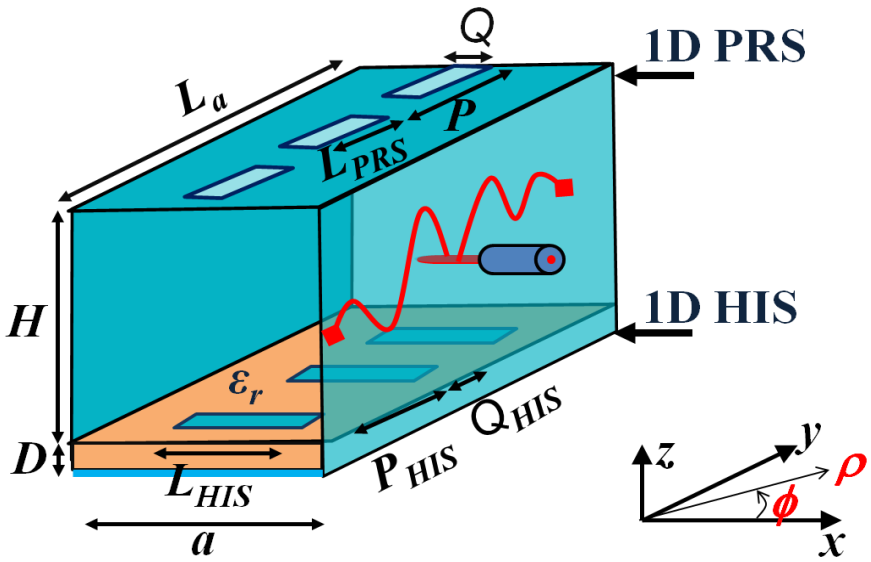

Fig. 4.4.4 Scheme of 1D and FP LWA with planar PRS and HIS (Dimensions: H = 10mm, a = P = 8.5 mm, D =1.13mm, Q = 3mm, P_{HIS} = 1.7mm, Q_{HIS} = 0.5mm, ε_r = 2.2).

For the previous reasons, although most of 1D LWAs have been used to scan in the elevation plane, recently there is an increased interest on the study of 1D LWAs which are symmetrically fed from its center position, and which present optimized broadside radiation when the leaky-mode satisfies the splitting condition [Chen 1998], [Yamamoto 1999], [Lovat 2006], [Li 2007], [Sutinjo 2008],[Komanduri 2010]. To this author´s knowledge, all previously reported designs of broadside-directed 1D LWAs are not tapered, and therefore, only exponential amplitude aperture illuminations are obtained. In these non-tapered situations, one can only choose a higher or a lower value of α_y/k_0 which is kept constant along the whole LWA length, as sketched in Fig. 4.4.3(a) and 4.4.3(b).

These non-tapered examples clearly show that the illumination of the radiating aperture becomes more uniform when α_y/k_0 is lowered [Fig. 4.4.3(b)]. Therefore, the reduction of α_y/k_0 could be considered as a first approach to improve the aperture efficiency (η_{AP}) of a FP LWA. However, when α_y/k_0 is decreased, more guided energy reaches the LWA far ends, as it can be seen in Fig. 4.4.3(b). Two possible solutions have been proposed to deal with this non-radiated power: *1)* to place matched loads at the antenna's edges to absorb it [Lovat 2006], [Li 2007], [Sutinjo 2008],[Komanduri 2010], or *2)* to use open or short circuited terminations [Chen 1998], [Yamamoto 1999]. In the first case, the radiation efficiency ($\eta_{RAD} = 1 - e^{-2\alpha L}$) falls as η_{AP} is increased (*i.e.*, as α/k_0 is decreased). As demonstrated in [Komanduri 2010], the theoretical compromise gives an ideal maximum normalized gain factor $\eta_{RAD} \times \eta_{AP} = 0.73$ when $\eta_{RAD} = 0.87$ and $\eta_{AP} = 0.84$. If the second solution is employed, the open or short circuits may create a standing leaky-wave [Chen 1998], [Yamamoto 1999], which further reduces the aperture efficiency (as a result of the generation of standing waves), and it also creates diffraction lobes due to the strong discontinuity at the edges. **This compromise between radiation and aperture efficiency can be overcome if the leakage rate is tapered along the LWA length, so that uniform illumination with ideal $\eta_{AP} = 1$ can be theoretically achieved whilst keeping radiation efficiency as high as possible,** as depicted in Fig. 4.4.3(c). Typically $\eta_{RAD} \leq 0.9$ is pursued, to avoid too high values of α at the last sections of the tapered LWA [Gómez 2006-III]. In this section, this approach is employed for the aperture efficiency enhancement of the 1D FP LWA of Fig. 4.4.4. This double layered FP structure is analogous to the one presented in Section 3.2, and also provides simultaneous and independent control over the leaky-mode phase constant (β_y) and leakage rate (α_y). In contrast to the 1D PRS-HIS LWA previously considered (see Fig. 4.2.1(a)), the PCB located at the top of the FP cavity now consists of a metallic sheet periodically perforated with slots (see Fig. 4.4.4), which again acts as partially-reflective surface (PRS). This PRS provides the control over α_y by modifying the length of its resonant slots (L_{PRS}, shown in Fig. 4.4.4). Particularly, low leakage will be induced when the slots in the PRS are short, and vice versa. As it was explained in Section 2.3, this structure can also be analyzed with the TEN-based technique developed.

The value of $\alpha(y)$ at any longitudinal position of the antenna that provides a desired field distribution along the LWA aperture can be found using the following well-known expression (already introduced in the previous section)

$$\frac{\alpha(y)}{k_0} = \frac{\lambda_0}{4\pi} \frac{|M(y)|^2}{\frac{1}{\eta_{RAD}} \int_{y=0}^{y=L_a} |M(y)|^2 \partial y - \int_{y=0}^{y=y_0} |M(y)|^2 \partial y} \tag{4.4.1}$$

The same tapering function is applied to the leaky wave phase constant $\beta(y)$, so that the splitting condition $\beta(y) = \alpha(\mathrm{y})$ is satisfied at any longitudinal position z of the antenna and broadside radiation is optimized along the whole LWA with length L_a in each one of the two directions.

As an illustrative example, a symmetrically fed 1D LWA with $L_a = 3\lambda_0$ is now considered. Three different cases of non-tapered antennas with $\alpha_y/k_0 = \beta_y/k_0 = 0.1, 0.05$ and 0.02 are designed. The corresponding near field patterns are depicted in Fig. 4.4.5(a), (b) and (c), which illustrate the previously explained effect of increasing the radiation rate in both the illumination and the diffraction level at the edges of the antenna. In particular, Fig. 4.4.5 shows the magnitude of the longitudinal electric field (plane *yz* in Fig. 4.4.4) and the poynting vector of the fields radiated by the aperture and the edges of the antenna. As α_y/k_0 is decreased in the uniform designs, the radiated wavefront in the aperture becomes more uniform; however, it can be clearly observed that the radiation efficiency is also decreased and more energy reaches the borders of the antenna, resulting in high diffraction. Both uniform illumination and high radiation rate (η_{RAD}=0.85) can be achieved at the same time by tapering the leakage constant, as Fig. 4.4.5(d) confirms. In this case, the needed modulation of the leakage rate and phase constant along the antenna corresponds to the red dashed line in Fig. 4.4.6. As this line shows, low leakage is required at the centre of the antenna (where the source is placed). The value of α_y/k_0 increases as the edges of the LWA are reached, compensating the natural exponential decay of the leaky-wave. This tapered value of $\beta_y/k_0 = \alpha_y/k_0$ is provided along the LWA length by modifying the length of the resonant elements in the periodic layers, as shown in Fig. 4.4.7. The blue dotted line in Fig. 4.4.6 indicates that the slots in the PRS are short in the centre of the antenna, providing the required low leakage close to the feed. Their lengths

increase as we move towards the edges, allowing the requested increase of α_y. In order to satisfy the splitting condition at each point of the LWA length (*i.e.,* to achieve the corresponding variation of $\beta_y = \alpha_y$), the lengths of the dipoles in the HIS must also be varied, as the red continuous line in Fig. 4.4.7 shows.

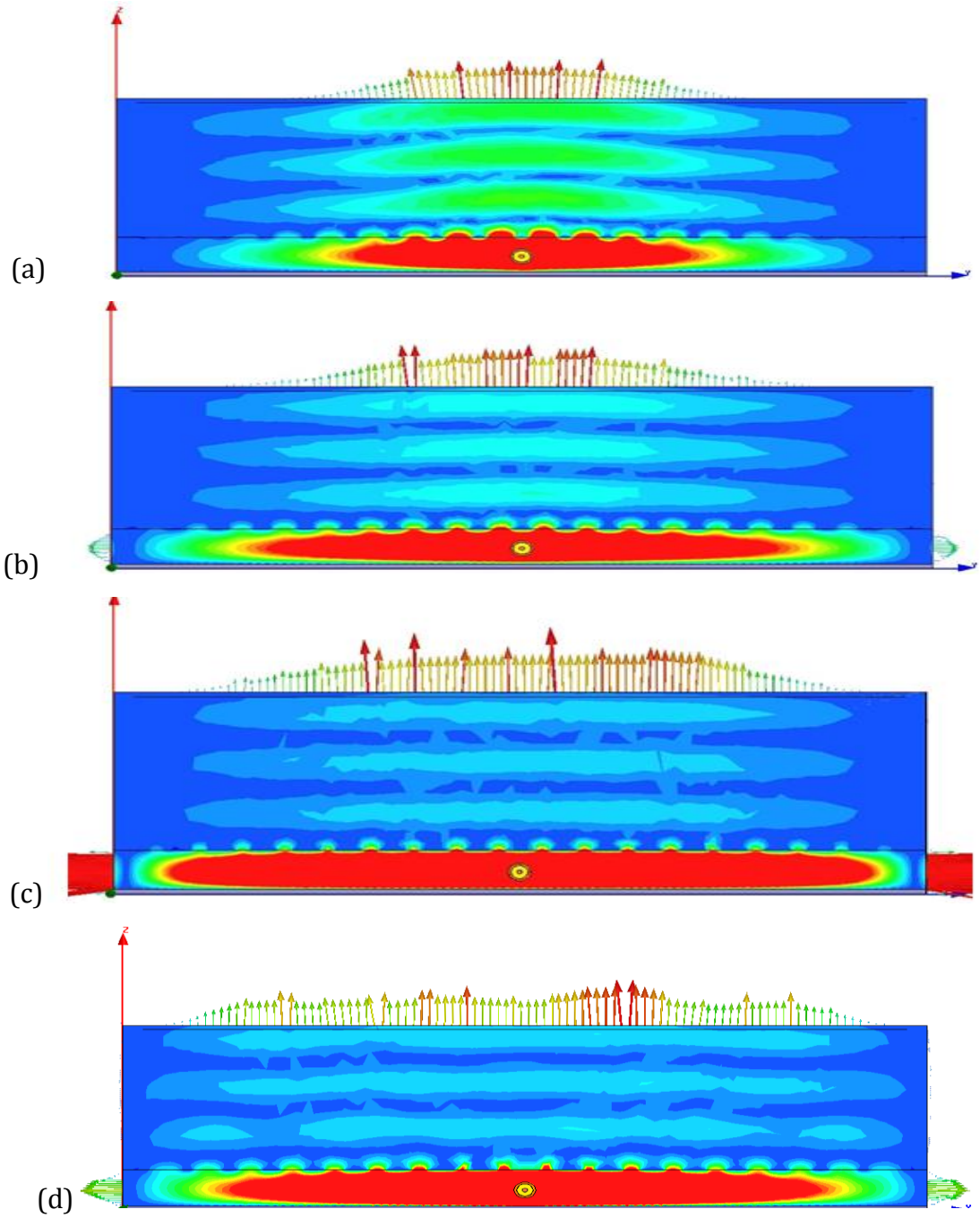

Fig. 4.4.5 Longitudinal near electric field and poynting vector (plane *yz,* see Fig. 4.44) in non-tapered 1D FP LWAs (a) $\alpha/k_0 = 0.1$, (b) $\alpha/k_0 = 0.05$, (c) $\alpha/k_0 = 0.02$ and (d) tapered $\alpha(y)$ (uniform illumination).

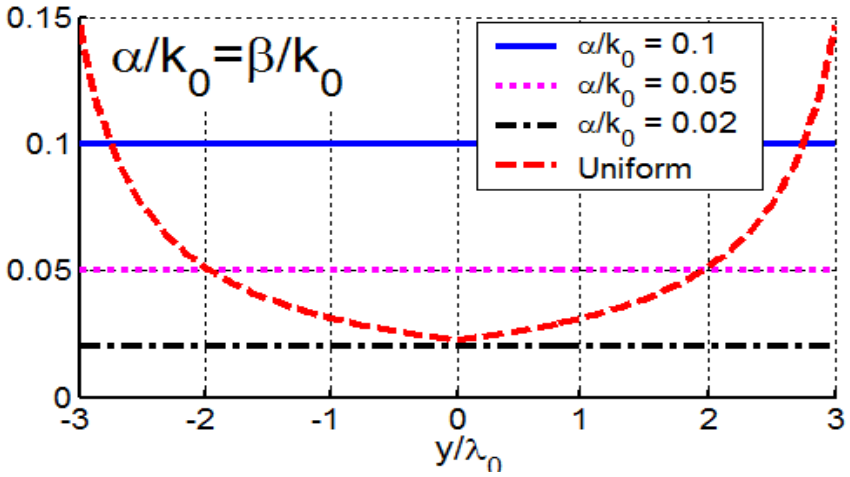

Fig. 4.4.6 Tapering function for 1D LWAs.

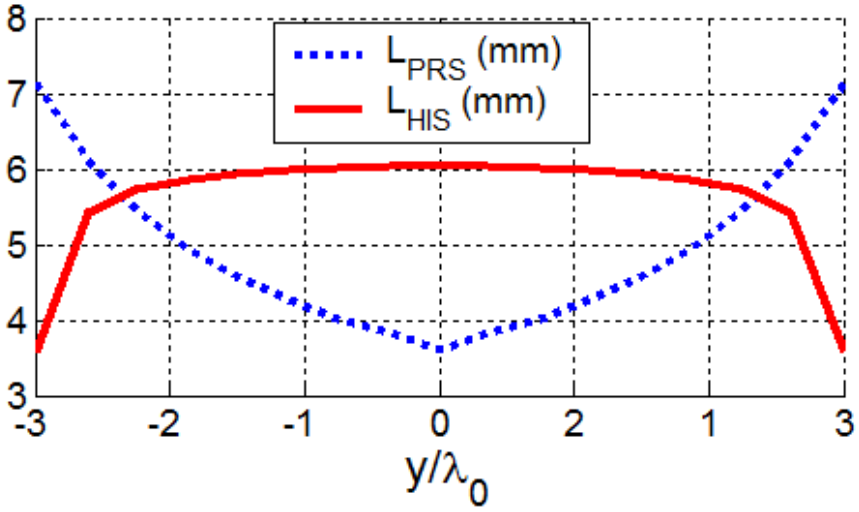

Fig. 4.4.7 Synthesized length of the slots in the PRS (L_{PRS}) and length of the dipoles in the HIS (L_{HIS}) which provides the tapered illumination of Fig. 4.4.5.

The tapered design with the central coaxial feeding is depicted in Fig. 4.4.8. The lengths of the slots in Fig. 4.4.8(b) and the dipoles in Fig. 4.4.8 (c) correspond to the synthesized dimensions plotted in Fig. 4.4.7.

The normalized radiation patterns obtained with [HFSS 2011] for the cases exposed in Fig. 4.4.5 are plotted in Fig. 4.4.8. As it corresponds to 1D LWAs, the patterns in Fig. 4.4.8 characterize fan-beams; the main beam is narrow in the H-plane [Fig. 4.4.8(a)] and wider in the E-plane [Fig. 4.4.8(b)]. The main differences between the four cases under study can be clearly identified in Fig. 4.4.8(a), regarding beamwidth, sidelobe level and diffraction level [measured at ±90° from the broadside direction in the H-plane of Fig. 4.4.8(a)].

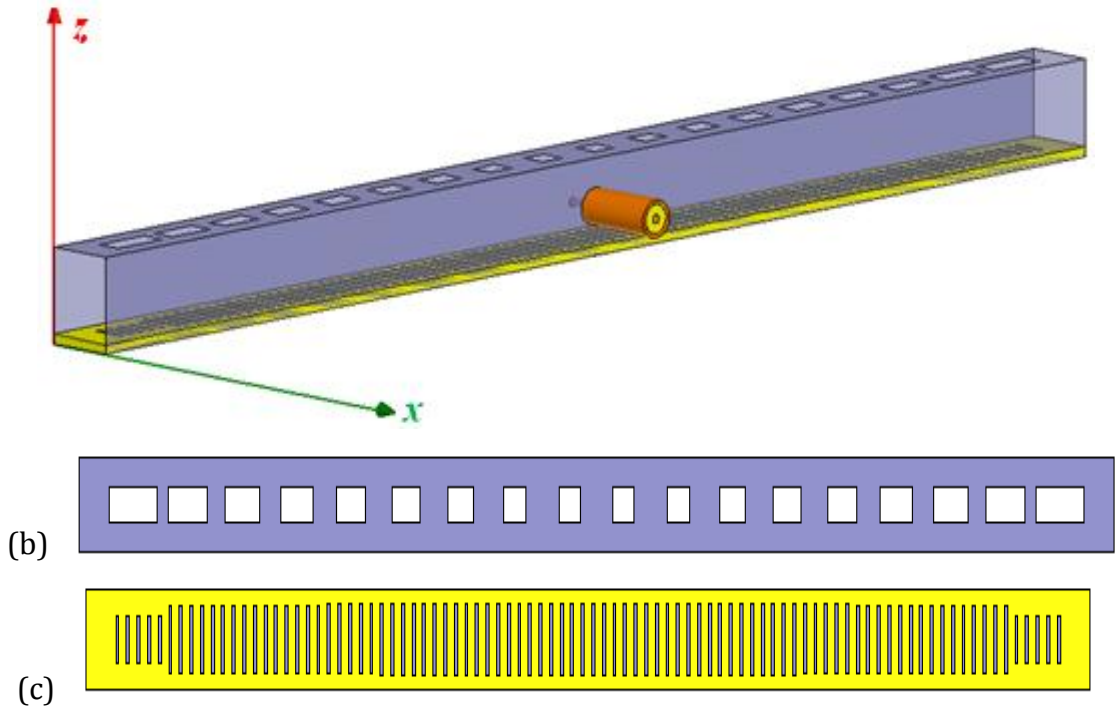

Fig. 4.4.7 Tapered 1D FP LWA (a) 3D model with central coaxial feeding (b) Tapered 1D slotted-based PRS, (c) Tapered 1D dipole-basded HIS.

The main concluding results are summarized in Table 4.4.1. As previously explained, the case of lowest leakage rate (α_y/k_0 = 0.02) provides the highest aperture efficiency η_{AP} = 99.6%. However, this is at the expense of the lowest radiation efficiency (η_{RAD} = 53%) and the highest diffraction level (-21dB) when compared to higher constant values of α_y/k_0 = 0.05, 0.1 (which are worse in the sense of aperture efficiency but present higher radiation efficiency and lower diffraction level). As explained before, the highest diffraction is due to higher energy reaching the LWA edges discontinuity (in this case it is a radiating open end), as a result of the lower radiation efficiency η_{RAD}. All these facts affect the directivity, which reaches a maximum value of D = 11.63 dBi for the non-tapered design with constant α_y/k_0 = 0.05. On the contrary, the 1D FP LWA with tapered $\alpha_y(y)$ makes available a directivity of D = 13.15 dBi. This is possible thanks to very high aperture efficiency η_{AP} = 0.98 as a result of the more uniform illumination, while it is kept very high radiation efficiency (η_{RAD} = 0.85). Also, the simulated SLL is reported in Table 4.4.1 for each case, observing how the SLL increases as the aperture is more uniformly illuminated, tending to theoretical -13dB for perfect uniform illumination.

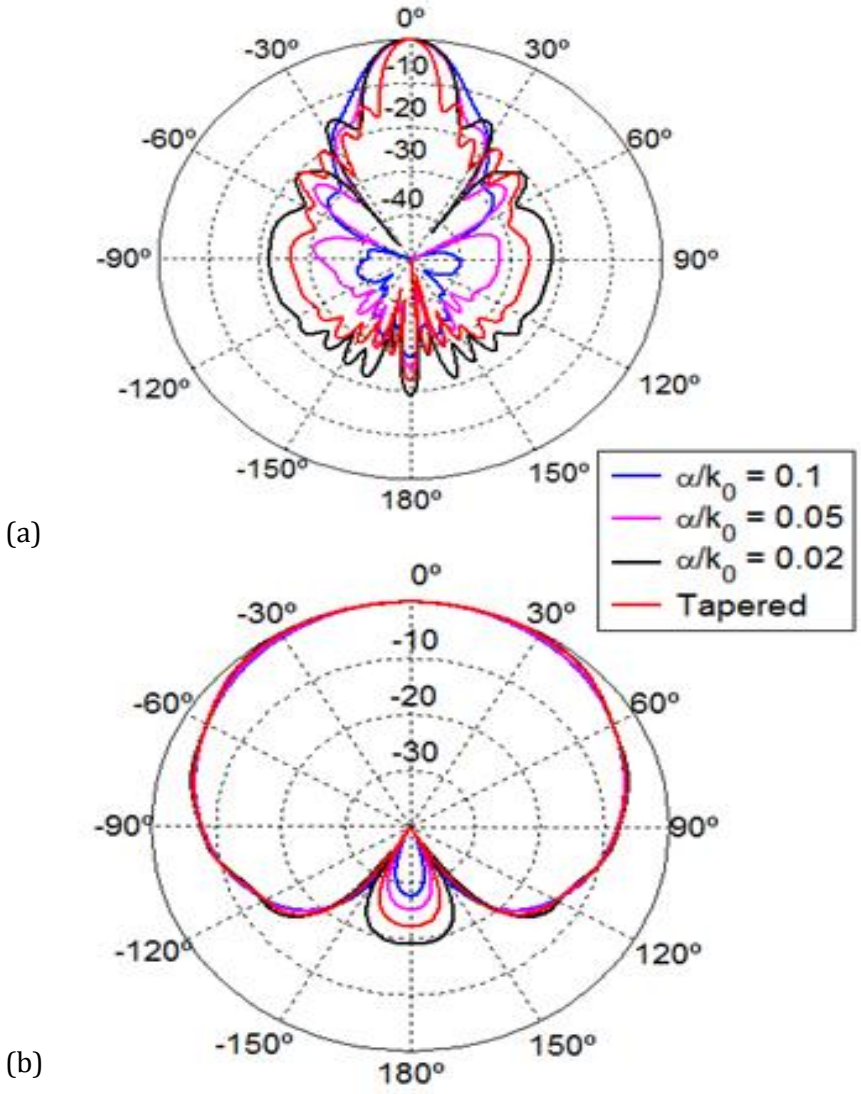

Fig. 4.4.8 Normalized radiation patterns in dB of 1D FP LWAs (a) H-plane (b) E-plane.

CASE	*D*(dBi)	η_{AP}	η_{RAD}	*Diffraction*	*Sidelobe*
α/k_0 = 0.1	11.15	60.8%	97.7%	-40 dB	-29 dB
α/k_0 = 0.05	11.63	88.4%	85%	-30 dB	-25 dB
α/k_0 = 0.02	11.02	99.6%	53%	-21 dB	-15 dB
Tapered α/k_0	13.15	98%	85%	-25 dB	-14 dB

Table 4.4.1 Directivity enhancement in H-plane of 1D FP LWAs

4.5 Control of the illumination at broadside of 2D FP LWA

Two-dimensional FP LWAs produce high-directive pencil beams radiating at broadside by exciting a cylindrical leaky wave from a single point source [Ip 1990]. However, they usually present very narrow bandwidth and low aperture efficiency due to the high quality factor of the resonator. Improved bandwidth is obtained when the PRS reflectivity is decreased at the cost of reducing the illumination efficiency [Alkhatib 2007]. Multiple fed FP LWAs have also been proposed to increase the bandwidth and illumination efficiency at the expense of a much more complex array feeding network [Weily 2007], [Leger 2005], losing one of the most interesting features of FP LWAs which is their simple feeding scheme. The use of double-layer PRS with slightly different resonant frequencies can extend the bandwidth; however, the reported gain and aperture efficiency were deficient [Vu 2007], [Moustafa 2008]. The use of step-sized HIS (also known as compound FP LWAs [Zhang 2007], [Wu 2010], or tapered AMC LWAs [Yeo 2009]) has been proposed to increase the gain-bandwidth product and the associated aperture efficiency. However, the tapered designs presented in [Zhang 2007], [Wu 2010] and [Yeo 2009] relied on full-wave simulations of the whole antenna, and an efficient technique to design the tapered dimensions of the HIS has not been proposed so far. Recently, a design procedure has been suggested for spiral

circularly polarized LWAs based on modulated surface impedance [Minatti 2011]. In this section, it is presented, for the first time a systematic approach to design tapered 2D FP LWAs, in which both periodic layers (PRS and HIS) are modulated to obtain high aperture efficiency while assuring pencil-beam broadside radiation. The structure of Fig. 4.5.1 is here considered, which is the two-dimensional version of the one-dimensional LWA studied in the previous section (see Fig. 4.4.4). It must be noticed that the tapering of 2D LWAs is a much more complicated task than the one performed for the 1D case, not only due to the cylindrical nature of the excited leaky-waves, but also due to the hybrid polarization of the radiating leaky-wave. A similar rationale to the one applied in [Takahashi 1991] is now followed to obtain the requested tapering of the cylindrical leaky-wave leakage rate as a function of the radial distance ρ.

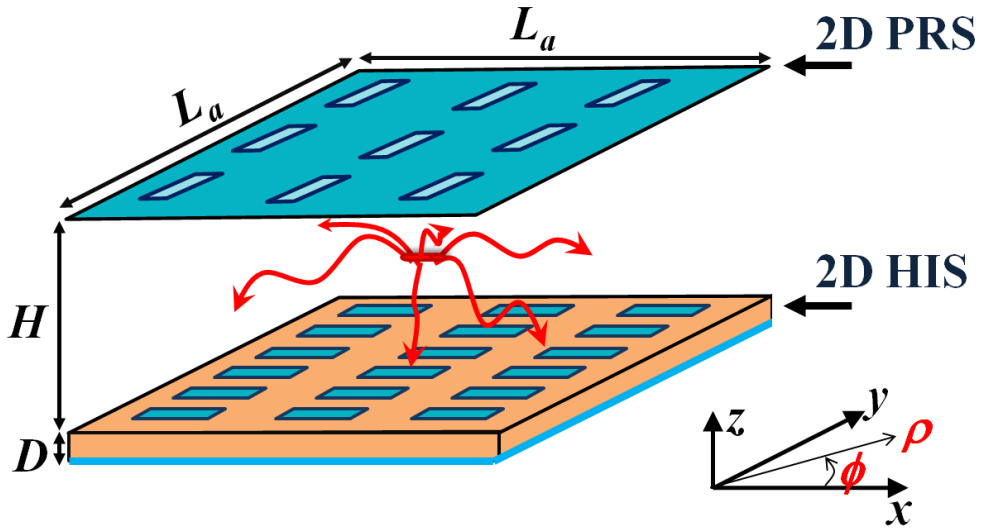

Fig. 4.5.1 Scheme of (a) 1D and (b) 2D Fabry-Perot Leaky-Wave Antennas with planar PRS and HIS (Dimensions: H = 10mm, a = P = 8.5 mm, D =1.13mm, Q = 3mm, P_{HIS} = 1.7mm, Q_{HIS} = 0.5mm, ε_r = 2.2).

The formulation regarding two-dimensional uniform LWAs was presented in Section 3.1.2. As it was explained there, because of the horizontal electric dipole that feeds the structure (see Fig. 4.5.1), two cylindrical leaky waves are excited. In particular, the x-polarized electric dipole placed in the middle of the cavity excites a pair of cylindrical leaky waves, a TE_z and a TM_z one. The x-polarized field can be considered as a TM wave when propagating in one of the main transverse axis [x-axis, ϕ = 0º in Fig. 4.5.1], a TE wave when propagating in the complementary axis

[y-axis, ϕ = 90º in Fig. 4.5.1], and a combination of both polarizations for any other transverse direction and azimuthal angle ϕ [Ip 1990]. Therefore, although the illumination of the 2D LWA is described employing Hankel functions (as it was explained in Section 3.1.2), the following approximated expression can be employed when considering one of the main planes [Takahashi 1991]

$$M(\rho,\phi) = \left.\sqrt{\frac{\alpha_\rho^{\mathrm{TM/TE}}(\rho,\phi)}{\rho}}\, e^{-\int_0^\rho \alpha_\rho^{\mathrm{TM/TE}}(\tau,\phi)d\tau} e^{-\int_0^\rho \beta_\rho^{\mathrm{TM/TE}}(\tau,\phi)d\tau}\right|_{\substack{\phi=0°,\mathrm{TM}_z \\ \phi=90°,\mathrm{TE}_z}} \tag{4.5.1}$$

where $\beta_\rho^{\mathrm{TM/TE}}$ and $\alpha_\rho^{\mathrm{TM/TE}}$ stand for the phase constant and leakage rate associated to the $\mathrm{TM_z}$ or $\mathrm{TE_z}$ cylindrical leaky waves, respectively. Equation (4.5.1) is very similar to the illumination of 1D LWAs (equation (3.1.12)), the only difference is the factor $1/\rho$, that in this case accounts for the cylindrical dispersion of the wave. Reversing the above expression it is possible to obtain the leakage rate which provides a certain cylindrical leaky wave illumination $M(\rho,\phi)$ in each of the main planes

$$\frac{\alpha^{\mathrm{TE/TM}}(\rho)}{k_0} = \frac{\lambda_0}{4\pi} \left.\frac{\rho|M(\rho,\phi)|^2}{\frac{1}{\eta_{RAD}}\int_{R_0}^{R}\rho|M(\rho,\phi)|^2\partial\rho - \int_{R_0}^{\rho}\rho|M(\rho,\phi)|^2\partial\rho}\right|_{\substack{\phi=0°,\mathrm{TM}_z \\ \phi=90°,\mathrm{TE}_z}} \tag{4.5.2}$$

The condition $\beta_\rho^{\mathrm{TM}} = \beta_\rho^{\mathrm{TE}} = \alpha_\rho^{\mathrm{TM}} = \alpha_\rho^{\mathrm{TE}}$ is imposed, in order to satisfy the splitting condition and therefore, broadside radiation. As an illustrative example, an antenna aperture of $10\lambda_0 \times 10\lambda_0$ is considered, and the quasi-uniform illumination of Fig. 4.5.2(a) is pursued (it is assumed to be ϕ-independent). Then, by applying Eq. (4.5.2) it is obtained the value of $\beta_\rho^{\mathrm{TM}} = \beta_\rho^{\mathrm{TE}} = \alpha_\rho^{\mathrm{TM}} = \alpha_\rho^{\mathrm{TE}}$ at each point of the aperture that supports the desired illumination (plotted in Fig. 4.5.2(b)). As it was proceeded in the 1D case, the geometry of both periodic PRS and HIS layers is now synthesized in order to achieve the desired leaky-mode complex propagation constant at each point of the antenna. Applying the equations approach described in Section 4.2, the dimensions of the PRS slots and the HIS dipoles are obtained (see Fig. 4.5.3). As the blue dotted line in Fig. 4.5.3 shows for

$L_{PRS}(\rho)$, the PRS slots are widened as we move far from the antenna center feed. This is needed to exponentially increase the leakage rate, so that both the cylindrical dispersion and the exponential energy drop are compensated, and quasi-uniform illumination is obtained across the whole antenna aperture. At the same time, the HIS dipoles lengths $L_{HIS}(\rho)$ must be complementarily tapered, so that the phase variations introduced by the PRS modulation are compensated, and the *splitting condition* is satisfied at any antenna aperture position. The modulation of the HIS dipoles lengths is plotted with red continuous line in Fig. 4.5.3.

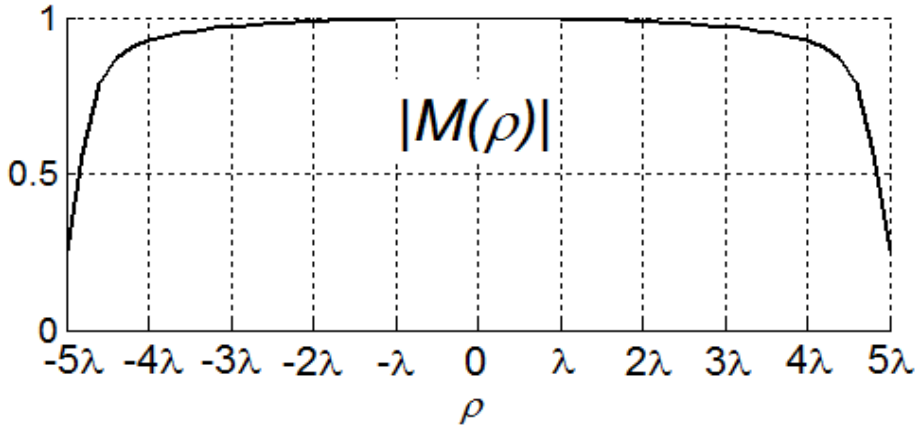

(a)

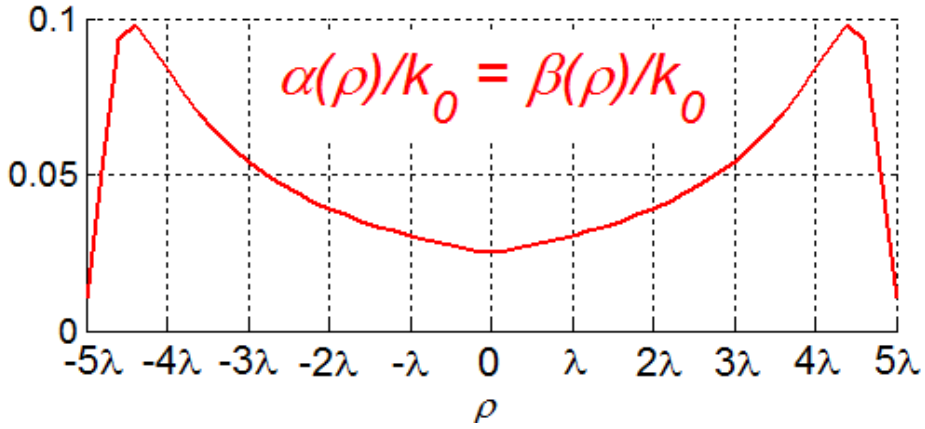

(b)

Fig. 4.5.2 (a)Quasi-uniform illumination in 2D FP LWA and (b) Leakage-rate that provides it.

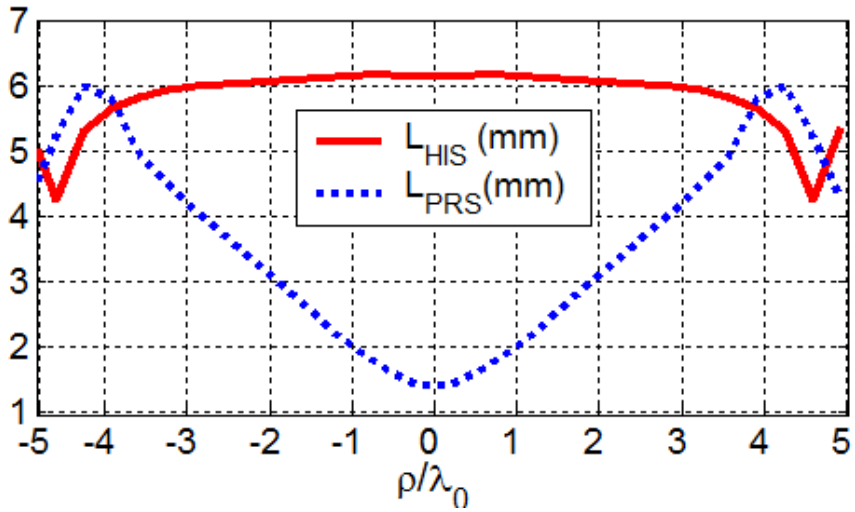

Fig. 4.5.3 Synthesized length of the slots in the PRS (L_{PRS}) and length of the dipoles in the HIS (L_{HIS}) which provides a tapered quasi-uniform illumination in a 2D FP LWA.

Figure 4.5.4 illustrates the near-field aperture illumination for three cases of 2D FP LWA with dimensions $10\lambda_0 \times 10\lambda_0$: the first case is a non-tapered LWA with high leakage-rate ($\alpha/k_0 = 0.07$), the second non-tapered case presents lower rate ($\alpha/k_0 = 0.015$), and the third case is a tapered design with quasi-uniform illumination and η_{RAD} = 90%. As it can be easily seen from the currents in the aperture, the most uniform distribution is obtained for the tapered case. The non-tapered case with leakage rate 0.07 provides simple exponential illumination with very poor aperture efficiency (η_{AP} = 24.3%) and therefore low directivity (D = 23.8dBi while the maximum achievable directivity is 29.9dBi). Negligible diffraction lobes are obtained as a result of the high η_{RAD} = 98% (as Fig. 4.5.4(b) shows, very little energy reaches the edges of the antenna). The non-tapered scenario with leakage rate 0.015 illuminates better the antenna surface, but it suffers from distortion of the aperture field as a consequence of the standing waves created by the low amount of radiated energy (η_{RAD} = 61%), and therefore the high amount of guided energy reaching the edges of the antennas [Sun 2012], [Muhammad 2012] (as it is pointed out in Fig. 4.5.4.(d)). The nulls and maxima associated to the standing wave can be clearly appreciated surrounding the aperture centre in Fig. 4.5.4(c). As a result, the directivity is increased by only 2.3dB when compared to the non-tapered case with higher leakage, obtaining D = 26.45dBi and η_A = 44.7%. However, the diffraction level strongly increases from

below -40dB up to -18dB, as summarized in Table 4.5.1. As it happened in the previous section with the 1D LWA, the tapered solution gives the best balance, providing η_{AP} = 73.2% and η_{RAD} = 90%, resulting in the highest directivity (D = 28.6dBi), and keeping low diffraction levels (below -30dB).

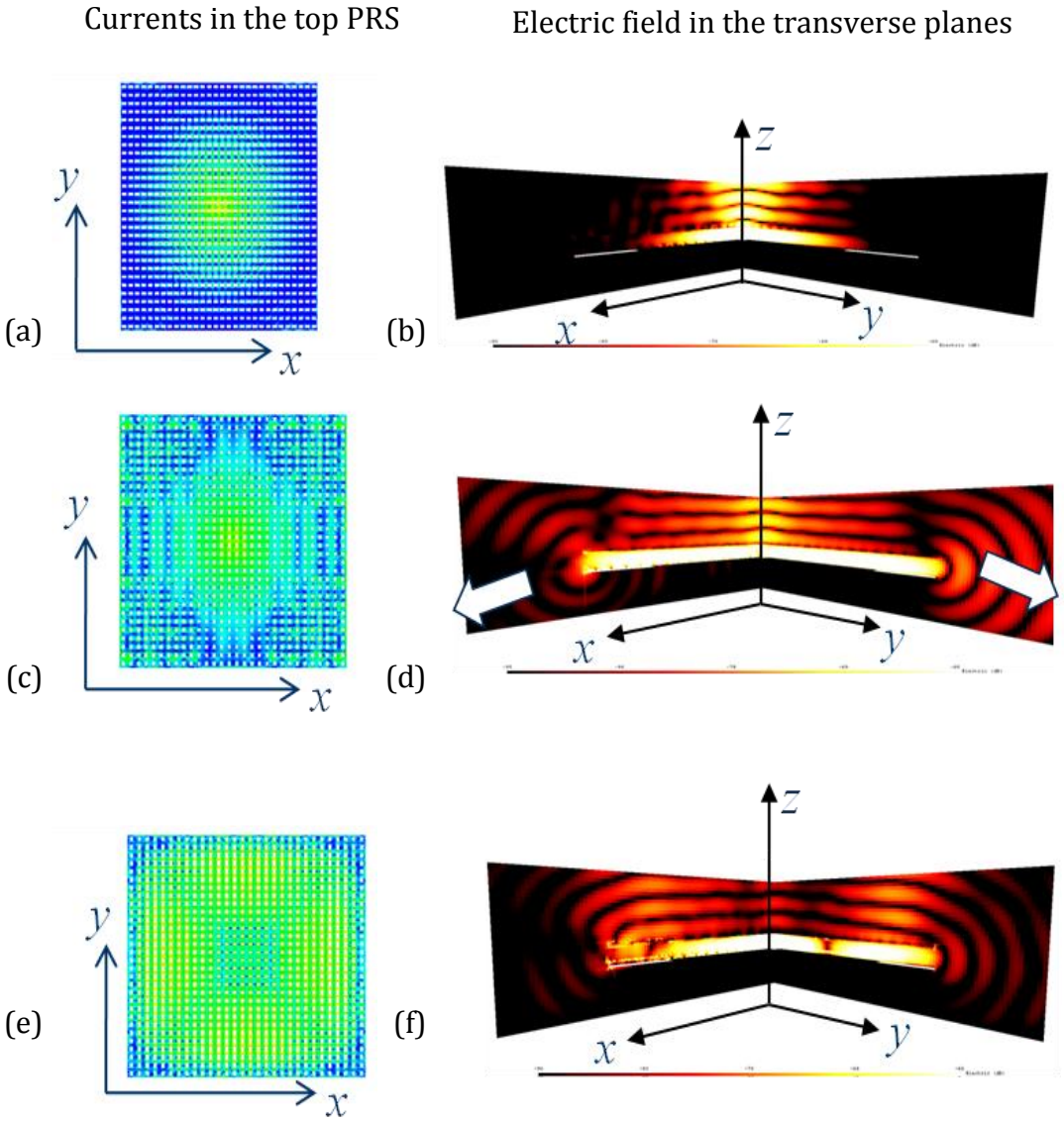

Fig. 4.5.4 Near fields in 2D FP LWAs (a,b) $\alpha/k_0 = 0.07$ (c,d) $\alpha/k_0 = 0.015$ (e,f) tapered $\alpha(\rho)$

The previous results are summarized in Table 4.5.1, and the normalized radiation patterns in both H and E planes are plotted in Fig. 4.5.5. In contrast to the fan-beam patterns obtained in the previous section (see Fig. 4.4.8), the main lobes in Fig. 4.5.5 are pencil beams, as it corresponds to a 2D FP LWAs. The previous numerical results are in coherence with these radiation patterns. It can be clearly

checked in both Fig. 4.5.5(a) and (b) that among the three studied LWAs, the tapered case provides both narrow beamwidth and low diffraction, thus validating the validity of the proposed tapering technique.

CASE	*D*(dBi)	η_{AP}	*Diffraction*
$\alpha/k_0 = 0.07$	23.8	24.3%	-40dB
$\alpha/k_0 = 0.015$	26.1	44.7%	-18dB
Tapered α/k_0	28.6	73.2%	-30dB

Table 4.5.1 Directivity enhancement in 2D FP LWAs.

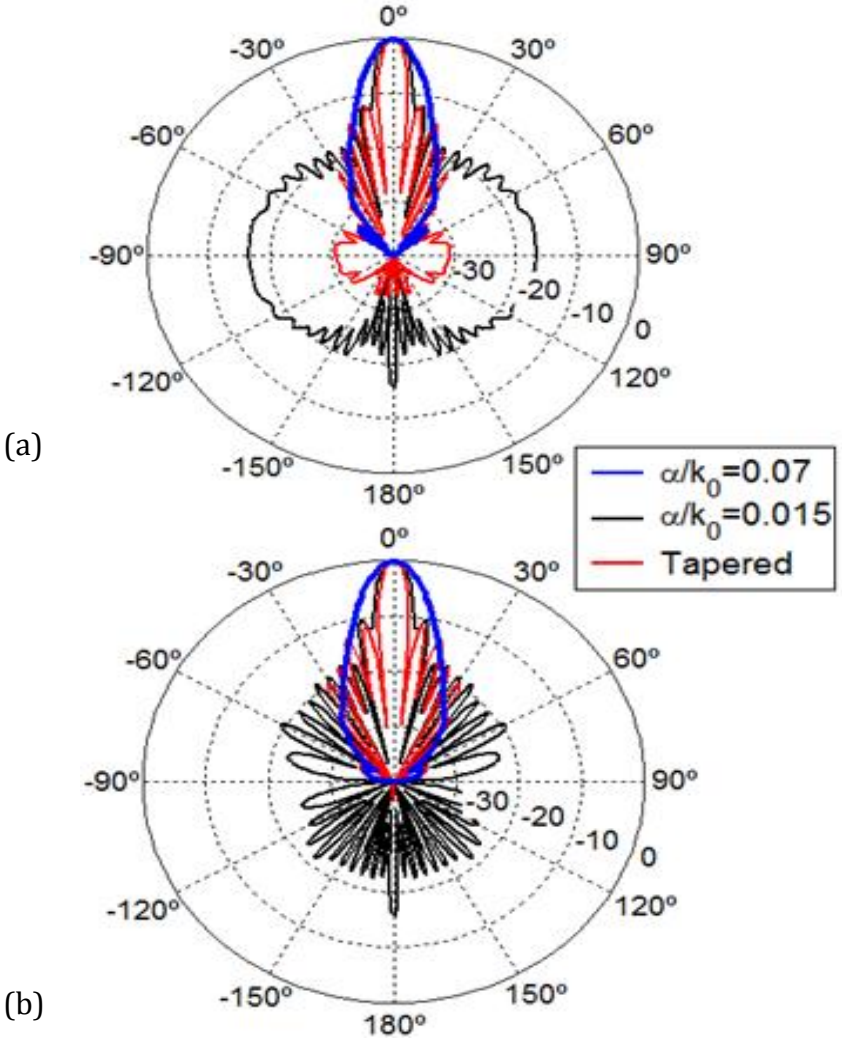

Fig. 4.5.5 Normalized radiation patterns in dB of 2D FP LWAs (a) H-plane (b) E-plane.

4.6 Conclusions

In this chapter, the efficient modulation of the illumination in 1D and 2D FP LWAs has been carried out. The basic concepts underlying the tapering procedure and its main applications were explained in Section 4.1.

Next, an efficient synthesis technique especially suited for double-layer FP LWAs has been proposed in Section 4.2. The approach is based on the numerical solution of two simple equations extracted from an equivalent transverse network, which yields the dimensions of the PRS and HIS circuits that produce the desired leaky-mode complex wavenumber. The approach is simple and requires the computation of the periodic layers response under the condition of plane-wave incidence, thus avoiding the much more expensive solution of leaky-mode dispersion problems.

Due to its efficiency, this approach can be directly applied to the design of tapered FP LWAs, which modulate the printed circuit dimensions to synthesize specific aperture distributions. As an example, in Section 4.3, two low-sidelobe tapered 1D LWAs were designed to point at 20º and 50º at 15GHz. Experimental results confirmed the accuracy of the proposed synthesis technique, and the tabulated simulation times demonstrated that it is much less time consuming than other known methods.

Finally, the optimization of the aperture illumination efficiency in 1D and 2D Fabry-Perot leaky-wave antennas was theoretically studied in Section 4.4 and 4.5. A quasi-uniform taper was proposed in order to achieve high aperture efficiency, while assuring high radiation efficiency to minimize diffraction and standing waves. Also, the splitting condition must be satisfied in all radiating sections of the LWA to obtain the highest directivity at broadside. In particular, the proposed technique was applied in the case of 1D and 2D LWAs loaded with a slotted-based partially-reflective surface (PRS) and a dipole-based high impedance surface (HIS). It was illustrated with various numerical examples how the proper modulation of the PRS and HIS surfaces makes possible to increase the directivity of this type of resonant antennas in a totally novel manner.

In conclusion**, the two objectives aimed at the beginning of this chapter (O6 and O7) have been successfully achieved**.

The work developed in this chapter has given rise to the publication of 1 peer-review international journal paper (IJ), 2 Spanish journal papers (SJ), 3 international conference papers (IC) and 3 Spanish conference papers (SC). These references are copied below; they have been extracted from the complete list of publications of Section 5.3.

IJ7. **M. García-Vigueras**, J. L. Gómez-Tornero, G. Goussetis, A. R. Weily, and Y. J. Guo, "Efficient Synthesis of Scanning Fabry-Perot Antennas with Low Sidelobe Levels," *IEEE Antennas and Wireless Propag. Lett.* (accepted with minor revisions).

SJ1. **M. García Vigueras**, A. Martínez Ros, R. Guzmán Quirós and José Luis Gómez Tornero, "Control de la Directividad en Broadside en Antena Leaky-Wave 1D", *IV Jornadas de introducción a la investigación de la UPCT*, nº4, págs.97-99. May 2011

SJ2. **M. García Vigueras**, R. Guzmán Quirós and José Luis Gómez Tornero, "Antenas Leaky-Wave 1D y 2D iluminadas eficientemente" *V Jornadas de introducción a la investigación de la UPCT*, págs. 90-92, April 2012

IC7. **M. García-Vigueras**, J.L. Gómez-Tornero, R. Guzmán-Quirós, F.Quesada-Pereira and A. Alvarez-Melcón "Control of the Radiation Properties of a FSS Loaded Leaky-Wave Antenna" ,European Conference on Antennas & Propagation 2010, Barcelona, Spain, 12-16 April, 2010.

IC9. **M. García-Vigueras**, J.L. Gómez-Tornero and R. Guzmán-Quirós "Beamwidth Control of 1D LWA Radiating at Broadside", *Proceedings of the 4th European Conference on Antennas & Propagation*, Rome, Italy, 11-15 April, 2011.

IC12. **M. García-Vigueras**, P. DeLara-Guarch, J.L. Gómez-Tornero and R. Guzmán-Quirós, G. Goussetis, "Efficiently illuminated broadside-directed 1D and 2D tapered Fabry-Perot leaky-wave antennas," *Proceedings of the 6th European Conference on Antennas & Propagation,* (Prague, Czech Republic), pp.247-251, 26-30 March 2012 (ANTENNA THEORY BEST PAPER AWARD)

SC3. **M. García-Vigueras**, J.L. Gómez-Tornero, R. Guzmán-Quirós, J.S. Gómez-Díaz, and A. Álvarez-Melcón, "Control de la Radiación de una Antena Leaky-Wave Cargada con una Superficie Selectiva en Frecuencia", XXV Simpósium Nacional de la Unión Científica Internacional de Radio URSI, Bilbao (Pais Vasco, Spain). 15-17 September 2010

SC4. **M. García-Vigueras**, R. Guzmán-Quirós, A. Martinez-Ros, J.S. Gómez-Díaz and J.L. Gómez-Tornero, " Síntesis de la Radiación en Broadside en Antena Leaky-Wave 1D," *XXVI Symposium Nacional de URSI*, (Leganés, Madrid, Spain), 7-9 September 2011.

SC7. **M. García-Vigueras**, J.L. Gómez-Tornero, R. Guzmán-Quirós and A. Martinez-Ros, " Optimización de la Directividad en Antenas Leaky-Wave 1D y 2D basadas en cavidades Fabry-Perot," *XXVII Symposium Nacional de URSI*, (Elche, Alicante, Spain), 12-14 September 2012.

Chapter 5:

Conclusions and perspectives

5.1 Conclusions

The main achievement of this thesis has been the **systematic and efficient control of the field distribution in double-layer Fabry-Perot Leaky-Wave Antennas** (FP LWAs). As it was explained in the first chapter of this dissertation, this accomplishment may become a relevant success for the antenna community, since it allows the synthesis and design of high gain antennas with very exotic features. However, it has not been possible to address this general problem without first tackling several specific issues along Chapter 2, 3 and 4, thus achieving many other goals throughout the development of this thesis.

The double-layered FP LWAs considered in this work are schemed in Fig. 5.1.1. Both, the one-dimensional (1D) and the two-dimensional (2D) scenarios have been studied, which are respectively depicted in Fig. 5.1.1(a) and (b). So far, 1D FP LWAs have been generally used for scanning purposes whereas 2D FP LWAs have been useful when they provided a pencil radiated beam at broadside [Jackson 2008]. The periodic layers which have been considered to form the structure are either arrays of metallic dipoles/patches or complementary metallic sheets periodically perforated with rectangular holes (see Fig. 5.1.1). These top and bottom Frequency Selective Surfaces (FSS) behave respectively as a Partially

Reflective Surface (PRS) and a High Impedance Surface (HIS). The performance of these layers is of key importance for the operation of the whole FP structure. Then, the first specific requirement for this thesis is now clear: the efficient and accurate modeling of periodic surfaces.

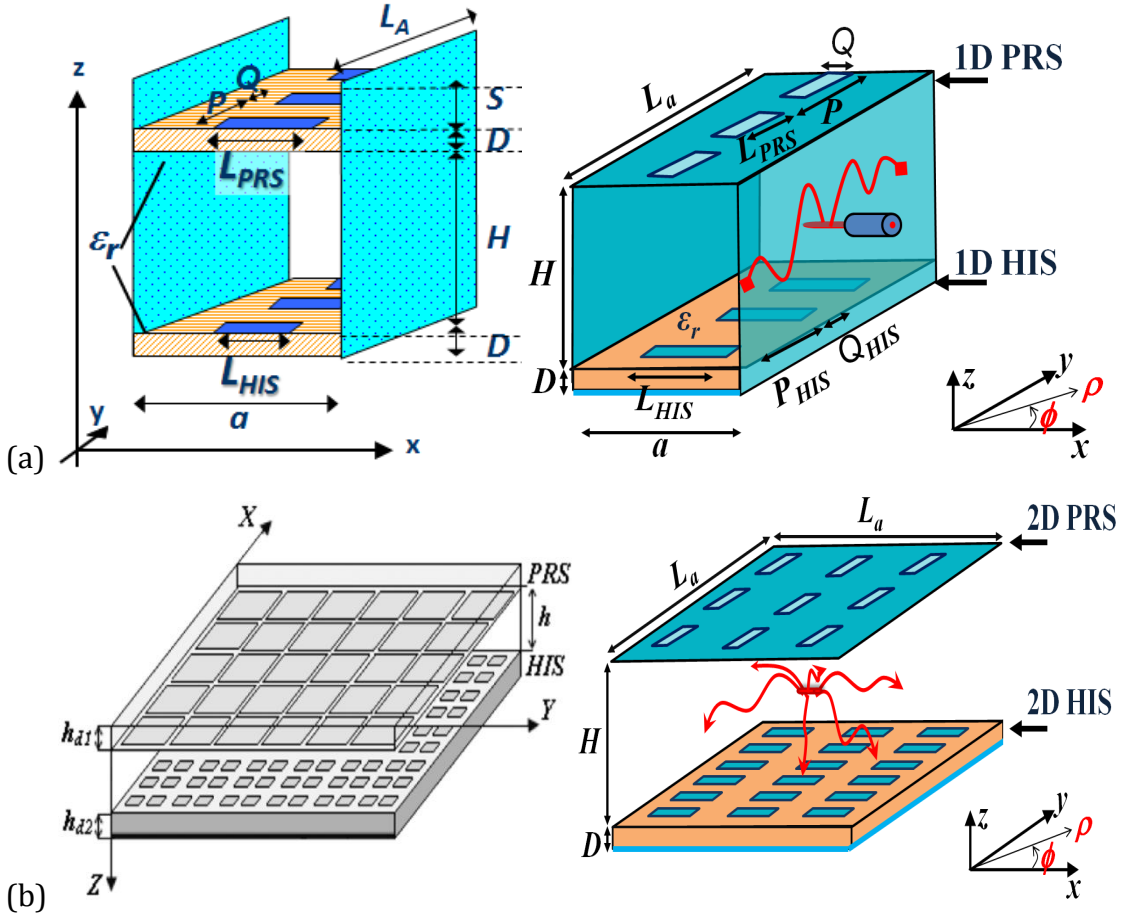

Fig. 5.1.1 Double-layer FP LWAs considered in this Ph. D both in (a) one-dimensional and (b) two-dimensional topologies.

Chapter 2 has been centered in obtaining pseudo-analytical expressions of the equivalent admittance of dipole-based frequency selective surfaces. Firstly, it is proposed a modification of the **pole-zero matching technique** developed in [Maci 2005]. The presented expansion allows to obtain an analytical expression which is a function of the wave unknown propagation constant and the length of the resonant dipoles. In this way, dispersion curves as a function of the dipoles length can be efficiently obtained for the first time, without any geometrical restriction. This technique is valid for any dimension of the dipoles, and also for square patches, apertures and slots. The only restriction is that the simple transverse

equivalent network is valid if higher-order Floquet-modes are below cut-off in the transverse direction. The novel technique has been illustrated by obtaining useful parametric curves for the design of practical structures based on printed-circuit FSS, such as a miniaturized HIS-loaded waveguide, and a Fabry-Perot resonant leaky-wave antenna. Results have been validated by comparing with more costly full-wave techniques based on method of moments and finite element method. Excellent agreement has been obtained for propagating modes and also for radiating leaky-waves, thus confirming the efficiency and versatility of the proposed approach.

A **software tool** which implements the previous pole-zero approach has been implemented in MATLAB®. This tool and is based on a Transverse Equivalent Network (TEN) technique and it is especially suited to the analysis of rectangular waveguides excited by TE_0 modes and loaded by FSSs. The tool lets the user obtain the dispersion diagrams of such structures. Its graphical user interface is very intuitive, and guides the user through different semiautomatic analysis steps. Its results are really similar to the ones obtained by full-wave techniques, which have higher computational cost.

Finally, in this chapter it has been proposed **a more physical insightful approach to the circuit modeling** of the reflection/ transmission features of 2-D arrays of printed dipoles. This approach is based on the physical modal decomposition of the electromagnetic fields around the scatterers (printed dipoles in our case). The contribution of the infinite number of very high order modes scattered by the printed surface can be represented by a simple inductor and a simple capacitor. Only TE and TM modes with cutoff frequencies in the region of interest must be treated explicitly. After setting up the appropriate connection characteristics of the proposed equivalent network, the specific contribution of these few modes can be extracted by solving a small linear system of equations whose coefficients comes from a few full-wave numerical simulations carried out at certain specific frequency points. The accuracy of the circuit model predictions has been demonstrated for two different polarizations and a wide range of frequencies and incidence angles. An example of the modeling of a printed dipole-

based FSS is shown in Fig. 5.1.2, where it can be clearly seen that the accuracy extends to the grating lobe regime.

The availability of a circuit model not only reduces the overall computational effort but, even more importantly, it also provides a theoretical frame for understanding the qualitative performance of the patterned surface and to design devices based on such structures. In particular, the extraordinary reflection behavior that has given place to various and controversial theories in the past is very simply accounted for by our model. It should be highlighted that this equivalent-circuit model can also be used to characterize FSS structures with more complicated geometries of the scatterers, with the condition that their current profile does not change significantly with frequency. As a representative example, Fig. 5.1.3 shows the modeling of two arrays with different printed elements (i.e., a cross-dipole and a symmetric ring).

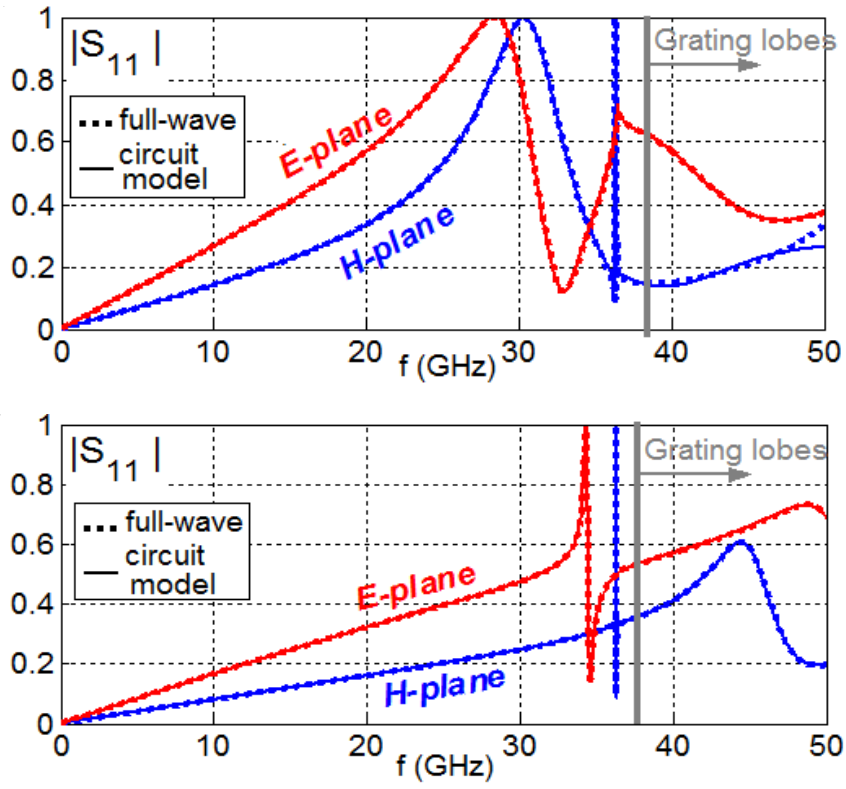

Fig 5.1.2 Magnitude of the reflection coefficient under θ = 40° incidence on E- and H-planes for a doubly periodic arrangement of metallic dipoles (the periodicity in both dimensions is 5mm) printed over a dielectric substrate (ε_r = 3 and width 0.5mm). The wave electric field is parallel to the dipoles, which width is 0.5mm and their length is (a) 3.5mm (b) 2mm.

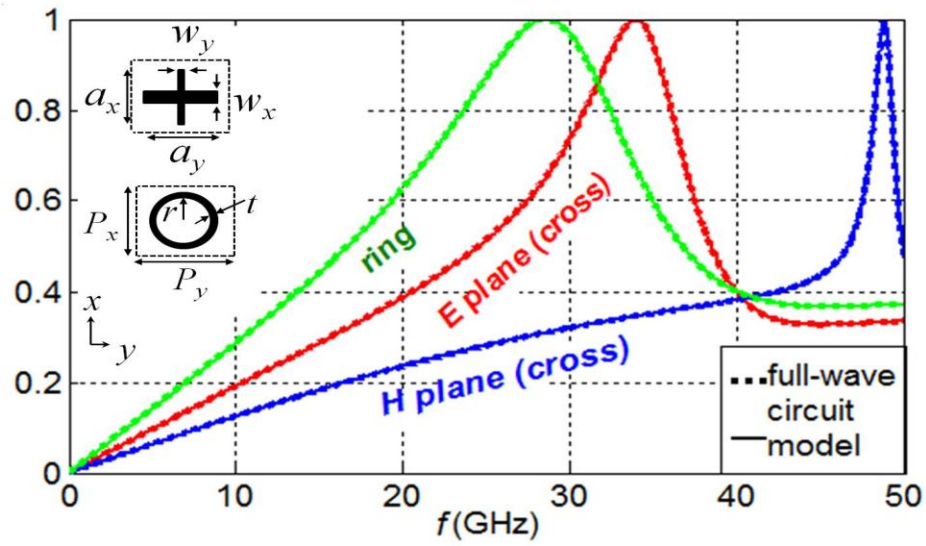

Fig 5.1.3 Magnitude of the reflection coefficient under TM normal incidence for periodic arrangements ($P_x = P_y$ = 5 mm) of circular rings (r = 3 mm, t = 0:5 mm,) and cross-dipoles (a_x = 2 mm, a_y = 3.5mm and $w_x = w_y$ = 0.5 mm). The arrays are printed on a substrate of ε_r = 2, d = 1 mm.

The work developed in Chapter 2 has given rise to the publication of 3 peer-review international journal papers (IJ), 4 international conference papers (IC) and 3 Spanish conference papers (SC) which correspond respectively to the references IJ1, IJ5, IJ6, IC1, IC9, IC10, IC11, SC1, SC5 and SC6detailed in Section 5.3.

After the periodic surfaces characterization, in **Chapter 3** it is possible to perform the analysis and design of uniform Fabry-Perot Leaky-Wave Antennas of Fig. 5.1.1. Firstly, the **novel one-dimensional leaky-wave antenna** shown in Fig. 5.1.1(a), with flexible control of the scanning angle and the leakage rate has been proposed and studied. This structure has been analyzed using the TEN-tool developed in the previous chapter, from which the leaky-mode dispersion curves are obtained. In addition, the TEN-tool also gives physical insight into the operating mechanism of this antenna. It has been demonstrated that, once the cavity dimensions are chosen to operate at a desired frequency, the length of the dipoles allow control of the leaky-mode propagation constant. Specifically, one PCB forms a PRS, whose transparency controls the leakage rate of the antenna. The second grounded PCB creates a HIS, whose equivalent reflection phase determines the effective cavity height, and the pointing angle of the antenna. This enables high-gain radiation patterns to be synthesized using standard photolithographic

processes, without the need for modifying the waveguide structure. Compared to previous hybrid LWAs based on PCBs in dielectric waveguides, the proposed antenna avoids dielectric losses since a hollow waveguide is used as the host medium. To verify the concept and design theory, several LWA antenna prototypes operating at 15 GHz have been fabricated. Measured results agree with the predicted ones. A coaxial-to-waveguide transition which serves as feeding and matched load device has been also carefully designed. A summary of the measured radiation patterns is shown in Fig. 5.1.4, which shows that it is indeed feasible to independently control the scanning angle and the directivity of the antenna at a fixed frequency, whilst keeping 90% radiation efficiency.

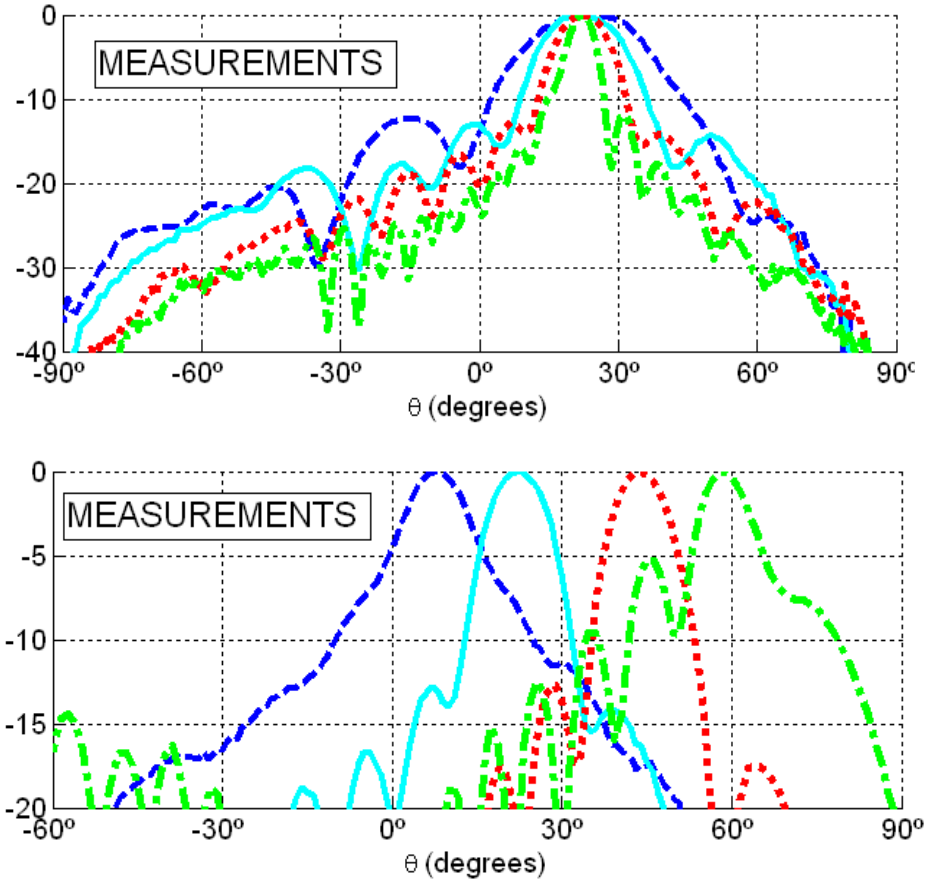

Fig 5.1.4 Measured radiation pattern of 1D FP LWA designs at 15GHz. (a) Designs with constant pointing angle and variable directivity. (b) Designs with fixed directivity and different pointing angles.

In Chapter 3, it was also demonstrated the **improvement in the frequency scanning sensitivity of a hollow LWA** due to the insertion of the HIS. The new topology increases the frequency scanning sensitivity, thus reducing the required

bandwidth to scan the main beam from near broadside to near endfire. It avoids the use of dielectric-filled waveguides, thus minimizing the associated dielectric losses. The HIS must be designed to introduce an Artificial Magnetic Conductor (AMC) resonance condition close to the cut-off of the leaky mode, so that the broadside and the endfire radiation frequencies are located in close proximity. Experimental results on fabricated prototypes have also been reported, showing very good agreement with theory. The designed 1D HIS-loaded LWA shows a scanning range of [5º,67º] in a bandwidth from 11GHz to 16GHz, achieving a frequency sensitivity of 12.4°/GHz. A similar LWA without HIS presents a scanning range of [7º,65º] in the frequency range from 13GHz to 26GHz, which has a frequency sensitivity of 4.5°/GHz. Therefore, the frequency sensitivity is almost three times higher when the HIS is added to the hollow LWA. A dielectric-filled LWA with similar frequency sensitivity as the HIS-loaded air-filled LWA would introduce 4dB higher insertion losses, subsequently decreasing the LWA radiation efficiency. It should be noted that the frequency-scanning enhancement shown in this work can be extended to any type of air-filled LWAs due to the fact that the HIS is able to perturb the leaky-mode by introducing a strongly dispersive AMC boundary condition.

Finally, this chapter ends with the **analysis and design of uniform 2D FP LWAs**. Here it is explained that, by applying the method of images, it is possible to characterize 2D antennas in the H and E planes by analyzing two one-dimensional scenarios employing the tool developed in Chapter 2. Three cases of 2D LWAs have been designed to point at broadside with different cavity heights. The dispersion characteristics of uniform 2D FP LWAs in the main planes are efficiently obtained. In addition, the employed approach has also enabled the design of the two printed circuits together with the height of the cavity, in order to obtain broadside radiation. The main restriction of this efficient TEN-based analysis technique is its limitation to a minimum height H between the PRS and HIS sheets in the order of $H=\lambda_0/10$. Below this limit there is a strong interaction between evanescent higher-order Floquet-Modes created at the PRS and HIS circuits, which is not modeled by the simple TEN circuits.

The work developed in Chapter 3 has given rise to the publication of 3 peer-review international journal papers (IJ), 5 international conference papers (IC) and 1 Spanish conference paper (SC) which correspond respectively to the references IJ2, IJ3, IJ4, IC2, IC3, IC4, IC5, IC6 and SC2 detailed in Section 5.3.

Thanks to the work developed in Chapter 3, in **Chapter 4** it was possible to perform the synthesis of tapered double-layer FP LWAs, both in one-dimensional and two-dimensional topologies. Here, non-uniform LWAs are designed, where the unit cell dimensions are tapered in order to synthesize any desired aperture distribution which creates a given radiated fields pattern. An efficient **synthesis technique** is firstly proposed, which is specially suited for double-layer Fabry-Perot leaky-wave antennas. The approach is based on the solution of two simple linear equations extracted from an equivalent transverse network. The previous equations must be solved to obtain the dimensions of the PRS and HIS circuits, which produce the desired near field illumination. Due to its efficiency, this approach can be directly applied to the design of tapered Fabry-Perot LWAs, which modulate their printed circuit dimensions to synthesize specific aperture distributions. The theory is quite simple (resembling the design equations of negative resistance oscillators), and requires the computation of the PRS and HIS response under plane-wave incidence (FSS response), avoiding the much more expensive solution of dispersion problems (modal solutions in the complex plane). This synthesis approach has been compared with more standard and costly leaky-mode dispersion methods showing significant reduction in synthesis time, which is very important for complex and electrically-large reconfigurable antennas.

Due to its efficiency, this approach can be directly applied to the design of tapered FP LWAs, which modulate the printed circuit dimensions to synthesize specific aperture distributions. As an example, **two low-sidelobe tapered 1D LWAs** have been designed to point at 20° and 50° at 15GHz. Experimental results confirm the accuracy of the proposed synthesis equations, and the tabulated simulation times demonstrate that it is much less time consuming than other known methods. An example of the sidelobe level reduction is shown in Fig. 5.1.5, when comparing the uniform (blue lines) and tapered (red lines) results. These

experiments confirm that the SLL can be effectively decreased below 20dB by properly modulating the LWA.

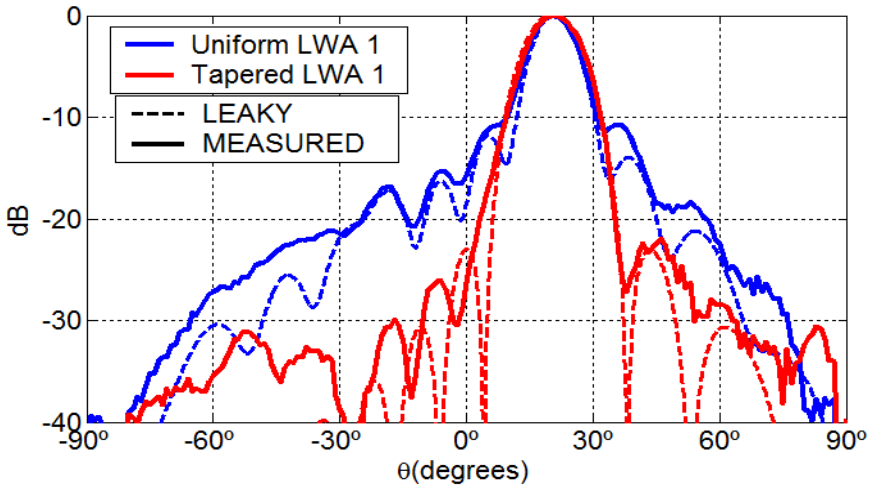

Fig 5.1.5 Measured radiation pattern of 1D FP LWA designs at 15GHz. (a) Designs with constant pointing angle and variable directivity. (b) Designs with fixed directivity and different pointing angles.

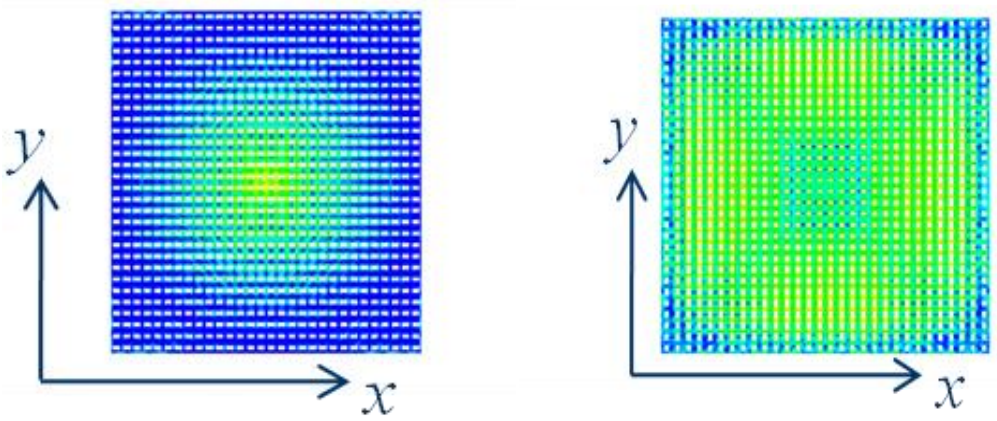

(a) (b)

Fig 5.1.6 Aperture illumination in 2D FP LWAs with 90% radiation efficiency. (a) Uniform desing, 25%aperture efficiency. (b) Quasi-uniform taper, 74% aperture efficiency.

Finally, the main objective of this thesis was tackled in **Chapter 4**; for the first time, it was performed the **optimization of the aperture illumination efficiency in 1D and 2D FP LWAs pointing at broadside**. A quasi-uniform taper is proposed in order to achieve high aperture efficiency, while assuring high radiation efficiency to minimize diffraction and standing waves. Also, the splitting condition must be satisfied in all radiating sections of the LWA to obtain the highest directivity at broadside. In particular, the proposed technique is applied in the case of 1D and 2D LWAs loaded with a slotted-based partially-reflective surface (PRS) and a dipole-based high impedance surface (HIS). It has been illustrated with various numerical examples how the proper modulation of the PRS and HIS surfaces makes possible to increase the directivity of this type of resonant antennas in a totally novel manner. As an illustrative example of a tapered 2D FL LWA, Fig. 5.1.6 shows how the aperture efficiency is increased from 25% to 74% by applying a quasi-uniform taper. The radiation patterns which correspond to this example are shown in Fig. 5.1.7, where it is clear that the quasi-uniform taper has enhanced the directivity in more than 4dBs. It should be highlighted that this work was presented in the 6th European Conference on Antennas and Propagation (EuCAP), in March 2012. This conference paper (reference IC12 in Section 5.3) was given the **Best paper Award on Antenna Theory**.

In addition, **the work developed in Chapter 4 has also given rise to the publication** of 1 peer-review international journal papers (IJ), 2 Spanish journal papers (SJ), 2 international conference papers (IC) and 3 Spanish conference paper (SC), which correspond respectively to the references IJ7, SJ1, SJ2, IC7, IC9, SC3, SC4 and SC7 detailed in Section 5.3.

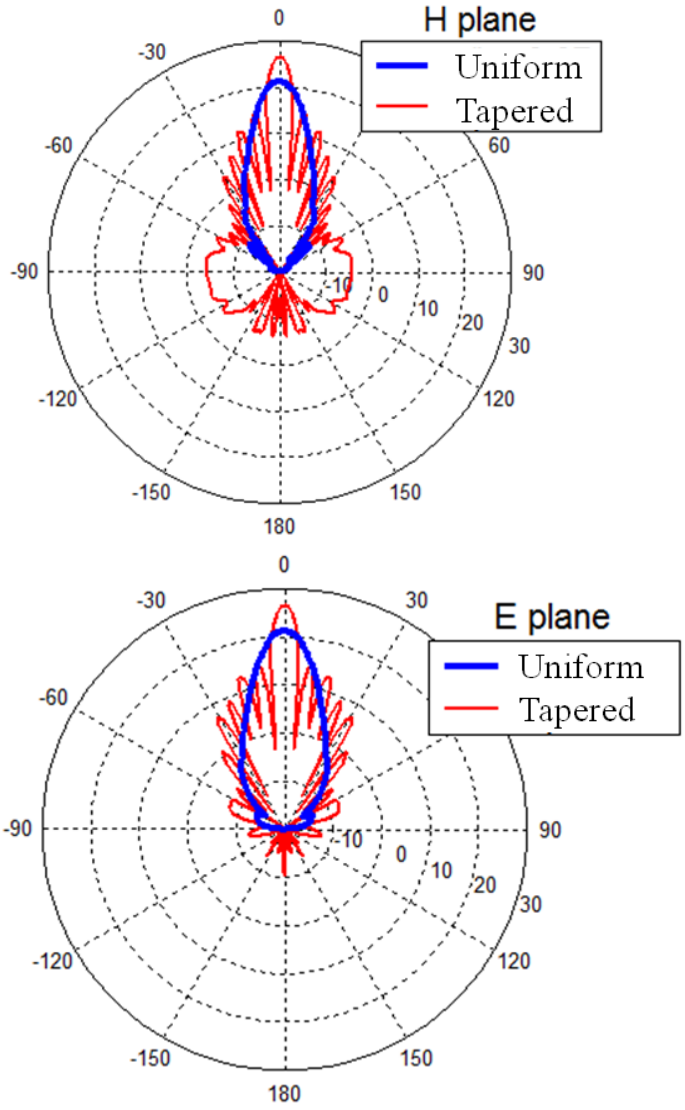

Fig 5.1.7 Radiation patterns in dB of high-gain uniform and tapered 2D FP LWAs.

5.2 Perspectives

The present Ph. D. dissertation has led to original ideas and results that could be further improved and which may generate several future research lines.

One immediate extension of this work is the **development of a electronically reconfigurable version of the 1D FP LWA** proposed in section 3.2. It is worth highlighting that, in the case of the present 1D FP LWA, the radiation pattern is mainly determined by the response of its two periodic layers, namely, the top Partially Reflective Surface (PRS) and the bottom High Impedance Surface (HIS). As these surfaces are very sensitive to the length of their resonant dipoles, varactor diodes could be used to electronically change their effective length and therefore, to enable the electronic control of the radiation pattern. More specifically, varactor diodes are characterized by a capacitance that can be electronically varied by changing their bias voltage. In addition, dipole-based frequency selective surfaces can be characterized by an equivalent L-C network, as it was explained in Section 2.4. Therefore, when varactor diodes are connected to the metallic dipoles, a variable capacitance is added to the FSS equivalent LC network, creating an electronically reconfigurable FSS. The scheme of the reconfigurable 1D FP LWA is depicted in Fig. 5.2.1. As it was explained in Section 3.3, by changing the length of the dipoles in the PRS and the HIS, it is possible to achieve any desired pointing angle and beamwidth. As a result, by properly

changing the bias voltage of the PRS and HIS varactor diodes, it is possible to electronically control the main features of the antenna radiation pattern at a fixed frequency.

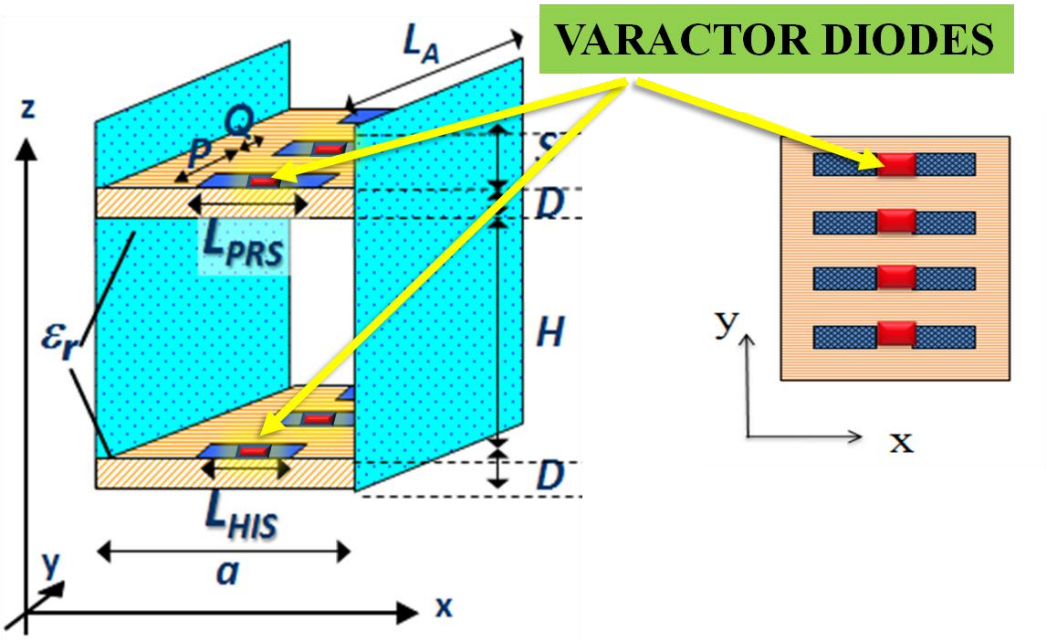

Fig 5.2.1 Electronically reconfigurable double-layer 1D FP LWA employing varactor diodes.

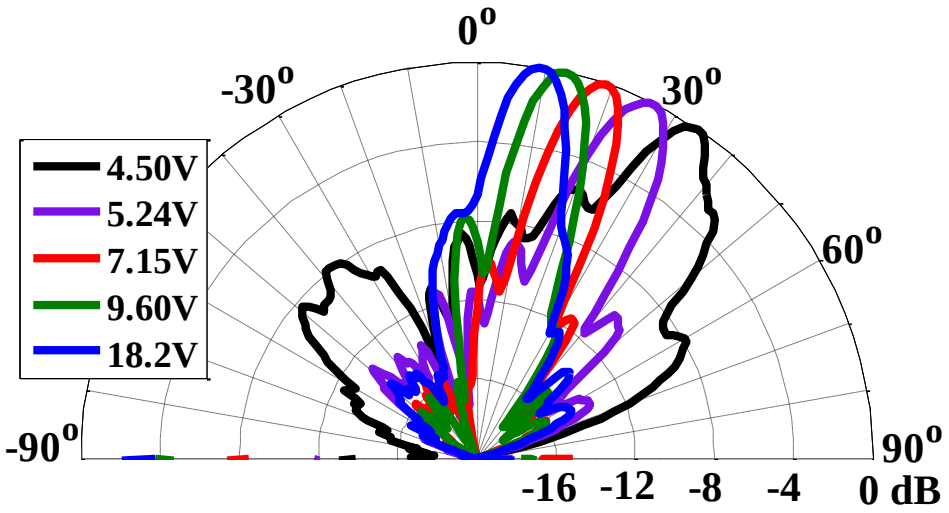

Fig. 5.2.2 Measured radiation patterns of reconfigurable double-layer 1D FP LWA at 5.6GHz as a function of the varactor´s bias voltage (from [Guzmán-Quirós *accepted*]).

The above research line is already being tackled within this research group. In particular, varactor diodes have been added to the HIS in order to vary the antenna pointing angle at a fixed frequency. This work has lead to the journal paper [Guzmán-Quirós *accepted*]. This contribution proves with both theoretic and measured results that it is possible to produce a continuous scanning from 9° to 30° in a prototype operating at the fixed frequency of 5.6GHz, by varying the varactors' bias voltage from $18V_{DC}$ to $5V_{DC}$ (see Fig. 5.2.2).

The work developed in Section 2.4 can be also extended in order to **characterize metallic surfaces perforated by holes and sandwiched by dielectric substrates**. The development of an accurate equivalent circuit for this scenario would enhance the modeling and synthesis techniques of many practical devices. For example, it would be greatly useful for applications at optical frequencies, where this kind of surfaces is commonly used.

The **manufacture and measurement of practical tapered 2D FP LWAs** is another straight forward continuation of this dissertation. For this purpose, a feeding device must be designed, because an ideal source has been considered so far in order to perform the theoretical studies of Section 4.5. As broadside radiation is required from this antenna, it operates very near the cutoff frequency of the Fabry-Perot cavity (as it was explained in Section 4.5). Therefore, it is not a trivial task to design a feeding network which couples energy to a mode which is almost at cutoff. This job will be tackled soon, in order to experimentally prove the optimization of 2D FP LWAs.

Another interesting continuation of this work is the application of the proposed tapering technique to the **beamforming of double-layer 2D FP LWAs**. For example, 2D LWAs could be synthesized which present: **broad-beam patterns** [Burghignoli 2003], [Gómez 2005-II], **radiation diagrams with wide nulls** [Gómez 2010], or **near-field focusing patterns** [Losito 2009], [Gómez 2011-IV]. In addition, the synthesis approach proposed in Section 4.2 could also be efficiently applied to the design of **conformal** 2D FP LWAs [Losito 2007], [Hashemi 2008], [Gómez 2011-III].

5.3 List of publications

This Ph. D. dissertation has introduced novel techniques and equivalent models that have been applied for the analysis, synthesis and design of new Fabry-Perot antennas working in the microwave regime. The publications of several technical and scientific international papers guarantee the quality and interest of the novel ideas proposed. Specifically, the work presented in this thesis has contributed to the publication of 7 peer-review international journal papers (5 of them as a first author), 2 Spanish national journal papers (all of them as a first author), 12 international conferences (7 of them as a first author, and 2 of them invited), and 7 Spanish national conferences (6 as a first author).

This section gives a list of the main relevant published contributions for the scientific community derived from the present work. The acronyms employed to denote and distinguish journals and conferences follows the structure of [NameNumber], where Name is related to the type of publication [J for peer-review international journal, SJ for Spanish national journal, IC for international conferences and SC for Spanish national conferences] and Number is related to the number of a specific paper within the same type of publication. It is worth mentioning that one of these published papers (IC12) presented in the 6th European Conference on Antennas and Propagation (EuCAP) in March 2012, was given the **Best paper Award on Antenna Theory**.

International Refereed Journals:

IJ1. **M. García-Vigueras**, J.L. Gómez-Tornero, G. Goussetis, J.S. Gómez-Diaz, and A. Álvarez-Melcón, "A Modified Pole-Zero Technique for the Synthesis of Waveguide Leaky-Wave Antennas Loaded with Dipole-Based FSS", *IEEE Trans. Antennas Propag.*, vol. 58, no. 6, pp. 1971 – 1979, June 2010.

IJ2. **M. García-Vigueras**, J.L. Gómez-Tornero, G. Goussetis, A. R. Weily, and Y. Jay Guo, "Enhancing frequency-scanning response of leaky-wave antennas using high impedance surfaces," *IEEE Antennas and Wireless Propag. Lett.*, vol. 10, pp. 7–10, March 2011.

IJ3. **M. García-Vigueras**, J. L. Gómez-Tornero, G. Goussetis, A. R. Weily, and Y. J. Guo, "1D Leaky wave antenna employing parallel-plate waveguide loaded with PRS and HIS," *IEEE Trans. Antennas Propag*., vol.59, no.10, pp.3687-3694, Oct. 2011.

IJ4. C. Mateo-Segura, **M. García-Vigueras**, G. Goussetis, A. P. Feresidis, and J.L. Gómez-Tornero, "A simple technique for the dispersion analysis of Fabry-Perot cavity leaky-wave antennas", *IEEE Trans. Antennas Propag.*, vol.60, no.2, pp.803-810, Feb. 2012.

IJ5. R. R. Berral, F. Medina, F. Mesa and **M. Garcia-Vigueras**, "Quasi-analytical Modeling of Transmission/Reflection in Strip/Slit Gratings Loaded with Dielectric Slabs", IEEE Trans. Microw. Theory Tech., vol.60, no.3, pp.405-418, March 2012.

IJ6. **M. Garcia-Vigueras**, F. Mesa, F. Medina, R. R. Berral and J.L. Gómez-Tornero "Simplified Circuit Model for Metallic Arrays of Patches Sandwiched between Dielectric Slabs under Arbitrary Incidence, " IEEE Trans. Antennas Propag., (in press).

IJ7. **M. García-Vigueras**, J. L. Gómez-Tornero, G. Goussetis, A. R. Weily, and Y. J. Guo, "Efficient Synthesis of Scanning Fabry-Perot Antennas with Low Sidelobe Levels," *IEEE Antennas and Wireless Propag. Lett.* (accepted with minor revisions).

Spanish Journals:

SJ1. **M. García Vigueras**, A. Martínez Ros, R. Guzmán Quirós and José Luis Gómez Tornero, "Control de la Directividad en Broadside en Antena Leaky-Wave 1D", *IV Jornadas de introducción a la investigación de la UPCT*, nº4, págs.97-99. May 2011

SJ2. **M. García Vigueras**, R. Guzmán Quirós and José Luis Gómez Tornero, "Antenas Leaky-Wave 1D y 2D iluminadas eficientemente" *V Jornadas de introducción a la investigación de la UPCT*, págs. 90-92, April 2012

International Conference Proceedings:

IC1. **M. García-Vigueras**, J. L. Gómez- Tornero, G. Goussetis and A. Alvarez-Melcon "Software tool for the leaky-mode analysis of waveguides loaded with frequency selective surfaces", *Proceedings of the 3rd European Conference on Antennas and Propagation*, Berlín, Germany, pp. 83-87, March 2009

IC2. **M. García-Vigueras**, C. Mateo-Segura, J.L. Gómez-Tornero, G. Goussetis and A. Feresidis "Analysis and Design of 1D and 2D High-Gain Leaky-Wave Antennas using Metallodielectric FSS and AMC", *Proceedings of the 3rd International Congress on Advanced Electromagnetic Materials in Microwaves and Optics*, London, UK, 30-4 September, 2009. (INVITED)

IC3. J.L. Gómez-Tornero, **M. García-Vigueras**, G. Goussetis, Andrew R. Weily, Y. Jay Guo "Efficient Analysis and Flexible Design of 1D Leaky- Wave Antennas composed by a Parallel-Plate Waveguide loaded with two Metallodielectric FSS", *Proceedings of the International Symposium on Antennas and Propagation*, Bangkok, Thailand, 20-23 October, 2009.

IC4. Mateo-Segura, **M. García-Vigueras**, G. Goussetis, J.L. Gómez-Tornero and A. Feresidis"Analysis of Sub-wavelength Cavity Leaky-Wave Antennas with High-Impedance Surfaces", *Loughborough Antennas & Propagation Conference*, Loughborough, UK, 16-17 November, 2009.

IC5. **M. García-Vigueras**, J.L. Gómez-Tornero, G. Goussetis, David Cañete, Fernando Quesada and A. Álvarez-Melcón, "Leaky-Mode Dispersion Analysis in Parallel-Plate Waveguides Loaded with FSS and AMC with Application to 1D Leaky-Wave Antennas", *IEEE AP-S Int. Symp*, Charleston, SC USA, June 1-5, pp. 1-4, 2009.

IC6. C. Mateo-Segura, **M. García-Vigueras**, G. Goussetis, J.L. Gómez-Tornero and A. Feresidis "Efficient dispersion analysis of 2D High-Gain Leaky-Wave Antennas",European Conference on Antennas & Propagation 2010, Barcelona, Spain, 12-16 April, 2010.

IC7. **M. García-Vigueras**, J.L. Gómez-Tornero, R. Guzmán-Quirós, F.Quesada-Pereira and A. Alvarez-Melcón "Control of the Radiation Properties of a FSS Loaded Leaky-Wave Antenna" ,European Conference on Antennas & Propagation 2010, Barcelona, Spain, 12-16 April, 2010.

IC8. F. Medina, F. Mesa, A.B. Yakovlev, R.R. Berral, and **M. García-Vigueras**, "*Overview on the Use of Circuit Models to Analyze Extraordinary Transmission and Other Related Phenomena*,'' 2010 IEEE AP-S/URSI-USNC International Symposium, (Toronto, Canada), 11-17 July 2010. (INVITED)

IC9. **M. García-Vigueras**, J.L. Gómez-Tornero and R. Guzmán-Quirós "Beamwidth Control of 1D LWA Radiating at Broadside", *Proceedings of the 4th European Conference on Antennas & Propagation*, Rome, Italy, 11-15 April, 2011.

IC10. **M. Garcia-Vigueras**, F. Mesa, F. Medina, R. R. Berral and J.L. Gómez-Tornero "Equivalent Circuits for Conventional and Extraordinary Reflection in Dipole Arrays", *2011 IEEE International Microwave Symposium, IMS 2011*, (Baltimore, Maryland, USA),5-10 June 2011.

IC11. F. Mesa, F. Medina, **M. García-Vigueras**, R. Rodríguez-Berral and J. L. Gómez-Tornero, "Circuit Approach for a General Study of Frequency Selective Surfaces," *2001 International Conference on Electromagnetics in Advanced Applications (ICEAA'11)* (Torino, Italy), pp. 122-125, 12-16 September 2011.

IC12. **M. García-Vigueras**, P. DeLara-Guarch, J.L. Gómez-Tornero and R. Guzmán-Quirós, G. Goussetis, "Efficiently illuminated broadside-directed 1D and 2D tapered Fabry-Perot leaky-wave antennas," *Proceedings of the 6th European Conference on Antennas & Propagation,* (Prague, Czech Republic), pp.247-251, 26-30 March 2012 (ANTENNA THEORY BEST PAPER AWARD)

Spanish Conference Proceedings:

SC1. **M. García-Vigueras**, J.L. Gomez-Tornero, G. Goussetis, D. Cañete-Rebenaque and A. Álvarez-Melcón. "Herramienta para el análisis modal en guías de onda cargadas con superficies selectivas en frecuencia", *XXIII Simposium Nacional de la URSI,* Madrid, 22-24 September 2008.

SC2. **M. García-Vigueras**, R. Guzmán-Quirós, J.L. Gómez-Tornero, J.S. Gómez-Díaz, and A. Álvarez-Melcón, "Estudio de la dispersión de modos Leaky en guías de onda de placas paralelas cargadas con FSS y AMC con aplicación en antenas Leaky-Wave", *XXIV Simpósium Nacional de la URSI*, Santander (Cantabria), 16-18 September 2009.

SC3. **M. García-Vigueras**, J.L. Gómez-Tornero, R. Guzmán-Quirós, J.S. Gómez-Díaz, and A. Álvarez-Melcón, "Control de la Radiación de una Antena Leaky-Wave Cargada con una Superficie Selectiva en Frecuencia", *XXV Simpósium Nacional de la URSI,* Bilbao (Pais Vasco), 15-17 September 2010

SC4. **M. García-Vigueras**, R. Guzmán-Quirós, A. Martinez-Ros, J.S. Gómez-Díaz and J.L. Gómez-Tornero, " Síntesis de la Radiación en Broadside en Antena Leaky-Wave 1D," *XXVI Symposium Nacional de URSI*, Leganés (Madrid), 7-9 September 2011.

SC5. R. Rodríguez-Berral, F. Medina, F. Mesa, **M. García-Vigueras**, "Modelo analítico para rejillas de difracción metálicas cargadas con dieléctricos," *XXVI Symposium Nacional de URSI*, Leganés (Madrid), 7-9 September 2011.

SC6. **M. García-Vigueras**, F. Mesa, F. Medina, R. Rodríguez-Berral, J.L. Gómez-Tornero, "Circuitos equivalentes para el modelado de la reflexión convencional y extraordinaria en arrays de dipolos," *XXVI Symposium Nacional de URSI*, (Leganés, Madrid), 7-9 September 2011.

SC7. **M. García-Vigueras**, J.L. Gómez-Tornero, R. Guzmán-Quirós and A. Martinez-Ros, " Optimización de la Directividad en Antenas Leaky-Wave 1D y 2D basadas en cavidades Fabry-Perot," *XXVII Symposium Nacional de URSI*, Elche (Alicante), 12-14 September 2012.

5.4 Academic contributions

This thesis has given rise to 2 Final Degree Projects (PFC1 and PFC2), and 1 Final Master Project (TFM):

PFC1: "Analysis of Leaky-modes in Waveguides Loaded With Frequency Selective Surfaces (FSS)", by Raúl Guzmán Quirós, July 2009. Universidad Politécnica de Cartagena. Supervisors: María García Vigueras and José Luis Gómez Tornero. Grade A (10).

PFC2: "Dispersion Analysis Of 1D Leaky-wave Antennas With Broadside Radiation", by Pablo de Lara Guarch, July 2011. Universidad Politécnica de Cartagena. Supervisors: María García Vigueras and José Luis Gómez Tornero. Grade A (10).

TFM: "Design And Optimization Of Electronically Reconfigurable 1d Leaky Wave Antennas", by Raúl Guzmán Quirós, September 2010. Universidad Politécnica de Cartagena. Supervisors: María García Vigueras and José Luis Gómez. Grade A (10).

Bibliography

[Akalin 2002] T. Akalin, J. Danglot, O. Vanbésien and D. Lippens, "A highly directive dipole antenna embedded in a Fabry-Pe´rot type cavity," *IEEE Microw. Wireless Compon. Lett.,* vol. 12, no. 2, pp. 48–50, Feb. 2002.

[Alexopoulos 1984] N. Alexopoulos and D.Jackson, "Fundamental superstrate (cover) effects on printed circuit antennas", *IEEE Trans. Antennas Propagat.*, vol.32, no.8, pp. 807- 816, Aug 1984.

[Al-Joumayly 2009] M. Al-Joumayly and N. Behdad, "A new technique for design of low-profile, second-order, bandpass frequency selective surfaces," *IEEE Trans. Antennas Propagat.*, vol. 57, no. 2, pp. 452-459, Feb. 2009.

[Alkhatib 2007] R. Alkhatib and M. Drissi, "Improvement of bandwidth and efficiency for directive superstrate EBG antenna," *Electron. Lett.*, vol. 43, no. 13, pp. 702–703, Jun. 2007.

[Antoniades 2008] M. Antoniades and G.V. Eleftheriades, "A CPS leaky-wave antenna with reduced beam squinting using NRI-TL metamaterials", *IEEE Trans. Antennas Propagat.*, vol.56, no.3, pp.708-721, March 2008.

[Azad 2005] A. K. Azad, W. Zhang, “Resonant terahertz transmission in subwavelength metallic hole arrays of sub-skin-depth thickness,” *Opt. Lett.*, vol. 30, no. 21, pp. 2945-2947, Nov. 2005.

[Bagby 1993] J. S. Bagby, L. Ching-Her, D. P. Nyquist, and Y. Yi, "Identification of propagation regimes on integrated microstrip transmission lines," *IEEE Trans. Microw. Theory Tech.*, vol. 41, no. 11, pp. 1887-1894, 1993.

[Balanis 2005] C. A. Balanis, *Antenna Theory Analysis and Design*, Wiley-Interscience, ISBN 978-047-1667-82-7, Hoboken (NJ), USA, 2005

[Balanis 2008] C. A. Balanis, *Modern Antenna Handbook*, John Wiley & Sons, Inc., 1680, 2008.

[Bayatpur 2008-I] F. Bayatpur, K. Sarabandi, “Single-layer higher-order miniaturized element frequency-selective surfaces,” *IEEE Trans. Microw. Theory Tech.*, vol. 56, no. 4, pp. 774-781, April 2008.

[Bayatpur 2008-II] F. Bayatpur, K. Sarabandi, “Multipole spatial filters using metamaterial based miniaturized-element frequency-selective surfaces,” *IEEE Trans. Microw. Theory Tech*., vol. 56, no. 12, pp. 2742-2747, Dec. 2008.

[Behdad 2009] N. Behdad, M. Al-Joumayly and M. Salehi, “A low-profile third-order bandpass frequency selective surface,” *IEEE Trans. Antennas Propagat.*, vol. 57, no. 2, pp. 460-466, Feb. 2009.

[Beruete 2004] M. Beruete, M. Sorolla, I. Campillo, J. S. Dolado, L. Martín-Moreno, J. Bravo-Abad, and F. J. García-Vidal, “Enhanced millimeter-wave transmission through subwavelength hole arrays,” *Opt. Lett.*, vol. 29, no. 21, pp. 2500–2502, Nov. 2004.

[Beruete 2005] M. Beruete, M. Sorolla, I. Campillo, J. S. Dolado, L. Martín-Moreno, J. Bravo-Abad, and F. J. García-Vidal, “Enhanced millimeter wave transmission through quasioptical subwavelength perforated

plates," *IEEE Trans. Antennas Propagat.*, vol. 53, no. 6, pp. 1897-1903, June 2005.

[Beruete 2007] M. Beruete, M. Sorolla, M. Navarro-Cía, F. Falcone, I. Campillo, V. Lomakin, "Extraordinary transmission and left-handed propagation in miniaturized stacks of doubly periodic subwavelength hole arrays," *Opt. Express*, vol. 15, no. 3, pp. 1107-1114, Jan. 2007.

[Beruete 2007-II] M. Beruete, I. Campillo, M. Navarro-C´ıa, F. Falcone, and M. Sorolla, "Molding left- or right-handed metamaterials by stacked cutoff metallic hole arrays," *IEEE Trans. Antennas Propagat.*, vol. 55, no. 6, pp. 1514-1521, June 2007.

[Beruete 2011] M. Beruete, M. Navarro-Cía, S. A. Kuznetsov, and M. Sorolla, "Circuit approach to the minimal configuration of terahertz anomalous extraordinary transmission," Appl. Phys. Lett. vol.98, pp. 014106(1–3), 2011.

[Besso 2003] P. Besso, M. Bozzi, L. Perregrini, L.S. Drioli, W. Nickerson, "Deep-space antenna for Rosetta mission: design and testing of the S/X band dichroic mirror," *IEEE Trans. Antennas Propagat.*,, vol.51, no.3, pp. 388- 394, March 2003.

[Bhattacharyya 2006] A. K. Bhattacharyya, *Phased Array Antennas Floquet Analysis, Synthesis, BFNs, and Active Array Systems*, Hoboken, NJ: Wiley, 2006.

[Biswas 2001] R. Biswas, E. Ozbay, B. Temelkuran, M. Bayindir, M. M. Sigalas, and K.-M. Ho, "Exceptionally directional sources with photonic bandgap crystals," *J. Opt. Soc. Am. B,* vol. 18, no. 11, pp. 1684–1689, Nov. 2001.

[Bliokh 2008] K. Y. Bliokh, Y. P. Bliokh, V. Freilikher, S. Savel'ev, and F. Nori, "Colloquium: Unusual resonators: Plasmonics, metamaterials, and random media," *Rev. Mod. Phys.*, vol. 80, pp. 1201-1213, Oct.-Dec. 2008.

[Born 1999] M. Born and E. Wolf, *Principles of Optics: Electromagnetic Theory of Propagation, Interference and Diffraction of Light*, Cambridge, Cambridge University Press, 1999.

[Boutayeb 2006] H. Boutayeb, K. Mahdjoubi, A.-C. Tarot, and T. A. Denidni, "Directivity of an antenna embedded inside a Fabry-Pérot cavity: Analysis and design," *Microw. Opt. Technol. Lett.,* vol. 48, pp. 12–17, Jan. 2006.

[Burghignoli 2003] P. Burghignoli, F. Frezza, A. Galli, and G. Schettini, "Synthesis of broadbeam patterns through leaky-wave antennas with rectilinear geometry," *IEEE Antennas Wireless Propag. Lett.,* vol. 2, pp. 136–139, 2003.

[Burghignoli 2006] P. Burghignoli, G. Lovat, and D. R. Jackson, "Analysis and optimization of leaky-wave radiation at broadside from a class of 1-D periodic structures," *IEEE Trans. Antennas Propag.*, vol. 54, no. 9, pp. 2593–2603, Sep. 2006.

[Burghignoli 2008] P. Burghignoli, G. Lovat, F. Capolino, D. R. Jackson, and D. R. Wilton, "Directive leaky-wave radiation from a dipole source in a wire-medium slab," IEEE Trans. Antennas Propag., vol. 56, no. 5, pp. 1329–1339, May 2008.

[Burghignoli 2010] P. Burghignoli, G. Lovat, F. Capolino, D.R. Jackson and D.R. Wilton, "Highly Polarized, Directive Radiation From a Fabry-Pérot Cavity Leaky-Wave Antenna Based on a Metal Strip Grating," *IEEE Trans. Antennas Propag.,*vol.58, no.12, pp.3873-3883, Dec. 2010.

[Burrell 1976] G.A. Burrell and B.A. Munk, "The array scanning method and applying it to determine the impedance of linear antennas in a lossy half-space," Ohio State Univ. ElectroScience Lab., Columbus, OH, Rep. 4460-1, Oct. 1976 (prepared under Contract DAAG53-76-0179 for U.S. Army Mobility Equipment Research and Development Command).

[Burstein 1974] E. Burstein, W. P. Chen, Y. J. Chen and A. Harstein, “Surface polaritons - propagating electromagnetic modes at interfaces”. *J.Vac.Sci.Technol*., vol. 11, pp. 1004-1019; June 1974.

[Caiazzo 2004] M. Caiazzo, S. Maci, N. Engheta, “A metamaterial Surface for Compact Cavity Resonators,” *IEEE Antennas Wireless Propag. Lett,* Vol. 3, pp. 261-264, 2004.

[Caloz 2005] C. Caloz and T. Itoh, *Electromagnetic Metamaterials: Transmission Line Theory and Microwave Applications.* Wiley and IEEE Press. (2005).

[Caloz 2011] C. Caloz, D. R. Jackson, and T. Itoh, “Leaky-wave antennas (chap. 9),” in Frontiers in Antennas: Next Generation Design and Engineering, F. B. Gross, Ed. McGraw Hill, 2011.

[Cano 1995] G. Cano, F. Mesa, F. Medina, and M. Horno, “Systematic computation of the modal spectrum of boxed microstrip, finline, and coplanar waveguides via an efficient SDA*,” IEEE Trans. Microwave Theory Tech.,* vol. 43, no. 4, pp. 866–872, Apr. 1995.

[Capolino 2010] F. Capolino, A. Vallecchi and M. Albani, "Transmission line model with X-circuit for a metamaterial layer made of pairs of dogbone-shaped planar conductors," *URSI International Symposium on Electromagnetic Theory (EMTS),* pp.643-645, 16-19 Aug. 2010

[Carbonell 2010] J. Carbonell, C. Croenne, F. Garet, E. Lheurette, J. L. Coutaz, D. Lippens, “Lumped elements circuit of terahertz fishnet-like arrays with composite dispersion,” *J. of Appl. Phys*., vol. 108, no. 14, pp. 014907,2010.

[Casares-Miranda 2006] F.P. Casares-Miranda, C. Camacho-Penalosa, C. Caloz, "High-gain active composite right/left-handed leaky-wave antenna," *IEEE Trans. Antennas Propag.*, vol. 54, no. 8, pp.2292-2300, Aug. 2006.

[Chang-Won 2003] L. Chang-Won and K. Joong-Pyo, "Radiation characteristics of corrugation loaded dielectric-coated conducting cylinder," *IEEE Trans. Antennas Propag.*, vol. 51, no. 6, pp. 1321- 1330, June 2003.

[Chen 1971] C.C. Chen, "Diffraction of electromagnetic waves by a conducting screen perforated periodically with circular holes," *IEEE Trans. Microw. Theory Tech.*, vol. 19, no. 5, pp. 475–481, May 1971.

[Chen 1973] C.C. Chen, "Transmission of microwave through perforated flat plates of finite thickness," *IEEE Trans. Microw. Theory Tech*., vol. 21, no. 1, pp. 1–6, Jan. 1973.

[Chen 1998] T. L. Chen and Y. D. Lin, "Aperture-coupled microstrip line leaky wave antenna with broadside mainbeam," *Electron. Lett.*, vol. 34, pp.1366–1367, July 1998.

[Cheng 2011] Y. J. Cheng, W. Hong, K. Wu, and Y. Fan, "Millimeter-wave substrate integrated waveguide long slot leaky-wave antennas and 2-D multibeam applications," *IEEE Trans. Antennas Propag*., vol. 59, no. 1, pp. 40–47, Jan. 2011.

[Cheype 2002] C. Cheype, C. Sérier, M. Thèvenot, T. Monédière, A. Reinex, and B. Jecko, "An electromagnetic bandgap resonator antenna," IEEE Trans. Antennas Propag., vol. 50, no. 9, pp. 1285–1290, Sep. 2002.

[Chien-Jen 1999] W. Chien-Jen, C. F. Jou, and W. Jin-Jei, "A novel two-beam scanning active leaky-wave antenna," *IEEE Trans. Antennas Propag.*, vol. 47, no. 8, pp. 1314-1317, 1999

[Collin 2000] R. E. Collin, Foundations for Microwave Engineering, 2nd ed. New York: Wiley-IEEE press, 2000.

[Cunningham 1983] C. T. Cunningham, "Resonant grids and their use in the construction of submillimeter filters," *Infrared Phys*., vol. 23, no. 4, pp. 207-215, 1983.

[Di Nallo 1995] C. Di Nallo, F. Frezza, A. Galli, and P. Lampariello, "Complete characterisation of leaky-wave antennas based on stepped rectangular waveguides," in *Proc. 25th Eur. Microwave Conf.*, Bologna, Italy, Sep. 1995, pp. 1062–1067.

[Di Nallo 1997-I] C. Di Nallo, F. Frezza, A. Galli, G. Gerosa, and P. Lampariello, "Stepped leaky-wave antennas for microwave and millimeter-wave applications," *Ann. Télécommun*, vol. 52, pp. 202–208, March 1997.

[Di Nallo 1997-II] C. Di Nallo, F. Frezza, A. Galli, and P. Lampariello, "Theoretical and experimental investigations on the 'stepped' leaky-wave antennas," in *Dig. IEEE Antennas and Propag. Int. Symp*., Canada, pp. 1446–1449, 13–18 Jul. 1997.

[Doumanis 2011] E. Doumanis, G. Goussetis, J. L. Gómez-Tornero, R. Cahill and V. Fusco, "Mm-wave Low-Profile Reflection Polarizer", *IEEE MTT-S International Microwave Workshop Series on Millimeter Wave Integration Technologies*, 15-16 September 2011, Barcelona, Spain

[Doumanis 2012] E. Doumanis, G. Goussetis, J. Gomez-Tornero, R. Cahill, V. Fusco, "Anisotropic Impedance Surfaces for Linear to Circular Polarization Conversion," *IEEE Trans. Antennas Propag.,* vol.60, no.1, pp.212-219, Jan. 2012

[Ebbesen 1998] T. W. Ebbesen, H. J. Lezec, H. F. Ghaemi, T. Thio, and P. A. Wolff, "Extraordinary optical transmission through sub-wavelength hole arrays," *Nature*, vol. 391, pp. 667–669, Feb. 1998.

[Eleftheriades 2005] G.V. Eleftheriades and K.G. Balmain, *Negative-Refraction Metamaterials: Fundamental Principles and Applications*. Wiley & IEEE Press, Hoboken, NJ. editors (2005).

[Encinar 1988] J.A. Encinar, M. Guglielmi and A.A. Oliner, "Taper Optimization for sidelobe control in millimeter-wave metal-strip-loaded dielectric antennas," *in Proc. URSI Radio Sri. Meet.*, pp. 379, 1988.

[Engheta 2006] N. Engheta, R. W. Ziolkowski, Electromagnetic Metamaterials: Physics and Engineering Explorations. Wiley-IEEE Press 2006.

[Ermert 1979] H. Ermert, "Guiding and radiation characteristics of planar waveguides," *IEE Journal on Microwaves, Optics and Acoustics,* vol. 3, no. 2, pp. 59 –62, Mar. 1979.

[Fano 1941] U. Fano, "The Theory of Anomalous Diffraction Gratings and of Quasi-Stationary Waves on Metallic Surfaces (Sommerfeld's Waves)," *J. Opt. Soc. Am.* vol. 31, pp. 213-222, March 1941

[Fano 1961] U. Fano, "Effects of configuration interaction on intensities and phase shifts," Phys. Rev. Lett., vol. 124, pp.1866.1878, 1961.

[Fehrembach 2001] A.-L. Fehrembach, S. Enoch, and A. Sentenac, "Highly directive light sources using two-dimensional photonic crystal slabs," *Appl. Phys. Lett.*, vol. 79, no. 26, pp. 4280–4282, Dec. 2001.

[Feresidis 2001] A. P. Feresidis and J. C. Vardaxoglou, "High gain planar antenna using optimized partially reflective surfaces," *Proc. Inst. Elect. Eng. Microw., Antennas Propag.*, pt. H, vol. 148, no. 6, pp. 345–350, 2001.

[Feresidis 2005] A. P. Feresidis, G. Goussetis, S. Wang and J. C. Vardaxoglou, "Artificial magnetic conductor surfaces and their application to low-profile high-gain planar antennas", *IEEE Trans. Antennas Propag.*, vol.53, no.1, pp.209-215, Jan. 2005.

[Florencio 2011] R. Florencio, R.R. Boix, J.A. Encinar, "Pole-zero matching technique for multilayered periodic structures with application to the design of reflectarray antennas," *IEEE AP-S Int. Symp*, pp.964-967, 3-8 July 2011

[Fong 2010] B.H. Fong, J.S. Colburn, J.J. Ottusch, J.L Visher, D.F. Sievenpiper,. "Scalar and tensor holographic artificial impedance surfaces" *IEEE Trans on Antennas Propagat,* vol. 58 n. 10, pp. 3212 – 3221, Oct. 2010.

[Frezza 1994] F. Frezza, M. Guglielmi, and P. Lampariello, “Millimeter-wave leakywave antennas based on slitted asymmetric ridge waveguides,” *Proc. Inst. Elect. Eng.: Microwaves, Antennas and Propagation*, vol. 141, pt. H, pp. 175–180, Jun. 1994.

[García de Abajo 2007] F. J. García de Abajo, “Colloquium: Light scattering by particle and hole arrays,” *Rev. Mod. Phys*., vol. 79, pp. 1267–1290, Oct.-Dec. 2007.

[García-Vidal 2010] F. J. García-Vidal, L. Martín-Moreno, T. W. Ebbesen, and L. Kuipers, “Light passing through subwavelength apertures,” *Rev. Mod. Phys.*, vol. 82, pp. 729-787, Jan.-March 2010.

[Gardelli 2006] R. Gardelli, M. Albani, and F. Capolino, “Array thinning by using antennas in a Fabry-Perot cavity for gain enhancement,” *IEEE Trans. Antennas Propag.,* vol. 54, no. 7, pp. 1979–1990, Jul. 2006.

[Genet 2007] C. Genet and T. W. Ebbesen, “Light in tiny holes,” Nature, vol. 445, pp. 39–46, Jan. 2007.

[Ghomi 1993] M. Ghomi, B. Lejay, J.L. Amalric and H. Baudrand, "Radiation characteristics of uniform and nonuniform dielectric leaky-wave antennas," *IEEE Trans. Antennas Propag.*, vol. 41, no. 9, pp.1177-1186, Sep 1993.

[Gómez 2004-I] J.L. Gómez-Tornero and A.A. Melcón, “Radiation analysis in the space domain of laterally-shielded planar transmission lines. Part I: Theory,” *Radio Sci.,* vol. 39, pp. 1–11, Jun. 2004.

[Gómez 2004-II] J.L. Gómez-Tornero and A.A. Melcón, “Radiation analysis in the space domain of laterally-shielded planar transmission lines. Part II: Applications,” *Radio Sci.,* vol. 39, pp. 1–11, Jun. 2004.

[Gómez 2004-III] J.L. Gómez and A.A. Melcón, "Non-orthogonality relations between complex-hybrid-modes: an application for the leaky-wave analysis of laterally-shielded top-open planar transmission lines",

IEEE Trans. Microwave Theory Tech., vol. 52, no.3, pp. 760-767, March 2004.

[Gómez 2005-I] J.L. Gómez, F.D. Quesada and A.A. Melcón, "Analysis and Design of Periodic Leaky-Wave Antennas for the Millimeter Waveband in Hybrid Waveguide-Planar Technology", *IEEE Trans. Antennas Propagat.*, Vol.53, No.9, pp. 2834-2842, September 2005.

[Gómez 2005-II] *Analisis de modos de fuga en estructuras planares apantalladas lateralmente y diseno de nuevas antenas "leaky-wave" en tecnologia hibrida impresa-apantallada* [Dr. dissertation]. Spain: Universidad Politecnica de Cartagena (Spain); 2005 In: Dissertations & Theses @ Universidad Politecnica de Cartagena [database on the Internet]. Available from: http://www.proquest.com/; Publication Number: AAT 3388885, ISBN: 978-11-0955-477-9; Source: Dissertation Abstracts International, Volume: 71-01, Section: B, page: 0534.; 466 páginas, Mayo 2005.

[Gómez 2005-III] J.L. Gómez , A. de la Torre, D. Cañete, M. Gugliemi and A. A. Melcón, "Design of tapered leaky-wave antennas in hybrid waveguide-planar technology for millimeter waveband applications", *IEEE Trans. Antennas Propag,* vol. 53, no. 8, pp. 2563-2577, Aug. 2005.

[Gómez 2005-IV] J.L. Gómez, D. Cañete and A. Álvarez-Melcón, "Printed-circuit leaky-wave antenna with pointing and illumination flexibility", *IEEE Microwave and Wireless Components Lett.*, vol. 15, no. 8, pp.536-538, August 2005.

[Gómez 2006-I] J. L. Gómez, J. Pascual and A. Álvarez-Melcón, "Efficient Full-Wave Analysis Method of Leaky-Wave Modes in Periodically Loaded Dielectric Waveguides with Application to Backward-to-Forward Frequency-Scannable Antennas and Metamaterials", *Int. Journal of Numerical Modelling: Special Issue on Numerical Modelling of*

Metamaterial Properties, Structures and Devices., Vol.19, No.2, pp.173-193, March 2006.

[Gómez 2006-II] J.L. Gómez, D. Cañete, F. Quesada, J. Pascual and A.A. Melcón, "P.A.M.E.L.A: A Useful Tool for the Study of Leaky-Wave Modes in Strip-Loaded Open Dielectric Waveguides", *IEEE Antennas and Propagat. Magazine*, Vol.48, No.4, pp.54-72, August 2006.

[Gómez 2006-III] J.L. Gómez, G.Goussetis, A.Feresidis, and A.A.Melcón, "Control of Leaky-Mode Propagation and Radiation Properties in Hybrid Dielectric-Waveguide Printed-Circuit Technology: Experimental Results", *IEEE Trans. Antennas Propagat.*, Vol.54, No.11, pp.1-9, November 2006

[Gómez 2006-IVJ. L. Gomez-Tornero, S. Martinez-Lopez, and A. Alvarez-Melcon, "Simple Analysis and Design of a New Leaky-Wave Directional Coupler in Hybrid Dielectric-Waveguide Printed-Circuit Technology," *IEEE Trans. Microwave Theory Tech.*, vol. 54, no. 9, pp. 3534-3542, Aug. 2006

[Gómez 2007] J. L. Gómez, G. Goussetis, and A. A. Melcón, "Correction of dielectric losses in leaky-wave antenna designs," J. Electrom. Waves Appl., vol. 21, no. 8, pp. 1025–1036, 2007.

[Gómez 2008] J.L. Gomez-Tornero, F.D. Quesada-Pereira and A. Alvarez-Melcon, "Novel Microwave Network for the Leaky-Wave Analysis of Evanescent Fields in Stub-Loaded Structures *IEEE Trans. Microwave Theory Tech.*, vol.56, no.6, pp.1405-1412, June 2008.

[Gómez 2010] J.L. Gomez-Tornero, A.J. Martinez-Ros and R. Verdu-Monedero, "FFT synthesis of radiation patterns with wide nulls using tapered leaky-wave antennas," *IEEE Antennas and Wireless Propag. Lett.*, vol. 9, pp.518-521, 2010.

[Gómez 2011-I] J.L. Gómez-Tornero, “Unusual tapering of leaky-wave radiators and their applications”, in *Proc. V European Conference Antennas Propag*, pp. 821–824, April 2011.

[Gómez 2011-II] J.L.Gómez Tornero, A.R. Weily, and Y. Jay Guo, “Rectilinear leaky-wave antennas with broad beam patterns using hybrid printed-circuit waveguide designs,” *IEEE Trans. Antennas Propag*, vol. 59, no. 11, pp. 3999 - 4007, Nov.2011.

[Gómez 2011-III] J.L. Gómez-Tornero, “Analysis and design of conformal tapered leaky-wave antennas,” *IEEE Antennas and Wireless Propag. Lett*, vol. 10, pp. 1068 - 1071, 2011.

[Gómez 2011-IV] J.L. Gómez-Tornero, F.D. Quesada, A.A. Melcón, G. Goussetis, A.R. Weily, and Y. Jay Guo, "Frequency steerable two dimensional focusing using rectilinear leaky-wave lenses," *IEEE Trans. Antennas Propagat*, vol. 59, no. 2, pp. 407–415, Feb. 2011.

[Gómez 2012] J.L. Gomez-Tornero, A. J. Martinez-Ros, N. Llombart, B. Darwin and E. Rajo-Iglesias, "Near-field focusing with holographic two-dimensional tapered leaky-wave slot antennas," *European Conference on Antennas & Propagation 2012, Prague, Czech Republic,* pp.234-238, 26-30 March 2012.

[Gordon 2007] R. Gordon, “Bethe’s aperture theory for arrays,” *Phys. Rev. A*, vol. 76(5), 053806, 2007.

[Gordon 2010] R. Gordon, A. G. Brolo, D. Sinton and K. L. Kavanagh, “Resonant optical transmission through hole-arrays in metal films: physics and applications,” *Laser & Photon. Rev*., vol. 4, no. 2, pp. 311–335, 2010.

[Goussetis 2006-I] G. Goussetis, A.P. Feresidis, J.C. Vardaxoglou, “Tailoring the AMC and EBG Characteristics of Periodic Metallic Arrays Printed on Grounded on Grounded Dielectric Substrate,” *IEEE Transactions Antennas and Propagation*, Vol. 54, No. 1, Jan. 2006, pp. 82-89.

[Goussetis 2006-II] G. Goussetis, A.P. Feresidis and P. Kosmas, "Efficient Analysis, Design and Filter Applications of EBG Waveguide with Periodic Resonant Loads," *IEEE Trans. Microw. Theory Tech*., Vol. 54, No. 11, pp. 3885-3892, November 2006.

[Goussetis 2007-I] G. Goussetis, N. Uzunoglou, J.-L. Gomez-Tornero, B. Gimeno, V.E. Boria, "An E-plane EBG Waveguide for Dispersion Compensated Transmission of Short Pulses", *IEEE Antenna and Propagation Symp. Dig.,* Honolulu, 9-15 June 2007.

[Goussetis 2007-II] G. Goussetis, A.P. Feresidis and R. Cheung, "Quality factor Assessment of Subwavelength Cavities at FIR Frequencies," *Journal of Optics A*, Vol. 9, pp. s355-s360, August 2007.

[Goussetis 2010] G. Goussetis, J.L Gómez-Tornero, A.P. Feresidis, and N. Uzunoglu, "Artificial impedance surfaces for reduced dispersion in antenna feeding systems", *IEEE Trans. Antennas Propag.*, vol.58, no. 11, pp. 3629–3636, Nov. 2010.

[Grbic 2002] A. Grbic and G.V. Eleftheriades, "Leaky CPW-based slot antenna arrays for millimeter-wave applications", *IEEE Trans. Antennas Propagat*., vol.50, no.11, pp. 1494- 1504, Nov 2002.

[Grimaldi 1665] F. M. Grimaldi. *Physico-mathesis de lumine, coloribus, et iride, aliisque adnexis libri duo*. Bologna. pp. 383. 1665

[Guerin 2006] N. Guerin, S. Enoch, G. Tayeb, P. Sabouroux, P. Vincent and H. Legay, "A metallic Fabry-Perot directive antenna," *IEEE Trans. Antennas Propagat*, vol.54, no.1, pp. 220- 224, Jan. 2006.

[Guglielmi 1989-I] M. Guglielmi and A. A. Oliner, "Multimode network description of a planar periodic metal-strip grating at a dielectric interface - Part I: Rigorous network formulations," *IEEE Trans. Microw. Theory Tech*., vol. 37, no. 3, pp. 535–541, March 1989.

[Guglielmi 1989-II]M. Guglielmi and A. A. Oliner, "Multimode network description of a planar periodic metal-strip grating at a dielectric interface – Part II: Small-aperture and small-obstacle solutions," *IEEE Trans. Microw Theory Tech*., vol. 37, no. 3, pp. 542–552, March 1989.

[Guglielmi 1991] M. Guglielmi and G. Boccalone, "A novel theory for dielectric-inset waveguide leaky-wave antennas," *IEEE Trans. Antennas Propag.*, vol.39, no. 4, pp. 497–504, Apr. 1991.

[Guglielmi 1993] M. Guglielmi and D. R. Jackson, "Broadside radiation from periodic leaky-wave antennas," *IEEE Trans. Antennas Propag.*, vol. 41, pp.31–37, Jan. 1993.

[Gupta 2009] S. Gupta, S. Abielmona and C. Caloz, "Microwave analog real-time spectrum analyzer (RTSA) based on the spectral–spatial decomposition property of leaky-wave structures," *IEEE Trans. Microw. Theory Tech.*, vol. 57, pp. 2989–2999, Dec. 2009.

[Guzmán-Quirós *accepted*] R. Guzmán-Quirós, J. L. Gómez-Tornero, A. R. Weily and Y. J. Guo, "Electronically Steerable 1D Fabry-Perot Leaky-Wave Antenna Employing a Tunable High Impedance Surface ", *IEEE Trans. Antennas Propagat*., *in press.*

[Hansen 1940] W. W. Hansen, "Radiating electromagnetic waveguide," Patent, 1940,U.S. Patent No. 2.402.622.

[Hansen 1998] R.C. Hansen, *Phased Array Antennas*, John Wiley & Sons, New York, 1998.

[Hashemi 2008] From M. R. Hashemi, and T. Itoh, "Dispersion Engineered Metamaterial-Based Transmission Line for Conformal Surface Application," *IEEE MTT-S Int. Microwave Symp*. Jun. 2008

[Hessel 1965] A. Hessel and A. A. Oliner, "A new theory of Wood's anomalies on optical gratings".*Appl.Opt.*, vol. 4, no. 10, pp. 1275-1297, Oct. 1965.

[Hessel 1969] A. Hessel, *Antenna Theory, Part II*, R. E. Collin and R. F. Zucker, Eds. New York: McGraw-Hill, 1969, chap. 19.

[HFSS 2011] *High Frequency Structure Simulator*, v11, Ansoft Corporation.

[Hines 1957] J. N. Hines and J. R. Upson, "A Wide Aperture Tapered-Depth Scanning Antenna," *Ohio State Univ. Res. Found.,* Report 667-7, Columbus, Ohio, December 1957.

[Holloway 2009] C.L. Holloway, A. Dienstfrey, E.F. Kuester, J.F. O'Hara, A.K. Azad and A.J. Taylor, "A discussion on the interpretation and characterization of metafilm/metasurfaces: The two dimensional equivalent of metamaterials", Metamaterials 3, 2009, pp.100-112

[Honey 1959] Honey, "A flush-mounted leaky-wave antenna with predictable patterns," *IRE Trans. Antennas Propag.*, vol.7, no.4, pp.320-329, Oct. 1959.

[Hong 2003] W. Hong, T.-L. Chen, C.-Y. Chang, J.-W. Sheen, and Y. D. Lin, "Broadband tapered microstrip leaky-wave antenna," *IEEE Trans. Antennas Propag*., vol. 51, no. 8, pp. 1922–1928, Aug. 2003.

[Hu 2008] W. Hu; R. Cahill, J.A. Encinar, R. Dickie, H. Gamble, V. Fusco and N. Grant, "Design and Measurement of Reconfigurable Millimeter Wave Reflectarray Cells With Nematic Liquid Crystal," IEEE Trans. Antennas and Propagat., vol.56, no.10, pp.3112-3117, Oct. 2008

[Huan 2008] J. Huang and J. A. Encinar, *Reflectarray Antennas*, Institute of Electrical and Electronics Engineers, John Wiley & Sons, 2008.

[Huang 2007] J. Huang, J.A. Encinar, "Reflectarray Antennas", Wiley-IEEE Press, ISBN: 978-0-470-08491-5, November 2007.

[Hum 2007] S. V. Hum, M. Okoniewski, and R. J. Davies, "Modeling and Design of Electronically Tunable Reflectarrays," *IEEE Trans. Antennas Propag.*, vol. 55, pp. 2200-2210, Aug. 2007.

[Ip 1990] A. Ip, and D.R. Jackson, "Radiation from cylindrical leaky waves," *IEEE Trans. Antennas Propagat*, vol.38, no.4, pp.482-488, Apr 1990.

[Irwin 1993] P. G. J. Irwin, P. A. R. Ade, S. B. Calcutt, F. W. Taylor, J. S. Seeley, R. Hunneman, and L. Walton, "Investigation of dielectric spaced resonant mesh filter designs for PMIRR," *Infrared Phys*. vol. 34, no. 6, pp. 549-563, 1993.

[Jackson 1985] D. Jackson, and N. Alexopoulos,"Gain enhancement methods for printed circuit antennas," *IEEE Trans. Antennas Propag.*, vol.33, no.9, pp. 976- 987, Sep 1985.

[Jackson 1988] D. R. Jackson and A. A. Oliner, "A leaky-wave analysis of the high gain printed antenna configuration," *IEEE Trans. Antennas Propag.*, vol. 36, no. 7, pp. 905–910, Jul. 1988.

[Jackson 1993] D. R. Jackson, A. A. Oliner and A. Ip, "Leaky-wave propagation and radiation for a narrow-beam multiple-layer dielectric structure *IEEE Trans. Antennas Propag.*, vol.41, no.3, pp.344-348, Mar 1993.

[Jackson 2008] D. R. Jackson and A. A. Oliner, *Modern Antenna Handbook*, C. A. Balanis, Ed. Wiley-Interscience, 2008.

[Jackson 2011] D. R. Jackson, P. Burghignoli, G. Lovat, F. Capolino, J. Chen, D. R. Wilton, and A. A. Oliner, "The Fundamental Physics of Directive Beaming at Microwave and Optical Frequencies and the Role of LeakyWaves," *Proceedings of the IEEE, Vol. 99, No. 10, pp.1780-1805, 2011.*

[James 1989] J.R. James, S.J. Kinany, P.D. Peel, G. Andrasic, "Leaky-wave multiple dichroic beamformers," *Electronics Letters* , vol.25, no.18, pp.1209-1211, 31 Aug. 1989.

[Jin-Wei 2010] W. Jin-Wei, C. F. Jou, W. Chien-Jen, "A compact wideband leaky-wave antenna with etched slot elements and tapered structure,"

IEEE Trans. Antennas Propag, vol. 58, no. 7, pp.2176-2183, July 2010.

[Johnson 1993] R.C. Johnson (ed.) *Antenna Engineering Handbook*, third edition, McGraw-Hill, New York, 1993.

[Katehi 1983] P. Katehi and N. Alexopoulos, "On the effect of substrate thickness and permittivity on printed circuit dipole properties," *IEEE Trans. Antennas Propagat.,* vol. 31, no. 1, pp. 34–39, Jan. 1983.

[Kelly 2008] J.R. Kelly, T. Kokkinos and A.P. Feresidis,, "Analysis and Design of Sub-Wavelength Resonant Cavity Type 2-D Leaky-Wave Antennas *IEEE Trans. Antennas Propagat*., vol.56, no.9, pp.2817-2825, Sept. 2008

[Kiani 2011] G.I. Kiani, L.G. Olsson, A. Karlsson, K.P. Esselle, and M. Nilsson, "Cross-Dipole Bandpass Frequency Selective Surface for Energy-Saving Glass Used in Buildings," *IEEE Trans. Antennas Propag.*, vol.59, no.2, pp.520-525, Feb. 2011

[Kildal 2005] P.-S. Kildal, A.A. Kishk and S. Maci, "Special Issue on Artificial Magnetic Conductors, Soft/Hard Surfaces, and Other Complex Surfaces", *IEEE Trans. Antennas Propagat*., vol.53, no.1, pp. 2- 7, Jan. 2005

[Kodera 2010] T. Kodera and C. Caloz, "Leakage control in the CRLH uniform ferrite-loaded open waveguide leaky-wave antenna using a transversally extending evanescent waveguide structure," *Proc*. *Microwave Asia-Pacific Conf.*, pp.869-872, 7-10 Dec. 2010.

[Komanduri 2010] V.R. Komanduri, D.R. Jackson, and S.A. Long, "Radiation characteristics of finite-length 1D-uniform leaky wave antennas radiating at broadside," *2010 IEEE Int. Symp. on Antennas and Propagat.*, pp.1-4, 2010

[Kosmas 2007] P. Kosmas, A. P. Feresidis and G. Goussetis, "Periodic FDTD analysis of a 2-D leaky-wave planar antenna based on dipole frequency

selective surfaces", *IEEE Trans. Antennas Propag*., vol. 55, no 7, pp. 2006-2012, July 2007.

[Kuznetsov 2009]S. A. Kuznetsov, M. Navarro-Cía, V. V. Kubarev, A. V. Gelfand M. Beruete, I. Campillo, M. Sorolla, "Regular and anomalous extraordinary optical transmission at the THz-gap," Opt. Express, vol. 17, no. 14, pp. 11730-11738, July 2009.

[Lampariello 1985] P. Lampariello and A. A. Oliner, "A new leaky-wave antenna for millimeter waves using an asymmetric strip in groove guide—Part I: Theory," IEEE Trans. Antennas Propag., vol. 33, pp. 1285–1294, 1985.

[Lampariello 1987] P. Lampariello, F. Frezza, H. Shigesawa, M. Tsuji, and A. A. Oliner, "Guidance and leakage properties of offset groove guide," in 1987 IEEE MTT-S Int. Microwave Symp. Dig., pp. 731–734.

[Lampariello 1998] P. Lampariello, F. Frezza, H. Shigesawa, M. Tsuji and A.A. Oliner, "A versatile leaky-wave antenna based on stub-loaded rectangular waveguide: Part III—comparisons with measurements," *IEEE Trans. Antennas Propagat,* vol.46, no.7, pp.1047-1055, July 1998.

[Lee 1986] K. S. Lee, "Microstrip line leaky wave antenna," Ph.D. dissertation, Polytechnic Inst., Brooklyn, New York, Jun. 1986.

[Lee 2000] M. T. Lee, K. M. Luk, S. J. Xu, and E. K. N. Yung, "Leaky wave antenna based on image NRD guide with staircase shaped dielectric slab," *Electron. Lett.,* vol. 36, no. 13, pp. 1102–1103, Jun. 2000.

[Lee 2000] Y. R. Lee, A. Charaya, D. S. Lockyer, and J. C. Vardaxoglou, "Dipole and tripole metallodielectric photonic bandgap (MPBG) structures for microwave filter and antenna applications," *IEE Proc.: Optoelectron.,* vol. 127, pp. 395–400, Dec. 2000.

[Leger 2005] L. Leger, T.Monediere, and B. Jecko, “Enhancement of gain and radiation bandwidth for a planar 1-D EBG antenna,” *IEEE Microw.Wireless Compon. Lett.*, vol. 15, no. 9, pp. 573–575, Sep. 2005.

[Li 2007] Y. Li, Q. Xue, E.K.-N. Yung and Y. Long, “Circularly-polarised microstrip leaky-wave antenna,” *Elect. Lett.*, vol.43, no.14, pp.1-2, July 2007.

[Lim 2004] S. Lim, C. Caloz and T. Itoh, “Electronically-scanned composite right/left-handed microstrip leaky-wave antenna”, *IEEE Microw. Wireless Compon. Lett.*, vol.14, no.6, pp. 277- 279, June 2004.

[Lin 1997] Y.-D. Lin, J.-W. Sheen, “Mode distinction and radiation efficiency analysis of planar leaky-wave source,” *IEEE Trans. Microw. Theory Tech.*, vol. 45, no.10, pp.1672-1680, November 1997.

[Liu 2002] L. Liu, C. Caloz and T. Itoh, “Dominant mode leaky-wave antenna with backfire-to-endfire scanning capability”, *Electron. Lett.*, vol.38, no.23, pp. 1414- 1416, 7 Nov 2002.

[Liu 2009] Z.G. Liu, Z.C. Ge and X.Y. Chen, "Research progress on Fabry-Perot resonator antenna," *Journal of Zhejiang University SCIENCE A*, Vol. 10, No. 4, 583-588, 2009.

[Lomakin 2005] V. Lomakin, E. Michielssen, “Enhanced transmission through metallic plates perforated by arrays of subwavelength holes and sandwiched between dielectric slabs,” *Phys. Rev. B*, vol. 71, p. 235117- 2005.

[Lomakin 2007] V. Lomakin and E. Michielssen, “Beam transmission through periodic subwavelength hole structures,” *IEEE Trans. Antennas Propag.,* vol. 55, no. 6, pp. 1564-1581, June 2007.

[Losito 2007] O. Losito, "Design of conformal tapered leaky wave antenna," *PIERS Online*, vol. 3, no. 8, 1316-1320, 2007.

[Losito 2009] O. Losito, "The diverging-focusing properties of a tapered leaky wave antennas," *Proc. III European Conference Antennas Propag.,* pp.1304-1307, 23-27 March 2009.

[Lovat 2006] G. Lovat, P. Burghignoli, and D. R. Jackson, "Fundamental properties and optimization of broadside radiation from uniform leaky-wave antennas," *IEEE Trans. Antennas Propag.*, vol. 54, pp. 1442–1452, May 2006.

[Lovat 2006-I] G. Lovat, P. Burghignoli, F. Capolino, and D. R. Jackson, "High directivity in low-permittivity metamaterial slabs: Ray-optic vs. leaky-wave models," Microwave Opt. Techn. Lett., vol. 48, no. 12, pp. 2542–2548, Dec. 2006.

[Lovat 2006-II] G. Lovat, P. Burghignoli, F. Capolino, D. R. Jackson, and D. R. Wilton, "Analysis of directive radiation from a line source in a metamaterials slab with low permittivity," IEEE Trans. Antennas Propag., vol. 54, pp. 1017–1030, Mar. 2006.

[Luukkonen 2008] O. Luukkonen, C. Simovski, G. Granet, G. Goussetis, D. Lioubtchenko, A.V. Räisänen, and S.A. Tretyakov, "Simple and Accurate Analytical Model of Planar Grids and High-Impedance Surfaces Comprising Metal Strips or Patches", *IEEE Trans. Antennas Propag*., vol. 56, No. 6 pp. 1624-1632, June 2008.

[Ma 1993] Z. Ma and E. Yamashita, "Wave leakage from groove NRD structures," *IEEE Microw. Guided Wave Lett.,* vol. 3, no. 6, pp. 170–172, Jun. 1993.

[Ma 1994] Z. Ma and E. Yamashita, "Leakage characteristics of groove guide having a conductor strip," IEEE Trans. Microw. Theory Tech., vol. 42, no. 10, pp. 1925–1931, 1994.

[Macfarlane 1946] G.G. Macfarlane; "Surface impedance of an infinite parallel-wire grid at oblique angles of incidence," *Electrical Engineers - Part IIIA:*

Radiolocation, Journal of the Institution of , vol.93, no.10, pp.1523-1527, 1946

[Maci 2003] S. Maci, R. Magliacani, and A. Cucini, "Leaky-wave antennas realized by using artificial surfaces," *in IEEE AP-S Int. Symp. Dig.*, Columbus, OH, June 23–27, pp. 1099–1102, 2003

[Maci 2005] S. Maci, M. Caiazzo, A. Cucini, M. Casaletti, "A Pole-Zero Matching Method for EBG Surfaces Composed of a Dipole FSS Printed on a Grounded Dielectric Slab," *IEEE Trans. Antennas Propag*., vol. 53, No. 1, pp. 70-81, Jan. 2005.

[Maci 2011] S. Maci, "Metasurfing: addressing waves on metasurfaces for realizing antennas and microwave devices", *Microwave, Antenna, Propagation, and EMC Technologies for Wireless Communications (MAPE)*, 2011 IEEE 4th International Symposium on, pp. 1 – 4, 2011.

[Maci 2012] S. Maci .G. Minatti, M. Casaletti,and M. Bosiljevac , "Metasurfing: addressing waves on impenetrable metasurfaces", *IEEE Antennas Wireless Propag. Lett.*, vol.10, pp.1499-1502, Jan. 2012.

[Majumder 1997] S. Majumder, D. R. Jackson, A. A. Oliner, and M. Guglielmi, "The nature of the spectral gap for leaky waves on a periodic strip-grating structure," *IEEE Trans. Microwave Theory Tech.,* vol. 45, no. 12, pp. 2296-2307, Dec.1997

[Malherbe 1988] J. A. G. Malherbe, "A leaky-wave antenna in nonradiative dielectric waveguide," *IEEE Trans. Antennas Propag.,* vol. 36, no. 9, pp. 1231–1235, Sep. 1988.

[Marconi 1919] G. Marconi and C.S. Franklin, ''Reflector for use in Wireless Telegraphy and Telephony'', US Patent 1,301,473, April 1919.

[Marcuvitz 1951] N. Marcuvitz*, Waveguide Handbook*. New York: McGraw-Hill, 1951, pp. 179–181.

[Marqués 2002] R. Marqués, J. Martel, F. Mesa, and F. Medina, “Left-handed-media simulation and transmission of EM waves in sub-wavelength split-ring resonator loaded metallic waveguides,” Phys. Rev. Lett., vol. 89, no. 18, Oct. 2002.

[Marqués 2009] R. Marqués, F. Mesa, L. Jelinek, F. Medina, “Analytical theory of extraordinary transmission through metallic diffraction screens perforated by small holes,” *Opt. Express*, vol. 17, no. 7, pp. 5571-5579, March 2009.

[Martínez-Ros 2011] A.J. Martínez-Ros, J.L. Gómez-Tornero, and G. Goussetis, “Planar leaky-wave antenna with flexible control of the complex propagation constant,” *IEEE Trans. Antennas Propag.*, vol.60, no.3, pp.1625-1630, March 2012.

[Martinez-Ros 2012] A.J. Martinez-Ros, J.L. Gomez-Tornero, and G. Goussetis, "Planar Leaky-Wave Antenna With Flexible Control of the Complex Propagation Constant", *IEEE Trans. Antennas Propagat.*, vol.60, no.3, pp.1625-1630, March 2012

[Martínez-Ros 2012] A.J. Martínez-Ros, J.L. Gómez-Tornero, and G. Goussetis, "Flexible pattern synthesis with SIW LWAs", in *6th European Conf. on Antennas and Propagat. (EuCAP 2012)*, Prague, Czech Republic, *in press*, March 2012.

[Mateo-Segura 2011] C. Mateo-Segura, G. Goussetis and A.P. Feresidis, "Sub-Wavelength Profile 2-D Leaky-Wave Antennas With Two Periodic Layers," *IEEE Trans. Antennas Propag*,, vol.59, no.2, pp.416-424, Feb. 2011

[Mateo-Segura 2012] C. Mateo-Segura, M. Garcia-Vigueras, G. Goussetis, J.-L. Gomez-Tornero and A. P. Feresidis, "A Simple Technique for the Dispersion Analysis of Fabry-Perot Cavity Leaky-Wave Antennas,” *IEEE Trans. Antennas Propag.*, vol.60, no.2, pp.803-810, Feb. 2012

[Medina 2008] F. Medina, F. Mesa, R. Marqués, "Extraordinary Transmission Through arrays of Electrically Small Holes from a Circuit Theory Perspective," *IEEE Trans. Microw. Theory Tech.,* Vol. 56, No. 12, pp. 3108-3120, Dec. 2008.

[Medina 2009] F. Medina, J. A. Ruiz-Cruz, F. Mesa, J. Rebollar, J. R. Montejo-Garai, R. Marqués, "Experimental verification of extraordinary transmission without surface plasmons," *Appl. Phys. Lett.*, vol. 95, p. 071102, Aug. 2009.

[Medina 2010-I] F. Medina, F. Mesa, and D. C. Skigin, "Extraordinary transmission through arrays of slits: a circuit theory model," *IEEE Trans. Microwave Theory Tech.*, vol. 58, no. 1, pp. 105-115, Jan. 2010.

[Medina 2010-II] F. Medina, F. Mesa, J. A. Ruíz-Cruz, Jesús M. Rebollar, and J. R. Montejo-Garai, "Study of extraordinary transmission in a circular waveguide system," *IEEE Trans. Microw. Theory Tech*., vol. 58, no. 6, pp. 1532-1542, June 2010.

[Mentzer 1970] C. A. Mentzer and B. A. Munk, "Resonant metallic radome," Report 2382-21, June 1970, Ohio State Univ. ElectroScience Lab., Columbus, OH, Rep. 2382-21, June 1970 (prepared under Contract F33615-67-C-1507 for Air Force Avionics Laboratory, Wright-Patterson Air Force Base, OH (AD 509525) (AFAG TR-70-86)).

[Menzel 1979] W. Menzel, "A new travelling-wave antenna in microstrip," *Archiv. Electrnik, Ubertrag Tech.,* pp. 137–140, Apr. 1979.

[Mesa 2002-I] F. Mesa, D.R. Jackson and M.J. Freire; "Evolution of leaky modes on printed-circuit lines," *IEEE Trans. Microw. Theory Tech.,* vol.50, no.1, pp.94-104, Jan 2002.

[Mesa 2002-II] F. Mesa and D.R. Jackson, "Investigation of integration paths in the spectral-domain analysis of leaky modes on printed circuit lines,"

IEEE Trans. Microw. Theory Tech., vol.50, no.10, pp. 2267- 2275, Oct 2002.

[Meyer 1934] C.F. Meyer, The Diffraction of Light, X-rays, and Material Particles, *The University Press*, Chicago, 1934.

[Miles 1946] J. W. Miles, "The equivalent circuit for a plane discontinuity in a cylindrical waveguide," *Proc. IRE*, vol. 34, pp. 728–742, Oct. 1946.

[Minatti 2011-I] G. Minatti, M. Casaletti, F. Caminita, P. De Vita, S. Maci, "Planar antennas based on surface-to-leaky wave transformation", *in 5th European Conf. on Antennas and Propagat. (EuCAP 2011)*, Rome, Italy, pp. 2033 – 2036, April 2011.

[Minatti 2011-II] G. Minatti, F. Caminita, M. Casaletti, S. Maci, "Spiral leaky-wave antennas based on modulated surface impedance," *IEEE Trans. Antennas Propagat*, vol. 59, no.12, pp. 4436 - 4444, Dec.2011.

[Mittra 1988], R. Mittra, C. H. Chan, T. Cwik,, "Techniques for analyzing frequency selective surfaces-a review," *Proceedings of the IEEE*, vol.76, no.12, pp.1593-1615, Dec 1988.

[Moreno 2006] E. Moreno, L. Mart´ın-Moreno, F. J. Garc´ıa-Vidal, "Extraordinary optical transmission without plasmons: the s-polarization case," *J. Opt. A: Pure Appl. Opt.*, vol. 8, p. S94-S97, 2006.

[Moustafa 2008] L. Moustafa and B. Jecko, "EBG structure with wide defect band for broadband cavity antenna applications," *IEEE Antenna Wireless Propag. Lett.*, vol. 7, pp. 693–696, 2008.

[Muhammad 2012] S. Muhammad, R. Sauleau and H. Legay, "Small-Size Shielded Metallic Stacked Fabry-Perot Cavity Antennas with Large Bandwidth for Space Applications," *IEEE Trans. Antennas Propagat.*, in press.

[Munk 1971] B. A. Munk, R. G. Kouyoumjian, and L. Peters, Jr., "Reflection properties of periodic surfaces of loaded dipoles," *IEEE Trans. Antennas Propagat*., vol. AP-19, no. 5, pp. 612-617, Sept. 1971.

[Munk 1974] B. A. Munk, "Periodic surface for large scan angles", United States Patent 3,789,404, Jan. 1974.

[Munk 1976] B. A. Munk and R. D. Fulton, "Transmission Through a Bi-Planar Slot Array Sandwiched Between Three Dielectric Layers, March 1973-Nov. 1975," Tech. Rept. 3622-7, Ohio State Univ. ElectroScience Lab., Dept. of Electrical Eng., Columbus, Feb. 1976.

[Munk 1977] B. A. Munk, G. A. Burrell, and T. W. Kornbau, "A General Theory of Periodic Surfaces in Stratified Media," Tech. Rept. 784346-1, Ohio State Univ. Electro Science Lab., Dept. of Electrical Eng., prepared under contract AFAL-TR-77-2 19, Nov. 1977.

[Munk 1979] B. A. Munk and G. A. Burrell, "Plane Wave Expansion for Arrays of Arbitrarily Oriented Piecewise Linear Elements and Its Application in Determining the Impedance of a Single Linear Antenna in a Lossy Half-Space,'' *IEEE Trans. Antennas Propag.,* vol.27, no.3, pp. 331-343, May 1979.

[Munk 2000] B. A. Munk, *Frequency Selective Surfaces*: Theory and Design, John Wiley and Sons, 2000.

[Nannetti 2007] M. Nannetti, F. Caminita, S. Maci. "Leaky-wave based interpretation of the radiation from holographic surfaces", *Antennas and Propagat Int. Symp*. 2007, 9-15 June 2007, pp. 5813 – 5816.

[O'Nians 1966] F. O'Nians and J. Matson, "Antenna feed system utilizing polarization independent frequency selective intermediate reflector," U.S. Patent 3-231-892, Jan. 1966.

[Ohtera 1999] I. Ohtera, “Diverging/focusing of electromagnetic waves by utilizing the curved leaky wave structure: Application to broad-beam antenna for radiating within specified wide-angle,” IEEE Trans. Antennas Propagat., vol. 47, pp. 1470–1475, Sep. 1999.

[Ohtera 2001] I. Ohtera, “On a forming of cosecant square beam using a curved leakywave structure,” IEEE Trans. Antennas Propagat., vol. 49, pp. 1004–1006, Jun. 2001.

[Ohtera 2002] I. Ohtera, “Estimation of the radiation patterns of diverging/focusing type of leakywave antennas,” Microwave Opt. Technol. Lett., vol. 33, pp. 358–360, Jun. 2002.

[Oliner 1959] A. A. Oliner and A. Hessel, “Guided waves on sinusoidally-modulated reactance surfaces,” *IRE Trans. Antennas Propag.*, vol. 7, pp. 201–208, Dec. 1959.

[Oliner 1960] A. A. Oliner, “Equivalent circuit for small symmetrical longitudinal apertures and obstacles,” *IRE Trans. Microw. Theory Tech*., vol. 8, pp. 72–80, Jan. 1960.

[Oliner 1979] A. A. Oliner and S. T. Peng, "A New Class of Leaky Modes on Open Dielectric Waveguides," 1979, pp. 569-571.

[Oliner 1985] A. A. Oliner, S. T. Peng, and K. M. Shang, “Leakage from a gap in NRD guide,” in *Proc. IEEE MTT Int. Microwave Symp. Dig.,* 1985, pp. 619–622.

[Oliner 1986-I] A. A. Oliner and K. S. Lee, "The Nature of the Leakage from Higher Modes on Microstrip Line," *IEEE MTT-S International Microwave Symposium Digest 1986*, pp.57-60, 2-4 June 1986

[Oliner 1986-I] A. A. Oliner and K. S. Lee, “The nature of the leakage from higher modes on microstrip line*,” in Int. Microwave Symp. Dig., MTT-S*, vol. 86, pp. 57–60*,* Jun. 1986.

[Oliner 1986-II] A. A. Oliner and K. S. Lee, "Microstrip leaky wave strip antennas," *in IEEE AP-S Int. Symp. Dig.*, Philadelphia, PA, pp. 443–446, Jun. 1986.

[Oliner 1987] A. A. Oliner, "Leakage from higher modes on microstrip line with application to antennas," *Radio Sci.*, vol. 22, no. 6, pp. 907–912, Nov. 1987.

[Oliner 1993] A. A. Oliner, "Leaky-Wave antennas," in *Antenna Engineering Handbook*, 3rd ed, R. C. Hansen, Ed. New York: McGraw-Hill, 1993, ch.10.

[Ortuo 2010] R. Ortuo, C. García-Meca, F. J. Rodríguez-Fortuo, J. Martí , A. Martínez, "Multiple extraordinary optical transmission peaks from evanescent coupling in perforated metal plates surrounded by dielectrics," *Opt. Express*, vol. 18, no. 8, pp. 7893-7898, April 2010.

[Palocz 1970] I. Palocz and A. A. Oliner, "Equivalent network of a multimode planar grating," *IEEE Trans. Microw. Theory Tech*., vol. 18, pp. 244–252, May 1970.

[Parker 1981] E.A. Parker and S.M.A. Hamdy, "Rings as elements for frequency selective surfaces," *Electron. Lett*., vol. 17, no. 17, pp. 612–614, Aug. 1981

[Parker 2001] E.A. Parker, A.D. Chuprin, J.C. Batchelor and S.B. Savia, "GA optimisation of crossed dipole FSS array geometry," *Electronics Letters* , vol.37, no.16, pp.996-997, 2001

[Pelton 1976] E. L. Pelton and B. A. Munk, "Periodic antenna surface of tripole slot elements", United States Patent 3,975,738, Aug. 1976.

[Pendry 2004] J. B. Pendry, L. Mart´ın-Moreno, and F. J. Garcia-Vidal, "Mimicking surface plasmons with structured surfaces," *Science*, vol. 305, pp. 847- 848, Aug. 2004.

[Pendry 2006] J. B. Pendry, D. Schurig, D.R. Smith "Controlling Electromagnetic field", Science , Vol. 312 no. 5781 pp. 1780-1782, 23 June 2006.

[Perruisseau-Carrier 2008] J. Perruisseau-Carrier and A. K. Skrivervik, "Monolithic MEMSbased reflectarray cell digitally reconfigurable over a 360° phase range," IEEE Antennas Wireless Propagat. Lett., vol. 7, pp. 138-141, 2008.

[Pozar 1997] Pozar, D. M., S. D. Targonski, and H. D. Syrigos, "Design of millimeter wave microstrip reflectarrays," *IEEE Trans. Antennas Propag.,* Vol. 45, No. 2, pp. 287-296, Feb. 1997.

[Pozar 2005] D. M. Pozar, *Microwave Enginnering*, (3rd Ed.) Hoboken, NJ: Wiley, 2005.

[Rayleigh 1907-I] Lord Rayleigh, "On the Dynamical Theory of Gratings", *Proc.Roy.Soc. (London),* A79, p. 399, 1907.

[Rayleigh 1907-II] Lord Rayleigh, "Note on the remarkable case of diffraction spectra described by Prof. Wood," *Philos. Mag.*, 14, pp. 60–65, 1907.

[Richmond 1974] J. H. Richmond, "Radiation and scattering by thin-wire structures in the complex frequency domain," Nat. Aeron. Space Admin., NASA CR-2396, May 1974.

[Ritchie 1957] R. H. Ritchie "Plasma losses by fast electrons in thin films", *Phys. Rev.*, vol. 106, pp.874 1957

[Rittenhouse 1786] D. Rittenhouse, "An optical problem, proposed by Mr. Hopkins, and solved by Mr. Rittenhouse", *Transaction of the American Philosophical Society*, Vol. 2, pp. 201-206, 1786.

[Rodríguez-Berral 2010] R. Rodríguez-Berral, F. Mesa, and F. Medina, "Circuit model for a periodic array of slits sandwiched between two dielectric slabs," *Appl. Phys. Lett.*, vol. 96 (16), pp. 161104(1–3), 2010.

[Romanofsky 2006] R. Romanofsky, “Special issues and features of a scanning reflectarray antenna based on ferroelectric thin film phase shifters,” in 1st European Conference on Antennas and Propagation (EuCAP 2006), Nice, France, 2006.

[Sánchez 1987] A. Sanchez and A. A. Oliner, "A New Leaky Waveguide for Millimeter Waves using Nonradiative Dielectric (NRD) Waveguide. Part I: Accurate Theory IEEE *Trans. Microw. Theory Tech.*, 35(8), pp. 737-747, 1987.

[Schuchinsky 2005] A. G. Schuchinsky, D. E. Zelenchuk, and A. M. Lerer, “Enhanced transmission in microwave arrays of periodic sub-wavelength apertures,” *J. Opt. A: Pure Appl. Opt.*, vol. 7, pp. S102-S109, 2005.

[Schwering 1983] F. K. Schwering and S. T. Peng, “Design of dielectric grating antennas for millimeter-wave applications,” IEEE *Trans. Microw. Theory Tech.*, Vol. 31, pp.199–209, 1983.

[Schwering 1983] F.K. Schwering and Song-Tsuen Peng, "Design of Dielectric Grating Antennas for Millimeter-Wave Applications," *IEEE Trans. Microw. Theory Tech.,* vol.31, no.2, pp.199-209, Feb. 1983.

[Schwering 1988] F. K. Schwering, and A. A. Oliner, "Millimeter-Wave Antennas", Chapter 17, vol. 3, Antennas Handbook, edited by Y. T. Lo and S. W. Lee, New York: Van Nostrand Reinhold, 1988, Ch. 17.

[Seager 1999] R. D. Seager and J. C. Vardaxoglou, "Characterisation of leaky wave antennas constructed from solid rectangular waveguides with a dipole frequency selective surface sidewall," *in IEE National Conference on Antennas and Propagation,* York, 31March-1 April 1999.

[Seman 2011] F. C. Seman, R. Cahill, V. F. Fusco, and G. Goussetis, “Design of a Salisbury screen absorber using frequency selective surfaces to improve bandwidth and angular stability performance,” *IET Microw. Antennas Propagat.*, vol. 5, no. 2, pp. 149-156, Jan. 2011.

[Shigesawa 1993] H. Shigesawa, M. Tsuji, and A. A. Oliner, "The nature ofthe spectral gap between bound and leaky solutions when dielectric loss is present in printed-circuit lines," *Radio Science*, vo1.28, no.6, pp.1235-1243, Nov.-Dec. 1993

[Shigesawa 1995] H. Shigesawa, M. Tsuji, and A. A. Oliner, "Simultaneous propagation of bound and leaky modes on printed-circuit lines: A general effect," *IEEE Trans. Microwave Theory Tech.,* vol. MTT-43, pp. 3007-3019, Dec. 1995.

[Shumpert 1999] Shumpert, J.D.; Chappell, W.J.; Katehi, L.P.B.; , "Parallel-plate mode reduction in conductor-backed slots using electromagnetic bandgap substrates," *IEEE Trans. Microw. Theory Tech*., vol.47, no.11, pp.2099-2104, Nov 1999.

[Sievenpiper 1999] D. Sievenpiper, L. Zhang, F. J. Broas, N. G. Alexopulos, and E. Yablonovitch, "High-impedance electromagnetic surfaces with a forbidden frequency band," *IEEE Trans. Microw. Theory Tech*, vol. 47, no. 11, pp. 2059–2074, Nov. 1999.

[Sievenpiper 2002] D. Sievenpiper, J. Schaffner, J.J. Lee, and S. Livingston, "A steerable leaky-wave antenna using a tunable impedance ground plane", *IEEE Antennas Wireless Propag. Lett.,* vol.1, no.1, pp.179-182, 2002.

[Sievenpiper 2003] D. Sievenpiper, J. Schaffner, H. Song, R. Loo, and G. Tangonan, "Two-dimensional beam steering using an electrically tunable impedance surface," IEEE Trans. Antennas and Propagat., vol. 51, no. 10, pp. 2713 – 2722, Oct. 2003.

[Sievenpiper 2005] D. Sievenpiper, J. Colburn, B. Fong, J. Ottusch, J. Visher, "Holographic artificial impedance surfaces for conformal antennas", IEEE APS/URSI Symposium, Washington, DC, July 2005.

[Sun 2012] Y. Sun, Z.N. Chen, Y. Zhang, H. Chen and T.S.P. See, "Subwavelength Substrate-Integrated Fabry-Pérot Cavity Antennas Using Artificial

Magnetic Conductor", *IEEE Trans. Antennas Propagat*., vol.60, no.1, pp.30-35, Jan. 2012

[Sutinjo 2008] A. Sutinjo, M. Okoniewski and R.H. Johnston, R.H., "Beam-Splitting Condition in a Broadside Symmetric Leaky-Wave Antenna of Finite Length," *IEEE Antennas Wireless Propag. Lett,*, vol.7, no., pp.609-612, 2008

[Takahashi 1991] J M. Takahashi, J.-I. Takada, M. Ando, and N. Goto, " A slot design for uniform aperture field distribution in single-layered radial line slot antennas," *IEEE Trans. Antennas Propagat*, Vol.39, No.7, pp. 954–959, July 1991.

[Tamir 1963-I] T. Tamir and A. A. Oliner, "Guided complex waves. Part 1: Fields at an interface," *Proc. Inst. Elec. Eng*., Vol. 110, pp. 310-324, no. 2, Feb. 1963

[Tamir 1963-II] T. Tamir, A. A. Oliner, "Guided Complex Waves, Part II: Relation to Radiation Patterns," *Proc. Inst. Elec. Eng*., Vol. 110, pp. 325-334, no. 2, Feb. 1963.

[Tamir 1969] T. Tamir, *Antenna Theory, Part II*, R. E. Collin and R. F. Zucker, Eds. New York: McGraw-Hill, 1969, chap. 20.

[Temelkuaran 2000] B. Temelkuaran, M. Bayindir, E. Ozbay, R. Biswas, M. M. Sigalas, G. Tuttle, and K. M. Ho, "Photonic crystal-based resonant antenna with a very high directivity," *J. Appl. Phys.,* vol. 87, no. 1, pp. 603–605, Jan. 2000.

[Thèvenot 1999] M. Thèvenot, C. Cheype, A. Reineix, and B. Jecko, "Directive photonic bandgap antennas," *IEEE Trans. Microw. Theory Tech.,* vol. 47, no. 11, pp. 2115–2122, Nov. 1999.

[Trentini 1956] G. V. Trentini, "Partially reflective sheet arrays," *IRE Trans. Antennas Propag.*, vol. AP-4, pp. 666–671, 1956

[Tretyakov 2003] S. A. Tretyakov, *Analytical Modeling in Applied Electromagnetics*. Norwood, MA: Artech House, 2003.

[Tsuji 2003] M. Tsuji, T. Harada, H. Deguchi, and H. Shigesawa, "Frequency-scanning antennas with low sidelobes using stub-loaded ridge-rectangular leaky waveguides," *2003 IEEE Topical Conference on Wireless Communication Technology*, pp.352-353, 2003.

[Tsuji 2007] M. Tsuji and H. Deguchi, "Stub-loaded ridge waveguides for frequency-scanning antenna application," *Dig. IEEE Antennas and Propag. Int. Symp*., pp.449-452, 9-15 June 2007

[Ulrich 1967-I] R. Ulrich, "Far-infrared properties of metallic mesh and its complementary structure," *Infrared Phys*., vol. 7, pp. 37-55, 1967.

[Ulrich 1967-II] R. Ulrich, "Effective low-pass filters for far infrared frequencies," *Infrared Phys*., vol. 7, pp. 65-74, 1967.

[Vardaxoglou 1997] John C. Vardaxoglou, *Frequency selective surfaces analysis and design*. Taunton Research Studies, 1997

[Varela 2012] J.E. Varela and J. Esteban, "Characterization of Waveguides With a Combination of Conductor and Periodic Boundary Contours: Application to the Analysis of Bi-Periodic Structures," *IEEE Trans. Microw. Theory Tech.,* vol.60, no.3, pp.419-430, March 2012.

[Veselago 1968] V.G. Veselago, "The electrodynamics of substances with simultaneously negative values of *e* and *μ*", *Soviet Physical Uspekhi*, vol.10, no.6, pp. 510–514. Jan. 1968.

[Vu 2007] T. H. Vu, K.Mahdjoubi, A. C. Tarot, and S. Collardey, "Bandwidth enlargement of planar EBG antennas," in *Proc. Loughborough Antennas Propag. Conf.*, Loughborough, U.K., pp. 125–128, Apr. 2007.

[Walter 1965] C. H. Walter, *Traveling Wave Antennas*, McGraw-Hill, New York, 1965.

[Weily 2007] A.R. Weily, K.P. Esselle, T.S. Bird, and B.C. Sanders, "Dual resonator 1-D EBG antenna with slot array feed for improved radiation bandwidth," *IET Microw. Antennas Propag.*, vol. 1, no. 1, pp. 198–203, 2007.

[Wexler 1967] A. Wexler, "Solution of waveguide discontinuitites by modal analysis," *IEEE Trans. Microw. Theory Tech*., vol. MTT–15, no. 9, pp. 508–517, Sept. 1967.

[Wood 1902] R. W. Wood, "On a remarkable case of uneven distribution of light in a diffraction grating spectrum," *Philos. Mag*., 4, pp. 396–402, 1902.

[Wood 1912] Wood, R. W. "Diffraction gratings with controlled groove form and abnormal distribution of intensity". *Philos. Mag*., 23, pp. 310-317; 1912.

[Wu 2010] Zhi-Hang Wu and Wen-Xun Zhang, "Broadband Printed Compound Air-Fed Array Antennas," *IEEE Antennas and Wireless Propag. Lett.*, vol.9, pp.187-190, 2010.

[Xu 1998] S. J. Xu, X.-Y. Zeng, K. Wu and K.-M. Luk, "Characteristics and design consideration of leaky-wave NRD-guides for use as millimeter-wave antenna," *IEEE Trans. Microw. Theory Tech.,* vol. 46, pp. 2450–2456, Dec. 1998.

[Yamamoto 1999] M. Yamamoto and K. Itoh, "Resonant type leaky-wave antenna using image NRD guide," *Elect. Lett.*, vol.35, no.11, pp. 857- 858, 27 May 1999.

[Yang 1987] H. Y. Yang and N. G. Alexopoulos, "Gain enhancement methods for printed circuit antennas through multiple superstrates," *IEEE Trans. Antennas Propag.,* vol. AP-35, no. 7, pp. 860–863, Jul. 1987.

[Yang 1999] F. R. Yang, K.-P. Ma, Y. Qian, T. Itoh, "A Novel TEM Waveguide Using Uniplanar Compact Photonic-Bandgap (UC-PBG) Structure," *IEEE*

Trans. Microw. Theory Tech., Vol. 47, No. 11, pp. 2092-2098, Nov. 1999.

[Yeo 2009] J. Yeo and D. Kim, "Novel Design of a High-gain and Wideband Fabry-Perot Cavity Antenna Using a Tapered AMC Substrate," *J. Infrared Milli. Terahz. Waves*, vol. 30, no. 3, pp. 217-224, March 2009.

[Yoneyama 1981] T. Yoneyama and S. Nishida, "Nonradiative dielectric waveguide for millimeter-wave integrated circuits," *IEEE Trans. Microw. Theory Tech.,* vol. 29, pp. 1188–1192, Nov. 1981.

[Zhang 2007] W. X. Zhang, D. L. Fu and A. N.Wang, "A compound printed air-fed array antenna," *in Proc. Int. Conf. Electromagn. Adv. Appl.*, Torino, Italy, Sep. 2007, pp. 1054–1057.

[Zhao 2004] T. Zhao, D. R. Jackson, J. T. Williams, and A. A. Oliner, "Simple CAD model for a dielectric leaky-wave antenna," I*EEE Antennas Wireless Propag. Lett.*, vol. 3, pp. 243–345, Dec. 2004.

[Zhao 2005-I] T. Zhao, D. R. Jackson, J. T. Williams, and A. A. Oliner, "General formulas for 2D leaky-wave antennas," *IEEE Trans. Antennas Propagat.*, vol. 53, No.11, pp.3525–3533, Nov. 2005.

[Zhao 2005-II] T. Zhao, D.R Jackson, J.T. Williams, H.-Y.D Yang, A.A Oliner, "2-D periodic leaky-wave antennas-part I: metal patch design," *IEEE Trans. Antennas Propag*, Vol. 53, No 11, pp. 3505-3514, Nov. 2005.

[Zhao 2005-III] T. Zhao, D. R. Jackson and J. T. Williams, "2-D periodic leaky-wave antennasVPart II: Slot design," *IEEE Trans. Antennas Propag.,* vol. 53, no. 11, pp. 3515–3524, Nov. 2005.

[Zong-Wen 1997] L. Zong-Wen and L. Gui-Sheng, "A 35 GHz low side-lobe leaky-wave antenna with periodic metallic grating structures of nonuniform width on the dielectric waveguide," *Proc. Asia-Pacific Microw. Conf.*, pp.641-644 vol.2, 2-5 Dec 1997.